LIGHT METAL BOROHYDRIDES AND Mg-BASED HYDRIDES FOR HYDROGEN STORAGE

by

SHENG GUO

A thesis submitted to the University of Birmingham
for the degree of

DOCTOR OF PHILOSOPHY

School of Metallurgy and Materials
College of Engineering and Physical Sciences
University of Birmingham
December 2014

UNIVERSITY OF BIRMINGHAM

University of Birmingham Research Archive

e-theses repository

Synopsis

This work has investigated structural and compositional changes in $LiBH_4$, $Mg(BH_4)_2$, $Ca(BH_4)_2$, $LiBH_4$-$Ca(BH_4)_2$ during heating. The crystal and vibrational structures of these borohydrides/composites were characterized using lab-based X-ray diffraction (XRD) and Raman spectroscopy, with particular attention to the frequency/width changes of Raman vibrations of different polymorphs of borohydrides.

The thermal stability and decomposition pathway of the borohydrides was studied in great detail mainly using differential scanning calorimetry (DSC) and thermogravimetric analysis (TGA), in/ex situ XRD and Raman measurements, whilst the gaseous products during heating were monitored using a mass spectrometry (MS). Hydrogen is the main decomposition gaseous product from all of these compounds, but in some cases a very small amount of diborane release was also detected. These studies suggest that the thermal decomposition of the metal borohydrides occurs via a wide range of reaction pathways, often in several steps, which may involve simultaneous, and in some cases coupled, competing reactions. This can include the formation of stable borane intermediates/by-products which largely precludes the possibility of reversibility. Furthermore, the role of diborane in the decomposition and formation of borohydrides, was later studied by heating metal borohydrides (or hydrides) to various temperatures in a gaseous diborane-hydrogen atmosphere; and different types of borane products were observed.

Attempts to synthesise Mg-B-Ti-H ternary hydrides which can store up to 10.6 wt% H_2 in a bulk powder form, were made in this work, by ball-milling mixtures of $0.4MgH_2+0.6B$, and

0.36MgH$_2$+0.58B+0.06TiX (TiX = Ti, TiH$_2$ or TiCl$_3$) in 100 bar H$_2$. As a result, a single-phase material has not yet been produced, as the composition and ball-milling conditions need to be further optimised. One of the MgH$_2$-B-Ti samples exhibited a 110 °C reduction in hydrogen desorption temperature and accelerated hydrogen sorption kinetics.

Finally, high-energy reactive milling of a Li-Mg ribbon alloy was carried out in 100 bar H$_2$, to attempt to directly insert H atoms into the sites of the ordered Li-Mg alloy phase. After milling, the majority of the Li-Mg phase was hydrogenated to form LiH and Mg$_{(1-x)}$Li$_x$H$_2$ (x = ~0.04) phases. In addition, MS shows a small release of H$_2$ at around 425 °C, which might suggest the formation of a minor Li-Mg-H phase. Although this dehydrogenation temperature is too high for mobile hydrogen storage, it may have properties that are of interest for other applications such as heat storage and electrodes in lithium batteries.

In summary, this investigation has showed for a number of light metal borohydrides and Mg-based hydride materials with good hydrogen storage capacities, that the hydrogen sorption process(es) is very complex. A better understanding of constituent phases and reaction pathways for sorption reversibility is required, before practical hydrogen media can be produced.

Acknowledgements

List of Abbreviations

ATR	Attenuated Total Reflectance
BEV	Battery-electric Vehicle
CCD	Charge-Coupled Device
CcH_2	Cryo-compressed Hydrogen
CGH_2	Compressed Gaseous Hydrogen
DFT	Density Functional Theory
DOE	US Department of Energy
DSC	Differential Scanning Calorimetry
FCEV	Fuel Cell Electric Vehicle
FTIR	Fourier Transform Infrared
ICE	Internal Combustion Engine
ICSD	Inorganic Crystal Structure Database
IEA	International Energy Agency
LH_2	Liquid Hydrogen
MOF	Metal-Organic Framework
MS	Mass Spectrometry
NMR	Nuclear Magnetic Resonance
PCT	Pressure-Composition-Temperature
PEC	Photo-electrochemical
PEMFC	Proton Exchange Membrane Fuel Cell
PLD	Pulsed Laser Deposition
PSD	Position Sensitive Detector
SEM	Scanning Electron Microscope
SMR	Steam Methane Reformation
TEM-EELS	Transmission Electron Microscopy - Electron Energy Loss Spectroscopy
TGA	Thermogravimetric Analysis
TPD	Temperature Programmed Desorption
XRD	X-ray Diffraction

Contents

1 Introduction

More than 80 % of the global energy consumption, is today supplied by fossil fuels in the form of coal, oil and natural gas (International Energy Agency, 2013). Due to a rapid growth in world population and industrialization (primarily in developing countries), finite fossil fuel resources cannot continue to be the primary source to meet the increasing energy demand. The combustion of fossil fuels also raises an equally (or arguably even more) severe problem: air quality deterioration and release of greenhouse gases (e.g. CO_2, NO_x) leading to climate change. As the source responsible for two-thirds of CO_2 emissions, the energy sector will be pivotal in determining whether or not climate change targets (limiting warming to 2 °C by the year 2035) can be achieved (International Energy Agency, 2013).

One option for lowering CO_2 emissions is to switch to CO_2-neutral energy sources, such as renewable energy generated from wind, solar, wave or geothermal. The share of global electricity produced from renewables was about 20 % in 2011, and is targeted to increase to 31 % by 2035 (International Energy Agency, 2013). Unfortunately, these renewable sources are intermittent, while energy consumption relies on periodic demand. Hence, the energy has to be stored to allow utilization when needed. Therefore, energy carriers, which are safe, efficient, and low-cost for applications (e.g. power production and transport), are required.

Hydrogen has drawn attention as a potential future energy carrier for mobile and stationary applications due to: its high gravimetric energy density of 120 MJ/kg (i.e. 2-3 times of natural gas or gasoline); and being a non-polluting fuel (H_2O and energy are the only by-products) at the point of use (Satyapal *et al.*, 2007). However, on a volume basis, hydrogen

has only about a quarter of the energy density of gasoline (8 MJ/L for liquid hydrogen versus 32 MJ/L for gasoline (**Figure 1.1**). This constitutes a fundamental drawback and a major challenge for hydrogen to be used in an efficient manner.
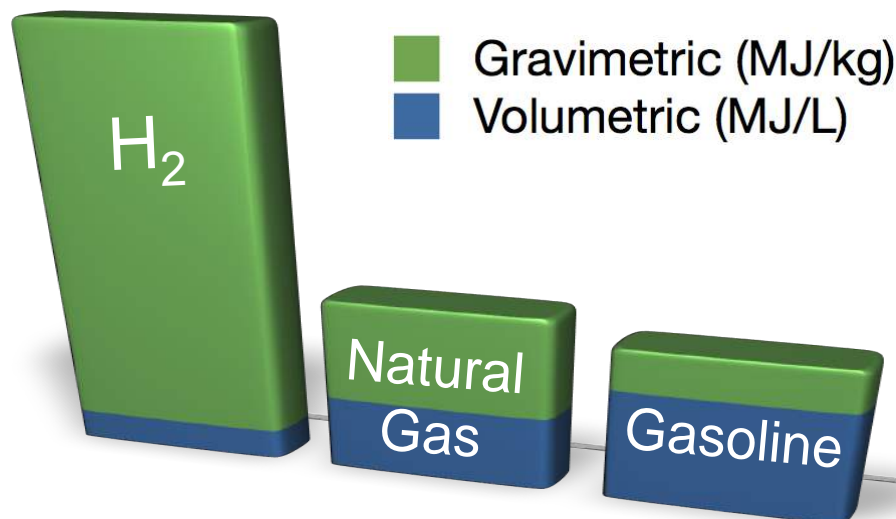
Figure 1.1 Comparison of energy densities by weight (MJ/kg) and volume (MJ/L) for hydrogen, natural gas and gasoline. Data was from National Renewable Energy Laboratory (2000).

1.1 Hydrogen production

Hydrogen is the simplest and most abundant element in the universe, and exists in stable compounds on Earth such as water and various organic compounds (e.g. fossil fuels). Although hydrogen very rarely occurs naturally on Earth in its pure molecular form, it can be produced via thermochemical, electrolytic or photolytic processes with or without CO_2 capture (US Department of Energy, 2014b).

1.1.1 Natural gas reformation

The majority of the hydrogen produced today is made via steam reformation of methane (SMR) (Borgschulte *et al.*, 2008). A mature SMR process involves two reactions. At high temperatures of 700-1100 °C, H_2O steam reacts with methane (CH_4) in the presence of a catalyst (e.g. Ni), to produce H_2 and CO (Equation 1.1). Heat for the reaction to proceed must be supplied by burning natural gas, which contributes further CO_2 emission. More

hydrogen along with side-product CO_2 is obtained by a subsequent gas-shift reaction of H_2O steam and CO using a catalyst (Equation 1.2). In the final step, CO_2 and other impurities are removed from the gas stream, leaving essentially pure hydrogen.

$$CH_4 + H_2O \rightarrow CO + 3H_2 \qquad \Delta H = 206 \text{ kJ/mol} \qquad (1.1)$$

$$CO + H_2O \rightarrow CO_2 + H_2 \qquad \Delta H = \text{-41 kJ/mol} \qquad (1.2)$$

Using some other hydrocarbons source (e.g. coal), a partial oxidation reaction is needed together with steam reformation and water gas shift reactions, known as "gasification". As the gasification process relies on the use of fossil fuels and the yield of CO_2, it cannot be considered a sustainable long-term solution. However, the principle of this technology can be applied to produce H_2 from carbon-containing sources, e.g. biomass and organic waste. If the side-product CO_2 can be completely sequestered, this technology would currently be the most efficient and lowest cost method of producing hydrogen (Borgschulte *et al.*, 2008).

1.1.2   Water electrolysis

Electrolysis is a process by which water is split into its constituents, hydrogen and oxygen, using electricity and an electrolyser device. An electrolyser is composed of an anode and a cathode separated by electrolyte. Alkaline solution (typically 20-40 % potassium hydroxide aqueous solution) or solid-polymer electrolytes are used in order to accelerate the electrolysis rate, compared to water on its own (Borgschulte *et al.*, 2008).

$$2H_2O \rightarrow 2H_2 \text{ (cathode)} + O_2 \text{ (anode)} \qquad (1.3)$$
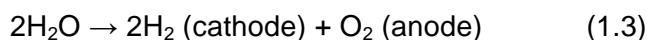
High-purity hydrogen production via electrolysis is a near-zero greenhouse gas emissions process and may be used to compensate for the intermittency of the electricity supply, if the electricity is generated from renewable sources (e.g. wind and solar) and nuclear power. However, the cost of the hydrogen production using electricity from renewable sources is very high: estimated to be US \$17-30 /GJ by wind power compared to US \$3-8/GJ for using fossil fuels as sources of energy in 2020 (Winter, 2004). Moreover, the efficiency and

emission impact of the electricity used in the electrolysis must be evaluated, as today's power grid is mostly produced from fossil fuels and is still struggling to fulfil the increasing energy demand.

1.1.3   Emerging processes

Photolytic processes are able to split water into hydrogen and oxygen by using solar energy in photo-electrochemical or photo-biological reactions. In the photo-electrochemical (PEC) system, a semiconductor absorbs solar photons to generate sufficient voltage to dissociate water (Hisatomi *et al.*, 2014); whereas in the photo-biological process, specialised microorganisms (e.g. green or purple algae) consume water and produce hydrogen as a byproduct of their natural metabolic processes, just as plants produce oxygen during photosynthesis (US Department of Energy, 2014b).

High-temperature water splitting is a thermochemical process in which water is directly dissociated to H_2 and O_2 at temperatures in excess of 2000 °C heated by a solar concentrator, or up to about 1000 °C by next-generation nuclear reactors (Borgschulte *et al.*, 2008). Intermediate compounds, e.g. ZnO (X in Equation 1.4 and 1.5) are used for a more efficient production:

$$H_2O + 2X \rightarrow 2XH + 0.5O_2 \qquad (1.4)$$

$$2XH \rightarrow 2X + H_2 \qquad (1.5)$$
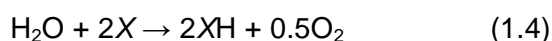
Most of these emerging processes are currently at an early research state, and so the problems of high material costs and the low production efficiencies have yet to be solved. However, these processes are promising in the long-term for the sustainable production of hydrogen with a low environmental impact.

1.2   Hydrogen as a fuel

Hydrogen can generate energy by: the combustion in conventional engines, e.g. internal combustion engine (ICE) and turbines; or, more efficiently, by electrochemical conversion in a fuel cell. The use of hydrogen as a fuel is especially important in the transportation sector, as transport is responsible for 25% of CO_2 emissions in 2012, and 36% of total consumption of final energy products in 2013 (Department of Energy & Climate Change, 2014).

1.2.1   Hydrogen internal combustion engines (HICE)

ICEs produce mechanical power by direct combustion of hydrogen, in the same manner as gasoline-powered engines, but with emissions of low levels of NO_x and no other greenhouse gases. The hydrogen ICE can be obtained from a petroleum ICE with minor modifications, and is capable of running on multi-fuels, which is a simpler and less expensive solution compared to fuel cells in the near term (White *et al.*, 2006). However, the limited efficiency of HICE (20-25%) means that twice as much hydrogen as for a fuel cell car is required, for the same driving range. Therefore, few car manufacturers (e.g. Mazda) maintain the development of HICE as an intermediate step until fuel cells become commercially viable (Parrott).

1.2.2   Hydrogen fuel cells

A fuel cell is an electrochemical device that can convert chemical energy into electricity. Proton exchange membrane fuel cells (PEMFCs) using hydrogen as fuel, have received particular attention for mobile applications. They are lightweight with excellent efficiencies of up to 60 % depending on waste heat, as well as with fast start-up times and a low operating temperature of 40-90 °C (Studer *et al.*, 2008). More importantly, it generates power with only the by-products of water and heat. A schematic of a PEMFC is shown in **Figure 1.2**.
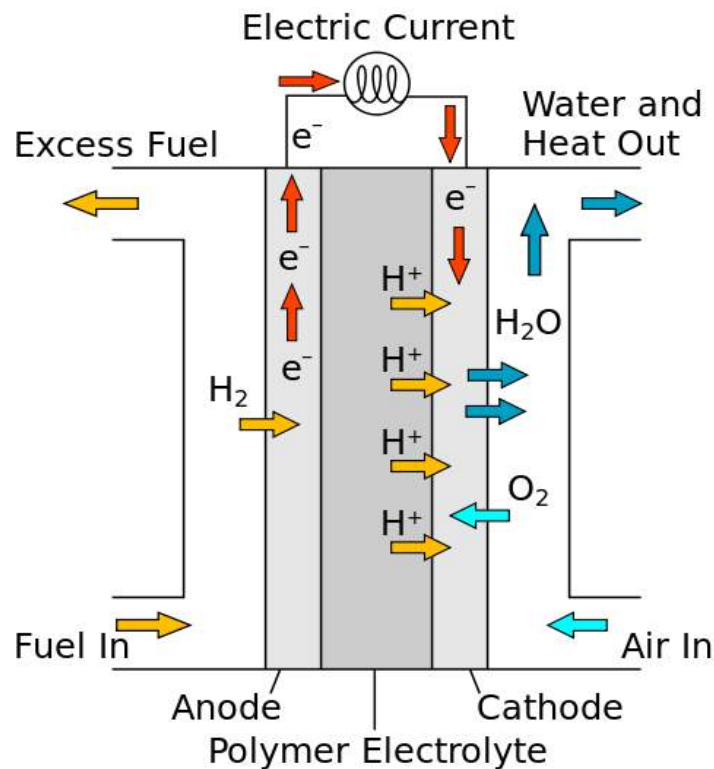
Figure 1.2 PEM fuel cell, adapted from (US Department of Energy, 2012).

In PEM fuel cells, H_2 is dissociated into protons and electrons by a catalyst (typically Pt) at the anode. The protons travel through a polymer electrolyte membrane to the cathode, whilst the electrons flow along an external circuit providing electricity. At the cathode, oxygen from the air recombines with protons and electrons to produce water and heat. The voltage of a single fuel cell only reaches 0.6-0.8 V; therefore, a stack of cells (2 to several 100) are electrically connected in order for a higher voltage in practical use (Friedrich *et al.*, 2008).

Several hundred fuel cell car prototypes have been developed by car companies and research institutes. In the next few years, several major car companies e.g. Toyota, Hyundai and Mercedes have decided to put hydrogen fuel cell vehicles on sale (Nelson). However, the widespread commercialization of hydrogen fuel cells needs to overcome a number of challenges, such as the cost, durability and reliability of fuel cell, the distribution of hydrogen, and particularly on-board hydrogen storage.

1.2.3   Fuel cell or battery electric vehicles at a glance

There have often been debates on the merits of hydrogen fuel cells (FCEV) versus pure battery-electric (BEV) vehicles as the possible replacement for the fossil fuel-based powertrain, between the general public, automotive manufacturers and the R&D community. However, this should not be the case since both technologies address very different energy densities for utilized energy carriers (**Figure 1.3**) and hence different areas of the vehicle market (Eberle *et al.*, 2012). For a car with a range of 500 km, the mass of a lithium-ion battery system is about 20 times heavier than that of today's diesel system, and a fast re-charging of the battery still requires at least 30 minutes. For the same vehicular range, FCEV only requires 6 kg of H_2 and can be re-fuelled within 3 to 5 minutes, despite the hydrogen storage system (700 bar compressed H_2) is increased to 125 kg and 260 L. This is still very competitive compared to a battery system.

Figure 1.3 Weight and volume of energy storage materials and systems for a vehicle with a driving range of 500 km, where CNG = compressed natural gas, CGH_2 = compressed gaseous hydrogen (Brinkman *et al.*, 2012).

Therefore, BEVs are considered as the choice for small urban vehicles with ranges up to 150 km based on existing technology, whereas FCEVs allow fast refuelling and a significantly longer driving range (Eberle and von Helmolt, 2010). In addition, electricity is

already a widely used energy vector and so building a recharging infrastructure for BEVs based on the existing power grid is likely to be significantly faster, since little infrastructure currently exists for hydrogen production, transmission and refuelling.

1.3   Hydrogen storage

As hydrogen is very difficult to store, both gravimetrically and volumetrically, the development of hydrogen storage systems is a demanding and challenging task for the FCEVs market. In addition, it is generally believed that if a suitable on-board hydrogen storage system can be found, then the problems regarding stationary and portable storage may be solved (Eberle *et al.*, 2009).

The US Department of Energy has set targets for an on-board vehicular storage system containing 5-6 kg H_2, to allow a driving range of over 500 km while meeting packaging, cost, safety, and performance requirements to be competitive with current vehicles: achieving the gravimetric and volumetric capacity of 5.5 wt% and 40 g H_2/L respectively by the year 2017, and ultimately a goal of 7.5 wt% and 70 g H_2/L (Klebanoff and Keller, 2013). It should be noted that these target values are designed for the entire storage system including other components such as tank, piping, regulators etc., which means the storage material must exhibit an even higher hydrogen capacity. Moreover, the targets for H_2 delivery temperature and pressure are -40 to 85°C and 5 to 12 bar, respectively. Refuelling of 5 kg H_2 to the vehicle should ideally be completed within 2.5 minutes. On top of all of these demands, the storage system should be safe, durable (1500 de/rehydrogenation cycles), and cost-effective (ultimately $ 8/kWh or $ 400/kg H_2) for widespread commercialisation.

A number of hydrogen storage methods have been investigated which can be broadly categorised into two groups: 1) physical storage – gaseous and liquid hydrogen tanks; and 2) materials-based storage - as a part of solid compounds attached to other element(s). **Figure 1.4** shows current hydrogen storage technologies in terms of gravimetric and

volumetric H_2 capacities (for an integrated system), together with the US DOE 2015 and ultimate targets (US Department of Energy, 2007).
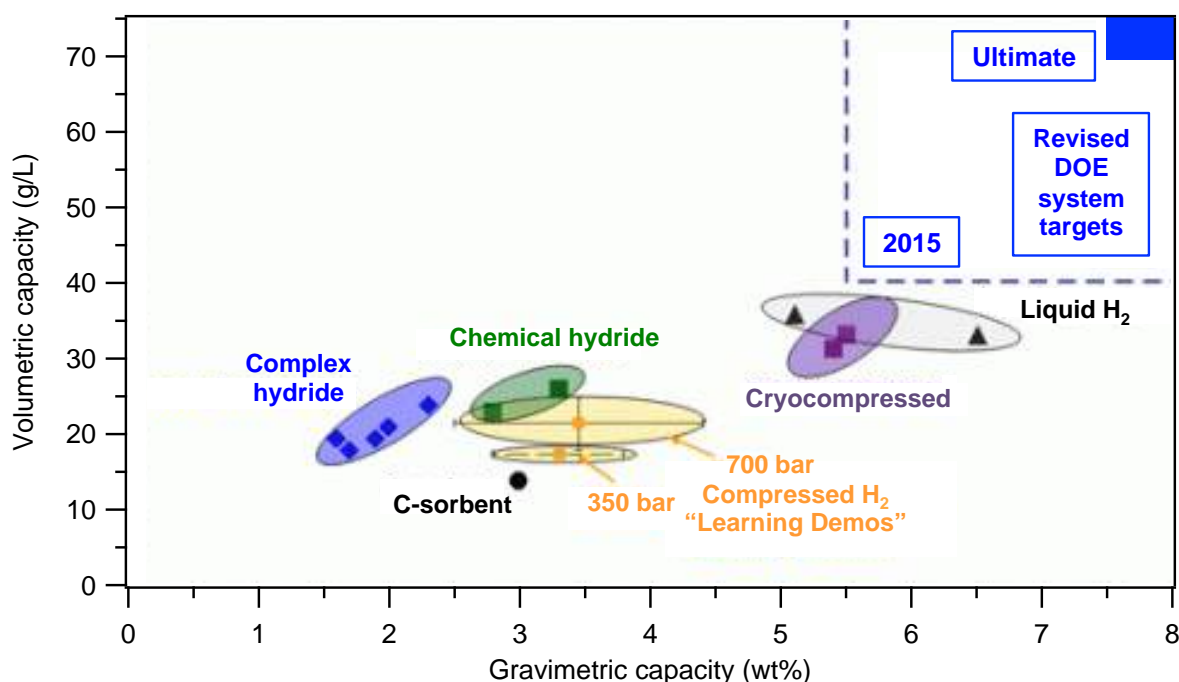
Figure 1.4 Comparison of gravimetric and volumetric H_2 capacities of different hydrogen storage systems. The data of "Learning Demos" was obtained across 138 vehicles with 350 bar and 700 bar compressed gaseous H_2 tank systems. Modified from US Department of Energy (2007).

1.3.1 Gaseous and liquid storage

Compressed gaseous hydrogen (CGH_2) tank is a well-established technology and is currently being used by nearly all manufacturers for hydrogen FCEV. The state-of-the-art tank made of carbon fibre-reinforced composite, can store 4.2 kg H_2 at 700 bar with a gravimetric system capacity of 3.1 wt% (von Helmolt and Eberle, 2007). The refuelling time is less than 3 min, and no extra energy is required to release the hydrogen. Such technology is already in use in the world's first production model FCEV - Hyundai ix35 (storing 5.64 kg H_2 in two 700 bar tanks) with a drive range of 590 km (Hyundai, 2013). However, the gaseous storage method is relatively inefficient in terms of volume and energy efficiency. The volumetric capacity is only 26 g H_2/L for a 700 bar tank (Hua *et al.*, 2011), which is much lower than the ultimate target of 70 g H_2/L. Extra energy is also required for

the H_2 pressurisation, which reduces the overall efficiency (by 12-16% at 800 bar) (Westerwaal and Haije, 2008). The high cost, largely due to the composite material for the tank, needs to be reduced by using lower-cost materials without compromising capacity and safety.

Cryogenic liquid hydrogen (LH_2) has an attractive volumetric density (70.8 g H_2/L). However, extra energy is required to maintain hydrogen at -252 °C in order to minimise hydrogen boil-off, which can consume a large fraction of the hydrogen energy (about 30 %) (Eberle *et al.*, 2009). Even with the best insulation, the gradual boil-off of hydrogen cannot be avoided. Also, equipment used for the delivery and storage of the liquid hydrogen must have excellent thermal insulation that incurs a further material and energy cost. Thus, this form of storage is energy inefficient for using on light-duty passenger vehicles, but becomes more efficient for larger liquefied tanks, e.g. liquid H_2 tank lorries.

More recently, a new physical approach of combining compression and cryogenic storage has been introduced, known as a cryo-compressed hydrogen (CcH_2) tank. The concept is based on cryogenic compressed gaseous H_2, compressed liquid H_2, and two-phases system of liquid H_2 with vapour in the headspace (Ahluwalia *et al.*, 2010). This type of tank is generally more compact (5.6 wt% and 41 g H_2/L) than conventional CGH_2 tanks, and has less energy and evaporative loss than LH_2 tanks, although the overall efficiency of 41% is too low to meet the DOE target of 60%.

1.3.2   Materials-based hydrogen storage

Materials-based hydrogen storage shows potential to fulfil the target of both hydrogen gravimetric and volumetric capacities for on-board hydrogen storage.

1.3.2.1 Physisorption

Physisorption is adsorption of molecular hydrogen onto the surface or within the pores of materials via van der Waals forces. The energy of these interactions is very low (typically 4-

10 kJ/mol H_2), which means low temperatures (e.g. -196 °C by the convenience of using liquid N_2) are required to maximise the amount of adsorbed H_2 (Walker *et al.*, 2008). A number of porous (high surface area) materials, e.g. carbon porous polymers and metal-organic frameworks (MOFs), have been demonstrated exhibiting a few wt% H_2 capacity at cryogenic temperatures and less than 1 wt% at ambient temperature and 100 bar, whereas the volumetric capacity are typically around or below 40 g H_2/L (Wang and Yang, 2008; Tedds *et al.*, 2011). The low working temperature and small hydrogen capacity hindered the practical use of physisorption materials, although some of these materials have advantages of rapid sorption kinetics, excellent reversibility and relatively low material cost.

1.3.2.2 Chemisorption – Metal hydrides

In chemisorption, atomic hydrogen is chemically bonded to other element(s) to form metallic, ionic or covalent hydrides. In fact, most of the natural elements can react with hydrogen, but a compound consisting of light host element(s) are preferred in order to achieve the necessary high gravimetric hydrogen density.

Alkali and alkaline earth metals (except Be and Mg) tend to form stoichiometric ionic hydrides (e.g. LiH and CaH_2), and exhibit high volumetric and gravimetric H_2 densities. In general, the binary ionic hydrides are too stable for hydrogen storage. MgH_2 consisting of a mixture of ionic and covalent bonding, is a special case, and will be discussed in detail in Chapter 2.6.

Metallic hydrides are the most common amongst the transition metals, and are often non-stoichiometric (i.e. variable composition) which allows for tailoring the properties. They are formed by the incorporation of atomic hydrogen into interstitial sites in the metal or alloy lattice. The absorption of hydrogen to the host metal can be described in terms of a pressure-composition isotherm, as illustrated in **Figure 1.5**.
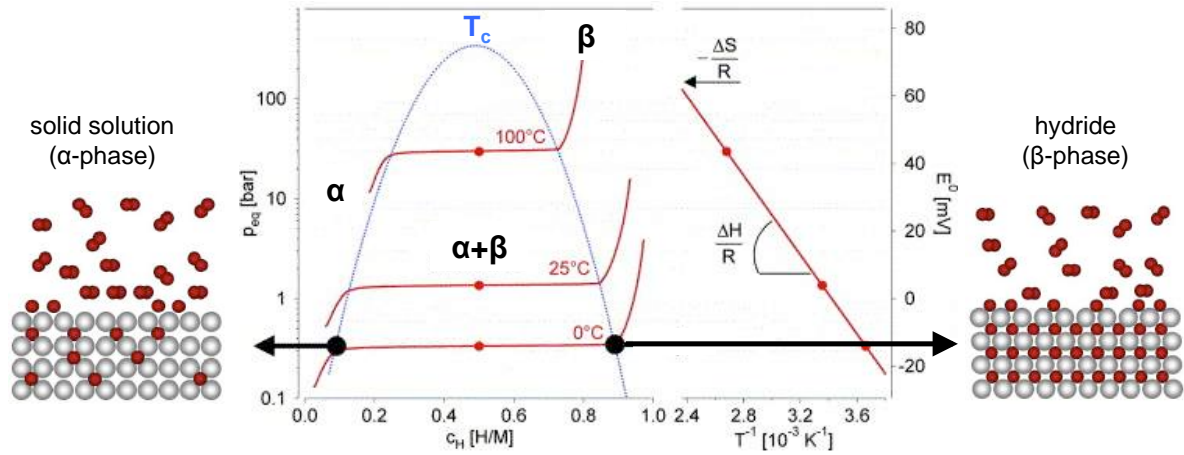
Figure 1.5 Pressure composition isotherm for the hydrogen absorption of metal hydrides, and van't Hoff plot giving the formation enthalpy of hydride. Modified from Züttel (2003).

Molecular Hydrogen is dissociated at the metal surface and diffuses into the metal forming a solid solution (α-phase) at a low H concentration. The α-phase has the same structure as the host metal, possibly accompanied with lattice expansion in order to accommodate the hydrogen atoms (Züttel, 2003). With increasing hydrogen pressure, more hydrogen is absorbed and the hydride phase (β-phase) starts to form. This leads to a plateau region in the isotherms, where α and β-phases coexist and the H concentration can radically increase with minor changes in the pressure or temperature. The length of the plateau determines the amount of hydrogen stored, which is particularly of interest for hydrogen storage applications. The plateau pressure increases with increasing temperature until a critical temperature (T_c) where the α-phase continuously transforms to β-phase. Once the pure β-phase is reached, the H concentration rises with increasing pressure.

The plateau pressure is determined by the enthalpy (ΔH) and entropy (ΔS) changes of the phase transformation as a function of temperature by the van't Hoff equation:

$$\ln \frac{P}{P_0} = \frac{\Delta H}{RT} - \frac{\Delta S}{R} \tag{1.6}$$

where P is the plateau pressure at temperature T (K), P_0 is the standard pressure of 1 bar, and R is the gas constant (8.3145 J/mol K). Hence, for a new material, the enthalpy change ΔH can be evaluated from the slope ($\frac{\Delta H}{R}$ in **Figure 1.5**) by plotting the plateau pressure (ln P)

against the inverse temperature ($1/T$) data from several Pressure-Composition-Temperature (PCT) isothermal measurements. This is of importance if the material can deliver hydrogen at a given temperature/pressure and the heat (exothermic or endothermic) from the reaction needs to be managed; hence, to be modified for practical applications. To reach an equilibrium pressure of 1 bar at 27 °C, ΔH should be 39.2 kJ /mol H_2 (Züttel, 2003).

Of special interest are the intermetallic hydrides, i.e. AB_xH_y in the simplest case, offering high volumetric H_2 density, and tend to exhibit favourable kinetic properties with excellent reversibility upon H_2 cycling at low temperature and pressure. For example, $LaNi_5H_{6.5}$ with gravimetric and volumetric densities of 1.4 wt% and 121 g H_2/L respectively, can rapidly de/absorb hydrogen at 25 °C below 2 bar (Bowman and Fultz, 2002). In one practical case, a canal boat (the "Ross Barlow") powered by a PEM fuel cell with a $TiMn_2$-based metal hydride store, has been constructed at the University of Birmingham (Bevan *et al.*, 2011). The low gravimetric hydrogen density is not a problem for a marine application (where ballast is needed anyway), but it is a significant drawback for vehicular applications. In addition, many types of metal hydride tend to consist of relatively expensive transition metals (e.g. Pd).

1.3.2.3 Chemisorption – Complex hydrides

Complex hydrides, in which hydrogen are covalently bound to a central atom in an anion, have being intensively investigated (Orimo *et al.*, 2007). The well-known examples are alanates $[AlH_4]$-, borohydrides $[BH_4]$-, and amides/imides $[NH_2]^-/[NH]^{2-}$, with charge compensation by cations of most alkali and alkaline-earth metals as well as many transition metals. Complex hydrides are very attractive due to their high intrinsic gravimetric hydrogen densities (up to 18 wt% in the case of $LiBH_4$ (Züttel *et al.*, 2003b)). But important drawbacks such as poor reversibility, high desorption temperature and the release of impurity gas(es) have so far prevented their use for vehicular applications.

Alkali metal alanates exhibit gravimetric hydrogen densities (e.g. 10.5 wt% by $LiAlH_4$ and

7.4 wt% by $NaAlH_4$), and release hydrogen in a temperature range of 200-300 °C (e.g. Li, 201 °C; Na, 265 °C), via two stages (Orimo et $al.$, 2007):

$$3M\text{AlH}_4 \rightarrow M_3\text{AlH}_6 + 2\text{Al} + 3\text{H}_2 \rightarrow 3M\text{H} + 3\text{Al} + \text{}^9\!/_2\text{H}_2 \qquad M = \text{Li or Na} \quad (1.7)$$
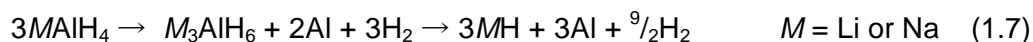
Further dehydrogenation of the binary metal hydride $M\text{H}_x$ occurs at temperatures above 400 °C. But in practice, the hydrogen uptake and release are limited by poor sorption kinetics. By adding Ti-based catalysts, the desorption temperature of $NaAlH_4$ was lowered to 150 °C while rehydrogenation could be achieved at 170 °C and 152 bar H_2 in 5 h showing a reversible capacity of 3-4 wt% (Bogdanović and Schwickardi, 1997).

In the case of the amide system, lithium nitride could be hydrogenated and dehydrogenated via a two-step reversible reaction (Chen et $al.$, 2002):

$$\text{Li}_3\text{N} + 2\text{H}_2 \leftrightarrow \text{Li}_2\text{NH} + \text{LiH} + \text{H}_2 \leftrightarrow \text{LiNH}_2 + 2\text{LiH} \qquad (1.8)$$
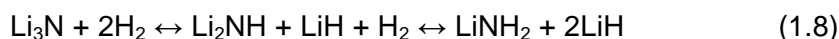
Although this Li-N-H system has the potential to release up to 10.4 wt% H_2, the absorption and desorption reactions of Li_3N occur very slowly even at temperatures in excess of 320 °C. As a result, only the second step of the Equation 1.8 involving 6.5 wt% H_2 is reversible under moderate temperature (255 °C) (Chen et $al.$, 2002). The mixed metal amide system (e.g. Li-Mg-N-H and Li-Ca-N-H) has also been investigated, and has shown improved reversibility (Umegaki et $al.$, 2009).

In general, borohydrides contain more hydrogen than alanates and amides (Orimo et $al.$, 2007). As part of this dissertation is devoted to studies on metal borohydrides, a detailed introduction of this class of material will be given in Chapter 2.

1.3.2.4 Chemical reactions – hydrolysis

Hydrogen can be generated by the reaction between chemical compounds and water. These hydrolysis reactions are often not directly "in-situ" reversible, which means the used materials and/or by-product needs to be removed from the vehicle and rehydrogenated off-board (Züttel, 2003). $NaBH_4$ has often been evaluated for this approach, since it can be

safely stored or delivered as a powder or liquid under ambient condition and its hydrolysis reaction is less violent than the lithium equivalent (Umegaki *et al.*, 2009). 10.8 wt% of H_2 can be generated from an aqueous $NaBH_4$ solution within 2.5 min at room temperature by using a fluorinated cobalt catalyst, according to the following reactions (Suda *et al.*, 2001):

$$NaBH_4 + 2H_2O \rightarrow NaBO_2 + 4H_2 \qquad (1.9)$$
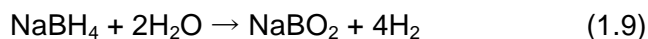
The "spent fuel" containing $NaBO_2$ can be later recycled back to $NaBH_4$ by heating with MgH_2 at 550 °C in 70 bar H_2 for 2 h (Kojima and Haga, 2003). However, the H_2 capacity at system-level is greatly reduced due to the need to store water on-board. Millennium Cell has reported that their $NaBH_4$-based Hydrogen on Demand™ system possesses a system gravimetric capacity of about 4 wt% (US Department of Energy, 2014a).

1.3.3   Summary

No single hydrogen storage method currently fulfils all the technical and economic demands. The physical methods (CGH_2 and CcH_2) are a near-term solution for initial vehicle commercialization and early markets, although the high cost and large size of the high-pressure composite tanks are challenges. Materials-based storage may be a long-term solution, as long as targets can be met for: an improved H_2 gravimetric capacity, accelerated hydrogen sorption kinetics (within an appropriate temperature range), and a lower overall system cost. **Figure 1.6** is a comparison of the observed hydrogen capacities and the operating temperatures for possible hydrogen storage materials. Microporous materials adsorb molecular hydrogen on the surface and pores through physisorption, and may fulfil the gravimetric capacity target at -196 °C. The intermetallic hydrides store atomic hydrogen in the interstitial sites of a metallic host material and can exceed the volumetric storage target easily with favorable sorption kinetics, although their limited gravimetric densities impede practical use. Complex hydrides chemically bound atomic hydrogen with other elements in complex forms, and most of them reach both gravimetric and volumetric

densities (for the material alone). However, upon hydrogen desorption, complex hydrides face issues of high operation temperatures and/or the evolution of additional gaseous products (e.g. diborane), and poor reversibility and hydrogen sorption kinetics.
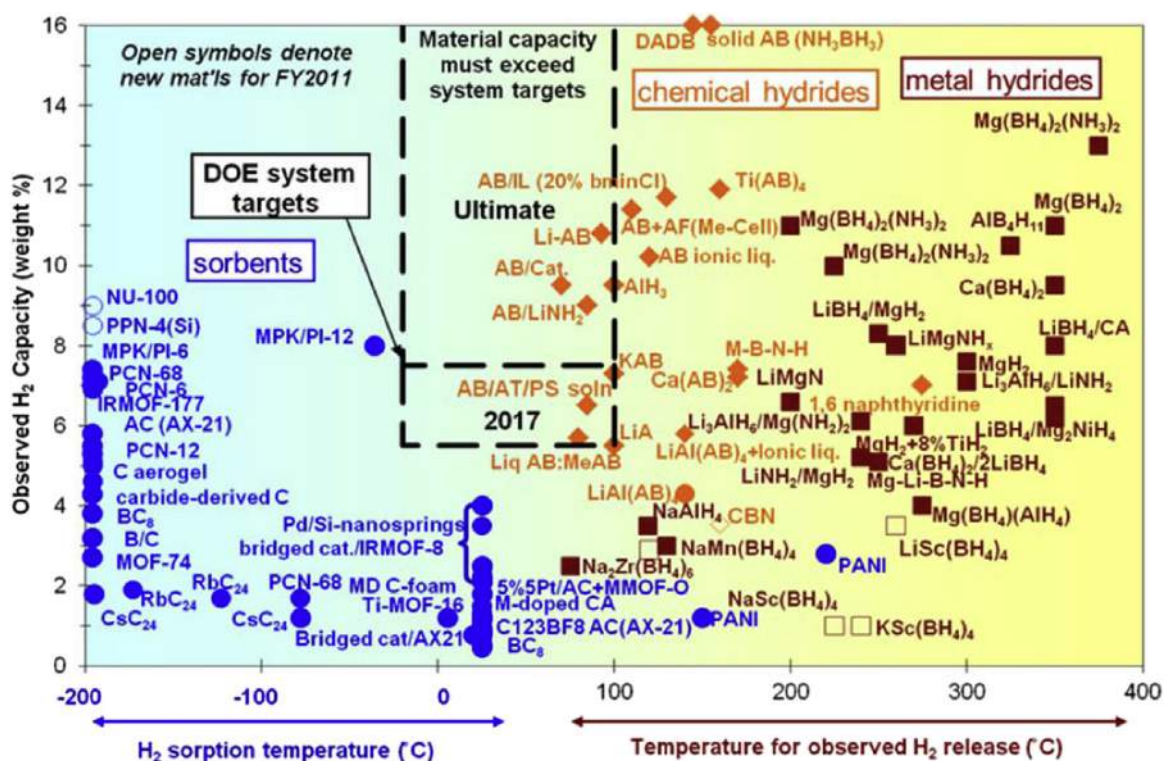

Figure 1.6 Observed hydrogen storage capacities of potential hydrogen storage materials with corresponding operating temperatures (Durbin and Malardier-Jugroot, 2013).

2 Metal borohydrides and Mg-based hydrides

2.1 Metal borohydrides

Borohydrides, also known as tetrahydroborates, have been investigated since the 1940s, but many of the results were not published before 1953 due to secrecy during World War II (Schlesinger *et al.*, 1953a). Nowadays some of them (e.g. $NaBH_4$ and KBH_4) are being used as strong reducing agents in organic and inorganic synthesis (Brown, 1975). In particular, borohydrides represent a class of complex hydrides with the largest gravimetric and volumetric hydrogen density values. In addition, favourable ionic conductivities have recently been discovered for $LiBH_4$ and $Mg(BH_4)_2$, which may be attractive for use as electrolytes in rechargeable batteries (Matsuo and Orimo, 2011; Mohtadi *et al.*, 2012).

2.1.1 Structures

In borohydrides, four hydrogen atoms at the corners of a tetrahedron are covalently bonded to a boron atom in the centre, where a metal cation M^{n+} coordinates to $[BH_4]^-$ anion(s) for charge compensation (Züttel, 2003). The hydrogen atoms are connected to the metal through either ionic or covalent bonds in three different coordinations: monodentate (one M-H-B bridge), bidentate (two M-H-B bridges), or tridentate (three M-H-B bridges). This is illustrated in Error! Reference source not found. (Marks and Kolb, 1977; Parker, 2010). The alkali metal borohydrides are ionic compounds, whereas rare earth and transition metal borohydrides are covalently bonded. The alkaline earth metal borohydrides are intermediate where they are still ionic but have more covalent character than the alkali metal compounds (Züttel *et al.*, 2007).
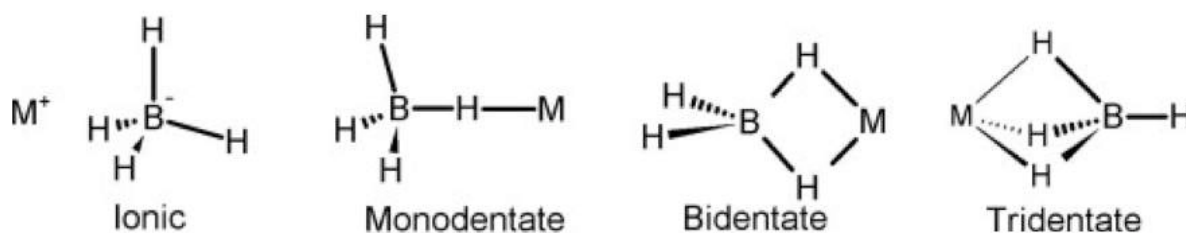
Figure 2.1 Typical ionic and covalent bonding configurations between metal (M) and BH_4 ligand (Marks and Kolb, 1977).

An ideal isolated $[BH_4]^-$ cluster belongs to T_d symmetry group with four normal vibrational modes: the B-H stretching modes v_1 (symmetric, A_1) and v_3 (asymmetric, T_2) located in the vibrational region of 2100-2500 cm^{-1}; and the H-B-H bending modes v_2 (symmetric, E) and v_4 (asymmetric, T_2) in the region of 900-1200 cm^{-1}. This is sketched in **Figure 2.2** (Ketelaar and Schutte, 1961; Zavorotynska *et al.*, 2011).

v_1 symmetric stretch v_2 symmetric bend v_3 asymmetric stretch v_4 asymmetric bend
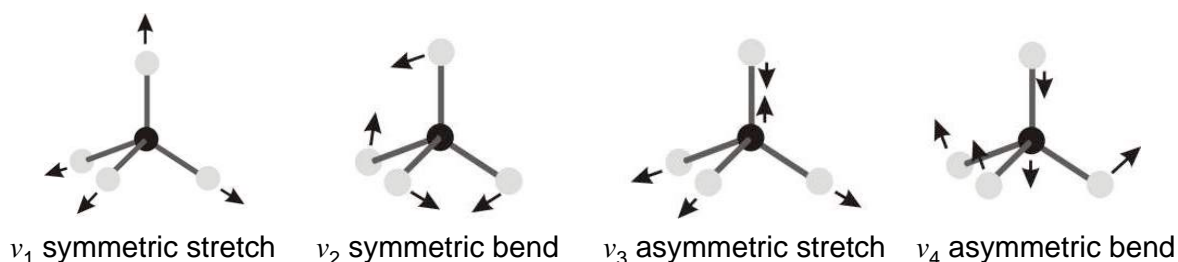
Figure 2.2 The vibrational modes of a tetrahedral cluster (Housecroft and Sharpe, 2012).

However, the symmetry of the $[BH_4]^-$ unit in solid crystals can be changed due to the participation of a cation affecting the site symmetry and crystal field (Marks and Kolb, 1977). This can lead to vibrations splitting into a less symmetric structure, or the presence of overtone and combination modes due to Fermi resonance and peak overlapping, respectively. This can make the spectra complicated and so the interpretation difficult. However, the terminal $B-H_t$ and bridging $B-H_b$ stretching modes are relatively distinguishable, as they are normally very intense and not masked by other vibrations in the spectra. The typical vibrational frequencies corresponding to the coordination between M and $[BH_4]^-$ are summarised in **Table 2.1**.

Table 2.1 Typical fundamental vibrational frequencies for single-cation $M(BH_4)_n$ (Marks and Kolb, 1977; Parker, 2010).

Structure	Frequency (cm^{-1})	Approx. type of internal coordinate	IR intensity	Raman intensity
Ionic	2200–2300	B–H$_t$ stretching	Strong, broad	Strong, broad
	1050–1150	BH$_2$ deformation	Strong, broad	Weak
Monodentate	2300–2450	B–H$_t$ stretching	Strong, probably a doublet	Strong
	~2000	B–H$_b$ stretching	Strong	
	~2000–1700	M–H$_b$ stretching	May be very broad	May be broad
	1000–1150	BH$_3$ deformation	Strong band, possibly with weaker one at slightly higher wavenumber	Strong
Bidentate	2400–2600	B–H$_t$ stretching	Strong doublet, 50-80 cm^{-1} splitting	Strong singlet, possible shoulder
	1650–2150	B–H$_b$ stretching	Strong band, possible shoulder	Medium-strong band
	1300–1500	Bridge stretching	Strong, broad	Strong, broad
	1100–1200	BH$_2$ deformation	Strong	Medium-strong, possibly a doublet
Tridentate	2450–2600	B–H$_t$ stretching	Strong singlet	Strong singlet
	2100–2200	B–H$_b$ stretching	Doublet, 50-80 cm^{-1} splitting	Strong singlet, possible shoulder
	1050–1150	Bridge deformation	Strong	Strong singlet

2.1.2   Thermodynamics and decomposition process

Metal borohydrides ($M(BH_4)_n$) release hydrogen via thermolysis through a variety of routes, which can be briefly summarised by Equations 2.1-2.4 (Nickels, 2010); without mentioning the formation of possible intermediates. However, the route may be altered depending on the starting polymorphs or decomposition conditions such as backpressure, temperature etc. (Rönnebro, 2011).

$$M(BH_4)_n \rightarrow MH_n + B + {}^{3n}/_2H_2 \qquad (2.1)$$

$$M(BH_4)_n \rightarrow M + nB + 2nH_2 \qquad (2.2)$$

$$2M(BH_4)_n \rightarrow 2MH_n + nB_2H_6 \qquad (2.3)$$

$$2M(BH_4)_n \rightarrow 2M + nB_2H_6 + nH_2 \qquad (2.4)$$
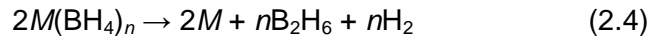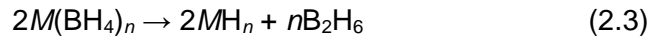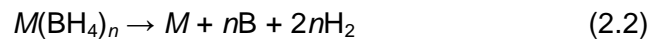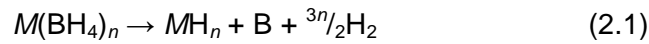
For the decomposition reaction, the Gibbs energy change ΔG_{dec} is:

$$\Delta G_{dec} = \Delta H_{dec} - T_{dec}\Delta S_{dec} \qquad (2.5)$$

In this case, ΔH_{dec} is equal to the negative enthalpy of formation of the hydride, ΔH_f. For most solid binary hydrides, the entropy change of decomposition ΔS_{dec} is primarily associated with the transformation of hydrogen from an ordered solid to a disordered gas, i.e. at a constant of $\Delta S_{dec} \approx S°_{H2} = 130$ J K^{-1}mol^{-1} H$_2$ (Grochala and Edwards, 2004). Thus, the thermodynamic stability can be evaluated by the enthalpy change ΔH_{dec}: the difference in the formation enthalpies between the $M(BH_4)_n$ and its decomposition products:

$$\Delta H_{dec} = \Delta H_{f\ products} - \Delta H_{f\ borohydride} \qquad (2.6)$$

Since the ΔH_{dec} is determined by the stabilities of both the $M(BH_4)_n$ and the decomposition products, the thermodynamic stability of the material can be expected to be tailored in two ways: (a) destabilisation of $M(BH_4)_n$ and/or (b) stabilisation of the dehydrogenation products, as illustrated in **Figure 2.3** (Li *et al.*, 2011b).
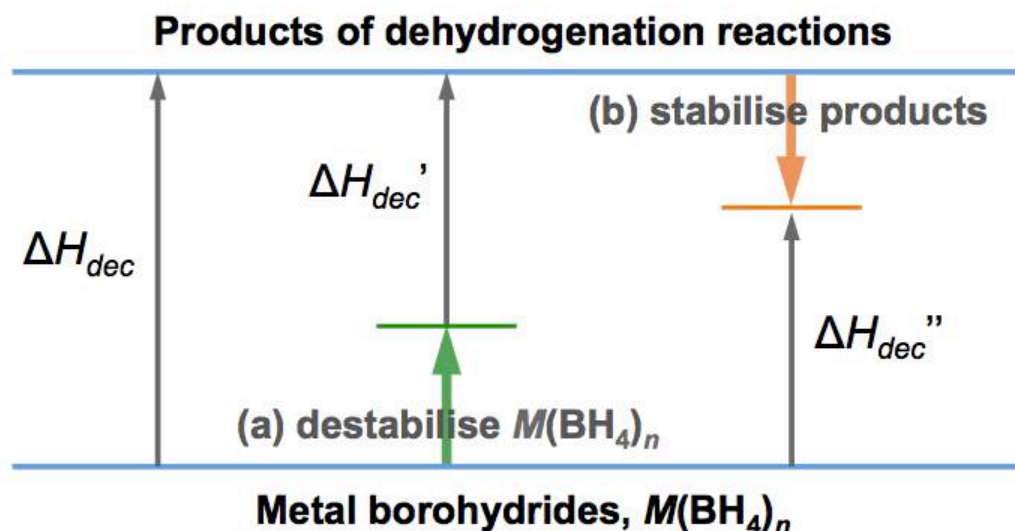
Figure 2.3 Schematic illustration of two main approaches to tailor the thermodynamic stabilities of metal borohydrides $M(BH_4)n$ (reproduced from Li *et al.* (2011b)).

Based on First-principles calculations of a range of borohydrides $M(BH_4)_n$ (M = Li, Na, K, Mg, Sc, Zr, Hf, Cu and Zn; n = 1-4), Nakamori *et al.* (2006b) proposed an empirical correlation between the ΔH_{dec} of $M(BH_4)_n$ and the Pauling electronegativity (χ_P) of M where the calculation of ΔH_{dec} was restricted by the Equation 2.2, despite most M existing in the form of a hydride and/or boride after dehydrogenation.

This correlation was also experimentally verified by thermal desorption measurements, in which the samples were prepared by mechanical-milling alkali-metal borohydrides with metal chlorides (Nakamori *et al.*, 2006a; Nakamori *et al.*, 2007; Nakamori *et al.*, 2008). The hydrogen desorption temperature (T_d) of $M(BH_4)_n$ decreases with increasing χ_P value of M (**Figure 2.4**). The $M(BH_4)_n$ with $\chi_P \geq 1.5$ (e.g. M = Mn, Ti and Al) are too thermodynamically unstable and are decomposed with the evolution of the toxic diborane in addition to hydrogen. Therefore, $M(BH_4)_n$ ($\chi_P < 1.5$) were suggested as promising candidates with appropriate and without releasing diborane. Furthermore, it was found that multi-cation borohydrides $MM'(BH_4)_n$, where M and M' have different χ_P, exhibit moderate thermodynamic stabilities between $M(BH_4)_n$ and $M'(BH_4)_n$ (Li *et al.*, 2007b). However, it should be noted that some of these borohydrides were investigated as a mixture which also

contained side product(s), mostly metal halides, from the metathesis reaction. Such side products could form solid solutions or compounds with starting materials or dehydrogenated products thereby changing thermodynamic stability and reaction path (Rude *et al.*, 2011; Park *et al.*, 2013).
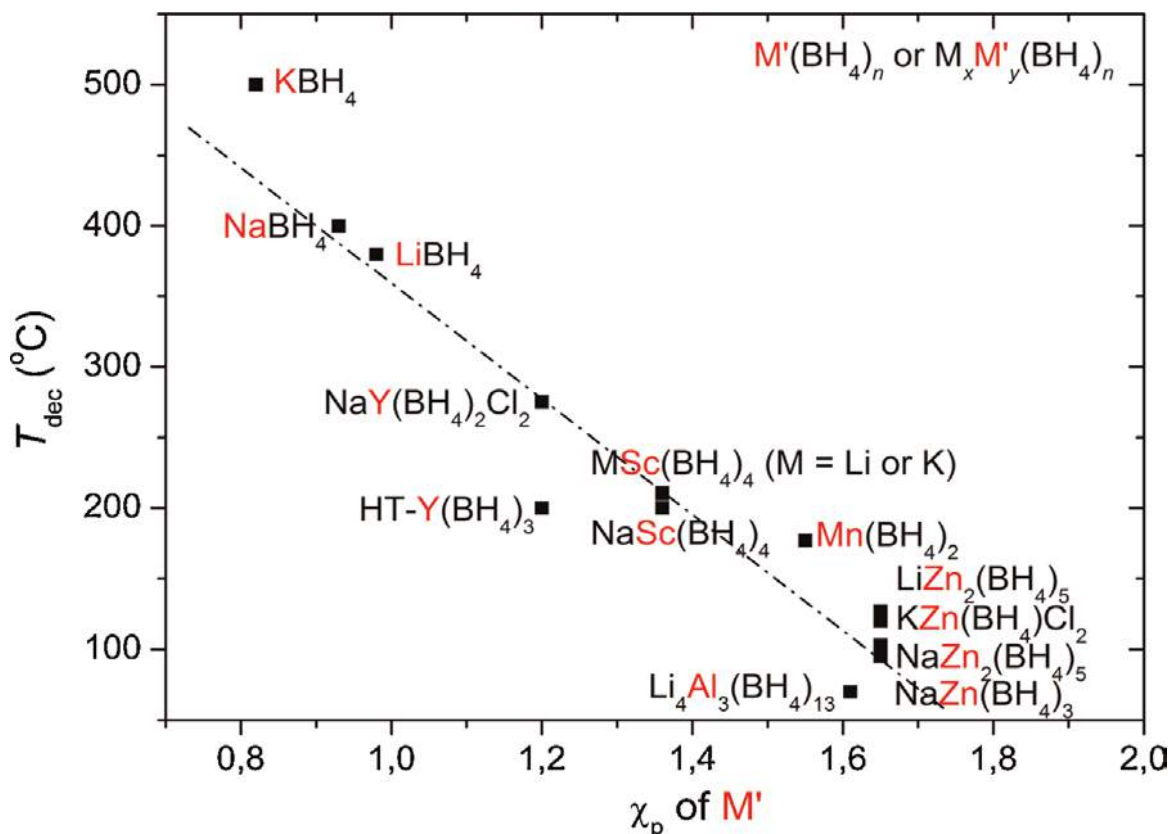
Figure 2.4 The desorption temperature T_d as a function of the Pauling electronegativity χ_P of the metal, M'. For the bimetallic borohydrides M' is the more electronegative of the two metals. (Rude *et al.*, 2011)

Since the modification of the electronegativity of a particular cation is very unlikely, the appropriate combination of cations might allow the thermodynamic property of a borohydride compound to be modified. Intensive structural studies revealed that the stable alkali metal borohydrides are dominated by strong ionic bonds between M^+ and $[BH_4]^-$, due to low χ_P value of the alkali metal resulting in almost complete charge transfer from M^+ to $[BH_4]^-$ (Ravnsbæk *et al.*, 2010a). However, in the alkaline earth and transition metals with higher χ_P, less charge is transferred from M to $[BH_4]^-$, and directionality and partial covalency were observed between M^{n+} and $[BH_4]^-$. This may explain the less stable alkaline

earth and transition metal borohydrides.

Tailoring thermodynamics and kinetics properties of known hydrogen storage materials can be achieved by means of: adding catalysts, nanoconfinement, and by controlling reaction pathway. A more favourable enthalpy change of dehydrogenation may be obtained by mixing a borohydride with a hydride to form a reactive hydride composite, however care must be taken to avoid a significant reduction in the gravimetric H_2 density (Vajo *et al.*, 2005). Nanoconfinement limits the particle size of the material to the pore size of the scaffold material, and thereby may improve the reaction kinetics, reversibility, stability, and possibly the thermodynamic properties of the chemical reactions. However, drawbacks like the reduction in gravimetric and volumetric capacity and possible reactions with the scaffold need to be overcome.

2.2   Alkali metal borohydrides

2.2.1   LiBH$_4$

$LiBH_4$ was the first metal borohydride to be considered as a candidate hydrogen storage material (Züttel *et al.*, 2003b), due to its very high theoretical gravimetric H_2 density of 18.5 wt % and volumetric H_2 density of 121 kgH_2 m^{-3}.

2.2.1.1 Synthesis and recombination

The synthesis of $LiBH_4$ was first reported by Schlesinger and Brown (1940) based on the reaction of ethyl-lithium (CH_3CH_2Li) with diborane (B_2H_6). Subsequently, Schlesinger *et al.* (1953a) developed a higher-yield synthesis approach via the reaction of lithium hydride with diborane in diethyl ether (Equation 2.7), where the ether was removed by heating to form pure $LiBH_4$. They found that the solvent played an indispensable role in the reaction to give the hydride more freedom to react with diborane, while also removing the newly formed $LiBH_4$ from the surface of the LiH. However, this wet chemistry method could not be applied

to the synthesis of other borohydride compounds.

$$2LiH + B_2H_6 + 2(C_2H_5)O \rightarrow 2LiBH_4 \cdot (C_2H_5)_2O \qquad (2.7)$$
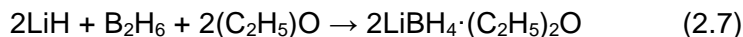
Nowadays, $LiBH_4$ is industrially produced by a metathesis reaction between $NaBH_4$ and a lithium halide in solvent of ether or isopropyl amine solution according to the Equation 2.8 (Brown *et al.*, 1981).

$$Na(BH_4) + LiCl \text{ or } LiBr \rightarrow Li(BH_4) + NaCl \text{ or } NaBr \qquad (2.8)$$
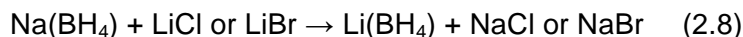
Direct (solvent-free) synthesis has the potential to produce pure borohydrides from the elements without impurities, i.e. solvent from wet chemical reactions, or salt by-products (e.g. NaCl) from mechano-chemical milling. However, the direct synthesis of $LiBH_4$ is thermodynamically unfavourable (the enthalpy of formation $\Delta H_{fboro} = -194.2$ kJ based on Equation 2.9), and the kinetic inertness 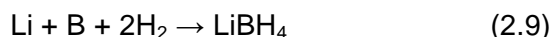of boron was thought to prevent its reaction with Li and H_2 to form $LiBH_4$ at lower temperatures (Züttel *et al.*, 2007).

$$Li + B + 2H_2 \rightarrow LiBH_4 \qquad (2.9)$$

Instead, Friedrichs *et al.* (2008) demonstrated the formation of $LiBH_4$ ($LiBD_4$), via a multi-step heat-treatment of elemental Li and B to form LiB_3 and/or Li_7B_6 alloys prior to hydrogenation of samples. Cakanyildirim and Guru (2008) applied a similar synthetic process to form $LiBH_4$ under 60 bar H_2, via the formation of LiB by pre-milling the elemental Li and B in Ar. Later, Remhof *et al.* (2008) explained the formation mechanism of $LiBD_4$ from LiB according to an in-situ neutron diffraction study. LiB initially reacted with D_2 to form LiD and amorphous B at 200 °C and an initial pressure of 150 bar, followed by the combination of LiD and B to generate $LiBD_4$ at 350 °C. However, these reactions were not complete under the experimental conditions used (up to 500 °C).

Orimo *et al.* (2005) demonstrated that the rehydrogenation of the decomposed $LiBH_4$ is possible at 600 °C under 350 bar H_2 for 12 hours. The decomposed sample contained LiH and amorphous B after being heated to 600 °C in 10 bar H_2. After rehydrogenation, the

formation of $LiBH_4$ was confirmed by XRD and Raman spectra. Agresti and Khandelwal (2009) showed the formation of $LiBH_4$ with a yield of ~27 wt% by ball-milling LiH and crystalline B in 10 bar H_2 for 138 h (Equation 2.10). Later, a $LiBH_4$ thin film (yield of 70 wt%) was made in 0.7 mbar H_2 at room temperature, by using pulsed laser deposition (PLD) and a LiB target (Wang *et al.*, 2010). $Li_2B_{12}H_{12}$ was also formed during the film formation process.

$$2LiH + 2B + 3H_2 \rightarrow 2LiBH_4 \qquad (2.10)$$

Recently, solvent-free synthesis of $LiBH_4$ through a gas-solid reaction of LiH and B_2H_6 was first presented by Friedrichs *et al.* (2009a), which will be discussed in detail in Section 2.5.2 (p63). The use of additives to improve the thermodynamics and kinetics has also been investigated. One example is that starting from AlB_2 instead of B strongly improved the kinetics of formation of $LiBH_4$, from LiH at 450 °C under 13 bar H_2 (Friedrichs *et al.*, 2009b). Some other examples of additives which not only affect the decomposition temperature but also the reversibility of $LiBH_4$, will be discussed in Section 2.2.1.5, (p34).

2.2.1.2 Crystal and vibrational structure

The first study on the crystal structure of $LiBH_4$ by XRD was published by Harris and Meibohm (1947), who suggested that the structure is orthorhombic with space group *Pcmn*. Soulié *et al.* (2002) used synchrotron XRD to refine the room-temperature structure of $LiBH_4$ to be orthorhombic (o-$LiBH_4$) with the space group *Pnma* (a = 7.17858(4) Å, b = 4.43686(2) Å, c = 6.80321(4) Å and V = 216.685(3) Å^3 at 20 °C) where each Li^+ cation is surrounded by four $[BH_4]^-$ ions and each $[BH_4]^-$ by four Li^+. The $[BH_4]^-$ tetrahedrons (point symmetry C_s) are aligned along two orthogonal directions accompanied by a great deal of distortion with respect to bond length B-H varying between 1.04 and 1.28 Å and H-B-H bond angle between 85.1 and 120.1°. However, the following synchrotron study found that the $[BH_4]^-$ ($[BD_4]^-$) cluster has a nearly ideal tetrahedral where the D-B-D bond angles varied between 107.2(3)° and 111.7(4)° at -269.5 °C (Hartman *et al.*, 2007), and the variation in B-D length

is less than 4 % (Buchter *et al.*, 2008a).

With increasing temperature, o-LiBH$_4$ undergoes a first order phase transition to h-LiBH$_4$ phase (hexagonal, space group $P6_3mc$). The lattice parameters of h-LiBH$_4$ are a = 4.27631(5) Å, c = 6.94844(8) Å, V = 110.041(4) Å^3 (at 135 °C). During the phase transformation from o-LiBH$_4$ to h-LiBH$_4$, the structure contracts along the orthorhombic a (hexagonal c) axis and expands in the orthorhombic b^*c (hexagonal *basal*) plane (**Figure 2.5**). Due to the rotational disorder, the [BH$_4$]$^-$ anions exhibit an increase in symmetry (point symmetry C_{3v}), and less distortion of the bond lengths (B-H 1.27-1.28 Å) and bond angles (H-B-H 106.4-112.4°). The phase transition temperatures were determined to be 111 °C by Hartman *et al.* (2007) and 108 °C by Filinchuk *et al.* (2008).
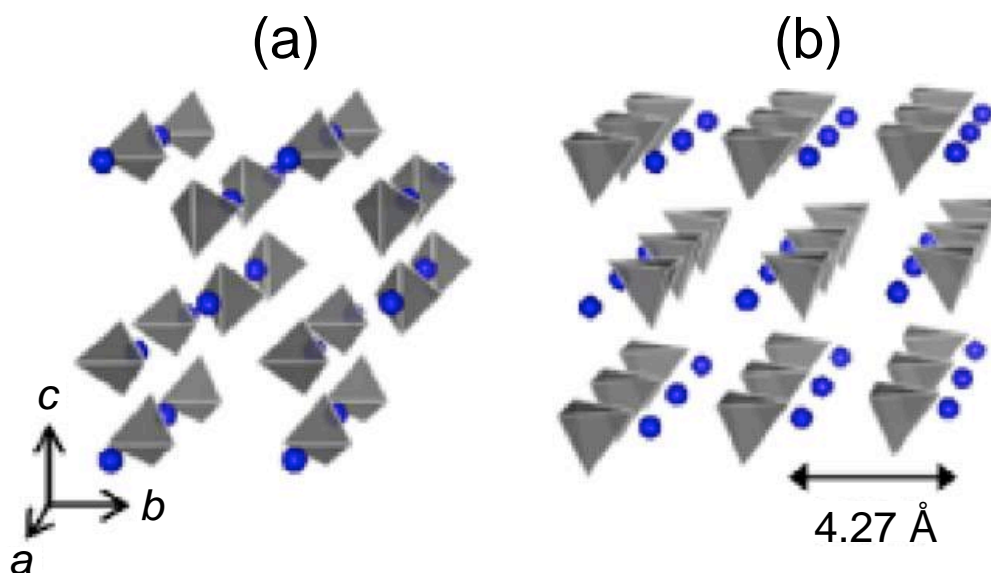
Figure 2.5 Crystal structures of LiBH$_4$ for the (a) orthorhombic and (b) hexagonal phases. Blue ball and grey tetrahedron show Li$^+$ and [BH$_4$]$^-$, respectively (Matsuo *et al.*, 2007).

Harvey and McQuaker (1971b) investigated the vibrational structure of LiBH$_4$ and reported that there are 36 expected Raman active bands for o-LiBH$_4$:

$$\Gamma = 11A_g + 7B_{1g} + 11B_{2g} + 7B_{3g} \qquad (2.11)$$

18 of which are external vibrations (i.e. the translational and librational motions between Li$^+$ and [BH$_4$]$^-$), and the other 18 are internal vibrations (i.e. the bending and stretching motions

of the [BH$_4$]$^-$). Recently, Racu *et al.* (2008) presented a high resolution Raman study of o-LiBH$_4$ and o-LiBD$_4$ phase as a function of temperature from -268 to 27 °C, and identified a total number 27 of the 36 single modes. The mass difference between H and D atoms results in a shift in the Raman spectrum, which can help to characterise the nature of the vibrational modes. The spectrum of LiBH$_4$ (LiBD$_4$) can be divided into three regions: external modes (< 350 cm^{-1}) relating to the translational and librational motions between Li$^+$ and [BH$_4$]$^-$ or [BD$_4$]$^-$; bending (1000-1350 cm^{-1} for H, and 800-1000 cm^{-1} for D) and stretching (2000-2500 cm^{-1} for H, and 1500-2000 cm^{-1} for D) modes are the internal vibrations of [BH$_4$]$^-$ ([BD$_4$]$^-$) tetrahedral, as shown in **Figure 2.6**.

Raman spectroscopy studies of by Gomes *et al.* (2002) and Hagemann *et al.* (2009), helped to confirm the crystallographic structures and the phase transition of LiBH$_4$, showing a sudden disappearance of the splitting mode due to the symmetry change from the point group C$_s$ of o-LiBH$_4$ to the more symmetrical C$_{3v}$ of h-LiBH$_4$. A strong, discontinuous jump in the peak width during the phase transition was also observed, which was related to a nearly isotropic disorder of the [BH$_4$]$^-$ ions in the hexagonal structure.
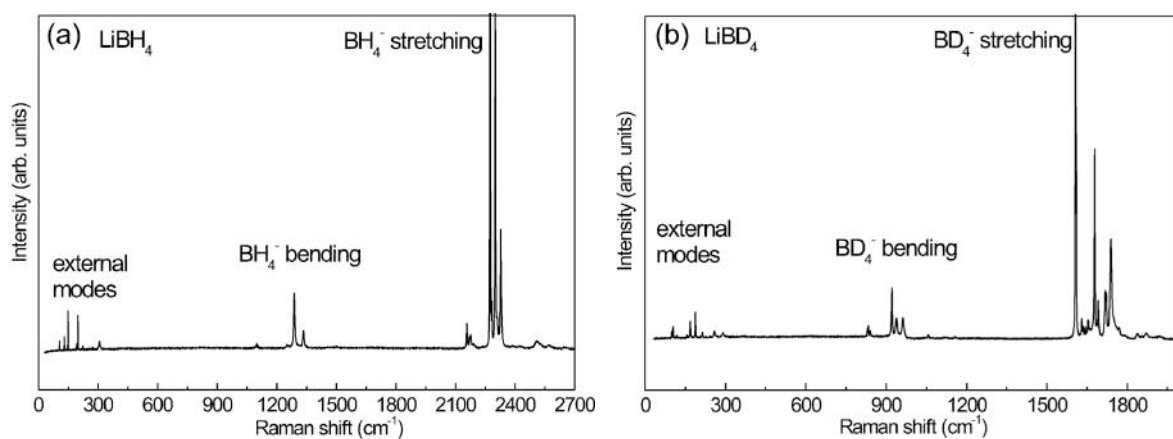

Figure 2.6 Raman spectra of (a) LiBH$_4$ and (b) LiBD$_4$ at -268°C (Racu *et al.*, 2008).

2.2.1.3 Hydrogen storage properties

Miwa *et al.* (2004) calculated the enthalpy change of reaction of LiBH$_4$ to be 56 kJ/mol based on the Equation 2.10 (in Section 2.2.1.1, p28). Later, Mauron *et al.* (2008)

determined the enthalpy and entropy change of the dehydrogenation of $LiBH_4$ to be 74 kJ mol^{-1} H_2 and 115 J K^{-1} mol^{-1} H_2, respectively. The enthalpy value achieved though the *PCT* measurement, was higher than the value calculated by Miwa *et al.* (2004), possibly because the slow kinetics of dehydrogenation reaction means that equilibrium was not fully reached.

Züttel *et al.* (2003a) investigated the thermal behaviour of $LiBH_4$ by thermal desorption spectroscopy and differential scanning calorimetry (DSC). A phase transition from o-$LiBH_4$ to h-$LiBH_4$ was observed at around 108 °C with a slight release of 0.3 wt% H_2, followed by melting at around 270 °C with no detectable mass loss. This 0.3 wt% hydrogen desorption during the transition is inconsistent with the previous Raman study by Gomes *et al.* (2002). The first and second significant H_2 desorption began at 320 and 400 °C, respectively, reaching a maximum at around 500 °C. A total of 9 wt% of H_2 was released upon heating to 600 °C, despite the distinct desorption peaks indicating several intermediate steps (Züttel *et al.*, 2003a). The maximum amount of desorbed hydrogen is limited to 13.5 wt% due to the formation of lithium hydride (LiH) which is stable up to 900 °C. Later, the decomposition products after heated to 600 °C were confirmed to be LiH, B and H_2 by XRD measurement (Orimo *et al.*, 2005).
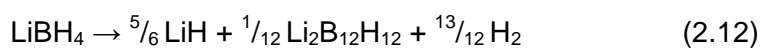
Intensive experimental and theoretical studies on intermediate / byproduct phases formed during the decomposition of metal borohydrides have been performed. Ohba *et al.* (2006) proposed that $Li_2B_{12}H_{12}$ and $Li_2B_{10}H_{10}$ are the most stable compounds among the LiB_3H_8 and LiB_nH_n (*n* = 5-12) compounds according to Density Functional Theory (DFT) calculations, of which the presence of $Li_2B_{12}H_{12}$ (at 427 °C, accompanied by a ~11 wt% H_2 release during $LiBH_4$ decomposition) was later experimentally confirmed by Orimo *et al.* (2006). The ex situ Raman spectrum of the observed $Li_2B_{12}H_{12}$ was consistent with a theoretical monoclinic ($P2_1/n$) structure of $Li_2B_{12}H_{12}$ given by Ohba *et al.* (2006).

Hwang *et al.* (2008) also observed amorphous $Li_2B_{12}H_{12}$ in the decomposition, by a comparison of the NMR spectra of the decomposed samples and the references $K_2B_{12}H_{12}$,

$K_2B_{10}H_{10}$ and amorphous boron. Reed and Book (2009) monitored the decomposition process by temperature-dependent Raman spectroscopy between -190 and 600 °C. $Li_2B_{12}H_{12}$ and amorphous boron were detected above 350 and 385 °C respectively, and was stable on further heating and subsequent cooling back to room temperature.

In addition, Kato *et al.* (2010) detected a concurrent evolution of hydrogen and diborane peaking at approximately 127 and 227 °C respectively, when heating $LiBH_4$ under ultra-high vacuum ($5*10^{-9}$ mbar). Since diborane is instable above around 250 °C, its signal vanished at 267 °C where the H_2 signal continues to increase beyond the $LiBH_4$ melting point. The evolution of diborane was observed only when certain experimental or detection methods applied (Borgschulte *et al.*, 2011a; Liu *et al.*, 2011).

Recently, Yan *et al.* (2012) reported the effect of back-pressure on the decomposition pathway of $LiBH_4$. Two pathways were proposed under corresponding conditions: the decomposition via $Li_2B_{12}H_{12}$ (Equation 2.12 and 2.13), and the direct decomposition into boron (Equation 2.13 only). When heated to 427 °C in 10 bar H_2 or 600 °C in 50 bar H_2, the major $LiBH_4$ phase was stable and only a small amount of $LiBH_4$ decomposed into $Li_2B_{12}H_{12}$. When $LiBH_4$ decomposed under a lower pressure range of 0.1 to 10 bar H_2 at 527 and 600 °C, the formation of boron as well as $Li_2B_{12}H_{12}$ were detected.

$$LiBH_4 \rightarrow \tfrac{5}{6} LiH + \tfrac{1}{12} Li_2B_{12}H_{12} + \tfrac{13}{12} H_2 \qquad (2.12)$$

$$\rightarrow LiH + B + \tfrac{3}{2} H_2 \qquad (2.13)$$

Hoang and Van de Walle (2012) performed a DFT study of defects in $LiBH_4$, and proposed a decomposition mechanism of $LiBH_4$ involving the formation and migration of ions/clusters via native defects. As a result, $LiBH_4$ was believed to release borane BH_3 at the surface or interface, leaving the negatively charged hydrogen interstitial (H_i) in the bulk material, which then acted as the nucleation site for LiH formation. The BH_3 could subsequently decompose into B and H_2, or dimerise to form B_2H_6. Furthermore, $Li_2B_{12}H_{12}$ might be formed from the

further polymerisation between borane species (e.g. B_2H_6 and/or higher boranes), and/or from the reaction between B_2H_6 and residual $LiBH_4$ (Friedrichs *et al.*, 2010c).

2.2.1.4 Structures of $[B_{12}H_{12}]^{2-}$ and $[B_{10}H_{10}]^{2-}$ clusters

Johnson and Brody (1982) first synthesised $Li_2B_{12}H_{12}$ using a wet chemistry method and reported its XRD pattern without structural solution. Ohba *et al.* (2006) calculated stabilities of $Li_2B_{12}H_{12}$ with difference structures: cubic (space group *Fm*-3) based on $K_2B_{12}H_{12}$, and monoclinic (*P2₁/n*) based on $K_2B_{12}(OH)_{12}$. The monoclinic type consisted of a closo-dodecaborate $[B_{12}H_{12}]^{2-}$ unit and two Li^+ ions, and appeared to be the most stable among the candidate materials. Her *et al.* (2008) synthesised a cubic $Li_2B_{12}H_{12}$ (*Pa-3*), following a wet chemistry method by Johnson and Brody (1982) who reported a XRD pattern of $Li_2B_{12}H_{12}$ without structural solution. This $Li_2B_{12}H_{12}$ (*Pa-3*) has a higher symmetry compared to the theoretical cubic $Li_2B_{12}H_{12}$ (*Fm*-3).

Vibrational spectra of $[B_{12}H_{12}]^{2-}$ and $[B_{10}H_{10}]^{2-}$ anions in aqueous solutions have been fully assigned (Leites *et al.*, 1982). Isolated $[B_{12}H_{12}]^{2-}$ icosahedrons with the symmetry point group of I_h are expected to have six Raman-active modes: two are polarized bands corresponding to symmetry A_g, and four are depolarized bands for H_g. In addition, there are three F_{1u} IR active modes. Ohba *et al.* (2006) also presented a theoretical vibrational spectrum of $Li_2B_{12}H_{12}$ which was divided into three regions: the displacements of Li atoms (< 300 cm^{-1}), the B-H bending modes (450-1100 cm^{-1}), and the B-H stretching modes (2400-2600 cm^{-1}). The frequencies of bending modes are lower than those for $LiBH_4$, while stretching modes are higher.

No crystal structure for $Li_2B_{10}H_{10}$ has been experimentally reported since Johnson and Brody (1982) published a set of XRD patterns without lattice parameter refinement. However, Hofmann and Albert (2005) have synthesised crystalline $M_2B_{10}H_{10}$ (M = Na, K, Rb) for other alkali metal elements, and determined that the compounds belong in the monoclinic space group *P12₁/n1*. The assignment of the vibrational spectra of

solid/aqueous $NaB_{12}H_{12}$ and $K_2B_{12}H_{12}$ indicated that the $[B_{10}H_{10}]^{2-}$ anion (point group D_{4d}) has lower symmetry than the $[B_{12}H_{12}]^{2-}$ anion, and therefore, should have 19 Raman actives: $\Gamma = 6A_1 + 6E_2 + 7E_3$, where A_1 is polarized, E_2 and E_3 are depolarized (Leites $et\ al.$, 1983).

More recently, the study of thermal stability of $Li_2B_{12}H_{12}$ revealed that the pure crystalline cubic $Li_2B_{12}H_{12}$ (Pa-3) began to partially decompose to amorphous $Li_2B_{12}H_{12-x}$ above 250 °C under either vacuum or H_2 backpressure, displaying a broad hump with a d-spacing range varying between 5.58 and 7.00 Å in XRD patterns, dependent on the amount of H released (Pitt $et\ al.$, 2013). $Li_2B_{12}H_{12-x}$ was stable at 600 °C under vacuum. New polymorphs: well-crystallised β-$Li_2B_{12}H_{12}$ and nanocrystalline γ-$Li_2B_{12}H_{12}$, were reported after the rehydrogenation of $Li_2B_{12}H_{12-x}$ at 450 °C in 125 bar H_2 for 24 h. However, the structures for both polymorphs were not solved in this work. Furthermore, it was suggested that $LiBH_4$ decomposes via γ-$Li_2B_{12}H_{12}$ to $Li_2B_{12}H_{12-x}$, instead of the cubic $Li_2B_{12}H_{12}$ (Pa-3).

2.2.1.5 Destabilisation and kinetic modification of LiBH₄

Many efforts by approaches of additives and nanoconfinement etc., have been carried out to attempt to modify the hydrogen storage properties of $LiBH_4$. Additives (e.g. oxides, halides, hydrides, metals etc.) can improve the hydrogen storage properties of $LiBH_4$, but detailed discussion of these is beyond the scope of this thesis. One of the most effective additives for $LiBH_4$ was found to be the mixture of $LiBH_4+0.2MgCl_2+0.1TiCl_3$ which released 5 wt% H_2 between 60 and 400 °C and could be rehydrogenated to 4.5 wt % at 600 °C under 70 bar H_2 (Au $et\ al.$, 2006). However, the catalytic mechanism for most additives is still uncertain and the effect usually varies with further de/re-hydrogenation cycling experiments. Another approach through the combination of $LiBH_4$ with another compounds to form a "reactive hydride composite", can significantly lower the overall reaction enthalpy change, as observed for the $2LiBH_4$-MgH_2 system whose T_{dec} was reduced from ca. 408 to 168 °C (Vajo $et\ al.$, 2005):

$$2LiBH_4 + MgH_2 \rightarrow 2LiH + MgB_2 + 4H_2 \qquad (2.14)$$
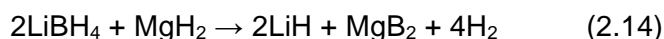
Nanoconfinement facilitates the de/re-hydrogenation of $LiBH_4$, resulting in faster sorption kinetics and possibly decreasing the capacity loss during cycling (Gross *et al.*, 2008). When $LiBH_4$ was incorporated within mesoporous carbon, the T_{dec} was lowered to 200 °C and the formation of unfavourable byproducts $Li_2B_{12}H_{12}$ and B_2H_6 was probably eliminated (Cahen *et al.*, 2009).

In summary, $LiBH_4$ has the highest theoretical H_2 density; but its elevated H_2 cycling conditions and poor kinetics as well as the stable by-products, hinder it from practical use. To improve its hydrogen storage properties, better understanding of its decomposition mechanism is needed.

2.2.2   NaBH$_4$

$NaBH_4$ has large gravimetric (10.8 wt%) and volumetric (114.5 kg H_2m^{-3}) H_2 densities and is much less expensive than $LiBH_4$ (Schlapbach and Züttel, 2001).

2.2.2.1 Synthesis and structure

A number of synthesis routes have been reported for $NaBH_4$ (Jain *et al.*, 2010a). Schlesinger *et al.* (1953c) synthesised $NaBH_4$ by the reaction between B_2H_6 and $NaBH(OCH_3)_3$ or $NaB(OCH_3)_4$ or $NaOCH_3$, of which the one with $NaBH(OCH_3)_3$ reacted very rapidly. $NaBH_4$ could also be prepared via the reaction of NaH and B_2H_6 in diglyme according to the Equation 2.15 (James and Wallbridge, 1970):

$$2NaH + B_2H_6 \rightarrow 2NaBH_4 \qquad (2.15)$$
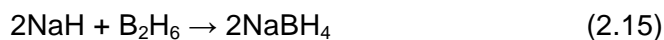
Nowadays, one commercial production route for $NaBH_4$ is based on the Schlesinger Process, where NaH reacts with $B(OCH_3)_3$ in mineral oil at 250-280 °C followed by extraction of $NaBH_4$ from the reaction mixture using isopropylamine (Equation 2.16) (Schlesinger *et al.*, 1953b; Soloveichik, 2007).

$$4NaH + B(OCH_3)_3 \rightarrow NaBH_4 + 3NaOCH_3 \qquad (2.16)$$

$NaBH_4$ has been used commercially as a hydrogen source via its hydrolysis reaction (Equation 2.17), and Kojima and Haga (2003) demonstrated that 97% of the product $NaBO_2$ could be recycled after heated with MgH_2 at 550 °C in 70 bar H_2 for 2 h (Equation 2.18).

$$NaBH_4 + 2H_2O \rightarrow 4H_2 + NaBO_2 \qquad (2.17)$$

$$NaBO_2 + 2MgH_2 \rightarrow NaBH_4 + 2MgO \qquad (2.18)$$

Recently, Garroni *et al.* (2013) announced that $NaBH_4$ (cubic *Fm-3m*) with a yield of 14 wt%, together with MgH_2, were obtained by ball milling a $2NaH+MgB_2$ mixture in 120 bar H_2 for 20h.

$NaBH_4$ has a face-centred cubic structure (space group *Fm-3m*) at room temperature, and undergoes a disorder-order phase transition to a tetragonal phase below -83 °C (Stockmayer and Stephenson, 1953; Abrahams and Kalnajs, 1954). Although this cubic phase was sometimes described as *F-43m* space group (Davis and Kennard, 1985; Fischer and Züttel, 2004) due to two different orientations of $[BH_4]^-$, it has been noted that the fully disordered *F-43m* model is completely identical to the *Fm-3m* model (Filinchuk and Hagemann, 2008). The vibration of $NaBH_4$ is divided into the external lattice mode, and the internal bending (1050 to 1300 cm^{-1}) and stretching (2100 to 2500 cm^{-1}) modes, which are very close to $LiBH_4$ vibrations (Harvey and McQuaker, 1971a).

2.2.2.2 Hydrogen storage properties

$NaBH_4$ starts to decompose at around 150 °C, with the release of 1 wt% of H_2 (Urgnani *et al.*, 2008). The major H_2 desorption event started at around 450 °C and shows a peak at temperatures slightly higher than 500 °C, where the material was already in the liquid state. A total amount of H_2 release of around 10.4 wt% was measured up to 600 °C, with no B_2H_6 detected by mass spectrometry during decomposition.

On the other hand, it is improbable that NaH would act as an intermediate during the decomposition of $NaBH_4$, since pure NaH decomposes into its constituent elements at a

lower temperature (425 °C) than $NaBH_4$ (Martelli *et al.*, 2010a). The complete dehydrogenation reaction of $NaBH_4$ can be simplified as follows (without mentioning the possible formation of intermediates) (Mao *et al.*, 2011):

$$NaBH_4 \rightarrow Na + B + 2H_2 \qquad 10.6 \text{ wt \% } H_2 \qquad (2.19)$$

However, the practical use of $NaBH_4$ for hydrogen storage through thermolysis is hindered by its high stability and slow sorption kinetics. In order to try to enhance the properties, approaches of composite destabilisation, nanosizing/nanoconfinement and catalysts have been developed. It was found that the presence of MgH_2 could destabilise $NaBH_4$ via two steps: the dehydrogenation of MgH_2 to Mg, and subsequently the reaction between Mg and $NaBH_4$ to form NaH and MgB_2 with H_2 evolution (Garroni *et al.*, 2009; Mao *et al.*, 2009). Later, Garroni *et al.* (2011) detected the formation of $Na_2B_{12}H_{12}$ in the decomposition of $2NaBH_4+MgH_2$ up to 450 °C using ex situ solid-state NMR.

Based on theoretical calculations, Caputo *et al.* (2010) proposed that $Na_2B_{12}H_{12}$ could be formed as a very stable product during decomposition, and could prevent the subsequent rehydrogenation process. Ngene *et al.* (2011) observed the formation of $Na_2B_{12}H_{12}$ and Na with 8.1 wt% H_2 loss in bulk pure $NaBH_4$ after heating in flowing Ar to 600 °C. By confinement in nanoporous carbon, $NaBH_4$ showed a greatly reduced decomposition temperature of 250 °C, and the reversibility with 43 % of H_2 reabsorbed at 325 °C in 60 bar H_2. 98% of the initial H_2 capacity could be rehydrided to $NaBH_4$, when extra Na was added to the nanocomposites.

2.2.3 KBH_4

KBH_4 was first prepared by Schlesinger *et al.* (1953c) using the reaction of B_2H_6 with $KB(OCH_3)_4$. Alternatively, KBH_4 can be made through the reaction of $NaBH_4$ and KOH (Equation 2.20) (Banus and Bragdon, 1955), or mechanically milling KBO_2 with excess MgH_2 (Equation 2.21) (Li *et al.*, 2003):

$$NaBH_4 + KOH \rightarrow KBH_4 + NaOH \qquad (2.20)$$

$$2MgH_2 + KBO_2 \rightarrow KBH_4 + 2MgO \qquad (2.21)$$
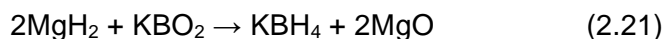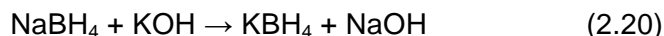
Similar to $NaBH_4$, KBH_4 has a face-centred cubic (fcc) structure (space group Fm-3m) at room temperature (Luck and Schelter, 1999). The cubic KBH_4 transformed to a tetragonal ($P4_2/nmc$) structure at -203 °C (Renaudin et $al.$, 2004). This phase change was also observed by Harvey and McQuaker (1971a), who assigned the vibrational spectra for both phases.

KBH_4 contains 7.5 wt% of H_2, and starts to decompose at 584 °C with a melting point at 607 °C when heated in hydrogen atmosphere (Orimo et $al.$, 2004):

$$KBH_4 \rightarrow K + B + 2H_2 \qquad (2.22)$$
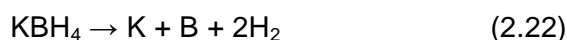
2.3 Alkaline earth metal borohydrides

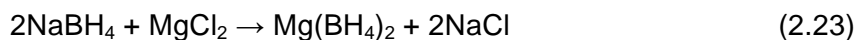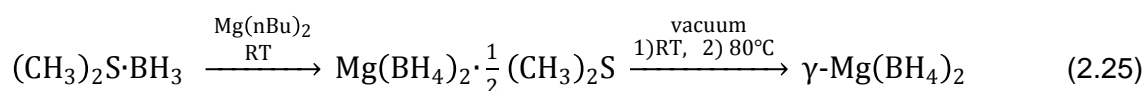### 2.3.1 Mg(BH$_4$)$_2$

2.3.1.1 Synthesis and recombination

The first reported synthesis of $Mg(BH_4)_2$ was published by Wiberg and Bauer (1950) who used diethylmagnesium (Et_2Mg) to react with diborane in ether. Different synthetic methods were consequently well described, but the purity and the structure were seldom assessed due to unisolated solvates or chlorides (Plešek and Heřmánek, 1966; Konoplev and Bakulina, 1971; Nakamori et $al.$, 2006b).

More recently, Chlopek et $al.$ (2007) tried various procedures based on mechanochemical and wet chemical synthesis. A mixture of $2NaBH_4+MgCl_2$ was pre-milled for 2 h according to Equation 2.23 and then dissolved into diethyl ether. Most of the solvent was removed by evacuation and heating at different temperatures. A yield of 50% of $Mg(BH_4)_2$ with 91 % purity was achieved. Another approach is to start with $(C_2H_5)_3N\cdot BH_3$ and the pre-milled

MgH_2 (Equation 2.24). After the removal of $(C_2H_5)_3N$, solvent-free α-$Mg(BH_4)_2$ with 95% purity was yielded with respect to 5 % unreacted MgH_2.

$$2NaBH_4 + MgCl_2 \rightarrow Mg(BH_4)_2 + 2NaCl \qquad (2.23)$$

$$MgH_2 + 2(C_2H_5)_3N \cdot BH_3 \rightarrow Mg(BH_4)_2 + 2(C_2H_5)_3N \qquad (2.24)$$

Later, Filinchuk *et al.* (2011) reported that a new polymorph γ-$Mg(BH_4)_2$ was synthesised from $(CH_3)_2S \cdot BH_3$ and $Mg(nBu)_2$ via the formation of $Mg(BH_4)_2 \cdot \frac{1}{2}S(CH_3)_2$ intermediate followed by evacuation at 80 °C and $2*10^{-5}$ bar for 12 to 16 h:

$$(CH_3)_2S \cdot BH_3 \xrightarrow[\text{RT}]{\text{Mg(nBu)}_2} Mg(BH_4)_2 \cdot \frac{1}{2}(CH_3)_2S \xrightarrow[\text{1)RT, 2) 80°C}]{\text{vacuum}} \gamma\text{-}Mg(BH_4)_2 \qquad (2.25)$$

Bateni *et al.* (2012) ball-milled $NaBH_4$ with $MgBr_2$ instead of $MgCl_2$, and obtained $Mg(BH_4)_2$ with some remaining NaBr after solvent purification. The advantage of $MgBr_2$ is that the reaction time is considerably shorter than $MgCl_2$, and the excess of $MgBr_2$ could act as an additive to lower the onset dehydrogenation temperature from 290 ºC to about 220 ºC.

A DFT calculation by Vajeeston *et al.* (2006) suggested that the synthesis of $Mg(BH_4)_2$ from its elements or its binary compounds, e.g. MgB_2 and MgH_2, is thermodynamically favoured. Severa *et al.* (2010b) showed the direct hydrogenation of MgB_2 to $Mg(BH_4)_2$ with a yield of 75 % at 400 ºC in 950 bar H_2 for 108 h (Equation 2.26). An amorphous $Mg(BH_4)_2$ was reported to be synthesized together with the formation of other $Mg(B_xH_y)_n$ species by ball-milling of MgB_2 and H_2 for up to 100 h (Pistidda *et al.*, 2010). Gupta *et al.* (2013) ball milled MgB_2 in 350 bar H_2 for 15 h: the formation of $Mg(BH_4)_2$ was observed as the final product through $[B_xH_y]^{n-}$ intermediates. This mixture can decompose completely into MgB_2 with the release of 4 % H_2 upon heating to 390 ºC. In order to overcome the poor kinetics of the hydrogenation of MgB_2. The use of nanostructured materials containing grain boundary defects introduced by mechanical milling might help (Li *et al.*, 2010a).

$$MgB_2 + 4H_2 \rightarrow Mg(BH_4)_2 \qquad (2.26)$$
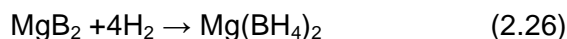
Zhang *et al.* (2012b) attempted to synthesis $Mg(BH_4)_2$ by ball milling Mg+B, MgH_2+B and

MgB_2 mixtures in 20 bar H_2 for 50 h. Amorphous Mg-B-H compound was found to form in Mg+B and MgH_2+B mixtures, whereas the formation of MgH_2 was also observed in Mg+B samples. Upon heating to 350 ºC, 3.7 and 3.9 wt% H_2 were released from Mg+B and MgH_2+B respectively, while only 0.25 wt% was released from MgB_2 sample. It should be noted that these values do not exclude the amount of H_2 desorbed from MgH_2.

Furthermore, Chong *et al.* (2011) reported that the decomposition intermediates $Mg(B_3H_8)_2$ could be rehydrogenated to $Mg(BH_4)_2$ at 250 °C in 120 bar H_2 for 48 h. The solvent-free gas-solid approach has also been demonstrated, by the reaction of MgH_2 and B_2H_6 (Friedrichs *et al.*, 2010b; Zhang *et al.*, 2013); this will be discussed in detail in Section 2.5.2 (p63).

2.3.1.2 Crystal and vibrational structures

Although various theoretical studies on the structure of $Mg(BH_4)_2$ have been performed, all these predictions differ substantially due to the extreme complexity of the structure (Charkin *et al.*, 1987; Nakamori *et al.*, 2006b; Vajeeston *et al.*, 2006). By synthesising high purity $Mg(BH_4)_2$, Chlopek *et al.* (2007) reported two sets of XRD data for a low temperature α and a high temperature β phase without fully solving their structures. This α-phase can irreversibly turn into the β-phase at around 190 °C. Independent studies by Černý *et al.* (2007) and Her *et al.* (2007) found that the α-phase exhibits a hexagonal structure with the space group $P6_1$, despite a higher symmetry structure $P6_122$ being predicted by DFT calculations (Dai *et al.*, 2008).

Later, Filinchuk *et al.* (2009a) refined structures of $Mg(BH_4)_2$ by using single-crystal and powder synchrotron X-ray diffraction and vibrational spectroscopy. They confirmed that the α-phase has a hexagonal structure in space group $P6_122$, while the β-phase is orthorhombic in space group *Fddd*. In addition, α-$Mg(BH_4)_2$ has 6.4% unoccupied voids (each of 37 $Å^3$), which could allow a small molecule (such as H_2O) to be accommodated into the structure. Thus, this porous structure could be considered as a potential new class

of framework materials for hydrogen storage. The β-phase is less dense by about 3% but contains no unoccupied voids.

The γ-Mg(BH$_4$)$_2$ has a highly symmetric cubic structure (space group *Ia-3d*) which consists of a remarkable 33% of unoccupied voids (Filinchuk *et al.*, 2011). As a result, an additional 3.0 wt% H$_2$ was stored into γ-phase at -193 °C under 105 bar H$_2$, which can be represented as γ-Mg(BH$_4$)$_2$·0.8H$_2$. This leads to an increase of the total gravimetric H$_2$ capacity of γ-Mg(BH$_4$)$_2$ from 14.9 wt% to 17.4 wt% H$_2$.

Recently, David *et al.* (2012) confirmed the structure of γ-phase theoretically and experimentally. No conversion between the γ- and α/β-phases is observed on heating. Instead, the γ-phase converted to a more disordered β'-phase and a metastable ε-phase at 135 °C under an Ar atmosphere. A detailed NMR study by Eagles *et al.* (2012) revealed a transformation of γ-Mg(BH$_4$)$_2$ to another phase occurred between 175 and 225°C under a static 0.9 bar N$_2$ atmosphere. This newly formed phase was reported to have a similar but not identical structure to the β-phase. A parallel study given by Paskevicius *et al.* (2012) indicated that γ-phase transformed to a disordered β-phase, via the formation of a new low temperature phase (also labelled as "ε-") at 150-205 °C in 1 bar H$_2$. It should be noted that this ε-phase differs from the one named by David *et al.* (2012), although structures for all these metastable phases remain unclear.

Filinchuk *et al.* (2011) also found that α-Mg(BH$_4$)$_2$ transformed to a new high-pressure polymorph δ-Mg(BH$_4$)$_2$ with a volume collapse of approximate 20% under 1.1-1.6 GPa of hydrostatic pressures; while γ-Mg(BH$_4$)$_2$ changed into a diffraction-amorphous phase at 0.4-0.9 GPa and then turns into crystalline δ-Mg(BH$_4$)$_2$ at about 2.1 GPa. This dense δ-Mg(BH$_4$)$_2$ has no unoccupied voids, resulting in a very high volumetric H$_2$ density (147 g H$_2$/L at ambient pressure). The δ-phase can be stable up to 15 GPa, and reverts to the α-phase at about 100 °C under ambient pressure. **Table 2.2** summarised different polymorphs of Mg(BH$_4$)$_2$ together with their H$_2$ densities.

Table 2.2 Different polymorphs of $Mg(BH_4)_2$ and their gravimetric (ρ_m) and volumetric (ρ_v) H_2 capacities.

Compound	Structure	Space group	ρ_m (wt%)	ρ_v (g H_2/L)	References
α-$Mg(BH_4)_2$	hexagonal	$P6_122$	14.9	117	(Filinchuk *et al.*, 2009a)
β-$Mg(BH_4)_2$	orthorhombic	*Fddd*	14.9	113	(Her *et al.*, 2007)
γ-$Mg(BH_4)_2$	cubic	*Ia*-3*d*	14.9	82	(Filinchuk *et al.*, 2011)
γ-$Mg(BH_4)_2 \cdot 0.8H_2$	cubic	*Ia*-3*d*	17.4	98	(Filinchuk *et al.*, 2011)
δ-$Mg(BH_4)_2$	tetragonal	$P4_2nm$	14.9	147	(Filinchuk *et al.*, 2011)

A number of vibrational spectroscopic studies of $Mg(BH_4)_2$ have been performed (Filinchuk *et al.*, 2009a; George *et al.*, 2009; Giannasi *et al.*, 2010; Filinchuk *et al.*, 2011; Reed and Book, 2011). The vibrational spectra of α- and β-phases can be divided into three regions: lattice modes including optical modes of between Mg^+ and $[BH_4]^-$ ions in the range of 200-300 cm^{-1} and librational modes of $[BH_4]^-$ ions at around 350 cm^{-1}; while bending (v_2 and v_4) and stretching (v_1 and v_3) internal modes for $[BH_4]^-$ tetrahedral are located at 1100-1400 cm^{-1} and around 2250 cm^{-1}, respectively (Giannasi *et al.*, 2010). The high value of bending mode v_2 (compared to that for $LiBH_4$) was due to the bidentate bonding of $[BH_4]^-$ to the Mg^{2+} ions; that is, the presence of the Mg ion leads to an increase in frequency of the symmetrical BH_2 bending mode (Filinchuk *et al.*, 2009a).

2.3.1.3 Hydrogen storage properties

$Mg(BH_4)_2$ is attractive for hydrogen storage due to its high theoretical capacity (14.9 wt%), and relatively low dehydrogenation enthalpy (67 kJ mol^{-1} H_2 by DSC measurement at 280-450 °C) which is favourable for a reversible reaction (Chlopek *et al.*, 2007). Matsunaga *et al.* (2008) reported a lower enthalpy value of 39.3 kJ mol^{-1} H_2 for the reaction from $Mg(BH_4)_2$ to MgH_2 at 290-350 °C, whereas Li *et al.* (2008) estimated it to be 57 kJ mol^{-1} H_2 by *pcT* measurement. This difference is possibly due to different measurement conditions, and the sluggish kinetics causing equilibrium to not be fully reached (Li *et al.*, 2011b). However, the

decomposition mechanism was found to be very complicated and might proceed through multiple steps as a function of conditions (i.e. temperature and atmosphere/backpressure), possibly with the formation of a series of metastable polyborane complexes (Rönnebro, 2011).

An situ XRD study under vacuum by Chlopek *et al.* (2007) showed that: after transformation from the α- to the β-phase, $Mg(BH_4)_2$ starts to decompose at 290 °C with the formation of MgH_2, MgB_2 and Mg, followed by the presence of Mg, MgB_2 and an unknown phase above 450 °C. But different products Mg, MgH_2 and MgB_4 were observed, if rapidly heating to 390 °C for 30 min and subsequently quenching to room temperature. Soloveichik *et al.* (2009) proposed that the decomposition proceeds in four steps under vacuum, via formation of intermediates $MgB_2H_{5.5}$ (285 °C) and $MgBH_{2.5}$ (350 °C) whose compositions were estimated based on the amount of released H_2. The formation of MgB_4, MgH_2 and $MgB_{12}H_{12}$ were also observed at 350 °C. MgH_2 subsequently decomposed into Mg and finally to MgB_2 at 450 °C.

Hanada *et al.* (2008) investigated the thermal behavior using DTA-TG-MS under flowing He and various H_2 pressures up to 50 bar, respectively. In a helium atmosphere, the main decomposition occurred at 250-410 °C with 12.2 wt% H_2 release via 4-5 distinct steps involving formation of amorphous intermediate species. Under hydrogen pressure, the decomposition events shifted to higher temperatures, indicating a thermodynamically determined decomposition temperature.

Li *et al.* (2009) observed that 14.4 wt% H_2 is released through a multi-step reaction between 247 and 527 °C followed by the formation of MgB_2 as the final product at 597 °C. Moreover, the decomposed sample showed partial reversibility of 6.1 wt% of H_2 which was rehydrided at 270 °C in 400 bar H_2, through the formation of a possible intermediate compound such as $MgB_{12}H_{12}$. **Figure 2.7** illustrats possible decomposition pathways and intermediates of α-$Mg(BH_4)_2$ during heating, proposed in previous studies.
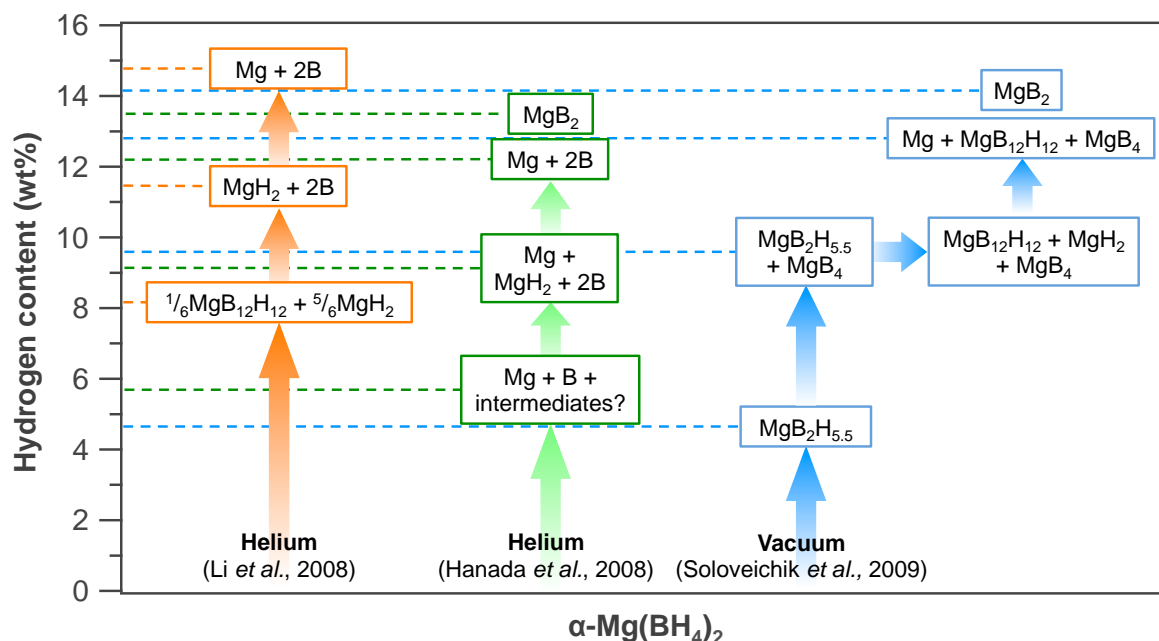
Figure 2.7 Possible dehydrogenation processes for α-Mg(BH$_4$)$_2$ based on the literature. The question mark means the possibility of the formation of an intermediate compound during dehydrogenation. Reproduced from Li *et al.* (2011b) and Soloveichik *et al.* (2009).

Hwang *et al.* (2008) suggested the existence of amorphous MgB$_{12}$H$_{12}$ in the partially decomposed borohydrides, by comparing solid-state NMR of the sample with a reference K$_2$B$_{12}$H$_{12}$; although this study lacked any crystal structure evidence. Ozolins *et al.* (2009) predicted that one of most likely structures for MgB$_{12}$H$_{12}$ was monoclinic (space group *C2/m*) which has the lowest energy configuration. Kulkarni *et al.* (2010) explained that the amorphous MgB$_{12}$H$_{12}$ observed experimentally might be actually composed of a mixture of many different crystalline phases having similar energies, according to the first principle calculations.

Moreover, Newhouse *et al.* (2010) suggested that there must be intermediate(s) Mg(B$_x$H$_y$)$_n$ formed before the formation of MgB$_{12}$H$_{12}$. Different types of boranes, such as MgB$_2$H$_6$, Mg(B$_3$H$_8$)$_2$, Mg$_3$(B$_3$H$_6$)$_2$ and MgB$_{10}$H$_{10}$, have been experimentally or theoretically studied (van Setten *et al.*, 2009; Yan *et al.*, 2011; Yang *et al.*, 2011; Zhang *et al.*, 2012a). One of the proposed phases, Mg(B$_3$H$_8$)$_2$, was identified by solution NMR after heating Mg(BH$_4$)$_2$

isothermally at 200 °C under vacuum for 5 weeks; it could subsequently absorb 2.5 wt% H_2 after being heated to 250 °C under 120 bar H_2 for 48 h (Chong *et al.*, 2011).

The thermal decomposition of γ-$Mg(BH_4)_2$ has been studied using in-situ X-ray diffraction, NMR and IR spectroscopy (David *et al.*, 2012; Paskevicius *et al.*, 2012). After a series of phase transformations, the decomposition of γ-$Mg(BH_4)_2$ proceeds in a similar manner to that observed for α- and β-$Mg(BH_4)_2$: via multiple steps together with the formation of amorphous compounds with concurrent evolution of hydrogen but no diborane. However, these amorphous species formed during decomposition has not been directly identified, e.g. possibly, $MgB_{12}H_{12}$ or $Mg(B_3H_8)_2$, etc..

The effect of ball milling on $Mg(BH_4)_2$ has also been carried out (Li *et al.*, 2007a; Bardaji *et al.*, 2011a). A transformation from a crystalline to an amorphous structure was observed for α/β-$Mg(BH_4)_2$ after ball milling. This amorphous phase recrystallizes into β-phase after heating to 150 °C in flowing He. However, no significant effect of ball milling on the dehydriding properties of $Mg(BH_4)_2$ was reported.

In terms of destabilization and kinetics modification, additives (especially $TiCl_3$) have been found to significantly reduce the decomposition temperature from 262 to 88 °C; although it is not clear if these additives are acting as catalysts or forming stable phases to drive the reaction towards completion (Li *et al.*, 2007a; Bardaji *et al.*, 2011a). After nanoconfinement of $Mg(BH_4)_2$ into activated carbon, the onset decomposition temperature was reduced to about 170 °C (Fichtner *et al.*, 2009). More recently, $Mg(BH_4)_2$ was infiltrated into mesoporous carbon (CMK3) containing dispersed Ni nanoparticles (Wahab *et al.*, 2013). The dehydrogenation reaction started at 75 °C and reached a peak at 155 °C: 5.2 wt% H_2 was released at 250 °C in 20 min. However, the mechanism needs further investigation.

In summary, $Mg(BH_4)_2$ has a high theoretical gravimetric H_2 density and has demonstrated partial reversibility. $Mg(BH_4)_2$ can exist as several polymorphs, as a result of different synthesis conditions; these can undergo a series of temperature- or pressure dependent

structural transitions. Dehydrogenation proceeds through multi-step reactions together with the formation of a series of intermediate compounds as a function of conditions. Two possible decomposition pathways can be simplified as follows (Rönnebro, 2011):

$$6Mg(BH_4)_2 \rightarrow MgB_{12}H_{12} + 5MgH_2 + 13H_2 \qquad 8.1\ wt\% > 350\ °C \qquad (2.27)$$

$$Mg(BH_4)_2 \rightarrow MgB_2 + 4H_2 \qquad\qquad\qquad 14.9\ wt\% > 450\ °C \qquad (2.28)$$
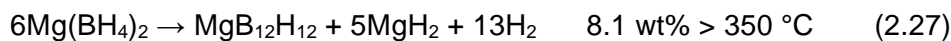
However, the detailed decomposition mechanism(s), as a function of conditions and the starting phase(s), is not clear.

2.3.2   Ca(BH$_4$)$_2$

2.3.2.1 Synthesis and recombination

The synthesis of Ca(BH$_4$)$_2$ by the reaction of diborane with calcium hydride/alkoxides was first reported by Wiberg *et al.* (1955) and Wiberg and Hartwimmer (1955). Parallel work by Kollonitsch *et al.* (1955) demonstrated the synthesis of Ca(BH$_4$)$_2$ through a reaction of NaBH$_4$ and CaCl$_2$ in an alcoholic solution between -50 and -20 °C according to Equation 2.29. However, Ca(BH$_4$)$_2$ in alcoholic solutions would decompose above -10 °C. Later, Mikheeva and Titov (1964) developed this method by using pyridine at room temperature and washing the product in tetrahydrofuran (C$_4$H$_8$O, THF) which consequently formed a solvent adduct Ca(BH$_4$)$_2$·(THF)$_2$. This technique has been adopted commercially for the production of Ca(BH$_4$)$_2$·(THF)$_2$. Adduct-free Ca(BH$_4$)$_2$ could be obtained by heating Ca(BH$_4$)$_2$·(THF)$_2$ at 160 °C under vacuum for 1 h (Miwa *et al.*, 2006). α-Ca(BH$_4$)$_2$ was mainly produced by this approach, but β-phase could be achieved if Ca(BH$_4$)$_2$·(THF)$_2$ was heated to a higher temperature or for a longer time.

$$2NaBH_4 + CaCl_2 \rightarrow Ca(BH_4)_2 + 2NaCl \qquad\qquad (2.29)$$
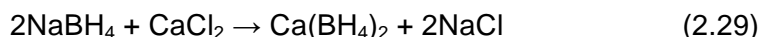
The preparation of Ca(BD$_4$)$_2$ from CaD$_2$ and (C$_2$H$_5$)$_3$N·BD$_3$ (Equation 2.30) was reported by Buchter *et al.* (2008b), based on the analogous synthesis of Mg(BH$_4$)$_2$ by Chlopek *et al.*

(2007). After removal of the solvent, a new polymorph γ mixed with β-phase was detected in the solid product by XRD.

$$CaH_2 + 2(C_2H_5)_3N \cdot BD_3 \rightarrow Ca(BH_4)_2 \cdot 2(C_2H_5)_3N \qquad (2.30)$$
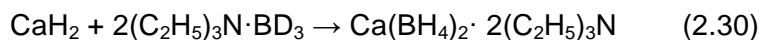
Nakamori *et al.* (2007) reported the mechanochemical synthesis of $Ca(BH_4)_2$ (and a byproduct of LiCl) by ball milling $LiBH_4$ and $CaCl_2$. Rönnebro and Majzoub (2007) produced α-$Ca(BH_4)_2$ with ~60% yield, by milling $2CaH_2+CaB_6$ with 4-8 mol% of dopants $TiCl_3+Pd$ and then exposing the mixture to 700 bar H_2 at 400-440 °C for 48 h (Equation 2.31). Alternatively, a yield of 19% could be achieved at room temperature in 140 bar H_2 for 24 h (Rongeat *et al.*, 2010).

$$2CaH_2 + CaB_6 + 10H_2 \rightarrow 3Ca(BH_4)_2 \qquad (2.31)$$
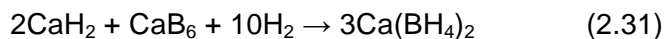
Barkhordarian *et al.* (2008) reported the formation of a α-$Ca(BH_4)_2+MgH_2$ composite by hydrogenation of a pre-milled mixture of CaH_2 and MgB_2 at 350 °C under 140 bar H_2 (Equation 2.32). The maximum H_2 capacity of 8.3 wt% H_2 was achieved for this composite. On the other hand, it was found that $Ca(BH_4)_2$ could not be formed directly from CaH_2 and B using the same method, possibly due to the high energy barrier of breaking the B-B bonds in icosahedral clusters of elemental boron. Each atom is connected to five other atoms via covalent bonds in an icosahedral unit, while each atom is bonded to a maximum of three other B atoms in MgB_2.

$$CaH_2 + MgB_2 + 4H_2 \rightarrow Ca(BH_4)_2 + MgH_2 \qquad (2.32)$$

Kim *et al.* (2010) showed that the decomposition products (CaH_2, CaB_6 and Mg) of the $Ca(BH_4)_2+MgH_2$ mixture, could be rehydrogenated through the formation of $Ca_4Mg_3H_{14}$ at 350 °C under 90 bar H_2 for 24 h. However, $Ca(BH_4)$ was not formed by hydrogenating a mixture of as-received CaH_2, CaB_6 and Mg compounds, possibly due to the effect of the particle size of the CaB_6. Another synthesis approach was to ball mill CaH_2 in gaseous B_2H_6, thereby producing $Ca(BH_4)_2$ (90%) mixed with the remaining CaH_2 (10%) (Friedrichs *et al.*, 2010b); this will be discussed in more detail in Section 2.5.2 (p63).

2.3.2.2 Crystal and vibrational structures

Miwa *et al.* (2006) first proposed that α-Ca(BH$_4$)$_2$ has a face-centred orthorhombic structure (space group *Fddd*) according to DFT calculations and lab-based XRD data on the desolvated Ca(BH$_4$)$_2$·(THF)$_2$ sample. This configuration was in agreement with the following theoretical study (Vajeeston *et al.*, 2007) and experimental work (Rönnebro and Majzoub, 2007; Aoki *et al.*, 2008). By performing high-quality synchrotron powder diffraction measurements, Filinchuk *et al.* (2009b) concluded that the space group of α-Ca(BH$_4$)$_2$ is *F2dd*, where the [BH$_4$]$^-$ anions are closer to an ideal tetrahedral shape than in the *Fddd* space group. In the same work, an intermediate tetragonal α'-phase (*I-42d*) was also proposed. The α-phase underwent a second order transformation to α'-phase at 130-180 °C, followed by a complete phase change to β-phase upon heating to 180 °C.

Riktor *et al.* (2007) performed in situ synchrotron diffraction measurements and identified β and γ polymorphs, which exhibited tetragonal and orthorhombic structures, respectively. The γ-phase undergoes a phase transformation to the β-phase upon heating to 330 °C, followed by the formation of an intermediate phase (tentatively labelled as δ-Ca(BH$_4$)$_2$) at 340 °C. This δ-Ca(BH$_4$)$_2$ phase was later confirmed to be Ca$_3$(BH$_4$)$_3$(BO$_3$) by Riktor et al. (2011).

By performing neutron and synchrotron powder diffractions and DFT calculations on Ca(BD$_4$)$_2$, the β polymorph was indexed as a tetragonal structure with the space group *P4$_2$/m*, whereas the γ-Ca(BH$_4$)$_2$ has an orthorhombic configuration with the space group *Pbca* (Buchter *et al.*, 2008b). However, theoretical calculations by Majzoub and Ronnebro (2009) suggested that the low energy structure of β-Ca(BH$_4$)$_2$ can be described by two different space groups *P*-4 and *P4$_2$/m*. Later, Filinchuk *et al.* (2009b) reported that *P*-4 was a slightly better structural fit for β-Ca(BH$_4$)$_2$, after carrying out Rietveld refinements on diffraction data of a desolvated Ca(BH$_4$)$_2$·(THF)$_2$ sample. Moreover, a theoretical study

showed that the stabilities of the different polymorphs are: α = β < γ at room temperature, and γ < α < β with increasing temperature (Buchter *et al.*, 2009).

Similarly to Mg(BH$_4$)$_2$, Ca(BH$_4$)$_2$ exhibits several polymorphs, α, α', β, and γ depending on the synthetic method and experimental condition used. However, the true crystal structures of the polymorphs of Ca(BH$_4$)$_2$ may not be accurately described until single crystal data is available (Rönnebro, 2011).

Comprehensive studies on the vibrational spectra for α-, β-, and mixed (β+γ)-Ca(BH$_4$)$_2$ were presented by (Fichtner *et al.*, 2008) and (Reed and Book, 2011). Eight external and librational modes below 1000 cm^{-1}, and nine internal vibrations including bending and stretching modes, and two overtones were assigned for α-Ca(BH$_4$)$_2$ in a region of 1000-2700 cm^{-1}. Only six internal modes and no lattice vibrations were observed for β-phase due to strong luminescent background. A continuous transition from α- to β-phase was observed at around 180 °C, accompanied by significant broadening in peak width for the v_2 mode in the bending region between 1230 and 1330 cm^{-1}.

A recent vibrational study showed different sharp librational modes for α- and γ-, which were not observed in β-Ca(BH$_4$)$_2$ (Llamas-Jansa *et al.*, 2012). This suggested the presence of partial disorder in the β-phase due to reorientation of [BH$_4$]$^-$, which is analogous to behaviour observed for the alkali borohydrides (Hagemann *et al.*, 2004).

2.3.2.3 Hydrogen storage properties

Ca(BH$_4$)$_2$ exhibits gravimetric and volumetric H$_2$ densities of 11.6 wt% and 124 kgm^{-3}, respectively (Rönnebro and Majzoub, 2007). Miwa *et al.* (2006) calculated the reaction enthalpy of Ca(BH$_4$)$_2$ to convert to CaB$_6$ and CaH$_2$ to be 32 kJ mol^{-1} H$_2$, and reported a yield of 9.6 wt% H$_2$ after heating to 527 °C by thermal gravimetric analysis, i.e. consistent with the predicted decomposition according to Equation 2.33.

$$Ca(BH_4)_2 \rightarrow {}^2\!/_3CaH_2 + {}^1\!/_3CaB_6 + {}^{10}\!/_3H_2 \qquad 9.6 \text{ wt% H}_2 \qquad (2.33)$$
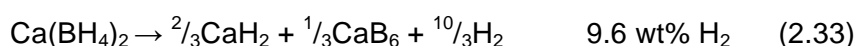
Rönnebro and Majzoub (2007) reported that the dehydrogenation of $Ca(BH_4)_2$ started at approximately 320 °C and released approximately 9 wt% H_2 with the formation of B, CaB_6 and CaH_2 up to 500 °C under vacuum. An unknown product was also formed at 320 °C, which is likely to be $CaB_{12}H_{12}$ by comparison with the NMR spectra of other $[B_{12}H_{12}]^{2-}$ species (Rönnebro and Majzoub, 2008).
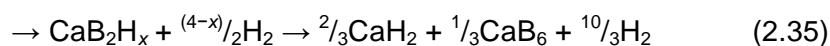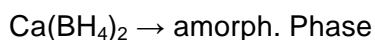
Kim et $al.$ (2008) also observed that the decomposition proceeds by two steps between 347 and 497 °C with 9.0 wt% H_2 loss under vacuum. This weight loss is lower than the predicted value by Equation 2.33, but higher than that for Equation 2.34. The formation of CaH_2 and an unknown intermediate compound was observed at 390 °C by in situ XRD, but CaH_2 was the only observed crystalline phase after the second desorption at 480 °C. Similar thermal decomposition behaviour was also recorded by Aoki et $al.$ (2008) in DSC-TGA-MS and XRD measurements. The following Raman study on the (partial) decomposed samples showed the formation of CaB_6 at 330 and 480 °C (Kim et $al.$, 2009).

$$Ca(BH_4)_2 \rightarrow CaH_2 + 2B + 3H_2 \qquad 8.7 \text{ wt\% } H_2 \qquad (2.34)$$
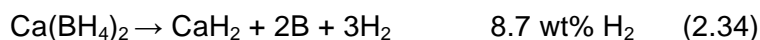
A small difference in decomposition behavior between polymorphs α, β and γ was noted theoretically and experimentally (Borgschulte et $al.$, 2011b; Llamas-Jansa et $al.$, 2012). The sample containing pure β-$Ca(BH_4)_2$ decomposed at about 6 °C lower than the sample containing α-$Ca(BH_4)_2$, followed by the polymorphic transformation to the same β-phase during heating; however, the pure α-$Ca(BH_4)_2$ appeared to release the largest amount of H_2.

Riktor et $al.$ (2007) investigated the thermal decomposition behaviour of $Ca(BH_4)_2$ containing a mixture of polymorphs β and γ. The major desorption event occurs between 335 and 400 °C with the formation of CaH_2, CaO and an unknown compound, followed by a small desorption event at 420-500 °C. This unknown compound was stable up to 400 °C; and was later proposed to have a composition of CaB_2H_x where x was most probably equal to 2, based on theoretical calculations (Riktor et $al.$, 2009). The formation of CaB_6 at 500 °C was also confirmed by room temperature Raman spectroscopy.

An investigation of the effect of H_2 backpressure on the dehydrogenation was reported by (Kim *et al.*, 2012a). Under 1 bar H_2, $Ca(BH_4)_2$ decomposes into CaB_2H_x or $CaB_{12}H_{12}$ via two competitive reactions (Equation 2.35 and 2.36). With increasing H_2 pressure up to 20 bar, the formation of CaB_2H_x was largely suppressed, while amorphous boron appeared and steadily increased in amount. Thus, by applying suitable dehydrogenation conditions (temperature and backpressure), the dehydrogenation pathway could be controlled in order to avoid the formation of the stable phases (i.e. too stable to recombine into $Ca(BH_4)_2$ under practical temperature and pressure conditions) $CaB_{12}H_{12}$ and amorphous boron. In addition, Kim *et al.* (2012b) also found CaB_2H_x and CaB_6 could be rehydrogenated to α- and β-$Ca(BH_4)_2$ without additives at 330 °C under 90 bar H_2 for 24 h, while $CaB_{12}H_{12}$ could not be rehydrogenated.

$Ca(BH_4)_2 \rightarrow$ amorph. Phase

$$\rightarrow CaB_2H_x + {}^{(4-x)}/_2 H_2 \rightarrow {}^2/_3 CaH_2 + {}^1/_3 CaB_6 + {}^{10}/_3 H_2 \qquad (2.35)$$

$$Ca(BH_4)_2 \rightarrow \text{amorph. Phase} \rightarrow {}^1/_6 CaB_{12}H_{12} + {}^5/_6 CaH_2 + {}^{13}/_6 H_2 \qquad (2.36)$$

Although it has been realised that there might be more than one decomposition path via formation of unidentified intermediate(s), e.g. CaB_2H_x, $CaB_{12}H_{12}$, there is little direct conclusive evidence. Vajeeston *et al.* (2011) suggested an orthorhombic CaB_2H_2 compound which is dynamically stable at ambient conditions; and simulated Raman and IR spectra for future experimental verification. However, Zhang *et al.* (2010) disagreed and thought that CaB_2H_6 was more likely to form as an intermediate than CaB_2H_2, according to DFT and prototype electrostatic ground state (PEGS) calculations.

In contrast, several theoretical studies have agreed that $CaB_{12}H_{12}$ is energetically favourable during decomposition (Ozolins *et al.*, 2009; Wang *et al.*, 2009; Kulkarni *et al.*, 2010). A pure $CaB_{12}H_{12}$ compound has been synthesised and the crystal structure has been determined to be monoclinic with a space group *C*2/*c* (Stavila *et al.*, 2010). Furthermore, it has been demonstrated that the presence of CaH_2 could significantly destabilise $CaB_{12}H_{12}$

to promote H_2 release, according to Equation 2.37. Unfortunately, the pre-milled (1 h) $CaB_{12}H_{12}$ and CaH_2 mixture could not be rehydrogenated to $Ca(BH_4)_2$ at 397 °C under 100 bar H_2.

$$CaB_{12}H_{12} + CaH_2 \rightarrow 2CaB_6 + 7H_2 \qquad (2.37)$$

Since the rehydrogenation of undoped $Ca(BH_4)_2$ appears to be difficult to achieve (under moderate temperature and pressure conditions), the effect of transition- and light-metal based additives have been investigated. These have been found to significantly improve the reaction kinetics, for example $Ca(BH_4)_2$ with 2 mol% additive desorbed 7 wt% H_2 at 360 °C after 20 min, compared to only 5.5 wt% for undoped $Ca(BH_4)_2$ (Rönnebro and Majzoub, 2008). Although $Ca(BH_4)_2$ does not show a lower onset decomposition temperature with the addition of MgH_2 (molar ratio of 1:1), the decomposition products can be partially rehydrogenated back to $Ca(BH_4)_2+MgH_2$ under the relatively moderate conditions of 350 °C in 90 or 145 bar H_2 for 24 or 43 h (Minella et al., 2011).

Similarly to other alkali and alkaline-earth borohydrides, nanoconfinement of $Ca(BH_4)_2$ into mesoporous carbon can significantly lower the onset decomposition temperature to about 100 °C and allow the re-uptake of 2.4 wt% H_2, i.e. ~69% of $Ca(BH_4)_4$ rehydrogenated for up to 18 cycles below 540 °C under 25-45 bar H_2 (Ampoumogli et al., 2012; Comănescu et al., 2012).

In summary, $Ca(BH_4)_2$ exhibits several polymorphs with different stability ranges, and dehydrogenation proceeds via two competitive pathways. The stable decomposition products $CaB_{12}H_{12}$ and amorphous B may be avoided by controlling the H_2 back-pressure or through the use of additives. Partial reversibility of $Ca(BH_4)_2$ has been demonstrated with the help of additives and/or nano-confinement.

2.4   Other borohydride systems

2.4.1   Single-cation borohydrides

A range of single-cation borohydrides $M(BH_4)_2$ (e.g. M = Rb, Be, Al, Mn, Y, Zr and Hf; n = 1-4) have also been prepared and their crystal structures and hydrogen storage properties have been investigated. Some other transition metal borohydrides, e.g. Sc, Ti, Zn and V, were synthesised by mechanical milling of corresponding metal chloride and $LiBH_4$/$NaBH_4$; but either have not been fully characterised or exist as dual-cation/anion compounds. A detailed review of all of these materials is beyond the scope of the thesis, however $Mn(BH_4)_2$ and $Y(BH_4)_3$ will be briefly discussed as examples.

$Mn(BH_4)_2$ with a H_2 content of 9.5 wt%, has a trigonal structure (space group $P3_112$) at room temperature (Černý *et al.*, 2009). By ball milling $LiBH_4$ (or $NaBH_4$) and $MnCl_2$, $Mn(BH_4)_2$ formed together with a LiCl (or NaCl) side product (Severa *et al.*, 2010a; Liu *et al.*, 2012). Since no pure $Mn(BH_4)_2$ is available yet, the investigation of $Mn(BH_4)_2$ was conducted under the presence of side products which may affect the thermal decomposition behavior.

Thermal decomposition of $Mn(BH_4)_2$ occurred with the concurrent evolution of hydrogen and diborane, in the range 130-181 °C with 8.4 wt% weight loss for the milled $2LiBH_4+MnCl_2$ sample and 105-145 °C with 8.1 wt% loss for $3LiBH_4+MnCl_2$, respectively (Liu *et al.*, 2012). The formation of Mn and amorphous B were identified for both samples, while three other unidentified phases were observed for the $3LiBH_4+MnCl_2$ sample between 320 and 400 °C. The overall decomposition reaction for $Mn(BH_4)_2$ is most likely:

$$Mn(BH_4)_2 \rightarrow Mn + {}^4/_3 B + {}^1/_3 B_2H_6 + 3H_2 \qquad (2.38)$$
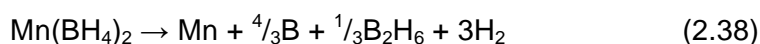
Due to the evolution of diborane, the dehydrogenation reaction of $Mn(BH_4)_2$ is irreversible.

$Y(BH_4)_3$ contains 9.06 wt% hydrogen and its thermal stability lies between stable borohydrides e.g. $LiBH_4$ and less stable ones like $Mn(BH_4)_2$ (Nakamori *et al.*, 2008).

Structures for the low temperature α and high temperature β were determined to be cubic with space groups *Pa*-3 and *Fm*-3*c*, respectively (Sato *et al.*, 2008; Frommen *et al.*, 2010). The phase transformation occurs at about 180 °C. $Y(BH_4)_3$ starts to decompose at 187 °C and releases 7.8 wt% H_2 up to 500 °C (Yan *et al.*, 2009). No diborane was detected during decomposition. Based on DSC-TGA-MS, XRD and NMR results, the decomposition mechanism can be proposed as (Frommen *et al.*, 2010; Ravnsbæk *et al.*, 2010b; Remhof *et al.*, 2012a):

$$Y(BH_4)_3 \rightarrow YH_3 + 3B + {}^9/_2H_2 \rightarrow YH_2 + 3B + 5H_2 \qquad (2.39)$$

$$YH_2 + 4B \rightarrow YB_4 + H_2 \qquad (2.40)$$
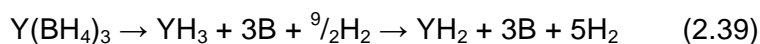
In addition, an unknown Y-B-H phase was observed at 215-280 °C (Ravnsbæk *et al.*, 2010b). Later, NMR analysis of samples partially decomposed at 240-350 °C, revealed the presence of $Y(B_3H_8)_3$ as the main intermediate instead of $Y_2(B_{12}H_{12})_3$ (Yan *et al.*, 2013b). Rehydrogenation of $Y(BH_4)_3$ is possible: the decomposed sample re-absorbed up to 1.3 wt% H_2 at 300 °C under 350 bar H_2 after 24 h (Yan *et al.*, 2009).

2.4.2 Mixed-cations borohydrides

As mentioned in Chapter 2.2-2.3, the alkali and alkaline earth metal borohydrides are too stable for practical applications. It is therefore necessary to try to destabilise these compounds.

Li *et al.* (2007b) investigated the thermal desorption properties of the stoichiometric $M\text{Li}_{(m-n)}(BH_4)_m$ (*M* = Zn, *n* = 2; *M* = Al, *n* = 3; *M* = Zr, *n* = 4; *n* ≤ *m*) compounds prepared by ball-milling $m\text{LiBH}_4$ and $M\text{Cl}_n$. The decomposition temperature of $\text{ZrLi}_{m-n}(BH_4)_m$ increases with an increasing compositional ratio of Li/Zr, i.e. 322 °C for $\text{LiZr}(BH_4)_5$ and 377 °C for $\text{Li}_2\text{Zr}(BH_4)_6$ compared to $\text{Zr}(BH_4)_4$ (167 °C) and LiBH_4 (467 °C); which are inversely proportional to the average electronegativities of their cations. However, no crystal structure determination has yet been reported to support whether new multinary compounds have

indeed been formed.

The crystal structure determination of a dual-cation borohydride $LiK(BH_4)_2$ (orthorhombic with space group *Pnma*) was first reported by Nickels *et al.* (2008). $LiK(BH_4)_2$ was synthesised by heating a $2LiBH_4+KBH_4$ mixture to 125 °C for 12 hours under flowing nitrogen in a tube furnace. This compound exhibits a decomposition temperature of 380 °C, which is close to the median point between the decomposition temperatures of $LiBH_4$ (330 °C) and KBH_4 (500 °C). Although the decomposition temperature for this particular example is still too high for hydrogen storage use, this suggests that the appropriate combination of cations is a promising approach to tailor the thermodynamic properties of borohydride-base materials (Li *et al.*, 2007b).

Ravnsbæk *et al.* (2009) reported the crystal structure of $LiZn_2(BH_4)_5$, $NaZn_2(BH_4)_5$ and $NaZn(BH_4)_3$ synthesised by mechanically milling $M(BH_4)_n$ (M = Li or Na) and $ZnCl_2$ for 2 h in Ar. The $LiBH_4$-$ZnCl_2$ mixture with a mole ratio of 2.5:1, underwent a complete reaction to $LiZn_2(BH_4)_5$ (Equation 2.41), which was the only new phase observed for the samples with other ratios as well.

$$5LiBH_4 + 2ZnCl_2 \rightarrow LiZn_2(BH_4)_5 + 4LiCl \qquad (2.41)$$
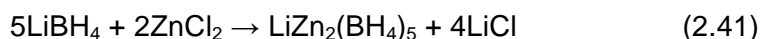
In the case of the $NaBH_4$-$ZnCl_2$ system, small deviations in the composition of the reactants resulted in different reaction products both in terms of the stoichiometry and the structural topology, i.e. $NaZn_2(BH_4)_5$ is formed from the sample $NaBH_4$:$ZnCl_2$ = 2:1, while the sample of $NaBH_4$:$ZnCl_2$ = 3:1 yields $NaZn(BH_4)_3$, as expressed in Equations 2.42 and 2.43.

$$5NaBH_4 + 2ZnCl_2 \rightarrow NaZn_2(BH_4)_5 + 4NaCl \qquad (2.42)$$

$$3NaBH_4 + ZnCl_2 \rightarrow NaZn_2(BH_4)_3 + 2NaCl \qquad (2.43)$$
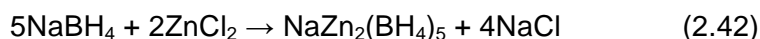
A further structural and thermal properties study on these alkali metal-zinc borohydrides compounds was later carried out by Černý *et al.* (2010). Unlike the bimetallic borohydride that the cations share $[BH_4]^-$ anions (Černý *et al.*, 2011), $MZn_2(BH_4)_5$ (M = Li, Na) consists of isolated $[Zn_2(BH_4)_5]^-$ anions coordinated with M^+ cations, while $NaZn(BH_4)_3$ contains isolated

$[Zn(BH_4)_3]^-$ anions and Na^+ cations. The decomposition of $LiZn_2(BH_4)_5$ occurs between 94 and 122 °C with the evolution of hydrogen and diborane according to Equation 2.44.

$$LiZn_2(BH_4)_5 \rightarrow 2Zn + LiBH_4 + 2B_2H_6 + 2H_2 \qquad (2.44)$$
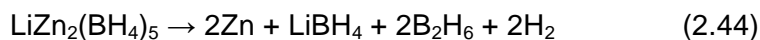
The $2NaBH_4+ZnCl_2$ sample consists of $NaZn_2(BH_4)_5$, $NaCl$, Na_2ZnCl_4 and metallic Zn after ball milling for 350 min. The $NaZn_2(BH_4)_5$ decomposes into metallic Zn and probably $NaBH_4$, diborane and hydrogen (Equation 2.45) between 69 and 92 °C. The $NaBH_4$ was believed to immediately react with $NaCl$ to form a solid solution $Na(Cl,BH_4)$ (Ravnsbæk *et al.*, 2009). However, no $NaZn(BH_4)_3$ was observed in this study, probably due to a longer milling time 350 min allowing the further reaction from $NaZn(BH_4)_3$ to $NaZn_2(BH_4)_5$, compared to the result for 120 min milling by Ravnsbæk *et al.* (2009). The $NaZn(BH_4)_3$ was formed by milling a $3NaBH_4+ZnCl_2$ mixture, which subsequently decomposed between 92 and 112 °C according to Equation 2.46.

$NaZn_2(BH_4)_5 \rightarrow 2Zn + NaBH_4 + 2B_2H_6 + 2H_2$

alternatively: $NaZn_2(BH_4)_5 + NaCl \rightarrow 2Zn + 2Na(Cl,BH_4) + 2B_2H_6 + 2H_2$ $\quad$ (2.45)

$NaZn(BH_4)_3 \rightarrow Zn + NaBH_4 + B_2H_6 + H_2$

alternatively: $NaZn(BH_4)_3 + NaCl \rightarrow Zn + 2Na(Cl,BH_4) + B_2H_6 + H_2$ $\qquad$ (2.46)
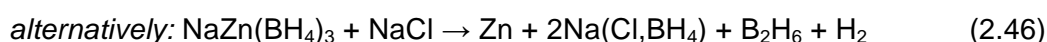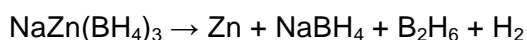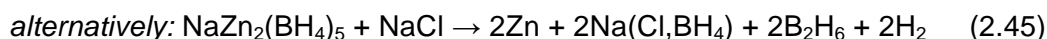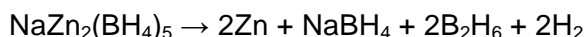
Some examples of dual-cations borohydrides are given in **Table 2.3**. Most of the $MM'(BH_4)_n$ compounds exhibit moderate thermodynamic stabilities between $M(BH_4)_n$ and $M'(BH_4)_n$. Unfortunately, none of the mixed cation-borohydride materials that have so far been reported, can be rehydrided after decomposition i.e. no reversibility (Klebanoff, 2012).

Table 2.3 Hydrogen storage properties of structural-solved dual-cation borohydrides, $MM'(BH_4)_n$ (modified from Li *et al.* (2011b) and Rude *et al.* (2011)).

Borohydrides	Space group	Theor. H$_2$ (wt%)	T_{dec} (°C)
LiK(BH$_4$)$_2$	*Pnma*	10.6	380
LiSc(BH$_4$)$_4$	*P-42c*	14.5	211
LiZn$_2$(BH$_4$)$_5$	*Cmca*	9.5	127
Li$_4$Al$_3$(BH$_4$)$_{13}$	*P-43n*	17.4	70
NaSc(BH$_4$)$_4$	*Cmcm*	12.7	200
NaZn(BH$_4$)$_3$	*P2$_1$/c*	9.1	103
NaZn$_2$(BH$_4$)$_5$	*P2$_1$/c*	8.8	95
KSc(BH$_4$)$_4$	*Pnma*	11.2	210

2.4.3 Eutectic borohydride system

2.4.3.1 LiBH$_4$-Mg(BH$_4$)$_2$

The investigation of the xLiBH$_4$ + (1-x)Mg(BH$_4$)$_2$ (x = 0-1) composite system was carried out by Bardaji *et al.* (2011b). Similarly to the LiBH$_4$-Ca(BH$_4$)$_2$ system, LiBH$_4$ and Mg(BH$_4$)$_2$ did not react to form a new compound after ball milling for 4 h. This result against to a previous study (Fang *et al.*, 2010) that reported the formation of a dual-cation borohydride with the composition x = 0.5; however there was no structural determination to support the XRD results. However, according to Bardaji *et al.* (2011b), the presence of the LiBH$_4$ led to a reversible phase transformation between α- and β-Mg(BH$_4$)$_2$. The eutectic composition was found to be at 0.5 < x < 0.6, exhibiting eutectic melting at 180 °C (**Figure 2.8**). The sample with x = 0.5, began to release H$_2$ and a small amount of B$_2$H$_6$ at 170 °C, i.e. at a much lower temperature than for pure LiBH$_4$ or Mg(BH$_4$)$_2$. 9.6 wt% of H$_2$ was liberated between 215 and 400 °C via two steps. A total weight loss of 12.6 wt% was observed up to 400 °C, lower than the theoretical capacity of 14.6 wt% H$_2$ for 0.5LiBH$_4$+0.5Mg(BH$_4$)$_2$. No intermediate or solid solution compounds were observed.
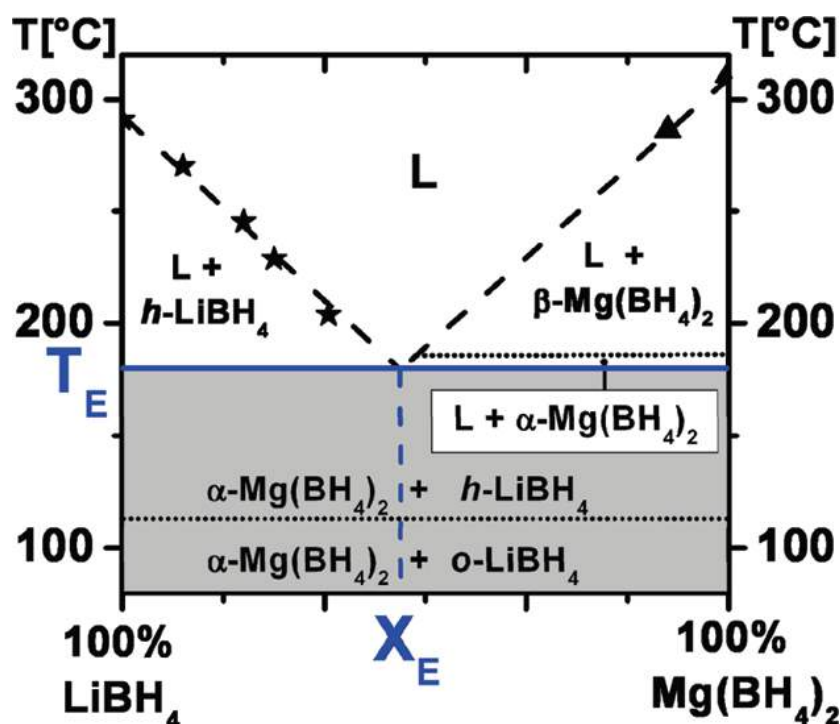
Figure 2.8 Tentative phase diagram for the LiBH$_4$-Mg(BH$_4$)$_2$ binary system (Bardaji *et al.*, 2011b).

A study of the thermodynamics and kinetics of a 0.6LiBH$_4$ + 0.4Mg(BH$_4$)$_2$ composition was later carried out by Nale *et al.* (2011), by means of TPD and pressure-composition isotherms between 25 and 540 °C under 0.1 to 150 bar H$_2$. This mixture exhibited four decomposition steps in 3 bar H$_2$ at 235, 315, 365 and 460 °C, respectively. The first and fourth steps were explained by the decomposition of pure remaining Mg(BH$_4$)$_2$ and LiBH$_4$, respectively. It was proposed that a fraction of LiBH$_4$ and Mg(BH$_4$)$_2$ would react together to form LiH, MgH$_2$, B and H$_2$ in the range 300-350 °C. The third step corresponded to the decomposition of MgH$_2$ formed in the first step. However, no compositional study was performed on those decomposed samples.

Recently, Sartori *et al.* (2012) infiltrated 0.5Li^{11}BD$_4$+0.5Mg(^{11}BD$_4$)$_2$ into a carbon scaffold (IRH33) at 190 °C in 40 bar D$_2$ for 1 h. Compared to the bulk Li^{11}BD$_4$-Mg(^{11}BD$_4$)$_2$ (onset T$_{dec}$ = ~180°C in vacuum), the dehydrogenation temperature was reduced by up to 60 °C in the nanoconfined system, with multi-step gas evolution at 125, 305 and 340 °C, respectively. The decomposition was completed upon heating to 460 °C. Notably, desorption for the

nanoconfined sample proceeded with no concurrent diborane release, which had occurred in the non-confined sample. During the decomposition of the nanoconfined sample no $[B_{12}D_{12}]^{2-}$ but boron was detected, which may be important for practical use as a hydrogen storage medium.

2.4.3.2 LiBH$_4$-Ca(BH$_4$)$_2$

The combination of two metal borohydrides does not necessarily need to form a new compound, but can result in a eutectic mixture which may have more favourable hydrogen storage and/or electronic properties. Lee *et al.* (2009a) and (2011) carried out systemic study of xLiBH$_4$ + (1-x)Ca(BH$_4$)$_2$ (x = 0-1) mixtures prepared by ball milling for 4 h in Ar. XRD of the milled samples showed that the starting materials existed as a physical mixture. However, DSC under Ar suggested that a eutectic melting point was observed at around 200 °C, and the eutectic composition for the LiBH$_4$-Ca(BH$_4$)$_2$ system was determined to be in the range of x = 0.65-0.7 at which the enthalpy change becomes maximum in DSC traces. The tentative phase diagram of the LiBH$_4$-Ca(BH$_4$)$_2$ system is shown in **Figure 2.9**.
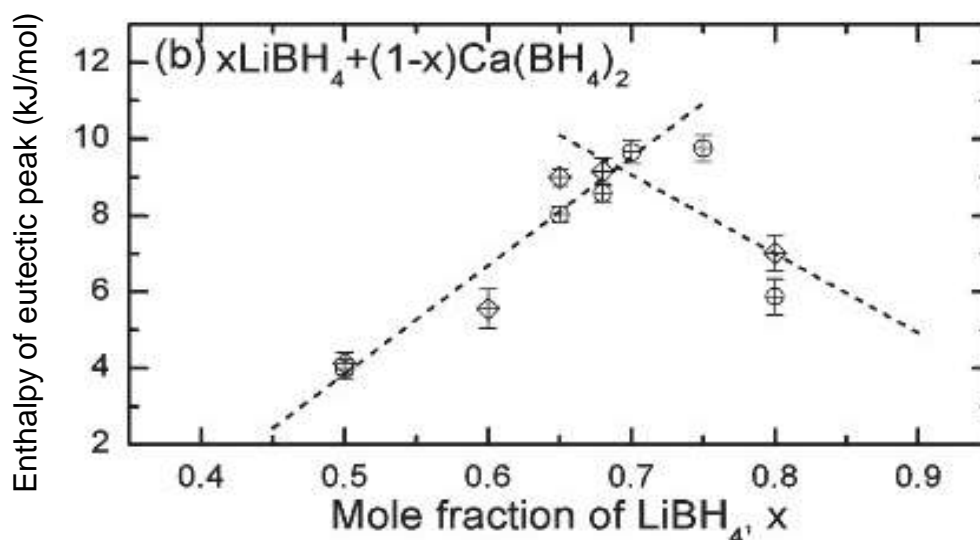
Figure 2.9 Tentative phase diagram for the xLiBH$_4$ + (1-x)Ca(BH$_4$)$_2$ (x = 0.5-0.8) composites. The measurement was repeated several times at the same composition x. The error bars show uncertainty in the peak area at each measurement. (Lee *et al.*, 2011)

With increasing temperature, the decomposition temperature varied with the composition x,

and the mixture at intermediate compositions released hydrogen at a lower temperature compared to pure $LiBH_4$ or $Ca(BH_4)_2$, e.g. about 10 wt% H_2 is released upon heating to 400 °C for the sample with $x = 0.4$. A partial reversibility of nearly 4 wt% H_2 was achieved for this system, when a catalyst such as NbF_5 was added.

For the $0.68LiBH_4+0.32Ca(BH_4)_2$ sample, phase transitions of o- to h-$LiBH_4$, α-/β- to γ-$Ca(BH_4)_2$ were observed at 117 and 143 °C, respectively, followed by decomposition starting right above the eutectic point 200 °C. Unfortunately, a certain proportion of $Ca_3(BH_4)_3(BO_3)$ and $LiCa_3(BH_4)(BO_3)_2$ were formed above 230 °C due to oxidation of $[BH_4]^-$. The dissociation of these borohydride borates with hydrogen release were thought to be responsible for the DSC peaks at 260 and 330 °C. In addition, improved hydrogen storage properties were achieved by melt-infiltration of $0.68LiBH_4+0.32Ca(BH_4)_2$ into mesoporous carbon (700-1200 m^2/g). The major dehydrogenation temperature was lowered to ~308 °C, compared with ~405 °C for the same composite without carbon.

An in situ NMR study demonstrated that the $0.68LiBH_4+0.32Ca(BH_4)_2$ mixture can form a solid solution between 140 and 170 °C, i.e. below the eutectic melting point (Lee *et al.*, 2012). More recently, the dehydrogenation mechanism for the $0.68LiBH_4+0.32Ca(BH_4)_2$ mixture was explored by Yan *et al.* (2013a) using dynamic pressure-composition isotherms, XRD and solid-state NMR. The mixture decomposed via two major steps between 330 and 450 °C, as illustrated in **Figure 2.10**. In the first step, $Ca(BH_4)_2$ decomposed to CaH_2, CaB_6, $CaB_{12}H_{12}$, H_2 (~ 4.9 wt%), and probably amorphous boron in all samples (isothermally heated at 330, 350, 375 or 425 °C). The CaH_2 was then reacted with molten $LiBH_4$ to form CaB_6, LiH, and H_2 and $Li_2B_{12}H_{12}$. Nevertheless, the formation of CaB_6 and $Li_2B_{12}H_{12}$/$CaB_{12}H_{12}$ were found to be competitive and temperature-dependent reactions: more CaB_6 and less $[B_{12}H_{12}]^{2-}$ containing phase was formed when the dehydrogenation process was isothermally controlled at a lower temperature. After isothermal decomposition at 330 °C, a $0.68LiBH_4+0.32Ca(BH_4)_2$ sample could be rehydrogenated by 6.8 wt% H_2 by heating to 400 °C in 140 bar H_2 for 20 h.
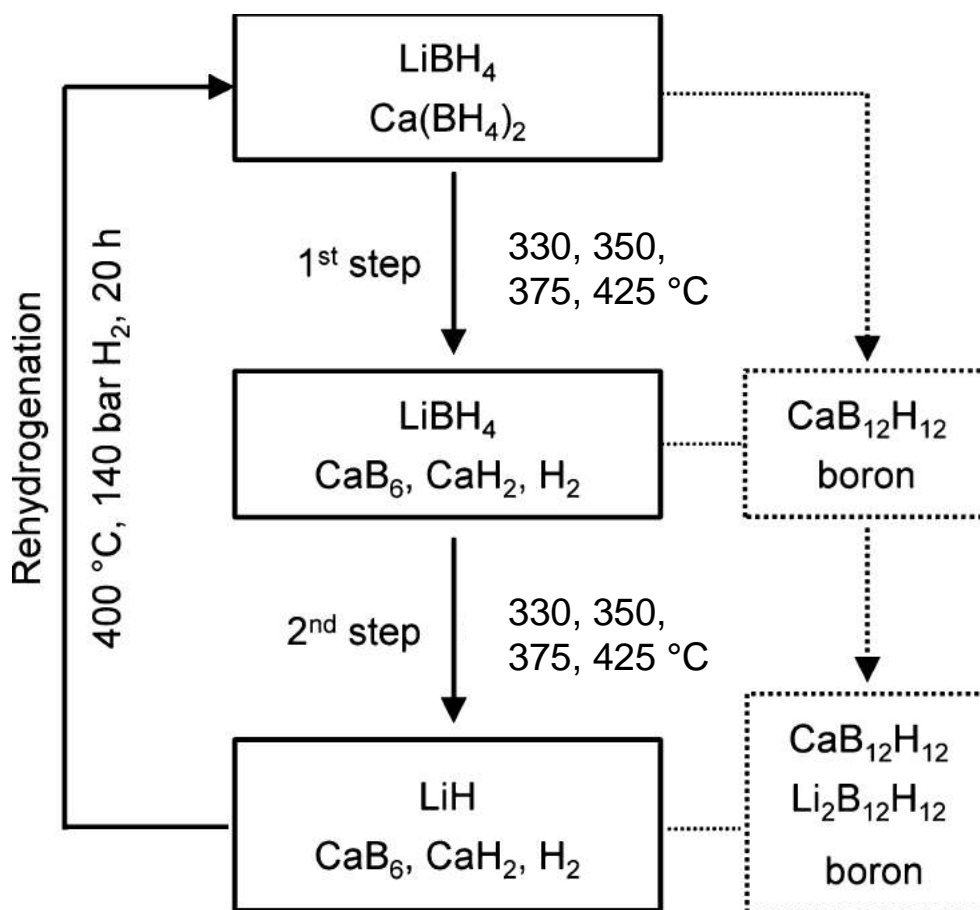
Figure 2.10 Schematic diagram of isothermal dehydrogenation routes for $0.68LiBH_4+0.32Ca(BH_4)_2$. $CaB_{12}H_{12}$, $Li_2B_{12}H_{12}$, and amorphous boron in the dashed boxes on the right side were not involved in the rehydrogenation reaction. (Yan *et al.*, 2013a)

2.5   Role of diborane in the H_2 cycling of borohydrides

2.5.1   Diborane, B_2H_6

Diborane, a colorless gas at room temperature, is highly reactive and versatile reagent for a variety of applications, including synthesis of other boranes directly or indirectly from it (Greenwood and Earnshaw, 1997). However, great care should be taken in all these reactions because B_2H_6 is spontaneously flammable especially in moist air and very toxic to humans and the environment.

The structure of B_2H_6 (**Figure 2.11**) was explained by the combination of two BH_3 fragments distorted to a pyramidal geometry, in which the two B atoms are covalently bridged by a pair

of H atoms (Housecroft, 1994). B_2H_6 adopts the symmetry of D_{2h} point group, exhibiting 18 fundamental vibrations: stretching and bending modes for B-H$_{terminal}$ and B-H$_{bridge}$ and H-B-H bridge twisting modes (Duncan *et al.*, 1981). In a Raman spectrum, the stretching modes of B-H$_{terminal}$ and B-H$_{bridge}$ vibrations are in a region of 2500-2600 cm^{-1} and 1700-2100 cm^{-1} respectively.
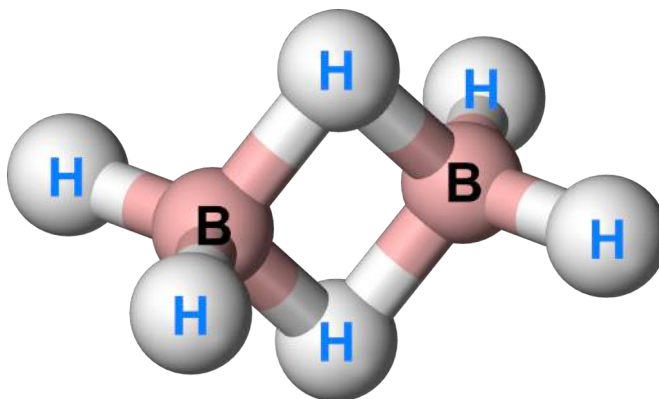
Figure 2.11 The structure of diborane, modified from Mills (2008).

The thermolysis of diborane is complicated and variable depending on the conditions used, e.g. backpressure and temperature (Polak and Obenland, 1964; Greenwood and Greatrex, 1987). General reactions of diborane tend to form other open-cage higher boranes such as B_4H_{10}, B_5H_9. For example, homogeneous dissociation at moderate temperatures and pressures can give:

$$B_2H_6 \leftrightarrow 2(BH_3) \qquad\qquad (2.47)$$

$$(BH_3) + B_2H_6 \leftrightarrow (B_3H_9) \leftrightarrow (B_3H_7) + H_2 \qquad (2.48)$$

$$(B_3H_7) + B_2H_6 \rightarrow B_{10}H_{14} + (BH_3) \qquad (2.49)$$
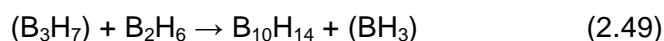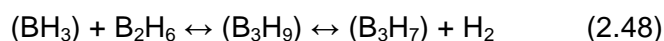
where brackets in the equations represent unstable intermediates. Diborane also decomposes very slowly at room temperature, forming higher boranes and a nonvolatile and insoluble yellow solid that consists of $B_{10}H_{14}$ and the polymeric species, BH$_n$ (Atkins *et al.*, 2010).

2.5.2   Role of B_2H_6 in the formation of borohydrides

It is known that diborane can be used to prepare a range of borohydrides, e.g. $LiBH_4$, $NaBH_4$, $Mg(BH_4)_2$ and $Ca(BH_4)_2$ (as discussed earlier), by reacting with corresponding metal hydrides/alkyls/alkoxide in solvent; a liquid medium was thought to be indispensable for the reaction to occur (Schlesinger and Brown, 1940; Schlesinger *et al.*, 1953c; Wiberg *et al.*, 1955; Plešek and Heřmánek, 1966; James and Wallbridge, 1970).

More recently, a novel gas-solid synthetic approach was developed: $LiBH_4$ was formed by heating LiH in a diborane atmosphere, without a solvent (Friedrichs *et al.*, 2009a). The gaseous diborane was produced from the decomposition of a pre-milled mixture of $LiBH_4$-$ZnCl_2$, which is known to release diborane and hydrogen upon heating (Section 2.4.2). $LiBH_4$ (a yield of approximately 72 wt%) accompanied with a minor impurity $Li_2B_{12}H_{12}$ were produced by heating the LiH powder in B_2H_6/H_2 atmosphere to 150 °C.

The following in situ neutron diffraction and transmission electron microscopy-electron energy loss spectroscopy (TEM-EELS) studies on the reaction between LiD and B_2D_6, revealed that the o-$LiBD_4$ already started to form at 100 °C, and h-$LiBD_4$ subsequently formed above the phase transition temperature (Friedrichs *et al.*, 2010a). However, only 50 % of the LiD was converted to $LiBD_4$, with the formation of a small amount of $Li_2B_{12}H_{12}$ upon heating to 185 °C. This limited yield was explained by the formation of a passivating borohydride layer at the surface of the compound, which hinders ionic diffusion through the surface resulting in incomplete reactions.

In order to break the passivation layer, the LiH and B_2H_6 mixture was ball-milled at room temperature (Friedrichs *et al.*, 2010b). The yield of $LiBH_4$ was increased to approximately 94 % without the formation of $Li_2B_{12}H_{12}$. This mechanochemical method was also applied to the synthesis of $Ca(BH_4)_2$ and $Mg(BH_4)_2$, giving yields of 91 % and 73 wt%, respectively. By milling YH_3/YH_2 mixture in diborane, a yield of 75 % of $Y(BH_4)_3$ was achieved with the remnant yttrium hydride (Remhof *et al.*, 2012a). However, ball milling TiH_2 in B_2H_6 by this

technique does not produce $Ti(BH_4)_3$ but rather TiB_2 (Remhof *et al.*, 2012b).

A detailed study of this synthesis mechanism was performed by Gremaud *et al.* (2011) who prepared H/D isotope labelled samples by the reaction of $LiBH_4+B_2D_6$. By tracing the H or D atoms in the borane or borohydride products by vibrational spectroscopies, the $[BH_4]^-$ anions were found to originate from the heterolytic splitting of diborane, substituting for H^- ions of LiH to form $LiBH_4$ on the surface. For the synthesis of borohydrides, the presence of H^- defects could be important in the delivery of $[BH_4]^-$ into the bulk material.

2.5.3   Role of B_2H_6 in the decomposition of borohydrides

It has been known that less stable borohydrides e.g. $Mn(BH_4)_2$ and $NaZn(BH_4)_3$ often release diborane as a byproduct during dehydrogenation, whereas more stable borohydrides such as $NaBH_4$, desorb at a higher temperature and so mainly release H_2 (Urgnani *et al.*, 2008; Ravnsbæk *et al.*, 2009; Liu *et al.*, 2012). The amount of diborane released was suggested to be inversely proportional to the borohydride stability which depends on the electronegativity of the corresponding cation (Callini *et al.*, 2013). In some borohydrides such as $LiBH_4$ and $Mg(BH_4)_2$, diborane was proposed to form during dehydrogenation (Züttel *et al.*, 2007; Chong *et al.*, 2011). However, the observation of diborane may depend on the experimental conditions and/or the detection methods used (Borgschulte *et al.*, 2011a).

By applying the gas-solid reaction techniques to $LiBH_4+B_2H_6$, the formation of $Li_2B_{12}H_{12}$ and $Li_2B_{10}H_{10}$ were observed within a temperature range of 150 and 200 °C by in situ XRD and ex situ NMR measurements (Friedrichs *et al.*, 2010c). As a result, it was thought that a concurrent evolution of B_2H_6 and H_2 should occur during the pure $LiBH_4$ decomposition. However, most of the B_2H_6 decomposed into B and H_2 at 250 °C, with some of the B_2H_6 reacting with the remaining $LiBH_4$ to form $Li_2B_{12}H_{12}$ and/or possibly $Li_2B_{10}H_{10}$. In summary, the overall de/re-hydrogenation mechanism of LiH and $LiBH_4$ reacting with diborane was proposed as follows:

$$\text{LiH} \xrightarrow[\text{RT}]{^1/_2\ \text{B}_2\text{H}_6} \text{LiBH}_4 \begin{array}{l} \xrightarrow[150°C]{^5/_2\ \text{B}_2\text{H}_6} \frac{1}{2}\ \text{Li}_2\text{B}_{12}\text{H}_{12} + {}^{13}/_2\ \text{H}_2 \\[2mm] \xrightarrow[200°C]{2\ \text{B}_2\text{H}_6} \frac{1}{2}\ \text{Li}_2\text{B}_{10}\text{H}_{10} + {}^{11}/_2\ \text{H}_2 \end{array}$$

(2.50)
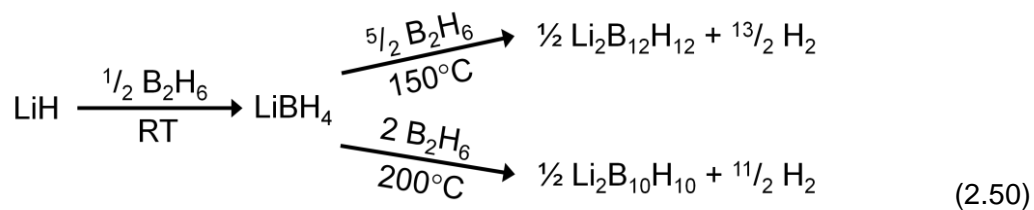
More recently, $MgB_{12}H_{12}$ was synthesized via the reaction of $Mg(BH_4)_2$ with gaseous B_2H_6 at 100-150 °C (Remhof *et al.*, 2014). A yield of 10.2-22.3 mol% $MgB_{12}H_{12}$ was achieved using bulk $Mg(BH_4)_2$ as the starting material. The incomplete reaction was due to a passivation layer made of newly formed species such as $Mg(B_3H_8)_2$, $MgB_{10}H_{10}$ and $MgB_{12}H_{12}$. The as-synthesized $MgB_{12}H_{12}$ slowly decomposed into amorphous B and H_2 between 400 and 600 °C, which did not match with one of the hydrogen desorption events of $Mg(BH_4)_2$ which shows three major desorption steps between 250 and 400 °C (Hanada *et al.*, 2008; Soloveichik *et al.*, 2009; Paskevicius *et al.*, 2012).

2.6   Mg-based hydrides system

Magnesium hydride (MgH_2) is an attractive medium for storing hydrogen due to a good theoretical hydrogen capacity of 7.6 wt%, which is much greater than most metallic hydrides (e.g. 1.4 wt% H_2 for $LaNi_5H_6$). Mg metal is also relatively low cost (ca. 3 USD/kg) and abundant (it is the 8th most common element, occupying 2.7 wt% of the Earth's crust) (Vigeholm *et al.*, 1980; Burstow, 2002). However, several key drawbacks hinder its practical application as a hydrogen storage medium, including: high thermodynamic stability of the hydride; poor sorption kinetics for the bulk material; and high reactivity toward air and oxygen (Zaluska *et al.*, 1999). Numerous efforts have focused on the modification of the hydrogen storage properties through various approaches, e.g. ball milling, additives (by alloying with other metal or introducing catalyst) and thin film formation (Jain *et al.*, 2010b). The Mg–Ti based hydrides are promising materials for not only hydrogen storage, but also various applications such as negative electrodes for Ni-MH batteries, switchable mirrors for smart solar collectors and optical hydrogen detectors (Rönnebro and Majzoub, 2008).

In this section, a brief discussion will cover the structure and hydrogen storage properties of bulk Mg/MgH_2, and the improvement of properties that can be achieved by ball milling and/or the addition of Ti-based compounds.

2.6.1   Structures of Mg and MgH_2

Pure Mg has a hexagonal close packed (HCP) structure with the space group $P6_3/mmc$. When Mg starts to absorb hydrogen, H atoms initially occupy tetrahedral interstitial sites in Mg lattice, to form a solid solution of H in Mg (up to ~ 0.07 at.% H at 643 °C at ambient pressure) (San-Martin and Manchester, 1987). Upon further absorption of H, α-MgH_2 forms a body centre tetragonal structure (TiO_2 type) with the space group $P4_2/mnm$, at low temperatures and ambient pressures (Zachariasen *et al.*, 1963; Noritake *et al.*, 2002).

α-MgH$_2$ can partially transform into orthorhombic γ-MgH$_2$ (α-PbO$_2$ prototype, space group *Pbcn*) when subjected to a high-pressure of 2.5–8GPa in the temperature range 250–900 °C (Bastide *et al.*, 1980; Bortz *et al.*, 1999). A metastable hexagonal δ-phase, which was denoted as β-MgH$_2$ in the original study (Bastide *et al.*, 1980), transformed into the γ-phase when the pressure was reduced.

Noritake *et al.* (2002) proposed that the bonding of H in MgH$_2$ actually consists of a mixture of ionic and covalent bonding. Weak covalent bonds exist between Mg and H as well as between H and H, which may benefit the hydrogenation and dehydrogenation properties. Weak ionisation was also found in MgH$_2$, and expressed as Mg$^{1.91+}$ and H$^{0.26-}$ which was similar but weaker than in ionic hydrides of alkali metals or other alkaline earth metals.

2.6.2 Hydrogen storage properties

The heat of formation of MgH$_2$ was first determined to be ΔH_f = -74.5 kJ mol^{-1} with a corresponding entropy ΔS_f = -135 J K^{-1} mol^{-1} H$_2$ according to Equation 2.51 (Stampfer *et al.*, 1960), which is comparable to a more recent study in which ΔH_f = -72.9 kJ mol^{-1} and ΔS_f = -132.2 J K^{-1} mol^{-1} H$_2$ (Bogdanović *et al.*, 1999). The formation enthalpy of MgH$_2$ is between those for covalent hydride BeH$_2$ and ionic hydride CaH$_2$ which have ΔH_f values of -18.9 and -181.5 kJ mol^{-1}, respectively (Grochala and Edwards, 2004). This is consistent with the bonding for MgH$_2$ having a mixed ionic and covalent character. However, the thermodynamic stability of MgH$_2$ is still relatively high, resulting in a desorption temperature of 288 °C at 1 bar equilibrium pressure.

$$Mg(s) + H_2(g) \rightarrow MgH_2(s) \qquad (2.51)$$

Another major drawback of MgH$_2$ is the slow absorption/desorption rate due to multiple energy barriers (Jain *et al.*, 2010b). The limiting absorption rate starts with the Mg surface, which provides sufficient active sites for H$_2$ molecule dissociation and penetration. Diffusion is not the limiting step initially, but rather the chemisorption of hydrogen onto the surface of

the Mg (Friedlmeier and Groll, 1997). As the hydrogen absorption process proceeds, the formation of a MgH_2 layer on the surface or the grain boundaries inhibits further penetration and diffusion of atomic H into the particles. Sufficient nucleation sites are also required within the bulk of Mg (Berube *et al.*, 2007). Moreover, the growth of the MgH_2 phase occurs via a slow motion of the Mg-MgH_2 interface where H atoms diffuse through (Vigeholm *et al.*, 1980). Although high H_2 pressure could lead to a thermodynamic driving force to promote MgH_2 phase growth, the hydrogenation still stops abruptly when the thickness of hydride layer exceeds 30-50 μm. Thus, the hydrogenation and dehydrogenation rate of MgH_2 is slow at moderate temperatures, and therefore needs to be maintained at 300-400 °C in order to achieve adequate sorption kinetics.

In addition, an MgO layer may easily form on the surface of Mg particles due to the high reactivity of Mg with respect to oxygen. This also inhibits hydrogen penetrating into the bulk material. An extra activation process (e.g. annealing at 400 °C) is therefore often needed to break down this passivating layer prior to hydrogenation of Mg (Chen *et al.*, 1993).

For the desorption process, the slow H diffusion through the MgH_2 layer and the relatively high thermal stability of the MgH_2 phase, remain the primary factors limiting the reaction rates (Berube *et al.*, 2007). Thus, there has been a significant effort to overcome both these thermodynamics and kinetics barriers for hydrogen sorption in Mg / MgH_2.

2.6.3   Effect of ball milling on sorption properties

To try to significantly improve the hydrogen sorption properties of MgH_2, ball milling has been used to modify its microstructure in terms of: creating and increasing fresh surface area; reducing the particle size; reducing the grain size; and introducing more defects as active sites for hydrogenation reactions (Jain *et al.*, 2010b). In addition, high-energy ball milling can also be used to introduce a phase change and/or a degree of disorder within MgH_2. Huot *et al.* (1999) showed that ~4 % of α-MgH_2 was transformed to the metastable γ-phase after 2 h milling; the γ phase reverted to α after the first H_2 sorption cycle.

Varin *et al.* (2009) performed systematic work on the effect of ball milling on commercial MgH$_2$ powder (purchased from Degussa–Goldschmidt and ABCR) as a function of time from 0.25 to 100 h. Scanning electron microscope (SEM) showed that the particles changed from solid blocks of MgH$_2$ with a smooth surface, to smaller sized particles with many asperities after milling. After milling for 5 h, the grain size was dramatically reduced from ~300 nm to ~12 nm, while the average particle size was reduced from ~40 μm to ~1 μm. With longer milling times up to 20 h, grain and particle sizes of ~10 nm and 0.6 μm, respectively, were observed; although some larger particles were present from agglomerations of smaller particles. No obvious lattice strain (> 0.5%) was observed in the samples.

As the hydrogen diffusion path length has been significantly reduced by the reduction in particle size, the hydrogen desorption rate is therefore enhanced as expected. The DSC measurement showed that the onset desorption temperature (T_{onset}) decreased from 406 °C for the as received MgH$_2$ to 342 °C for the 100 h-milled sample (Varin *et al.*, 2006). By plotting T_{onset} as a function of particle size, a near linear reduction in the onset desorption temperature was observed from ~375 to ~340 °C, corresponding to a reduction in particle size from ~2 to 0.5 μm. However, no correlation between the nanograin size of MgH$_2$ and its corresponding desorption temperature was found.

An improvement of sorption kinetics by milling was demonstrated by Huot *et al.* (1999): the milled MgH$_2$ could fully hydrogenate at 300 °C and dehydrogenate at 350 °C within a few minutes, which was five times faster than for unmilled MgH$_2$. This might be associated with small and rough particles with more dissociation/nucleation sites and shorter diffusion lengths created by milling. In addition, H$_2$ sorption cycling of milled MgH$_2$ appeared to not affect the particle size but promoted grain growth (from ~3 nm after 100 h milling, to ~56 nm after cycling) without deterioration in absorption kinetics (Varin *et al.*, 2011). Thus, the particle size was thought to be responsible for improving absorption kinetics rather than a nanoscale grain size.

On the other hand, a side effect of milling is to probably introduce contamination into the material, which may affect sorption properties. MgO, as one typical example, more readily forms on the Mg surface since ball milling produces more fresh surface area. A considerable amount of MgO (2-10 wt%) was observed in the milled samples due to oxygen contamination during milling (Fournier *et al.*, 2002; Varin *et al.*, 2006). The formation of MgO/Mg(OH)$_2$ layers on the Mg/MgH$_2$ surface could be a risk when storing milled nanocrystalline MgH$_2$ in an inert atmosphere for long durations.

Reactive ball milling is used to synthesise metal/alloy hydrides by milling metal(s) under certain hydrogen pressures. Chen and Williams (1995) produced MgH$_2$ and TiH$_{1.9}$ by ball milling Mg and Ti powder under 3.4 bar H$_2$ for 25 and 5.5 h, respectively. Doppiu *et al.* (2007) found that the formation rate of hydrides strongly depends on the H$_2$ pressure, where the reaction rate of a Mg+0.1Ni mixture milled in 10 bar H$_2$ was significantly slower than for a sample under 90 bar H$_2$.

Cuevas *et al.* (2012) started with coarse Mg powder (< 800 μm) instead of fine power in order to reduce the amount of MgO. A total of 7.1 wt% H$_2$ was absorbed by the Mg after milling for 2 h under 80 bar H$_2$. The final product was found to consist of 76 wt% α-MgH$_2$, 21 wt% γ-MgH$_2$ and 3 wt% MgO; with a mean crystallite size of 6 nm. 90 % of the desorption or absorption reaction could be completed within 23 min at 300 °C during the first cycle, although the sorption kinetics became worse after further cycling. After the first desorption, this material re-absorbed 6.76 wt% H$_2$ at 275 °C, and the capacity subsequently decreased to 5.07 wt% after 14 cycles.

Although milled MgH$_2$ has achieved improved sorption kinetics, its desorption temperature cannot be reduced much lower than 300 °C. Numerous additives have been tried, to attempt to further enhance the hydrogen storage properties. One of the examples is to dope 1 mol% Nb$_2$O$_5$ to MgH$_2$ by 20 h milling (Hanada *et al.*, 2006). After dehydrogenation under a high vacuum condition for 8 h at 200 °C, this mixture could absorb ~4.5 wt% H$_2$ even at

room temperature under a pressure below 10 bar within 15 s, and finally 5 wt% H_2 after 8 h hydrogenation. The sample after rehydrogenation could release H_2 at 160 °C within 100 min under flowing He. However, reviewing the effect of all these additives is beyond the scope of this thesis, except for Ti-based compounds.

2.6.4 Effect of Ti-base additives

Liang *et al.* (1999) ball-milled α-MgH_2+0.16Ti for 20 h, and observed the formation of TiH_2 and a small fraction of γ-MgH_2 with remaining α-MgH_2. The MgH_2 phase in this mixture was dehydrided completely within 17 min at 250 °C, while TiH_2 was too stable to decompose in the temperature range of interest. In contrast, the milled MgH_2 did not release any H_2 at this temperature. They also claimed that absorption could occur to form α-MgH_2 at a temperature as low as 29 °C under 10 bar H_2 according to Sieverts measurements. Charbonnier *et al.* (2004) milled a mixture of α-MgH_2+0.16Ti up to 60 h, and thought that various TiH_x phases were formed as a function of time: $TiH_{1.92}$ appeared for a milling time above 20 h milling and $TiH_{1.7}$ for 42 and 60 h milling. The influence of Ti on the stability of MgH_2 was investigated by Song *et al.* (2004) using first principle calculations: they suggested that the presence of Ti in the MgH_2 lattice could weaken the Mg-H bond resulting in a lower heat of formation.

Instead of forming separate phases MgH_2 + $x$$TiH_2$ (x < 0.1), the addition of more Ti to MgH_2 could result in the formation of ternary hydrides $Mg_xTi_{100-x}H_y$ (29 < x < 87.5) which have a face-centred cubic (FCC) structure. Asano and Akiba (2009) synthesised $Mg_{40}Ti_{60}H_{113}$ (2.9 wt% H_2) and $Mg_{29}Ti_{71}H_{57}$ (1.4 wt% H_2) by ball milling MgH_2+Ti and MgH_2+0.25Ti for 200 h, respectively.

Another ternary hydride Mg_7TiH_x was found from a reaction of MgH_2+$x$$TiH_{1.9}$ (x = 0.14, 0.17 and 0.33) at 600 °C and 8 GPa in a high-pressure anvil cell (Kyoi *et al.*, 2004). This compound has a very similar face-centered structure to $TiH_{1.9}$ (cubic, Fm-3m, a = 4.440 Å) but a slightly different lattice parameter (see **Figure 2.12**). Mg_7TiH_x could release 4.7 wt%

H_2 to form Mg and $TiH_{1.9}$ at 330 °C. This desorption temperature was about 130 and 220 °C lower than those for pure MgH_2 and $TiH_{1.9}$, respectively. This may possibly be attributed to the ternary hydride exhibiting weaker metal-hydrogen bonding than the two binary hydrides. Subsequently, the value of x was determined to be 16 or 13 by Rönnebro et $al.$ (2005). Mg_7TiH_{16} (~7.6 wt% H_2) was not stable and would transform to Mg_7TiH_{13} (~5.5 wt% H_2) while it was being stored for a long time.
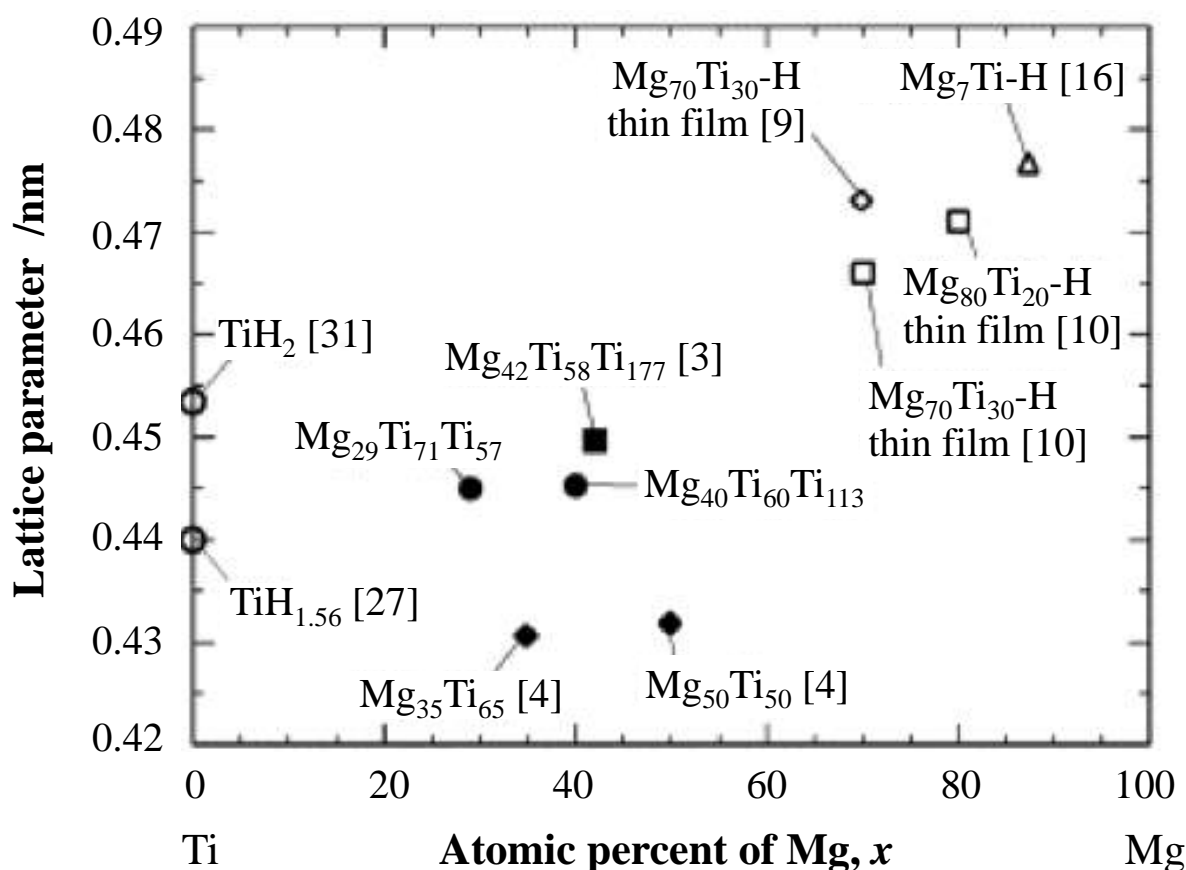
Figure 2.12 Lattice parameters of Mg–Ti–H FCC hydrides (Asano and Akiba, 2009).

Choi et $al.$ (2009) studied the milling of $MgH_2 + xTiH_2$ as a function of x (x = 0-0.25) and milling time (0.5-16 h), and concluded that the hydrogen properties for $MgH_2+0.1TiH_2$ are optimum (TGA showed 6 wt% H_2 release with an onset temperature of 126 °C) after milling for 4 h in 150 bar H_2. In contrast, a similar study by Sabitu et $al.$ (2010) did not observe such a significant decrease in the desorption temperature, but rather the onset was at 265 °C. Excellent reversibility without loss of capacity over 80 cycles (dehydrogenation and

rehydrogenation under 0.01 and 20 bar H_2 at 300 °C, respectively) was also demonstrated for a MgH_2+0.1TiH_2 mixture (Lu *et al.*, 2009). By using transmission electron microscopy (TEM), the grain size of MgH_2+0.1TiH_2 was confirmed to be a nanoscale of 5-10 nm with a uniform distribution of TiH_2 among the MgH_2 particles, and was almost unchanged after 80 cycles.

In another study, Shao *et al.* (2011) milled Mg+0.1TiH_2 in 300 bar H_2 up 20 h. The final product was identified as α-MgH_2 and TiH_2 (cubic) with a mean crystallite size of 5 nm. The addition of TiH_2 lowered the MgH_2 desorption temperature by about 100 °C to 342 °C (T_{DSC} $_{peak}$). Later, Cuevas *et al.* (2012) performed a similar study by milling Mg+xTi (x = 0-1) powder under 80 bar H_2 pressure for 2 h. The absorption occurred in two consecutive steps: ε-TiH_2 (tetragonal) was formed within the first 15 min of milling, followed by α+γ-MgH_2. The presence of TiH_2 speeded up the MgH_2 sorption rate and inhibited grain coarsening during milling, and subsequent H_2 cycling.

Ma *et al.* (2010) investigated the effect of Ti-based additives – TiF_3, $TiCl_3$, TiO_2, TiN and TiH_2 – on the hydrogen absorption properties of Mg. Among these compounds, TiF_3 appeared to be a particularly effective additive promoting the absorption of 3.8 wt% H_2 into Mg within 0.5 min at 150 °C, which was at least 10 times faster than others Ti-based additives. The added TiF_3 led to the formation of nano MgF_2 during the first desorption. Therefore, MgF_2 might offer more nucleation sites for absorption, since its rutile structure is very similar to MgH_2 (Mulder *et al.*, 2012). Growth of the MgH_2 phase was proposed to initiate at interfaces with the abundant small MgF_2 particles, leading to grain refinement of the MgH_2 phase.

Amieiro-Fonseca *et al.* (2011) used high-throughput physical vapour deposition (HT-PVD) to produce Mg-Ti-B ternary alloy films with varying atomic compositions across the ternary of Mg (0-56 at%), B (33-98 at%) and Ti (2-11 at%), as shown in **Figure 2.13**. An optimum composition was determined to be $Mg_{0.36}Ti_{0.06}B_{0.58}$ with a gravimetric density value of 10.6

wt% and an onset desorption temperature of 262 °C. A Raman spectrum showed the existence of B-H bonding in this thin film, suggesting that a metal borohydride might be formed. Partial reversibility for the thin film material has been observed, but it has not yet been possible to isolate this composition in a bulk form.
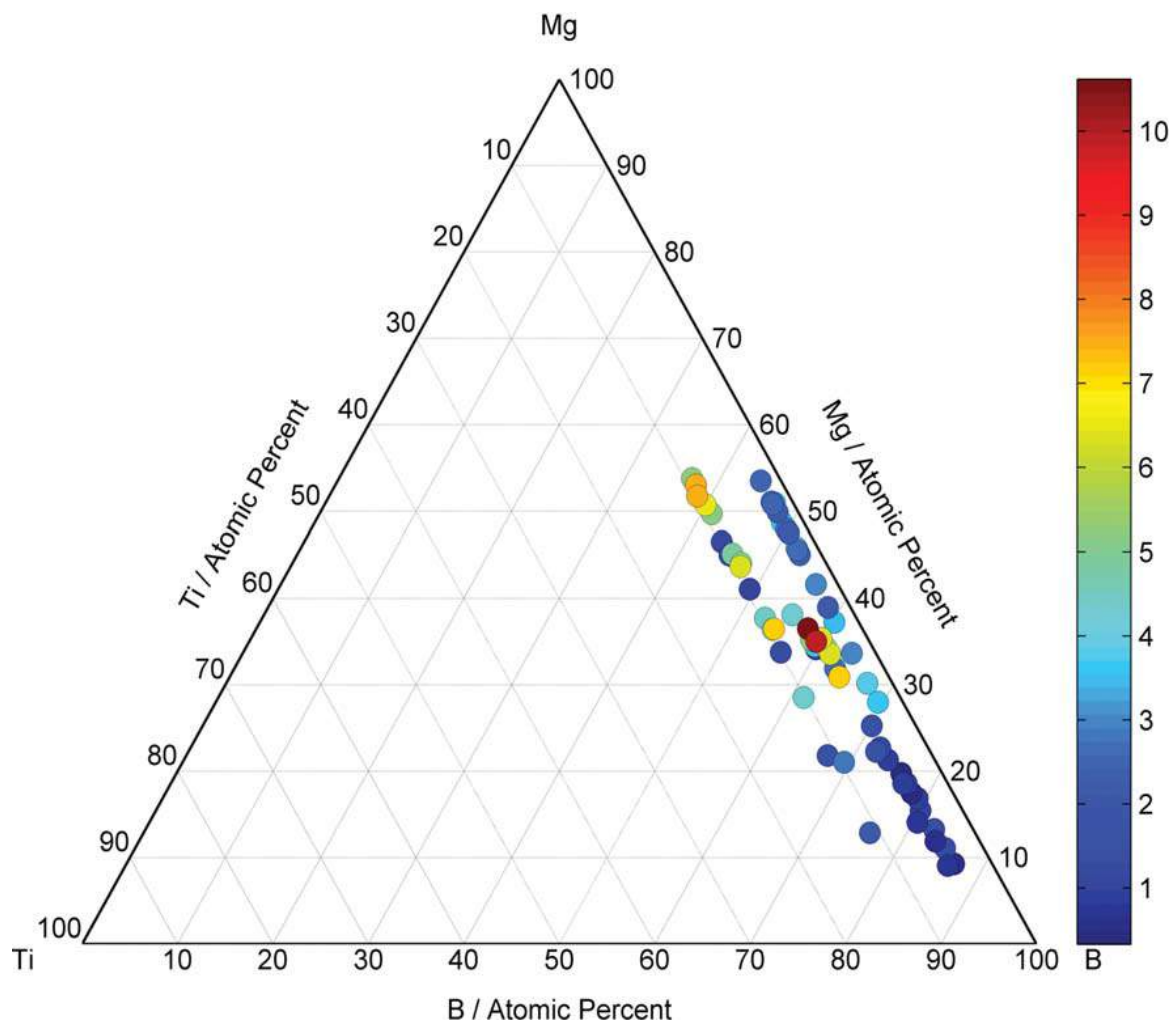
Figure 2.13 Gravimetric capacity (in wt%) across the Mg-Ti-B hydride ternary. TPD was carried out at a heating rate of 23 °C s^{-1} (Amieiro-Fonseca *et al.*, 2011).

2.6.5 Mg-based binary-metal hydrides

Ternary metal hydrides are of significant importance in the development of advanced hydrogen storage system as discussed previously. But only a few Mg-based ternary metal hydrides containing alkali and alkaline-earth elements were discovered until the 1990s

(Gingl *et al.*, 1992). So far a large family of this type of compound has been characterised, which is summarised in **Table 2.4** by Yvon and Bertheville (2006).

Table 2.4 The compositional, structural properties and hydrogen capacities of Mg-based ternary metal hydrides containing alkali and alkaline elements. Modified from Yvon and Bertheville (2006).

Compound	Structure	Space group	Theor. H_2 (wt%)	g H_2/L
$NaMgH_3$	Orthorhombic	*Pnma*	6	88.3
$KMgH_3$	Cubic	*Pm-3m*	4.6	77.1
K_2MgH_4	Tetragonal	I4/*mmm*	3.8	59.9
$RbMgH_3$	Hexagonal	*P6$_3$/mmc*	2.7	69.7e
Rb_2MgH_4	Orthorhombic	*Pnma*	2	45.5
Rb_3MgH_5	Tetragonal	I4/*mcm*	1.8	42.7
$Rb_4Mg_3H_{10}$	Orthorhombic	*Cmca*	2.4	56.9
$CsMgH_3$ (hp) [a]	Trigonal	*R-3m*	1.9	60
$CsMgH_3$ (lp)	Orthorhombic	*Pmmn*	1.9	56.9
Cs_2MgH_4 (hp) [a]	Tetragonal	I4/*mmm*	1.2	48.5
Cs_2MgH_4 (lp)	Orthorhombic	*Pnma*	1.4	40
Cs_3MgH_5	Tetragonal	I4/*mcm*	1.2	37.1
$Cs_4Mg_3H_{10}$ [a]	Orthorhombic	*Cmca*	1.6	52.7
$Ca_4Mg_3H_{14}$	Hexagonal	*P-62m*	5.7	98.9
$Ca_{19}Mg_8H_{54}$ [a]	Cubic	*Im-3*	5.4	100.9
$SrMgH_4$	Orthorhombic	*Cmc2$_1$*	3.5	88.5
$Sr_2Mg_3H_{10}$	Monoclinic	*C2/m*	3.9	95.1
Sr_2MgH_6 [a]	Trigonal	*P-3m1*	2.9	91.3
Ba_2MgH_6	Trigonal	*P-3m1*	2	78.3
$Ba_2Mg_3H_{10}$	Monoclinic	*C2/m*	2.8	86.5
$Ba_6Mg_7H_{26}$	Orthorhombic	*Immm*	2.6	83.7

hp = high-pressure modification; *lp* = low-pressure modification; *a* = synthesized under high hydrostatic pressure.

These Mg-based hydrides were usually synthesised by solid-state reactions between binary hydride powder mixtures (e.g. $NaMgH_3$) or hydrogenation of binary metal alloys and/or elements under moderate H_2 pressure (up to 160 bar) and temperatures (up to about 430 °C). But the synthesis of some hydrides required very high quasi-hydrostatic pressure in a multi-anvil press, such as Sr_2MgH_5 prepared at 35000 bar and 597 °C. However, most of them have relatively low H_2 capacities of 1-3 wt%, and high equilibrium desorption

temperature (approaching 400 °C) at atmospheric pressure, and so are less attractive for mobile hydrogen storage applications.

$NaMgH_3$ exhibits the highest H_2 capacity of 6 wt% among this group of hydrides whose structures have been experimentally fully characterised (Rönnebro et $al.$, 2000). This compound was synthesised by ball milling NaH and MgH_2 powder for 20 h (Ikeda et $al.$, 2005a). The sorption measurements showed that nearly 6 wt% H_2 was released from $NaMgH_3$ within 8 min at 400 °C via two steps (Equation 2.52 and 2.53). The decomposition enthalpy change for the first and second step were determined to be 93.9 and 102.2 kJ mol^{-1} H_2, which was too high to compete with a catalysed MgH_2 material, but still attractive as a potential solar heat storage material.

$$NaMgH_3 \rightarrow NaH + Mg + H_2 \qquad\qquad (2.52)$$

$$NaH + Mg + H_2 \rightarrow Na + Mg + {}^3/_2H_2 \qquad\qquad (2.53)$$
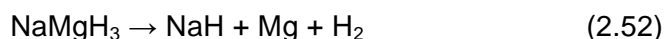
$NaMgH_3$ could be rehydrided from the decomposed phases of elemental Na and Mg under 10 bar H_2 at 400 °C. Sheppard et $al.$ (2011) indicated that macroscopic segregation of metallic Na and Mg kinetically hinders rehydrogenation to $NaMgH_3$. Thus, partial H_2 desorption to NaH and Mg was more kinetically favourable for recombination.

Later, Pottmaier et $al.$ (2011) demonstrated the formation of 96 wt% of $NaMgH_3$ and 4 wt% of NaH+MgO phases by ball milling MgH_2 and NaH for 5 h. The vibrational modes of $NaMgH_3$ were assigned in a region of 600-1100 cm^{-1} according to calculated and experimental results. The two-step desorption was confirmed by DSC and in situ XRD patterns: the formation of NaH+Mg and Na+Mg at 391 and 436 °C, respectively. Direct hydrogenation of NaH+Mg to $NaMgH_3$ was also observed at 350 °C under 5 bar H_2.

With high theoretical gravimetric H_2 densities (8.8 and 9.5 wt% for $LiMgH_3$ and Li_2MgH_4, respectively), attempts have been made to try to synthesis a Li-Mg-H ternary compound by ball-milling LiH and MgH_2, however this did not succeed (Ikeda et $al.$, 2005b). Instead, Martinez-Coronado et $al.$ (2012) obtained $Na_{1-x}Li_xMgH_3$ ($0 \leq x \leq 0.18$) by hydrostatically

pressurising a mixture of MgH_2, NaH and LiH to 2 GPa at 750 °C. $Na_{1-x}Li_xMgH_3$ hydrides have an orthorhombic structure with the space group *Pnma* which is the same with $NaMgH_3$. The desorption of $Na_{1-x}Li_xMgH_3$ occurs in the region of 413-435 °C depending on the composition; the temperature decreases as the amount of Li is increased.

Vajeeston *et al.* (2008) and Li *et al.* (2011a) predicted the most likely structures for Li-Mg-H ternary hydrides to be: a trigonal $LiMgH_3$ with the space group R3c; and/or orthorhombic Li_2MgH_4 (*Pbam*). However, the formation from LiH and MgH_2 is not energetically favourable. Thus, a synthesis route from elemental Li and Mg in H_2 atmosphere was suggested, although it might be kinetically inhibited by pure phase separation.

Alternatively, inserting H atoms into the sites of ordered Li-Mg alloy phases has been considered as a synthesis approach by Li *et al.* (2011a). Li-Mg alloys are the lightest metallic alloys, having densities near that of plastics (Taylor *et al.*, 2010). The Li-Mg binary phase diagram is shown in **Figure 2.14** (Nayeb-Hashemi *et al.*, 1984). The hcp-Mg starts to transform into a body-centred-cubic (bcc) structure by adding 13 at% Li, the complete conversion occurs when Li exceeds 33 at%.

However, attempts to hydrogenate magnesium-rich Li-Mg alloy (4.7, 8.9, 16.8 and 30.1 at% Li) at 40 bar H_2 and 200-400 °C did not yield the target hydrides but only MgH_2, while the elemental Li was segregated to the surface to form a passivating layer of LiOH or Li_2O (Fischer *et al.*, 1991).
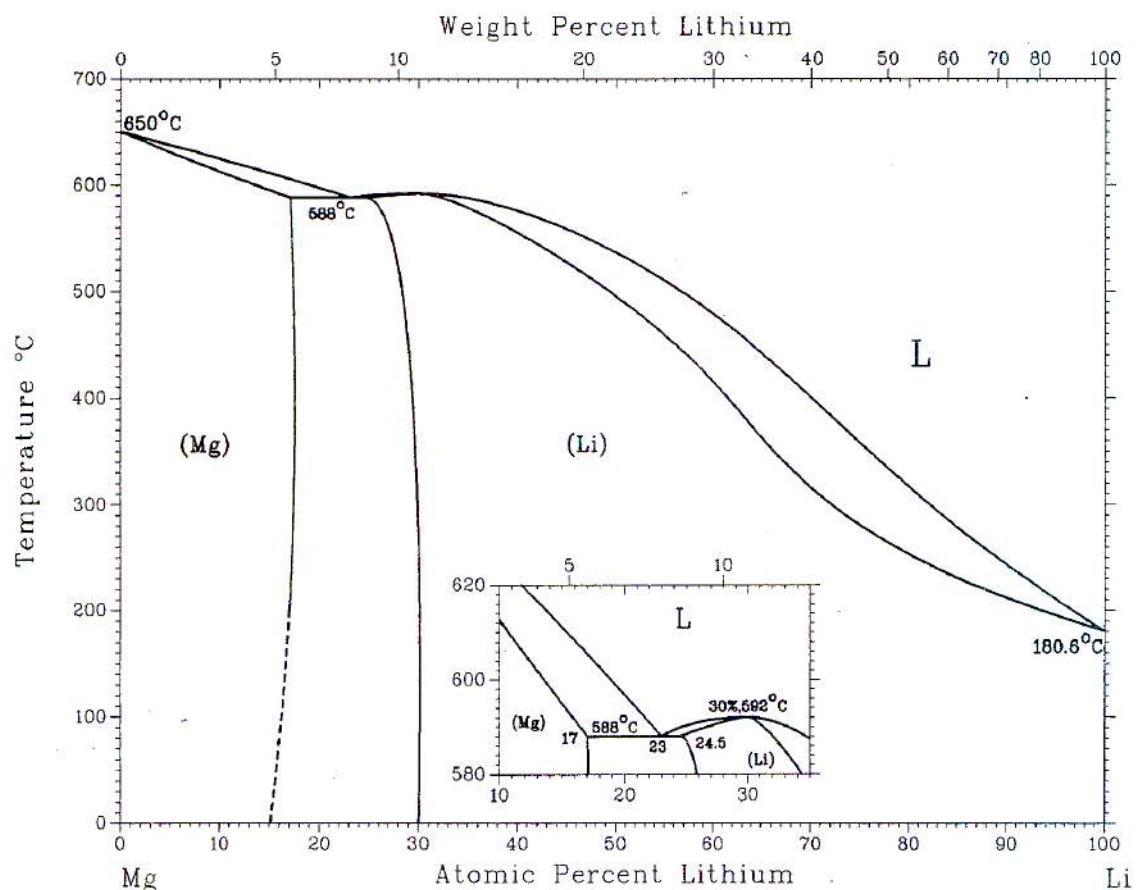
Figure 2.14 Li-Mg alloy phase diagram (Nayeb-Hashemi *et al.*, 1984).

In summary, due to the great abundance and low price of elemental Mg, Mg-based compounds are being investigated for various applications. As a potential candidate of hydrogen storage materials, MgH_2 has a relatively large hydrogen capacity of 7.6 wt% and good reversibility. However, the sorption kinetics need to be increased and the temperature of operation reduced, prior to practical use. Many nanotechnology approaches have been studied in the literature. In this section, the effect of ball milling and Ti-based additives on sorption properties of MgH_2, as well as novel Mg-based binary-metal hydrides, have been described. Although the sorption kinetics could be greatly enhanced by introducing a nanostructure and adding a catalyst(s), the MgH_2 phase itself is still too stable (i.e. the thermodynamics of the MgH_2 phase needs to be modified). On the other hand, stable Mg-based compounds are being considered for applications as: electrodes and/or electrolyte materials in batteries, and thermal energy storage media for use in solar thermal power

plant where the working temperatures may be above 250 °C (Rönnebro and Majzoub, 2008).

2.7 Aims and objectives

The aim of this project is to gain a greater understanding of the hydrogen sorption mechanisms of metal borohydrides and Mg-based hydrides, and to tailor their hydrogen storage properties, in an effort to produce an easily reversible, and high capacity hydrogen storage medium. The research focused on four aspects:

1. A more detailed understanding of the structural and thermal properties of the borohydride systems of: $LiBH_4$ (Chapter 4), $Mg(BH_4)_2$ (Chapter 5), $Ca(BH_4)_2$ and the eutectic mixture $LiBH_4$-$Ca(BH_4)_2$ (Chapter 6). Particular attention was paid characterising the phase transformations (crystal and vibrational), dehydrogenation temperatures and reaction intermediates/products, using DSC-TGA-MS, and in situ XRD and Raman spectroscopy.

2. Investigate the role of B_2H_6 and the formation mechanism of higher boranes in the decomposition and formation of $LiBH_4$, $NaBH_4$, $Ma(BH_4)_2$ and $Ca(BH_4)_2$ (Chapter 7). Samples will be synthesised by solid-gas reactions of $M(BH_4)_n$ or MH_n (M = Li, Na, Mg or Ca; n = 1 or 2), with a mixture of gaseous B_2H_6 and H_2 at various temperatures. The resulting products will be characterised by ex situ XRD and Raman spectroscopy.

3. Attempt to synthesize novel Mg-Ti-B-H hydrides by high-energy high-pressure ball milling of mixtures of MgH_2, amorphous boron, and Ti-based compounds; and understand the role of amorphous boron and Ti-based compounds in tailoring the thermodynamic and kinetic properties of MgH_2 (Chapter 8). Structural and compositional changes of milled samples during heating will be studied using DSC-TGA-MS and in situ XRD. Finally, the H_2 reversibility shall be tested by manometric hydrogen storage analysis.

4. Attempt to synthesise novel Li-Mg-H ternary hydrides by high-energy reactive milling of a Li-Mg ribbon alloy. The structural and thermal properties of the milling products during heating will be studied using DSC-TGA-MS and in situ XRD measurements (Chapter 9).

3   Experimental Methods

This Chapter describes the experimental techniques and the methods used for data analysis, and outlines some of the principles behind these techniques. The chapter sections are shown in **Figure 3.1**.
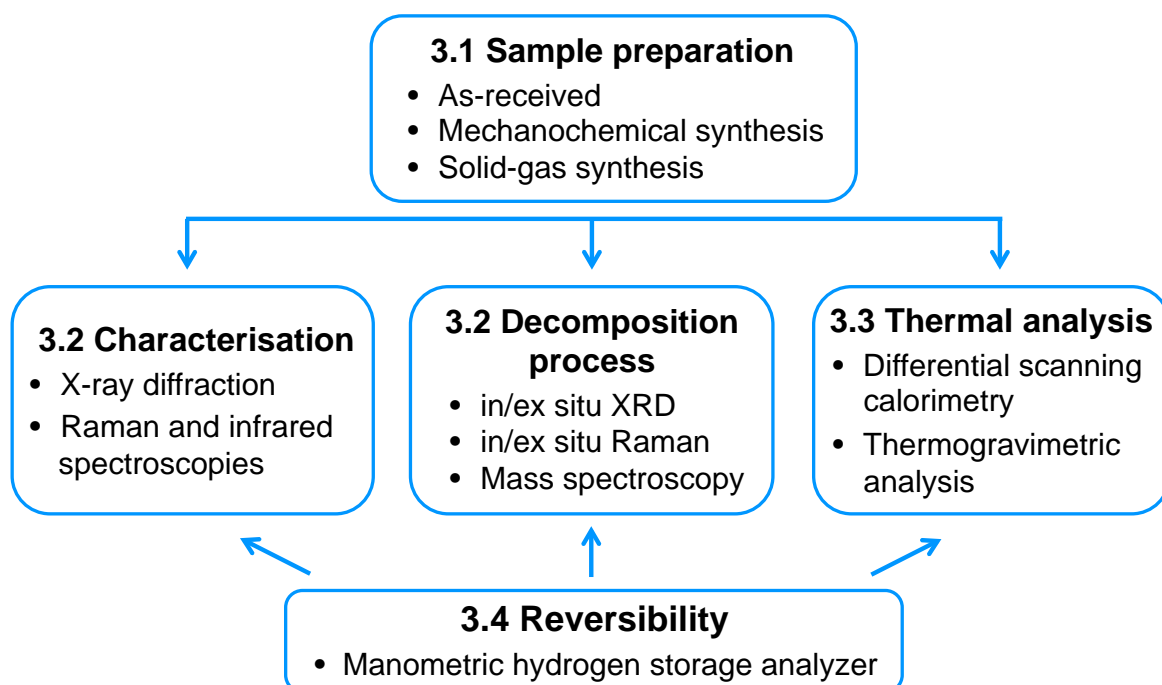
Figure 3.1 Experimental techniques used.

3.1   Materials and sample preparation

All the chemicals and samples were stored in an argon glove box (O_2 < 50 ppm, H_2O < 0.1 ppm) and used under either argon or helium, to try to prevent any reaction with air or moisture. The diborane source (section 3.1.2.1), exhibiting low thermal stability, was stored in an air-tight container at 0-5 °C in a fridge before use. All chemicals were used as

received from the chemical manufacturer (**Table 3.1**). Samples were weighed out using an analytical balance (up to ±0.1 mg accuracy) if needed.

Table 3.1 Chemical compounds used in this work.

Chemicals	Purity	Manufacturer	Notes
$LiBH_4$	≥ 95 %	Sigma-Aldrich	
	≥ 95 %	Katchem Ltd.	
$LiBD_4$	≥ 95%	Sigma-Aldrich	
	98 % D	Katchem Ltd.	
$NaBH_4$	99.9 %	Sigma-Aldrich	
$NaBD_4$	96 % D	Sigma-Aldrich	
$Mg(BH_4)_2$	-	Sigma-Aldrich	Batch no. MKBB6388
	95 %		84096JM
	-		06496HMV
$Ca(BH_4)_2$	-	Sigma-Aldrich	Batch no. 17696LKV
LiH	95 %	Sigma-Aldrich	powder, ~30 mesh
NaH	95 %	Sigma-Aldrich	
MgH_2	-	Sigma-Aldrich	
	95 wt%	Degussa–Goldschmidt	
$K_2B_{10}H_{10}$	-	Katchem Ltd.	
$K_2B_{12}H_{12}$	-	Katchem Ltd.	
Amorphous boron	≥ 95 %	Sigma-Aldrich	
Ti	99.7 %	Sigma-Aldrich	powder, ~100 mesh
TiH_2	-	Sigma-Aldrich	
$TiCl_3$	99.99 %	Sigma-Aldrich	
$ZnCl_2$	100%	Alfa Aesar	

3.1.1   Mechanochemical synthesis

Mechanical milling is used for not only physical mixing and size reduction of materials, but also synthesising new compounds, doping additives, or modifying microstructures.

A Retsch PM400 Planetary Mill (**Figure 3.2**), which consists of four grinding pots and one main disk, was used for this work. The pot containing the reaction mixture and a number of balls is mounted on the main disk. When the pot rotates around its own axis and the main disk rotates in an opposite direction (like the Earth rotates around the Sun), powder

mixtures undergo high-energy collisions with the milling balls and the inner walls of the pot, and leading to morphological changes and/or chemical reactions within or between powder particles.

However, these high-energy collisions can also cause wear of the milling media (pot and balls), resulting in the incorporation of impurities into the powder (Suryanarayana, 2001).

The magnitude of contamination will depend on the milling conditions (e.g. energy, speed, time), and the difference in the strength/hardness of the powder and the milling medium. In this work, hardened steel milling medium was used: the pot consists of Fe 84.89, Cr 12.00, C 2.20, Mn 0.45, Si 0.40, P 0.03 and S 0.03 (in wt%), and milling balls contain Fe 95.85, C 1.05, Cr 1.65, Si 0.35, Mn 0.45, Ni 0.30, Cu 0.30, P 0.03 and S 0.03 (Retsch GmbH, 2014). According to Suryanarayana (2001), 1-4 wt% Fe is normally present as an impurity in most of the powders milled with a steel milling medium. It can thus be reasonably assumed that in the work reported here a level of Fe contamination was present in all milled samples, although no other evidence for this was observed.
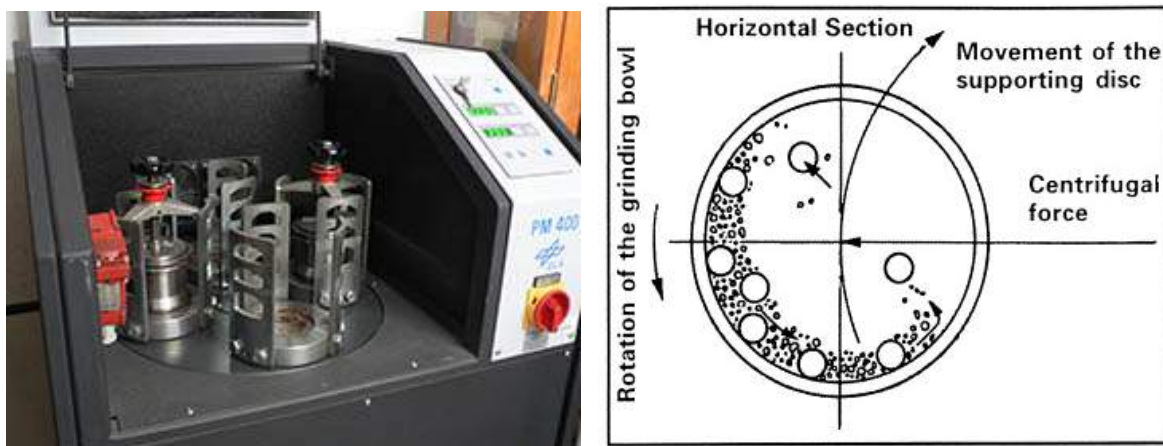
Figure 3.2 Left: Retsch PM400 Planetary Mill. Right: schematic view of motion of the ball and powder mixture (Suryanarayana, 2001).

Several milling parameters were adjusted for specific samples as summarised in **Table 3.2**. Minor alterations of the milling speed (175 or 200 rpm unless specified) and powder-to-ball weight ratios (30:1 – 60:1) as well as different milling pots and balls were used in the

sample preparation. The total milling time is a very important parameter, and needs to be adjusted to follow the progress of chemical reactions occurring during milling. The milling time applied for specific samples was based on previous studies in different subjects. All milling was performed with 10 or 15 minute of milling followed by a 10 or 15 minute rest period (unless specified) in an effort to minimize local temperature increases.

The pressure of the selected gas can be up to 100 bar using a high pressure milling pot (evico-magnetics). This pot is made of hardened steel and has an internal volume of 220 ml. The high pressure milling technique could minimise possible decomposition of samples during milling, and in some cases, induce solid-gas reactions between the solid compounds and the reactive gases (e.g. H_2).

Table 3.2 Samples prepared by ball milling.

Precursors	Milling time (h)	Milling speed (rpm)	Ball to powder weight ratio	Pot volume (ml) / ball's diameter (mm)	Atmosphere
$NaBH_4$, $ZnCl_2$	1	200	30:1	250 / 12	1 bar Ar
$Mg(BH_4)_2$	2	200	50:1	220 / 10	100 bar H_2
$LiBH_4$, $Ca(BH_4)_2$	10	200	50:1	50 / 10	1 bar Ar
MgH_2	2	200	40:1	220 / 10	1 bar Ar, 100 bar H_2
MgH_2, B	2, 20	200	40:1	220 / 10	1bar Ar, 100 bar H_2
MgH_2, B, TiX (TiX = Ti, TiH_2, $TiCl_3$)	2, 20	200	40:1	220 / 10	100 bar H_2
Li-Mg ribbon alloy	1, 2, 5	200	50:1	220 / 10	100 bar H_2

3.1.2 Solid-gas synthesis

3.1.2.1 Diborane (B_2H_6) source

A small and controlled amount of diborane gas was produced from a diborane source (heating zinc-based borohydride) in a closed reactor. Due to the toxicity of diborane, this was safer than trying to use a gas cylinder (NB. A detailed Risk Assessment was prepared by the research group, considering the safe use of small volumes of diborane gas).

The zinc-based borohydride was prepared by milling a mixture of $2NaBH_4+ZnCl_2$ to yield $NaZn(BH_4)_3$ and $NaZn_2(BH_4)_5$, which are known to release diborane and hydrogen between 69 and 112 °C (see Section 2.4.2, p53). In addition, other boranes e.g. B_4H_{10}, B_5H_9 and $B_{10}H_{14}$ might be also formed due to the complexity of B_2H_6 thermolysis (Srinivasan *et al.*, 2008).

3.1.2.2 Gas-solid reaction

For gas-solid reactions, $LiBH_4$ or $NaBH_4$ samples were pre-ground to a fine powder using an agate mortar and pestle under an Ar atmosphere. MgH_2 was used as received or as milled (2 h in Ar). LiH, NaH, $Ca(BH_4)_2$ and $Mg(BH_4)_2$ were used as received.

Around 6 g of the diborane source (including side-product NaCl after milling) and 150 mg of the metal hydrides or metal borohydrides sample were loaded into separate borosilicate glass test tubes, in a stainless steel reactor (**Figure 3.3**). The reactor was placed into a temperature-controlled oven and then was evacuated and sealed before heating. The samples were heated to 120-200 °C for 40 h at heating rate of 2 °C/min, and then cooled. The temperature of the samples was measured using a thermocouple. It was not possible to monitor the pressure during the experiment.
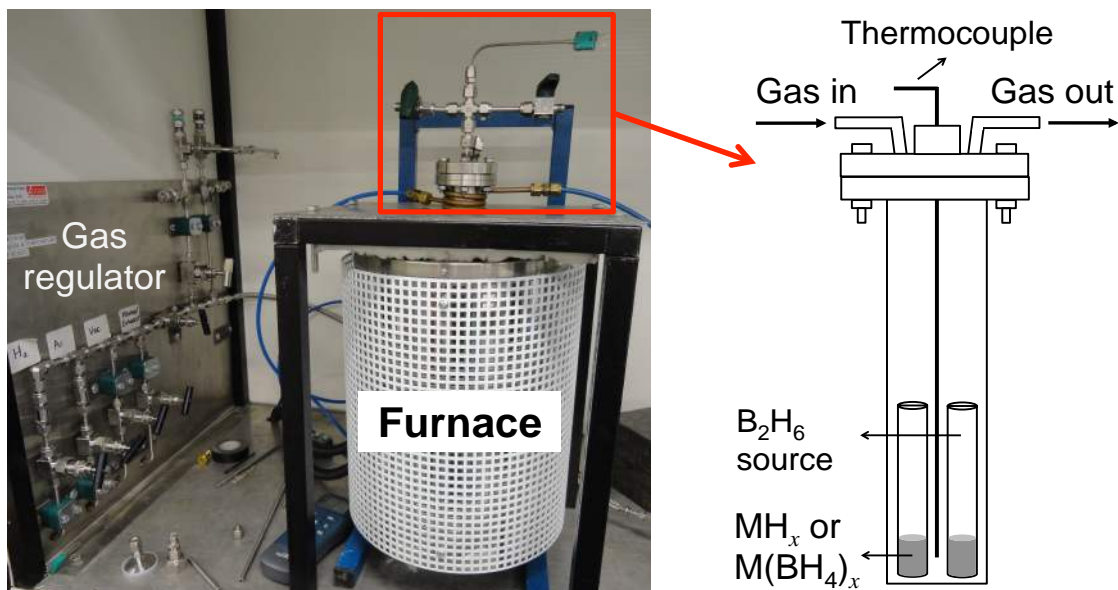
Figure 3.3 Left: experimental setup for the gas-solid synthesis system. Right: schematic sketch of the reactor (M = Li, Na, Ca and Mg; x = 1 or 2)

3.2 Material characterisation and analysis

3.2.1 X-ray diffraction (XRD)

3.2.1.1 X-ray diffraction and Bragg's Law

X-ray diffraction is a powerful technique for crystal structure determinations. X-rays are a form of high-energy electromagnetic radiation with short wavelength (size similar to the distance between atoms in solids) (Atkins *et al.*, 2010). When an X-ray beam is incident on a crystalline material, a portion of this beam is scattered from a series of parallel atomic planes, of which diffraction may occur according to the Bragg's law:

$$2d \sin\theta = n\lambda \qquad (3.1)$$

Figure 3.4 is a demonstration of the Bragg's Law. If scattering is considered as equivalent to reflection from two consecutive parallel planes of atoms separated by a distance *d*, two X-rays of wavelength λ are reflected off these planes at an angle of reflection equal to the angle of incidence *θ*. Constructive interference (i.e. diffraction) of the scattered waves

occurs only when the path difference of two waves is equal to a multiple of the wavelength $n\lambda$, i.e. satisfying the Bragg's law. If the path difference is other than $n\lambda$, then reflected beams are out of phase and destructive interference occurs.
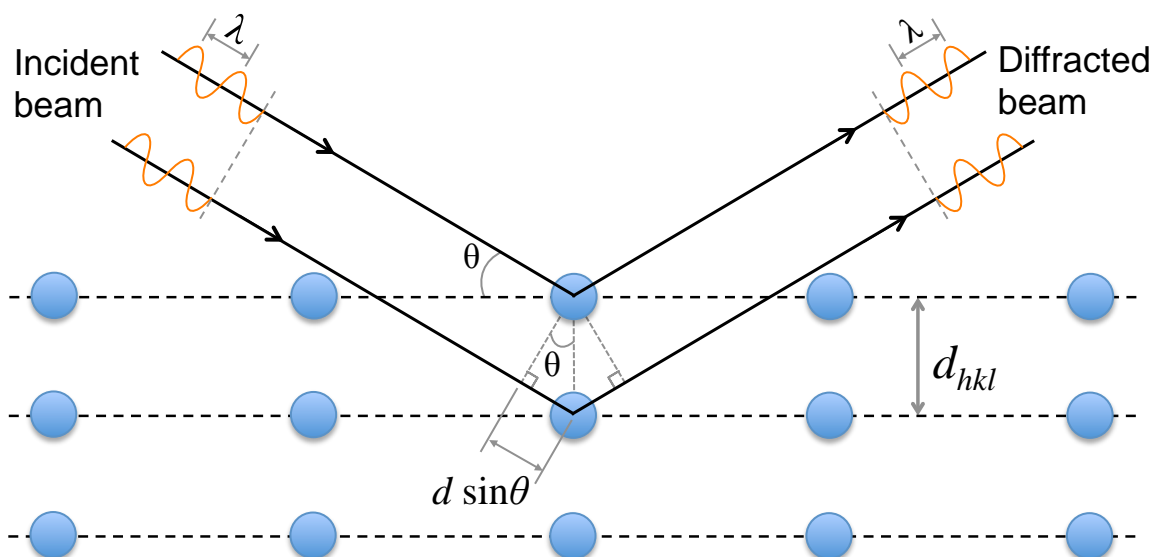
Figure 3.4 Simplified demonstration of the Bragg's Law.

3.2.1.2 Powder X-ray diffraction (PXRD)

Powder X-ray diffraction allows the structure of materials to be determined that are only available in powder or polycrystalline form consisting of randomly oriented crystallites, or can only be studied as powders (e.g. under specific in situ conditions) (David *et al.*, 2006). In addition to solving crystal structures, PXRD can also allow qualitative and quantitative phase compositions to be estimated. However, in the case of complex hydrides, hydrogen atoms are too light compared to the heavy constituent nuclei, so their position in the structure are unlikely to be determined directly by XRD. This can be compensated by the isotopic replacement of the heavier D atom, and by locating the position of B in clusters, e.g. tetrahedron $[BH_4]^-$ by XRD (Ravnsbæk *et al.*, 2010a). It should be noted that the latter method is effective only when the position of the BH_4 units has been refined and their orientations are fixed.

In the current work, all the XRD measurements were performed using a Bruker D8 Advance X-ray Diffractometer. Monochromatic X-rays are generated with a Cu-Kα radiation (λ = 1.54 Å) source with a Göbel mirror. For powder samples containing randomly oriented crystallites, the X-rays are diffracted in all possible directions by every single crystallite, thus, giving rise to a cone of diffraction (**Figure 3.5**). A Vantec position sensitive detector (PSD) moves along the circumference of a circle and cuts through the diffraction cones at the various diffraction maxima, then recording the intensity of the x-rays as a function of 2θ. To prevent samples reacting with air or water, all ex situ measurements at room temperature were performed under inert atmosphere using a Perspex airtight dome-shaped specimen holder. In order to gain better compositional homogeneity of the surface and inside of bulk powder (e.g. Mg(O) and MgB_2 phase segregation in the decomposed $Mg(BH_4)_2$ due to oxidation during heating, see Chapter 5.2.1), some samples were ground briefly using an agate mortar and pestle prior to measurement. Data was typically collected between 5 and 90° 2θ with scanning times of 0.25 to 5 h depending on the data quality for the specific sample.
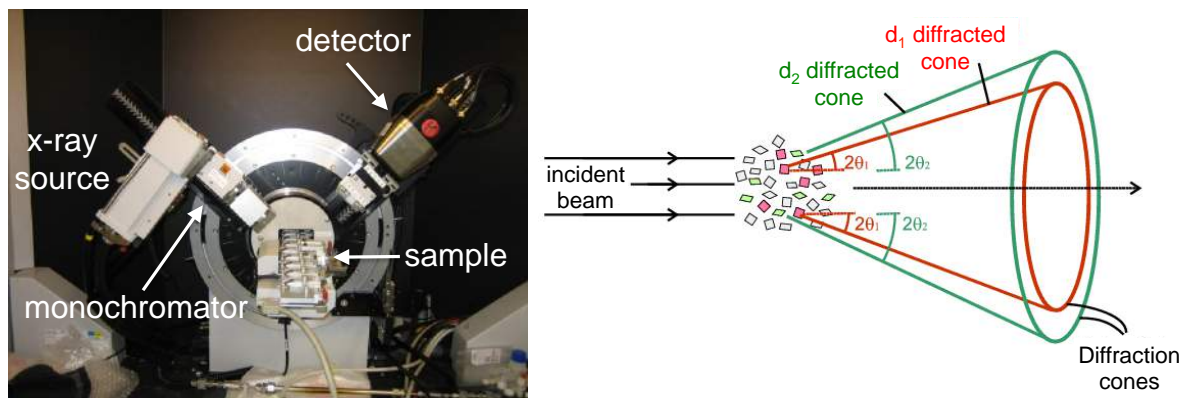
Figure 3.5 Left: Bruker D8 advanced XRD with 9 position multi-changer sample stage, reproduced from Reed (2010); Right: Cones of diffraction by powder sample, reproduced from Barnes *et al.* (2006).

3.2.1.3 In situ powder X-ray diffraction

In order to gain a better understanding of the dehydrogenation mechanism(s) of novel compounds, the structural and compositional changes of the crystalline phase(s) in the

samples were monitored as a function of temperature and/or pressure under He or H_2 atmosphere, using a D8 Advance XRD coupled with an Anton Paar XRK900 reactor chamber. The sample was loaded into a boron nitride or alumina crucible and transferred into the chamber under an Ar atmosphere. For the in situ experiments, the samples were heated at a rate of 6 or 12 °C/min under He or H_2 (flowing at 100 ml/min at 2-3 bar, or static pressure of 9.5 bar). Each scan included a dwell for 5 min after the sample reached a target temperature allowing a homogeneous sample temperature to be reached. Data was then collected isothermally in a 2θ range of 5 to 90° (step size 0.03°) with a total collection time (dwell and scanning time) of 18 to 60 min.

3.2.1.4 Analysis of X-ray diffraction data

Diffraction patterns were initially analysed by comparison with data from crystal structure databases or literature, followed by Rietveld refinement using Topas-Academic and jEdit softwares (Coelho, 2007). The database used in this work was obtained in form of *Crystallographic information files* (.cif) from the Inorganic Crystal Structure Database (ICSD Web, 2013). The initial identification of diffraction peaks gives an approximate estimate of the sample composition. In a Rietveld refinement, the experimental pattern is fitted to a pattern calculated from a given crystal structure (i.e. from a .cif file). The series of parameters (e.g. unit cell lattice parameter, atomic coordinates, zero shift etc.) that are used to construct the calculated pattern, are adjusted to minimise the difference between the observed and calculated data. Hence, more accurate qualitative and quantitative results for the sample composition may be obtained. However, the accuracy and precision of the results using this method are affected by resolution/quality of the XRD data, the grain size and crystallinity of the sample, temperature factors during in situ measurements.

3.2.2 Raman and infrared spectroscopies

Vibrational spectroscopy can detect molecular motions, and determine local coordination of atoms in molecules; so can provide information on chemical and physical properties of compounds (Schrader, 1995). Samples may be characterised either in bulk or in microscopic particles over a wide range of temperatures and physical states, such as solid, liquid or vapours, powders or thin films. Once a spectrum is obtained, vibrations may be assigned according to: 1) characteristic vibrations of specific groups in molecules, which are defined by certain ranges of frequencies and intensities in IR or Raman spectra; 2) the comparison of experimental and simulated vibrations using theoretical calculation, which is particularly useful for the identification of novel compounds. When studying complex hydrides, the hydrogen atoms are usually too light to be probed by lab-based XRD. However, vibrational spectroscopy is one method which can help to determine hydrogen/deuterium position in borohydride/borane-based compounds.

Raman scattering and infrared absorption are the two principal techniques for measuring vibrational spectra. Both are based on the interaction of incident radiation on molecular vibrations; but they are different in how photon energy is transferred to the molecule by promotion from the ground to the excited state.

3.2.2.1 Raman spectroscopy

In Raman spectroscopy, a single frequency of radiation (wavelength from infrared to ultraviolet) interacts with molecule and distorts the electron cloud surrounding the nuclei to form a shot-lived state (Smith and Dent, 2005). The energy difference between the incident beam and scattered beam is detected. This short-lived state, also called a "virtual state", is unstable and rapidly collapses back to a real lower state by the emission of photons.

Due to the very light nature of electrons, most photons only distort the electron cloud and maintain the same energy before and after scattering. This elastic process is known as

Rayleigh scattering. When nuclear motion is involved in scattering, the photons transfer energy to molecules to excite vibrations. Hence, the frequency of the scattered photon differs from that of the incident photon by amounts equivalent to vibrational frequencies of the molecule. This inelastic process is called Raman scattering. A schematic of the energy transfer in these scattering is shown in **Figure 3.6**.
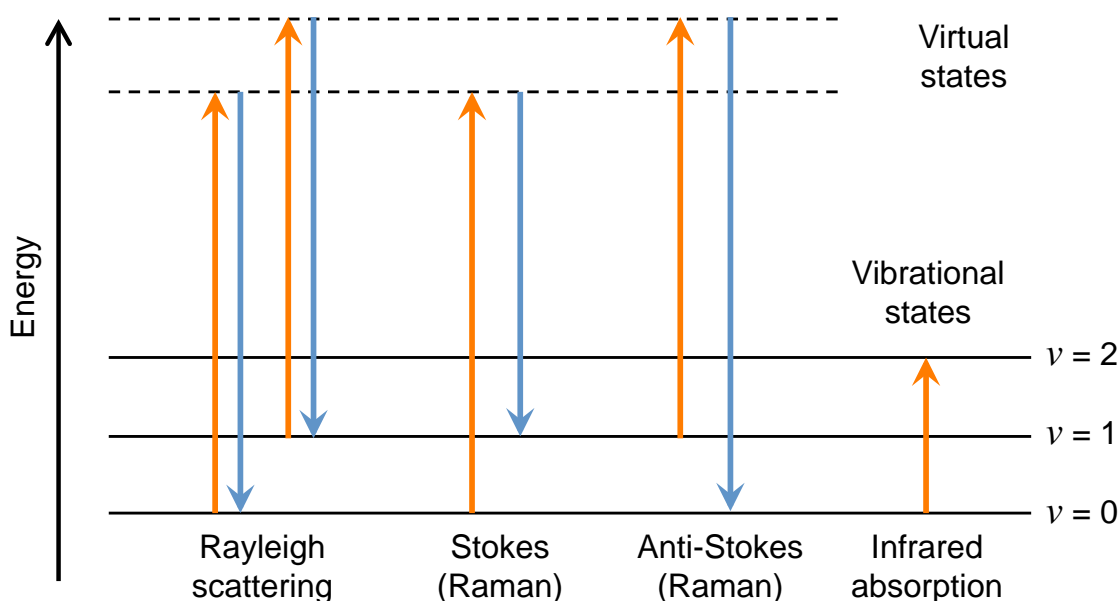
Figure 3.6 Energy transfer of the Rayleigh and Raman scattering and infrared absorption.

If the photon transfers energy to promote the molecule from a ground to a virtual state and then drops back down to a higher energy vibrational state, the scattered photon will have a lower energy than the incident photon: so called Stokes scattering. If the molecule in an excited vibration state undergoes scattering to a ground state, the vibrational energy will be transferred to the scattered photon which then has higher energy compared to the incident photon: this process is called anti-Stokes scattering. Usually, only Stokes scattering is recorded since anti-Stokes scattering is typically a much weaker effect. However, when the thermal energy (temperature) is increased, anti-Stokes will increase relative to Stokes scattering. For a molecular vibration to be Raman active, the vibration must cause a change in the polarization of the electron cloud round the molecule. Hence, the symmetrical vibrations usually give the most intense peaks in a spectrum, when the

asymmetric vibrations are relatively weak.

In this work, Raman spectra were collected using a Renishaw InVia Reflex Raman spectrometer with a confocal microscope with a x20 objective (**Figure 3.7**). The incident laser beam (wavelength: 488, 633 or 785 nm) with a power of between 20 and 200 mW was focused onto the sample with a ~50 µm diameter spot. The scattered radiation is then directed back through a notch filter to remove Rayleigh scattering. The remaining photons are then directed and separated by slits and gratings (2400, 1800 or 1200 grooves/mm) before detection by a charge-coupled device (CCD). The spectral resolution of the Raman spectra is ~3 cm^{-1}. The measurement parameter was optimized for different samples in order to obtain well-resolved spectra.

Around 10 mg of sample was placed into an aluminum crucible in an Instec HCS621V sample cell that allowed the atmosphere and temperature to be controlled (under 1-2 bar Ar or H_2, between -190 and 600 °C at a heating/cooling rate of 1-10 °C/min). The vibrational modes were analysed and assigned using Renishaw Wire 3.4 (Renishaw plc., 2008) and Igor Pro software.
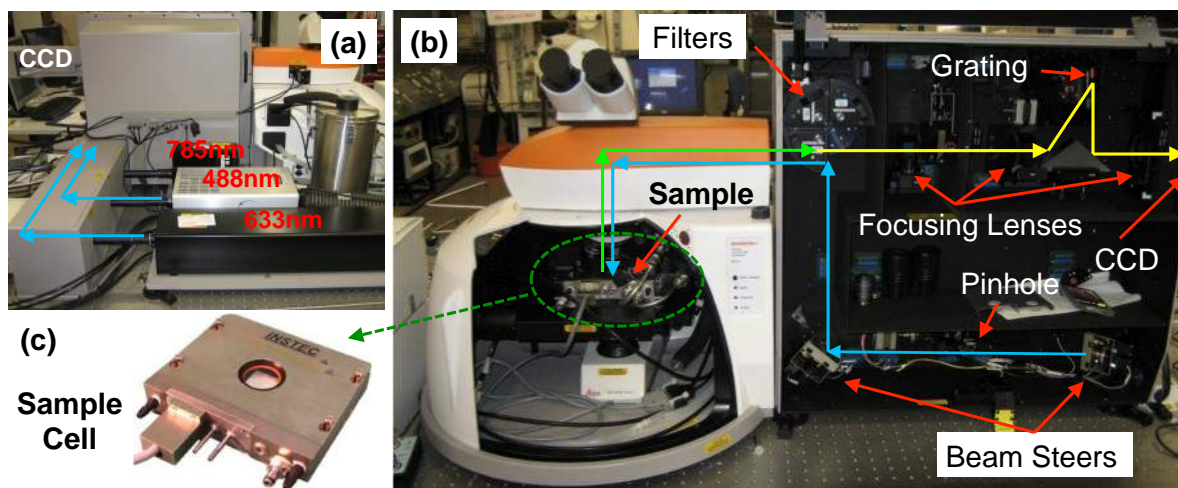
Figure 3.7 (a) Laser source of wavelength: 488, 633 or 785 nm, (b) Renishaw inVia Raman Microscope with (c) Instec HCS621V sample cell. Blue line: incident beam, green solid line: scattered beam, yellow line: remaining beam after removal of the Rayleigh scattering. Reproduced from Reed (2010)

3.2.2.2 Infrared spectroscopy

Different to Raman scattering, infrared spectroscopy (IR) uses a range of frequencies of radiation to irradiate molecules. When the frequency of the incident radiation matches the energy gap between the ground and excited states of a molecule, the molecule may be excited to a higher energy (not virtual) state and the absorbed frequency of the radiation is then recorded by infrared spectroscopy (as illustrated in **Figure 3.6**). The absorption bands due to the molecular vibration transition typically occurs in the wavenumber region of λ = 2.5 - 1000 μm, which is equivalent to the mid-infrared region in the electromagnetic spectrum (4000 cm^{-1} to 10 cm^{-1}).

The IR active occurs only when the molecular vibration involves dipole moment change. Thus, asymmetric vibrations usually cause the intense IR absorption but no or weak Raman scattering. In general, the symmetry of molecules determines what vibrations are Raman or IR active, and sometimes vibrations can be active in both. Therefore, Raman and IR spectroscopies are often complementary; together giving a better overall understanding of the vibrational structure of a molecule.

A Thermo Nicolet 8700 Fourier Transform Infrared (FTIR) spectrometer was used in this work. The sample was loaded into a Specac 'Golden Gate' Attenuated Total Reflectance (ATR) attachment under Ar atmosphere (Reed, 2010). This attachment allows sample being measured under inert atmosphere. Prior to the measurements, the spectrometer was purged with high-purity N_2 for 20 min, to minimise water and carbon dioxide signals in the background. Each spectrum was accumulated from 100 scans at a resolution of 0.5 cm^{-1}.

3.2.3 Mass spectrometry (MS) and temperature programmed desorption (TPD)

Mass spectrometry is an analytical technique to measure the mass-to-charge (m/z) ratio of gaseous ion fragments, and to quantitate the relative amount of various species detected.

In this work, a Hiden Analytical HAL IV quadrupole MS was used to analyse the evolution of gas(es) from thermal decomposition. The MS measurement processes occur in three main steps: ionization, separation and detection.

The gaseous analyte compound is bombarded by high-energy electron beam from a hot filament; and is usually ionised to cations by the loss of an electron. Meanwhile, some large molecules may be fragmentised into smaller species by excess energy, which can also be detected according to their lower m/z values. The cations are then accelerated and directed towards a quadrupole mass analyser where separation occurs.

A quadrupole mass analyser consists of four parallel rods (see **Figure 3.8**) that are applied with direct current (DC) and alternating current (AC) oscillating at radio frequency. For given voltages, only ions in a certain m/z ratio pass through the filter, and all other ions are thrown out of their original path. The varied voltage brings ions of different m/z ratios to the detector, building up a mass spectrum. Two different types of detector were used in this work: 1) a Faraday cup is for monitoring high concentration gas, e.g. the carrier gas Ar; and 2) a secondary electron multiplier which has a much larger sensitivity, is used to identify low concentration gases, e.g. possible species of the released gaseous phase from a sample. The MS was set up to measure the concentrations of H_2 (m/z = 2) and B_2H_6 (m/z = 26), H_2O (m/z = 18), O_2 (m/z = 32) and Ar (m/z = 40). For the sample containing $Mg(BH_4)_2$, DMSO (m/z = 77) and DMS (m/z = 62) were also recorded.
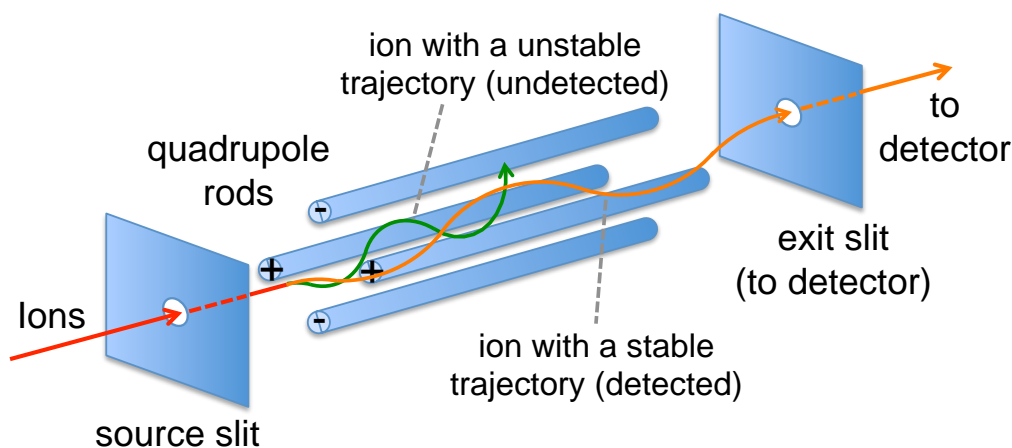
Figure 3.8 Schematic of a quadrupole mass spectrometer

The MS was used coupled with either a Thermogravimetric Analysis (TGA, see Section 3.2.5) or a TPD. **Figure 3.9** is a schematic diagram of TPD-MS: a sample (~100 mg) loaded in a quartz reaction tube, was heated at 2 °C/min under flowing Ar (100 ml/min), while the gaseous desorption products are analysed by mass spectrometry.
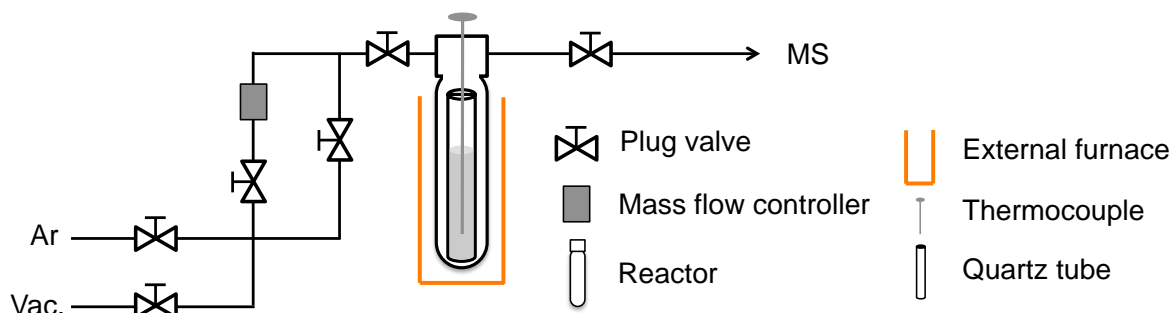
Figure 3.9 Schematic diagram of TPD-MS system, modified from Chater (2010).

3.2.4   Differential scanning calorimetry (DSC)

DSC is a thermo analytical technique used to study the thermal events occurring in a sample, such as polymorphic phase transitions, crystallization, melting, and decompositions, as a function of temperature. It measures the difference in heat flow (power) applied to a sample and a reference, as both are subjected to the same temperature program. In an endothermic process, e.g. melting, heat is absorbed, and therefore, heat flow to the sample is higher than that to the reference in order to maintain both at the sample temperature. Likewise, a sample undergoing an exothermic reaction (e.g. crystallisation), requires less heat to maintain the temperature compared to the reference.

In a heat flux DSC instrument (a Netzsch DSC 204 HP used in the current work), a sample and reference are placed on a disk-shaped sensor in a furnace (cf. **Figure 3.10**). Based on a homogeneous temperature field in the furnace, the equal heat is transferred to the sample and reference through the disk. When the sample has different heat capacity or undergoing a thermal event, the subsequent difference in heat flow causes temperature

gradients at the thermal resistances of the area sensor (Hemminger and Sarge, 1998). Sensitive temperature sensors record these gradients and measure every difference in the heat flow quickly and accurately. The temporary deviations are shown as exothermal or endothermal peaks over a flat, horizontal DSC baseline.
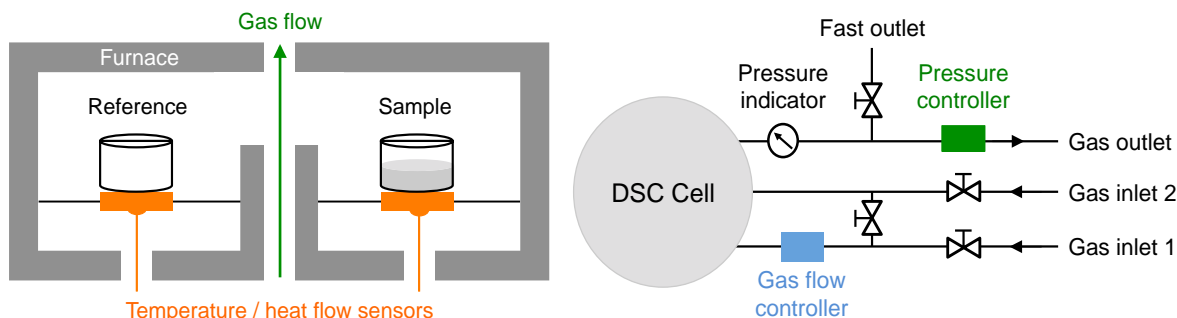
Figure 3.10 Left: schematic of a heat-flux DSC cell, modified from Chater (2010). Right: high-pressure DSC system (Netzsch DSC 204 HP) with input gas.

A multi-point temperature calibration was performed using the well-defined melting point of high purity metals (In, Bi, Sn, Pb and Zn) in the temperature range desired. By comparison of the standard and observed melting temperature, calibration curves are produced for measurements using different heating rates. A baseline also needs to be determined using an empty pan under the same conditions (temperature and atmosphere) to the sample measurement, to reduce the effect of the background conditions on the sample measurement.

The Netzsch DSC 204 HP was mounted in a flowing argon glove box. Approximately 5-10 mg of sample (pre-weighted using a TGA with an accuracy of 0.001 mg) was loaded in an Al crucible with a lid. An empty Al crucible with a lid was used as the reference. The measurement was performed upon to 500 °C at heating and cooling rates of 2 °C/min and 4 bar Ar (4 or 11 bar H_2 in some cases) flowing at 100 ml/min.

3.2.5   Thermogravimetric analysis (TGA)

TGA measures the mass change of a sample due to decomposition or reaction, as a function of temperature/time. When coupled with a MS, TGA can monitor the amount of hydrogen released from a sample at different stages in the dehydrogenation process, and hence may provide information on the possible composition(s) of unknown intermediate phase(s).

A TGA (Netzsch TG209, see **Figure 3.11**) consists of a precision microbalance (accuracy ±0.001 mg), a temperature-programmable furnace and a controller, which enables the sample to be simultaneously heated and weighed. The temperature of the furnace can be: increased linearly, maintained isothermally, as well as controlled by multiple heating/cooling schemes. During the measurement, the sample is situated within an enclosed system so that the atmosphere can be controlled. An inert gas at ambient pressure flows over the sample and may carry away the evolved gas(es) from a sample, which can be subsequently analysed by a MS.
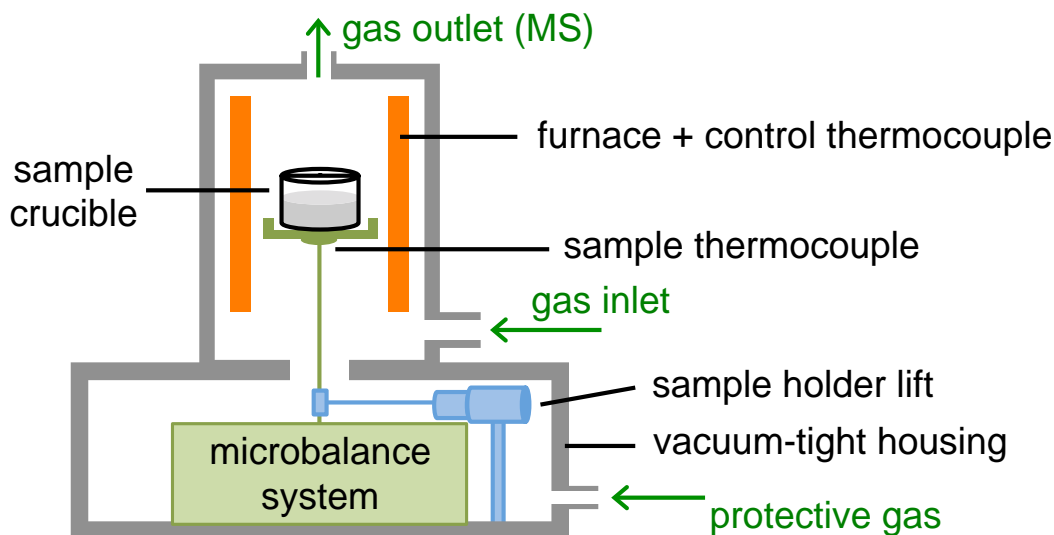
Figure 3.11 Simplified internal view of a Netzsch TG209 analyzer.

Since the TGA measures the change in weight of a sample over a given temperature range, the instrument need to be calibrated for both temperature and weight signals. Similar to

DSC, the temperature is calibrated with high-purity materials (KNO_3, In, Bi, Sn, Zn and Al). Calcium oxalate is used to check the temperature calibration and mass loss. In order for optimum weight loss sensitivity, a baseline is performed using an empty sample holder within the desired temperature range, to minimise the buoyancy effect (which is due to the density of the gas decreasing during heating).

The Netzsch TG209 connected to a MS was used to simultaneously analyse thermogravimetric changes and the evolution of gas(es). Some samples exhibiting a melting point below the decomposition temperature (e.g. $LiBH_4$, $Ca(BH_4)_2$), would be assessed the maximum safe temperature to avoid melting and foaming that may damage the TGA and DSC system. Approximately 10-40 mg of sample was loaded in an alumina crucible with a lid, and heated at 2 °C/min in flowing Ar (40 ml/min, ~1.5 bar). A small hole in the lid allows gas formed during decomposition or reactions to be released.

3.2.6   Manometric hydrogen storage analyzer

The manometric (Sieverts) method is the most common technique for gas sorption measurements, in which the sorbed quantity is determined by measuring the change in pressure in a system of fixed volume (Broom and Thomas, 2013). By recording temperature and gas pressure accurately, the amount of H_2 absorbed by a sample can be calculated using the real gas law:

$$n = PV / ZRT \qquad (3.2)$$

where P is pressure, V is volume, n is the number of moles, Z is the gas compressibility, R is the universal gas constant and T is the temperature.

A Hiden Isochema HTPS-2 volumetric system was used to attempt rehydrogenation of materials. A simplified schematic diagram of the system is presented in **Figure 3.12**. V_1 and V_2 are the dosing volume (~6 ml) and the reactor volume (~5 ml), respectively. Valve A is the gas inlet which has different gas supply options (H_2, N_2 and He), whereas B controls

the gas outlet connected to a vacuum or MS: both A and B allow the control of the hydrogen pressure in V_1. Valve C is used for introducing or removing gas in V_2. The temperature of the sample is controlled by a temperature-programmable furnace and monitored by multi-point sensors.
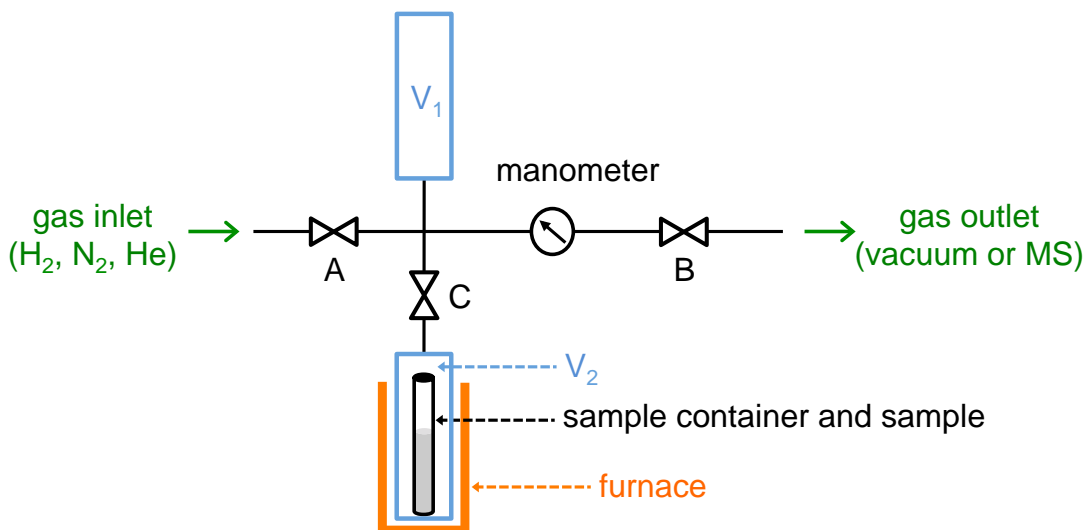
Figure 3.12 A schematic diagram of a basic manometric system, modified from Broom (2011).

Prior to measurement, the volume of empty sample container (quartz tube) and sample needs to be determined by using a non-interacting gas, i.e. helium in this work. This process is normally taken repeatedly up to 50 times and the average pressure difference is recorded. The measurement was conducted in the isotherm mode, which is for the determination of volumetric H_2 uptake as a function of set pressures over a range of temperatures.

For absorption measurements, a pre-weighed sample is placed in V_2 and its volume is measured by the following procedure. Valve B and C are opened to evacuate V_1 and V_2 up to a pressure of 5×10^{-6} mbar, and then are closed. V_1 is subsequently filled with H_2 through valve A, and an accurate pressure P_1 is measured using a manometer. Valve A is then closed, and valve C subsequently opened to fill V_2 with H_2, followed by another pressure measurement P_2. Any drop in pressure beyond that due to the volumetric difference between V_1 and (V_1+V_2) is then assumed to be the result of H_2 uptake by the sample, which

is given in terms of the number of moles (Broom, 2011):

$$\Delta n = (P_1 V_1) / (Z_{1,T} RT) - [P_2 (V_1 + V_2)] / (Z_{2,T} RT) \qquad (3.3)$$

This dosing and measurement process is repeated for each data point, and therefore plots of the amount absorbed or adsorbed and desorbed as a function of pressure at fixed temperature can be mapped out.

In this work, PCT Measurements were performed between 5×10^{-6} and 100 bar H_2 in 0.5-10 bar increments between 200 and 400 °C, and each pressure step was held for 20 min to 2 h. Smaller increments were used along the region of the sorption plateau pressure in order to obtain an accurate equilibrium value.

4 LiBH$_4$

The focus of this chapter is to: characterise both the crystal structure and vibrational frequencies of LiBH$_4$ (LiBD$_4$) through an orthorhombic to hexagonal structural transformation using in-situ x-ray diffraction and in-situ Raman spectroscopy; and to investigate the thermal decomposition mechanism of LiBH$_4$ (LiBD$_4$) by in-situ Raman spectroscopy in combination with ex situ XRD and TPD measurements. Samples were as received from Sigma Aldrich.

4.1 Phase transformation

4.1.1 X-ray diffraction

Figure 4.1 shows the refined diffraction data for the as-received LiBH$_4$. The sample consisted of only orthorhombic LiBH$_4$ with no impurity phases (that could be detected by lab-based XRD), and its lattice parameters were determined to be a = 7.185(4) Å, b = 4.440(3) Å, c = 6.810(4) Å and V = 217.2(2) Å^3, which is in good agreement with previously published data by Soulié et $al.$ (2002).
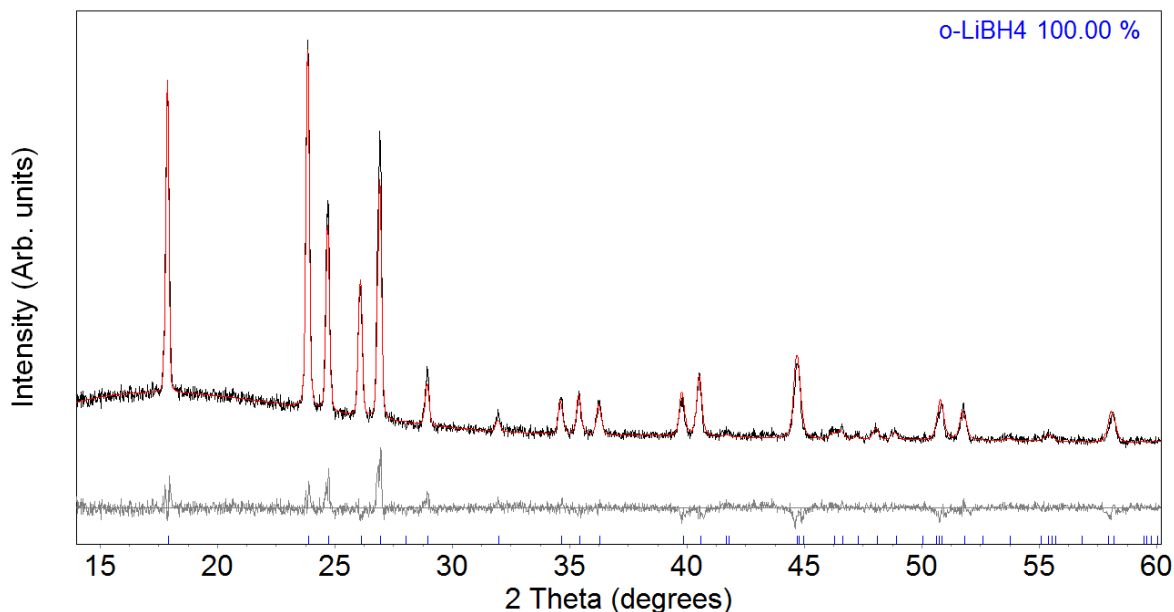
Figure 4.1 Rietveld refinement profile of X-ray diffraction data for the as-received LiBH$_4$, showing the observed data (Y$_{obs}$, black), the calculated fit to the data (Y$_{calc}$, red) and the difference (Y$_{obs}$-Y$_{calc}$, grey). Goodness-of-fit = 1.288.

Variable temperature XRD analysis was conducted on the as-received LiBH$_4$ in order to characterise the orthorhombic and hexagonal phases as a function of temperature. The LiBH$_4$ sample was loaded into an Al$_2$O$_3$ crucible and heated from 30 to 200 °C, followed by cooling to 30 °C at a ramp rate of 12 °C/min. The data in the range 15° to 50° 2θ (step size 0.03°) was collected isothermally at 10 °C intervals, with a collection time of around 18 minutes per scan. This corresponds to an average ramp rate of 0.5 °C/min.

Figure 4.2 is a surface plot of the in situ diffraction patterns if viewed from above. The reversible phase transformation between the orthorhombic and hexagonal LiBH$_4$ phases was observed between 110 and 120 °C on heating, and 100 and 110 °C on cooling. The temperature region of phase change was in good agreement with the observed temperature at 111 and 108 °C, respectively, by Hartman *et al.* (2007) and Filinchuk *et al.* (2008). In addition, thermal expansion/contraction was also seen in the gradual shift to lower/higher angle of the o/h-LiBH$_4$ diffractions throughout the heating and cooling, respectively. At 30 and 40 °C, a set of diffraction peaks (labelled as symbol "?") due to LiBH$_4$•H$_2$O appeared: this may be a result of reaction of the surface of the sample with air

during sample transfer, even though this transfer took place under an argon atmosphere. However, the LiBH₄•H₂O disappeared above 60 °C, and does not appear to have affected the LiBH₄ phase transformation.
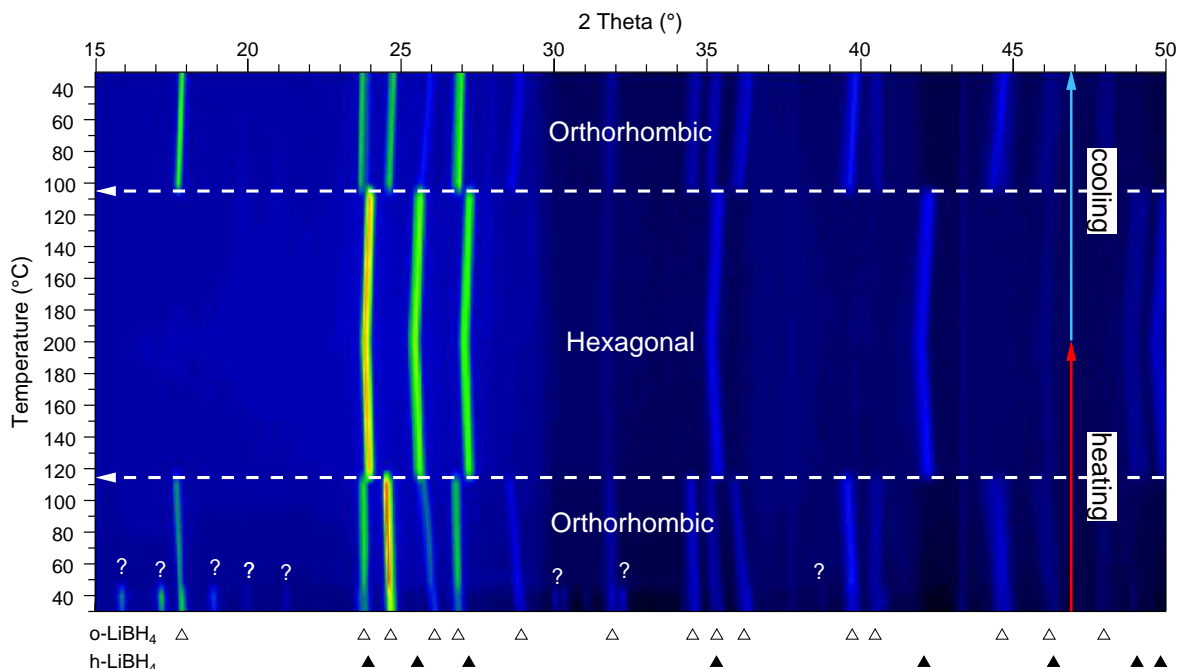
Figure 4.2 In-situ XRD of LiBH₄ heated (cooled) at 12 °C/min in flowing helium (at 100 ml/min and 2 bar). The patterns were taken every 10 °C. A brighter colour corresponds to higher diffraction intensity. Bragg diffraction positions for for the o-LiBH₄ at room temperature and h-LiBH₄ at 135 °C reported by Soulié *et al.* (2002) are shown as symbols △ and ▲ respectively. Symbol "?" represented LiBH₄•H₂O phase.

Figure 4.3 showed variations of the unit cell volume of LiBH₄ going through the phase transition. Thermal lattice expansion resulted in approximate 1.8% increase in cell volume at 110 °C prior to the phase change. At 120 °C, the lattice parameters of hexagonal LiBH₄ phase were found to be: $a = 4.274(3)$ Å, $c = 6.940(5)$ Å, and $V = 109.9(2)$ Å^3, based on the space group $P6_3mc$. The cell volumes of the h-LiBH₄ monotonically increased with temperature, giving an overall expansion of 2.4% at 200 °C. Lattice size changes for both the orthorhombic and hexagonal phases during heating, were in good agreement with previous synchrotron powder diffraction data (Filinchuk *et al.*, 2008).
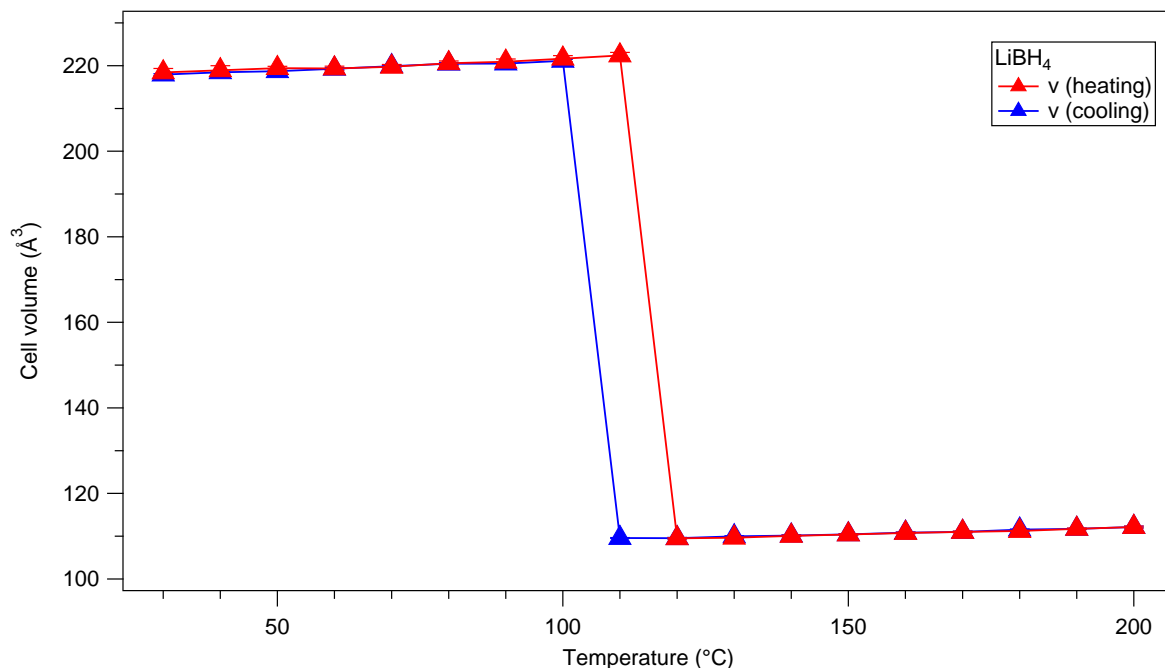
Figure 4.3 The unit cell volume of LiBH$_4$ varied with temperature. Red and blue lines correspond to heating and cooling, respectively. Where error bars are not shown, they are smaller than the data symbols. The lines between symbols are given as a guide for the eyes.

4.1.2   Raman spectra

Figure 4.4 is a comparison of Raman spectra of o-LiBH$_4$ and o-LiBD$_4$ measured at room temperature and -190 °C. The spectra of LiBH$_4$ (LiBD$_4$) could be divided into three regions: external modes (< 350 cm^{-1}) relating to the translational and librational motions between Li$^+$ and [BH$_4$]$^-$ or [BD$_4$]$^-$; bending (1000-1350 cm^{-1} for H, and 800-1000 cm^{-1} for D) and stretching (2000-2500 cm^{-1} for H, and 1500-2000 cm^{-1} for D) modes are the internal vibrations of [BH$_4$]$^-$ ([BD$_4$]$^-$) tetrahedral according to previous reports (Gomes *et al.*, 2002; Racu *et al.*, 2008). A total of 11 of the 18 internal vibrational modes of LiBH$_4$ were identified, and were summarised in Table 3.1.1 by comparing to theoretical values.

The external modes were only partially observed (e.g. 191 cm^{-1} for LiBH$_4$, and 183 cm^{-1} for LiBD$_4$ at room temperature), due to limitations in the Raman system (the holographic notch filters prevent measurements being made below 100 cm^{-1}, and thermal vibrations can obscure lattice vibrations).
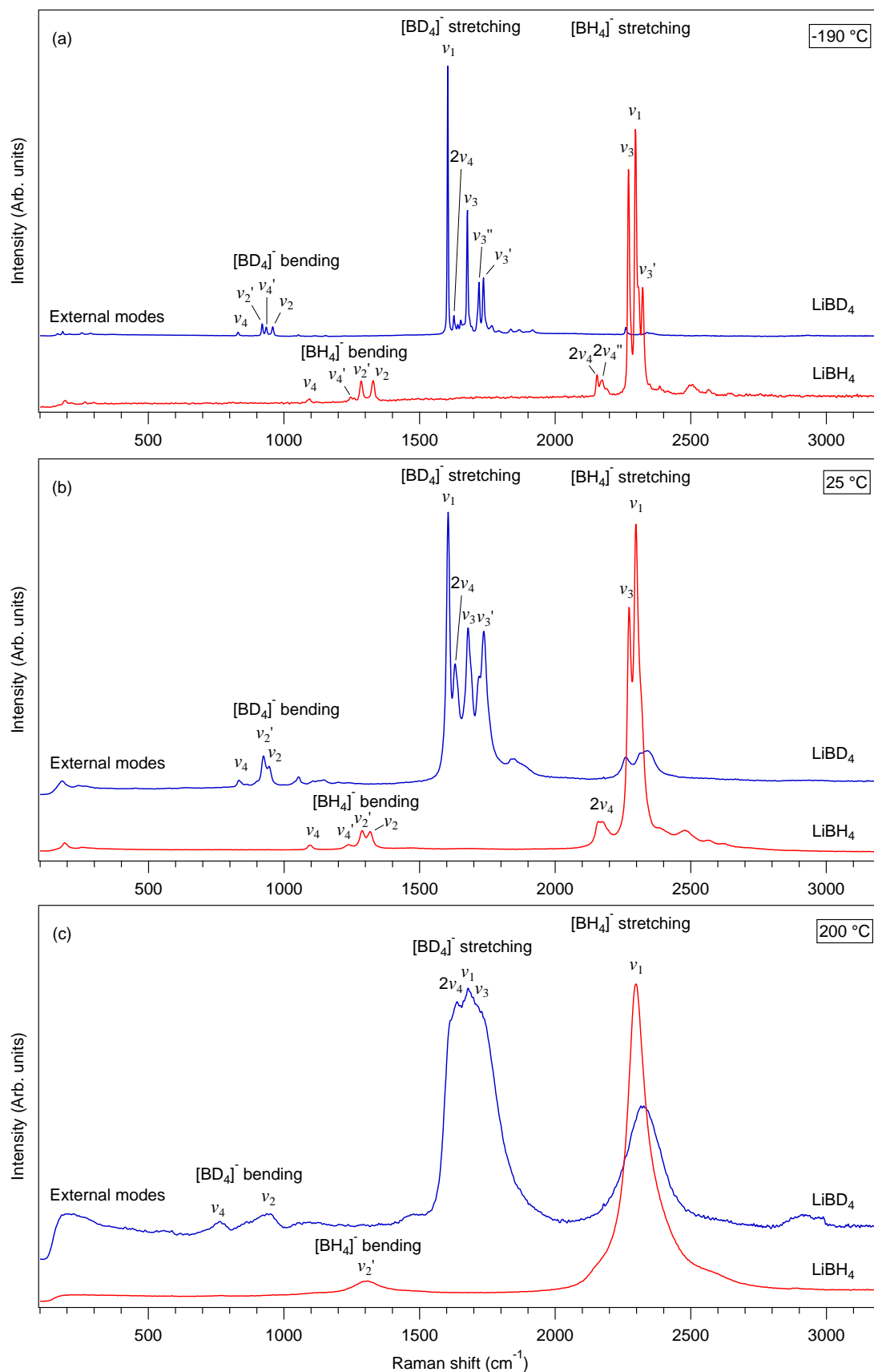
Figure 4.4 Raman spectra of LiBH$_4$ and LiBD$_4$ using a 488 nm laser at (a) -190 °C (b) 25 °C and (c) 200 °C under flowing argon (100 ml/min) with a heating/cooling rate of 5 °C.

Table 4.1 Experimental Raman frequencies (cm^{-1}) of LiBH$_4$ and LiBD$_4$ at -190, 25 and 200 °C, compared to theoretical calculations.

Mode	LiBH$_4$				LiBD$_4$				H/D ratio (-190 °C)	Exp. H/D ratio (-268 °C)*	H/D theo. ratio*
	-190 °C	25 °C	200 °C	Theo.*	-190 °C	25 °C	200 °C	Theo.*			
Internal bending											
v$_4$ (A$_g$)	1095			1062.6	831	831	818	805.5	1.32	1.31	1.31
v$_4$ (B$_{2g}$)				1064.66				805.7			1.32
v$_4$" (B$_{1g}$)				1070.3				807.7		1.32	1.32
v$_4$" (B$_{3g}$)				1070.3				809.13			1.32
v$_4$' (A$_g$)	1239			1235.3	920			919.7	1.35	1.33	1.34
v$_4$' (B$_{2g}$)				1242.3				920.6			1.34
v$_2$' (B$_{1g}$)	1289	1285		1260	935	923		897.43	1.38	1.39	1.40
v$_2$' (B$_{3g}$)				1265.3				901.1			1.40
v$_2$ (A$_g$)	1318	1328	1302	1311.6	955	944	930	938.6	1.38	1.38	1.39
v$_2$ (B$_{2g}$)				1315.6				940.2			1.39
Internal stretching											
v$_3$ (A$_g$)	2271	2272	2347	2329	1676	1678	1724	1758.6	1.35	1.35	1.32
v$_3$ (B$_{2g}$)	2279			2329	1693			1768.6	1.35	1.34	1.31
v$_1$ (A$_g$)	2296	2297	2298	2371.6	1604	1604	1607	1649.56	1.43	1.43	1.43
v$_1$ (B$_{2g}$)	2308			2384.6				1752.16		1.43	1.44
v$_3$" (B$_{1g}$)				2387.6	1719	1716		1772.8			1.34
v$_3$" (B$_{3g}$)				2389.3				1774			1.34
v$_3$' (A$_g$)	2323	2314		2414	1736	1735		1794.7	1.34	1.33	1.34
v$_3$' (B$_{2g}$)				2427.3	1765			1801.9			1.34

* Racu *et al.* (2008)

In the B-H stretching region, the spectra of the orthorhombic LiBH$_4$ consisted of the symmetric v_1, the asymmetric v_3 modes with its splitting mode v_3', and the combination modes such as $2v_4$. The symmetric v_2 and asymmetric v_4 with their splitting modes v_2' and v_4' are B-H bending vibrations. The LiBD$_4$ spectra exhibited some residual B-H bonding as an impurity, as shown by the broad peaks around 2300 cm^{-1}; the B-D vibrations were shifted to lower wavenumbers than for the B-H vibrations in LiBH$_4$. This is because bonds containing heavier atoms (i.e. B-D) usually vibrated at lower frequencies in a tetrahedral symmetry arrangement where the vibrations can be treated as a simple harmonic oscillator following Hooke's Law (Renaudin *et al.*, 2004; Smith and Dent, 2005):

$$v = \frac{1}{2\pi} \sqrt{\frac{k}{\mu}} \qquad \mu = \frac{m_A m_B}{m_A + m_B} \qquad (4.1)$$

where v is the vibration frequency, k is the force constant of the bond between atom A and B, μ is the reduced mass of atoms A and B, and m$_A$ and m$_B$ are the masses of the atoms.

Therefore, the ratio of $v_{\text{B-H}}/v_{\text{B-D}}$ was expected to be close to 1.41 if only the H/D atom was moving significantly in the bond vibration (Equation 4.2), and to be close to 1.36 if the B atom also participated in the vibration (Equation 4.3) (Harvey and McQuaker, 1971b; Gremaud *et al.*, 2009).

$$\frac{v_H}{v_D} = \sqrt{\frac{\frac{2 \times 2}{2 + 2}}{\frac{1 \times 1}{1 + 1}}} = 1.41 \qquad (4.2)$$

$$\frac{v_{B-H}}{v_{B-D}} = \sqrt{\frac{(\frac{10.8 \times 2}{10.8 + 2})}{(\frac{10.8 \times 1}{10.8 + 1})}} = 1.36 \qquad (4.3)$$

According to **Table 4.1**, the H/D ratio of 1.43 for the v_1 mode was the closest to 1.41, suggesting that it mainly originated from H or D atom movement. The v_2 and v_3 with factors of 1.38 and 1.35, respectively, were also affected by significant movement of the B atoms. In addition, vibrations (e.g. v_3 and v_4) with values lower than 1.36, might also include contributions due to resonance with other internal or external vibrations. These results were

in a good agreement with the observations reported by Renaudin *et al.* (2004) and Racu *et al.* (2008).

When heating through the phase transition temperature, the hexagonal phase resulted in simpler Raman spectra than the orthorhombic phase (**Figure 4.4**c). Only two Raman bands v_1 and v_2 appeared in the LiBH$_4$ spectrum at 200 °C, as v_3 greatly broadened in peak width and could be characterised only by curve fitting. External vibrations were not observed for the hexagonal phase.

In-situ Raman measurements on LiBH$_4$ were performed by Reed and Book (2009), allowing the continuous collection of spectra as a function of temperature. In this work, a similar in situ measurement was performed on LiBD$_4$ from -190 to 200 °C. The spectra were collected between 650 and 1250 cm^{-1} every 5 seconds with the focus position of the laser adjusted every 5th spectrum. Both the peak position and width were calculated by curve fitting using the Wire 3.2 software (Renishaw plc., 2008), as shown in **Figure 4.5**.

Figure 4.5a shows the change in peak position of the v_2, v_2', v_4 and v_4' bending modes between -190 and 200 °C. Upon heating, the v_4' mode was no longer observed above -50 °C, which could be masked by v_2' with a thermal broadening. There was little change in the peak position of the v_4 mode until it disappeared at 140 °C, and simultaneously the v_2 and v_2' modes combined to form a single v_2. The combination of v_2 and v_2' could be explained by the increased point group symmetry of the [BH$_4$]$^-$ anion from C$_s$ to C$_{3v}$ during the phase transition from orthorhombic to hexagonal (Gomes *et al.*, 2002). **Figure 4.5**b is a plot of the Raman peak width of the bending mode v_2 of LiBD$_4$ against temperature. The peak width (half-width at half maximum, HWHM) abruptly jumped from approximate 30 to over 85 cm^{-1} during the phase transition at around 140 °C; and increased more quickly on further heating. This was possibly due to large amplitude librational motions resulting in an increase in dynamic disorder of the [BH$_4$]$^-$ as the phases change from o-LiBH$_4$ to h-LiBH$_4$ (Gomes *et al.*, 2002; Reed and Book, 2009).
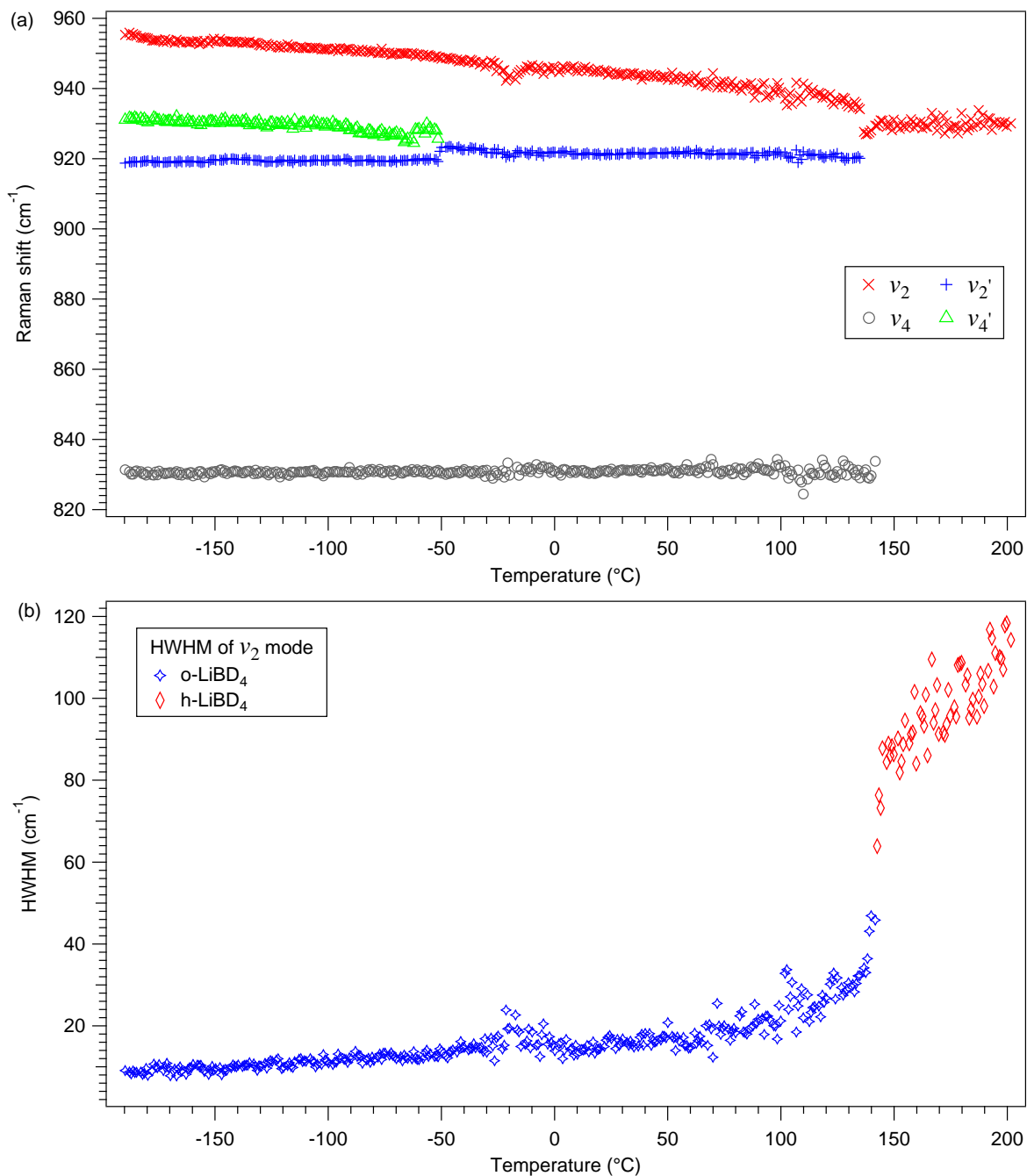
Figure 4.5 (a) Positions of Raman shift of v_2, v_2', v_4 and v_4' modes and (b) HWHM of the v_2 mode of LiBD$_4$ *vs.* temperature during heating at 1 °C/min under flowing Ar (100 ml/min).

Furthermore, the H/D ratio for the v_1 mode from the high-temperature phase was 1.43, as the same as the o-LiBH$_4$; whilst those for the v_2 and v_3 increased to 1.40 and 1.36 which is close to the ideal value of 1.41 for pure H or D atom vibration (i.e. in which the B boron atom moves in the same direction relative to the H/D atom), and 1.36 for the B-H bond vibrations in free borohydride ions. These results suggest that the [BH$_4$]$^-$ vibrations may be

less affected by external lattice vibrations, and have increased freedom in their rotational motion in the high-temperature phase.

However, the orthorhombic to hexagonal phase transition temperature of around 140 °C observed in the Raman spectra, is higher than the 110 - 120 °C range seen during in situ XRD studies (**Figure 4.2**). This might be because the temperature was measured using a thermocouple whose head was situated inside the heater block of the Raman cell, and so a heat transfer delay between the heater and the sample (which is in an Al sample pan, which sits on top of the heater block) may be likely.

4.1.3   DSC-TGA

DSC traces of the as-received LiBH$_4$ on two consecutive heating and cooling cycles are shown in **Figure 4.6**. An endothermic peak on heating (116°C) and an exothermic peak (104 °C) on cooling were observed, which correspond well to the temperature range of the orthorhombic-hexagonal phase change seen during the in situ XRD measurements. These phase change reactions were reversibly measured over two cycles. No mass loss of LiBH$_4$ was detected by thermogravimetric analysis (TGA) over two heating-cooling cycles between 30 and 200 °C, which disagrees with previous work by (Züttel *et al.*, 2003a) who reported that 0.3 wt% of hydrogen was released between 100 and 200 °C. This difference might be because it is not possible to detect such a small mass change (i.e. 0.03 mg for a 10 mg sample) using the current TGA set-up. The TGA trace on the first heating cycle is shown in **Figure 4.6** (green line).
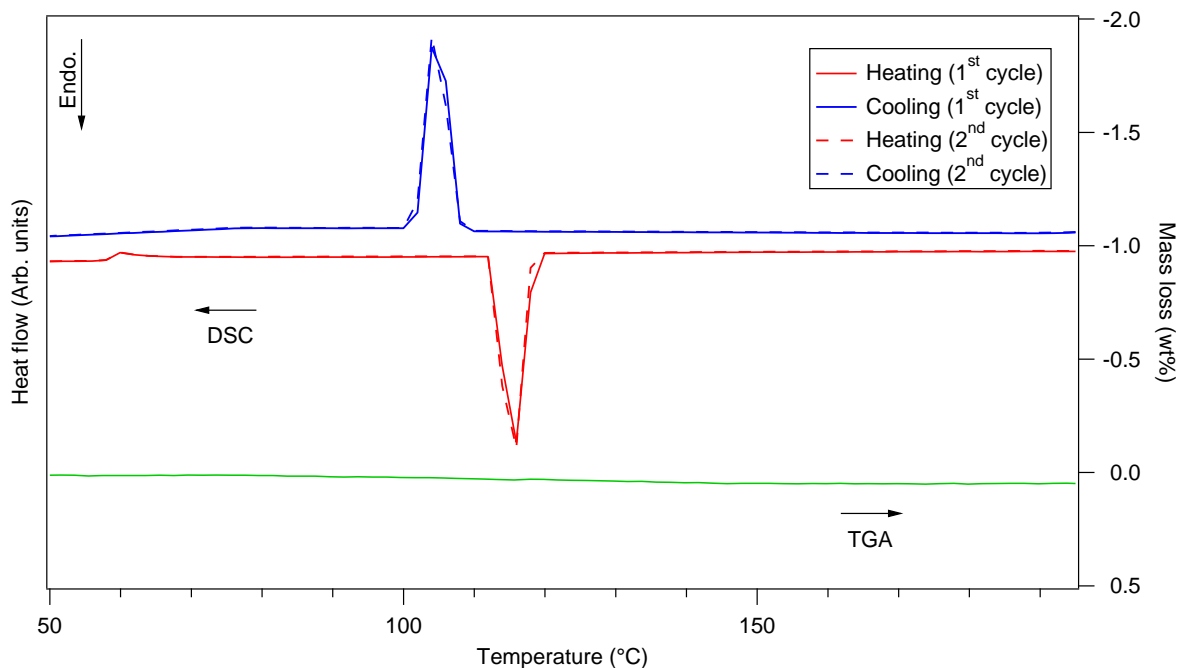
Figure 4.6 DSC-TGA traces of the as-received LiBH$_4$ heated up to 200 °C (and subsequently cooled) under flowing Ar at a heating rate of 2 °C/min.

4.2   Thermal decomposition of LiBH$_4$

The gaseous thermal desorption products from pure LiBH$_4$ were investigated using the TPD-MS system. Approximately 100 mg of LiBH$_4$ was heated at 5 °C/min from room temperature to 600 °C under 1.4 bar Ar flowing at 100 ml/min. The mass spectrometer was set to monitor B$_2$H$_6$ (*m/z* = 26) and H$_2$ (*m/z* = 2) release. **Figure 4.7** is a plot of the hydrogen and diborane evolution of the sample as a function of temperature.

No hydrogen was observed in the temperature range corresponding to the orthorhombic-hexagonal phase transition at 116 °C, which is consistent with the TGA data that no mass loss was seen. The first significant increase in hydrogen signal started at 312 °C, peaked at 325 °C and ended at around 380 °C. The major desorption was comprised of two overlapping hydrogen peaks, onset at around 480 °C to form a shoulder centred at 490 °C, then reaching its maximum at 512 °C. The hydrogen release was discontinued on further heating to 540 °C. The main dehydrogenation event occurred in a similar temperature range to that reported by Züttel *et al.* (2003a) (T$_{peak}$ = 500 °C, at a heating rate of 2 °C/min

under vacuum). However, these temperatures are higher than those given by Mauron *et al.* (2008) (T$_{peak}$ = 430 °C, at a heating rate 0.5 °C/min under flowing 1 bar H$_2$). It has been reported that the dehydrogenation route of a borohydride may be affected by: the composition of the starting materials (e.g. impurities); and/or the decomposition conditions, such as backpressure and heating rate. Both a vacuum/argon atmosphere and a slower heating rate should kinetically promote a lower dehydrogenation temperature (Hanada *et al.*, 2008; Pendolino *et al.*, 2009), whereas surface oxidation of the starting material can enhance the dehydrogenation rate (Kato *et al.*, 2010). This shows the difficulty in trying to explain differences in dehydrogenation temperature between this work and other studies.
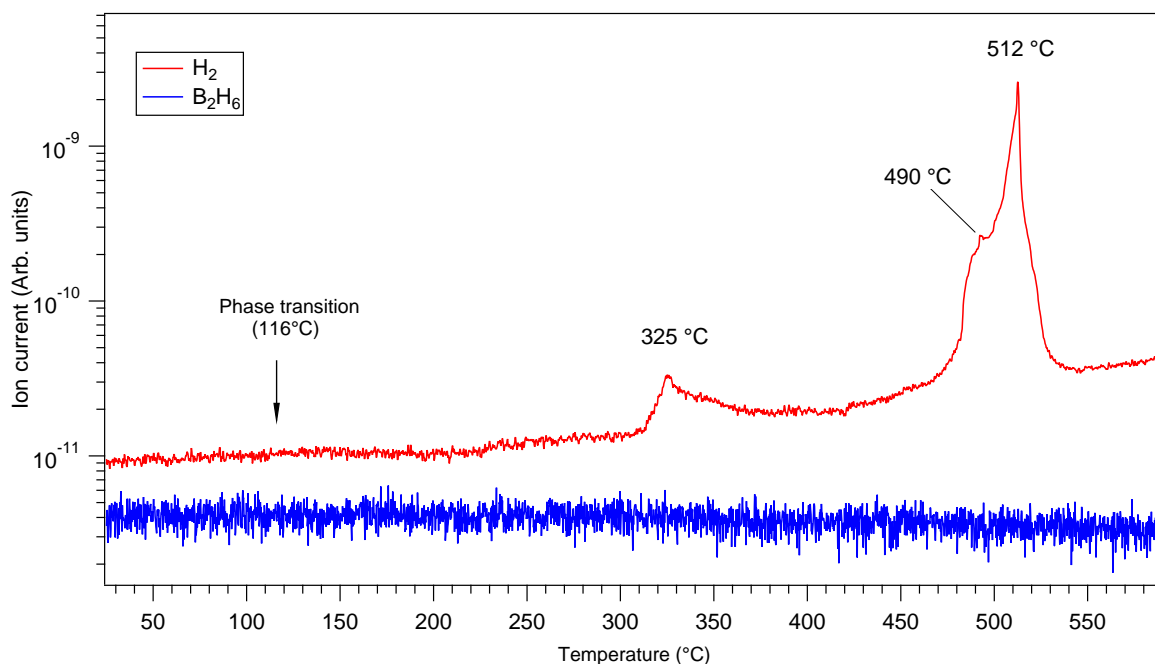
Figure 4.7 TPD-MS of LiBH$_4$ with a heating rate of 5 °C/min. The desorbed hydrogen was carried by 1.4 bar Ar flowing at 100 ml/min and measured by the MS.

No diborane release was detected throughout the TPD measurement, which is contrary to some studies that a concurrent liberation of H$_2$ and B$_2$H$_6$ is observed at 127 and 227 °C when LiBH$_4$ is heated under ultra-high vacuum (UHV) (Kato *et al.*, 2010; Liu *et al.*, 2011). This difference is possibly due to the: different location of the detection method in the system (e.g. as discussed in Chapter 3.2.3 p93, in this work the mass spectrometry is

connected to the TPD system via a heated capillary tube. It may be possible to detect B$_2$H$_6$ release with greater sensitivity if the mass spectrometer head could be situated directly above the sample); and/or the different experimental conditions used, such as backpressure, heating-rate and surface condition of sample (e.g. oxidation). A gaseous desorption study based on a combination of FTIR spectroscopy and UHV-MS, found that diborane emission depended sensitively on the reaction conditions and was kinetically driven by a UHV environment (Borgschulte *et al.*, 2011a). Nevertheless, it was also claimed by Kato *et al.* (2010), that the diborane evolution could be largely suppressed by forming a Li$_2$O layer on the surface of LiBH$_4$.

Figure 4.8 shows ex situ XRD patterns of LiBH$_4$ samples that have been heated to 400 and 550 °C in the TPD-MS system. At 400 °C, LiBH$_4$ remains as the major phase with a small amount of the impurity LiBH$_4$•H$_2$O present (about 4 mol%) with no formation of LiH seen. This indicates that the partial decomposition products were amorphous, after the first desorption stage (between 310 and 380 °C shown in the MS trace).
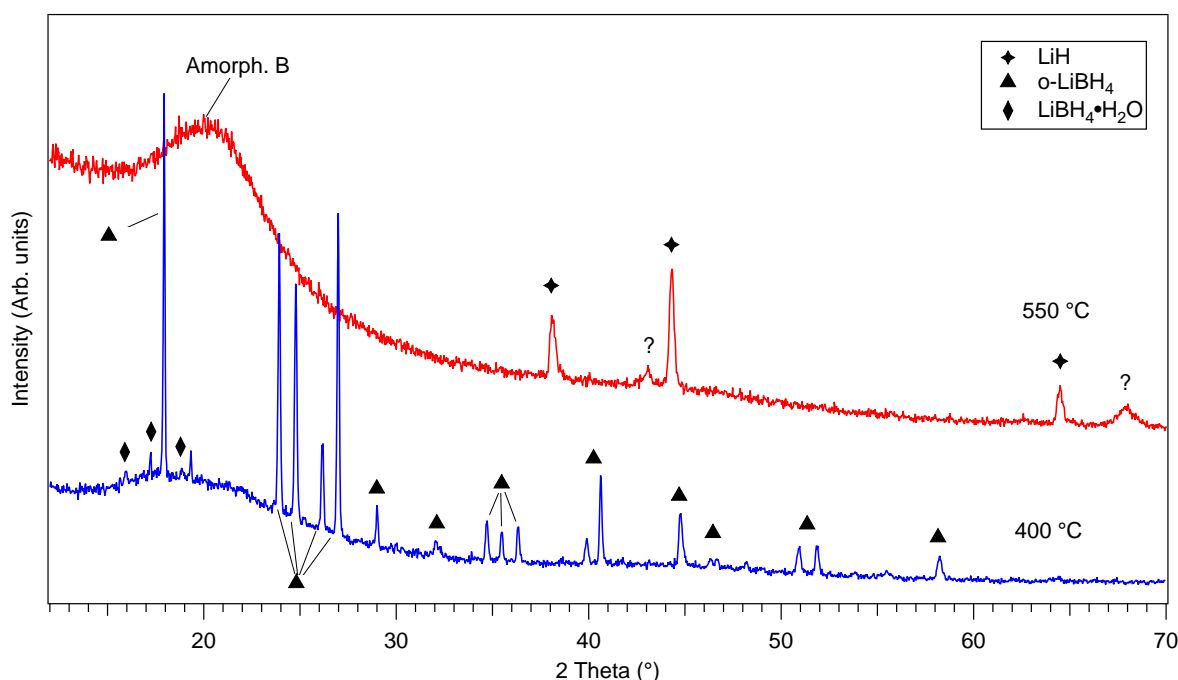
Figure 4.8 Ex situ room temperature XRD patterns of LiBH$_4$ samples that had been heated to 400 and 550 °C at 5 °C/min in a TPD-MS system under flowing Ar.

After heating to 550 °C where the major desorption was expected to be completed, the diffraction pattern of the decomposed LiBH$_4$ sample was dominated by LiH, with a broad amorphous bump centred at 20.2° 2θ (4.4 Å d-spacing). This bump was assigned as amorphous boron according to the published diffraction data (Jiang et $al.$, 2006; Pitt et $al.$, 2011). In addition, two new small reflections at 43.1° (d = 2.1 Å) and 67.9° 2θ (d = 1.4 Å) were also observed, which do not correspond to the known decomposition products of LiBH$_4$, such as Li$_2$B$_{12}$H$_{12}$ and α-B$_{1-x}$Li$_x$ (reported by Pitt et $al.$ (2013), or oxides/hydroxides contaminations (e.g. Li$_2$O).

An overview of the decomposition process of LiBH$_4$ and LiBD$_4$ through in situ Raman spectroscopy is shown in **Figure 4.9**. The measurement was performed using a 488 nm laser and heating sample from 25 to 600 °C at a ramp rate of 5 °C /min under flowing argon (100 ml/min). The spectra were collected isothermally at each selected temperature.

At room temperature, Raman peaks attributed to LiBH$_4$ were seen in a region of 1200-1400 cm^{-1} for [BH$_4$]$^-$ bending modes, and in 2200-2400 cm^{-1} for stretching modes; whereas those for LiBD$_4$ were in a region of 800-1000 cm^{-1} for bending modes, and 1500-1900 cm^{-1} for stretching modes. In addition, the LiBD$_4$ spectra exhibited some residual B-H bonding due to the presence of LiBH$_4$ as an impurity; but this should not affect the assignment of B-D Raman modes, as there was a significant shift between the vibrational frequencies for B-H and B-D bonds (see Section 4.1.2).

On heating to 200 °C, both the [BH$_4$]$^-$ and [BD$_4$]$^-$ vibrations became broader and simplier in shape, indicating an increase in symmetry of the tetrahedron structure after the orthorhombic-hexagonal phase transition, as discussed in Section 4.1. When heating the sample to 350 °C where the melting and partial decomposition began, a clear broadening and shift of Raman peaks was observed for the [BH$_4$]$^-$ anion in conjunction with a small decrease (approximately 8 cm^{-1}) in peak position to 2289 cm^{-1} for the streching mode v_1, whilst the v_1 from LiBD$_4$ persisted at 1608 cm^{-1}, giving a H/D ratio of 1.42. This might be

related to an increase in translational and reorientational freedom of the borohydride ions in the liquid state which was observed by Martelli *et al.* (2010b) using incoherent quasielastic neutron scattering.
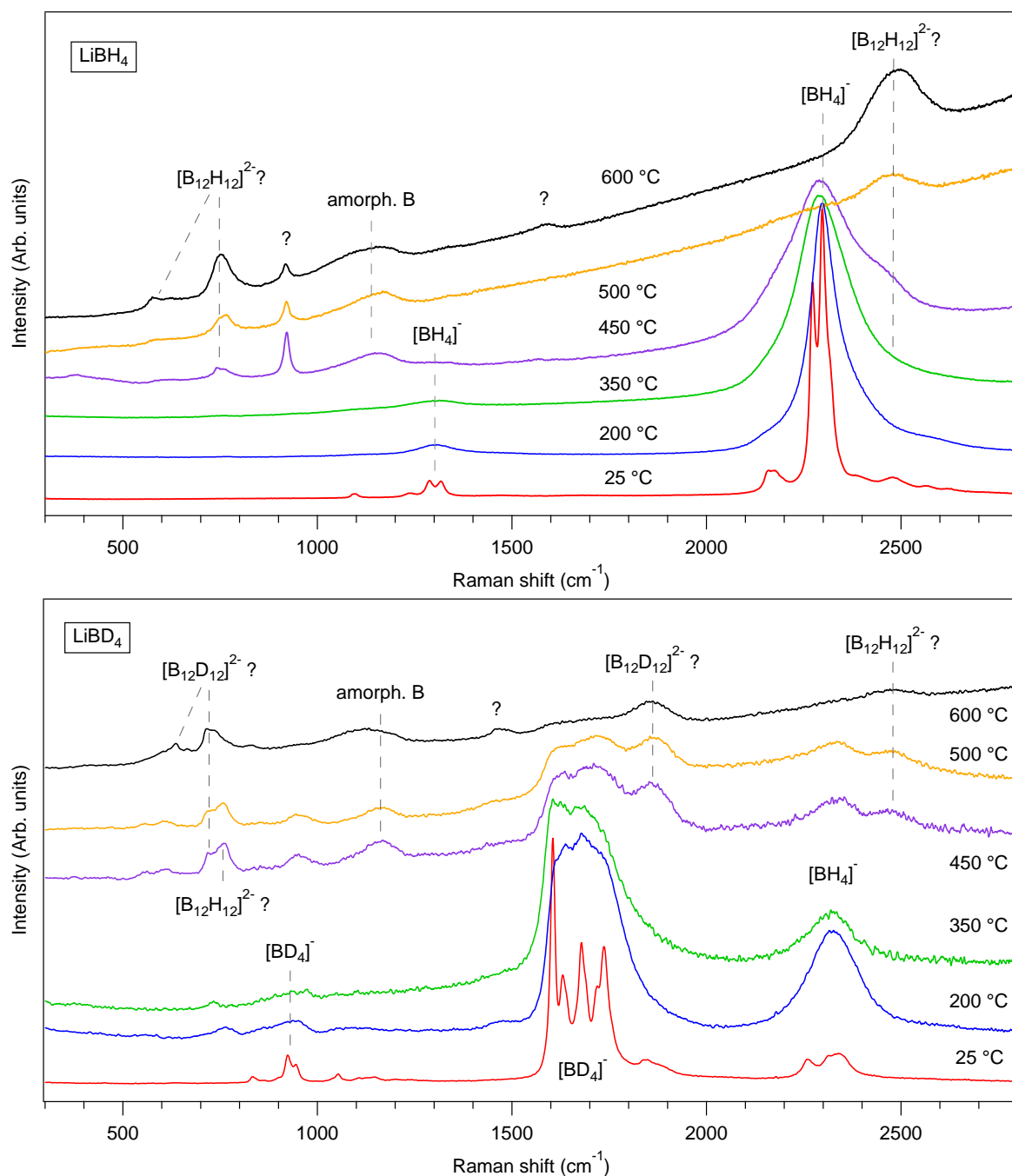
Figure 4.9 In situ Raman spectra (488 nm laser) of LiBH$_4$ (top) and LiBD$_4$ (bottom) heated at of 5 °C /min under flowing argon (100 ml/min). The intensity of all spectra were normalised in order for easy comparison, and the intensities of LiBD$_4$ spectra at 400, 500 and 600 °C were further multiplied by three times. The grey dashed lines between certain Raman peaks and the labels are guides for the eye.

With increasing temperature to 450 °C, a broad Raman peak centered at approximately 1150 cm^{-1} appeared, and no obvious shift in peak position occurred between LiBH$_4$ and LiBD$_4$ samples. Thus, this vibration did not involve H/D atoms, and is most likely associated with the B-B bonding of the amorphous boron, according to: the Raman data of Kuhlmann *et al.* (1994) who investigated the vibrations of B$_{12}$ icosahedra within amorphous boron; and also by Orimo *et al.* (2006) who assigned the α-B vibration from ex situ Raman spectra for the LiBH$_4$ after heating to 470 °C.

No peaks due to [BH$_4$]$^-$ vibrations are found in the LiBH$_4$ sample above 500 °C, even though there appear to be vibrations at similar frequencies to the [BD$_4$]$^-$ stretching modes present in the LiBD$_4$ sample. On the other hand, several new peaks appeared in both LiBH$_4$ and LiBD$_4$ between 450 and 600 °C. **Table 4.2** is a list of the positions of the new peaks collected from the spectra of the LiBH$_4$ and LiBD$_4$ samples at 500 and 600 °C, compared with the Raman peak positions assigned to [B$_{12}$H$_{12}$]$^{2-}$ by Leites *et al.* (1982).

Table 4.2 New peaks present in the Raman spectra of LiBH$_4$ and LiBD$_4$ at 500 and 600 °C respectively, in contrast to vibrational assignments of [B$_{12}$H$_{12}$]$^{2-}$ and [B$_{12}$D$_{12}$]$^{2-}$ anions in aqueous solutions by Leites *et al.* (1982). The vibration intensity was indicated by: s = strong, m = medium and w = weak.

Observed	LiBH$_4$		[B$_{12}$H$_{12}$]$^{2-}$ *	LiBD$_4$		[B$_{12}$D$_{12}$]$^{2-}$ *
	500 °C	600 °C		500 °C	600 °C	
			2517 s			1899 m
	750	754	745 s	720	726	713 s
Possible [B$_{12}$H$_{12}$]$^{2-}$	2470	2482	2470 m	1856	1858	1854 m
([B$_{12}$D$_{12}$]$^{2-}$) peaks			955 w			891 w
	765		770 m	608	627	616 s
	582	576	580 m	554		531 w
Unknown peaks	920	919 1572			1470	

* in aqueous solution at room temperature (Leites *et al.*, 1982).

Most of the new peaks appear to be associated with Li$_2$B$_{12}$H$_{12}$ (Li$_2$B$_{12}$D$_{12}$), with some degree of shift in frequencies. The shift may well be because the reference data was taken

from samples dissolved in aqueous solutions where the icosahedral anions had complete rotational freedom; whereas vibrational frequencies for a solid sample would also be affected by the cation, or other factors (e.g. temperature). The vibrational assignment of the Li$_2$B$_{12}$H$_{12}$ will be discussed in more detail in Chapter 7.2.2. The in situ observation of the Li$_2$B$_{12}$H$_{12}$ and amorphous boron as decomposition products is consistent with the ex situ room temperature Raman study by Orimo *et al.* (2006) and the DFT calculations by Ohba *et al.* (2006).

However, peaks were also observed at 919 and 1572 cm^{-1} for the LiBH$_4$ sample, in which the 919 cm^{-1} peak gradually decreased in intensity with increasing temperature from 450 to 600 °C. These new peaks could not be assigned as: LiH, or oxidation products (Harbach and Fischer, 1975; Chryssikos *et al.*, 1990; Stowe and Smyrl, 2012). Despite the Li$_2$B$_{12}$H$_{12}$ or adducts thereof were thought to be stable up to 600 °C as decomposition by-products based on ex situ Raman and NMR measurements (Yan *et al.*, 2012), a more recent study indicated that Li$_2$B$_{12}$H$_{12}$ could partially decompose to Li$_2$B$_{12}$H$_{12-x}$ via nanocrystalline γ-Li$_2$B$_{12}$H$_{12}$ between 250 and 650°C under vacuum (Pitt *et al.*, 2013). Since the structures for both γ-Li$_2$B$_{12}$H$_{12}$ and Li$_2$B$_{12}$H$_{12-x}$ have not yet been solved, the identity of the phase(s) responsible for the unknown Raman peak at 1572 cm^{-1} remains uncertain.

For the LiBD$_4$ sample, peaks at around 756 and 2470 cm^{-1} appeared at 450-500 °C, and should be associated with Li$_2$B$_{12}$H$_{12}$ from the impurity LiBH$_4$ decomposition. An unknown peak at 1470 cm^{-1} was stable at 600 °C, which might be the isotopic form of the unknown compound observed as a Raman peak at 1572 cm^{-1} from the decomposed LiBH$_4$. However, it is difficult to distinguish the nature of these unknown amorphous compounds as some of their Raman vibrations might overlap and be hidden by a high fluorescence background. The LiH (LiD), which would be expected to form, were not observed in any of these Raman spectra, as their ionic Li-H bonding did not give Raman scattering but the emission of a broad fluorescence band (Stowe and Smyrl, 2012).

4.3 General discussion and conclusion

The crystal structure and vibrational modes of LiBH$_4$ were investigated using in situ XRD, Raman spectroscopy, DSC and TGA as a function of temperature. The crystal structure of the low-temperature phase of LiBH$_4$ was confirmed to be consistent with the orthorhombic structure (space group *Pnma*) proposed by Soulié *et al.* (2002), exhibiting lattice parameters of *a* = 7.185(4) Å, *b* = 4.440(3) Å, *c* = 6.810(4) Å and *V* = 217.2(2) Å^3. During heating, the o-LiBH$_4$ underwent a phase transition to a hexagonal polymorph at 116 °C, according to a combination of results from in situ XRD and DSC measurements. At 120 °C, the hexagonal LiBH$_4$ had a relatively small unit cell with the lattice parameters of *a* = 4.274(3) Å, *c* = 6.940(5) Å, and *V* = 109.9(2) Å^3, based on the space group of *P*6$_3$*mc*. Approximately linear thermal expansion and contraction of the lattice parameters was observed throughout the heating and cooling of LiBH$_4$, respectively.

From Raman spectrocopy at -190 °C, 11 out of the 36 vibrational modes of the orthorhombic LiBH$_4$ (LiBD$_4$) could be identified, and the observed B-H stretching and bending frequencies are in a good agreement with the assignments proposed by Racu *et al.* (2008). The external modes were only partially observed due to limitations in the Raman system used. Substituting hydrogen for deuterium significantly affected the B-H bond vibrations, and resulted in frequency shifts between LiBH$_4$ and LiBD$_4$ due to the increased mass of deuterium compared to hydrogen. When going through the phase transition on heating, the local arrangement of tetrahedral [BH$_4$]$^-$ ([BD$_4$]$^-$) became more symmetrical and led to more reorientational freedom, thus inducing a dramatic broadening in the Raman line-width of the high-temperature phase. However, the in situ Raman study showed that the phase transition temperature occured at around 140 °C, which was higher than the temperature of 116 °C determined by in situ XRD and DSC results, due to a delay in transferring between the heater and the sample in the Raman sample cell.

Thermal desorption analysis of LiBH$_4$ was carried out using in situ Raman and MS spectroscopy under flowing argon, showing a multi-step decomposition process. No gaseous product was detected by TGA-MS during the phase transition, in contrast to the liberation of 0.3 wt% H$_2$ (up to 200 °C) (Züttel *et al.*, 2003a). The first desorption started at 312 °C, however it was not possible to determine the partial decomposition products, as the ex situ XRD and in situ Raman measurements only showed the presence of LiBH$_4$. No diborane evolution was observed during heating under 1 bar flowing argon, which may be because: B$_2$H$_6$ detection depends on the location of the detector within the TGA-MS system; and/or B$_2$H$_6$ evolution is sensitive to the reaction conditions such that is can be kinetically driven by a UHV environment.

The main hydrogen evolution consisted of two stages, starting at 480 °C and peaking at 512 °C with concurrent formation of LiH, amorphous boron, and amorphous B-H bond containing intermediate phases. One of these intermediates was most likely to be Li$_2$B$_{12}$H$_{12}$ and/or adducts Li$_2$B$_{12}$H$_{12-x}$, which appeared to be stable up to 600 °C based on the B-H vibrations observed in the in situ Raman spectra. However, the presence of Li$_2$B$_{12}$H$_{12}$ only partially explains these unknown Raman peaks. Further investigation into the structure and thermal stability of intermediate phases is required to assign these peaks, e.g. by using a combination of various characterisation techniques such as solid NMR, quantitative XRD and quantitative gaseous desorption measurements.

LiBH$_4$ continues to be an interesting material for hydrogen storage applications. With a better understanding of the thermal decomposition and hydrogen evolution it may be possible to "tune" a more favourable reaction pathway (e.g. control the formation of stable intermediates by adjusting the dehydrogenation conditions) and thereby lower the temperature and pressure required to achieve reversibility.

5   Mg(BH$_4$)$_2$

The structural and compositional properties of both as-received (crystalline) and ball-milled (amorphous) γ-Mg(BH$_4$)$_2$ have been investigated by in situ XRD and Raman spectroscopies, DSC and TGA-MS measurements as a function of heating, to try to identify more favourable reaction pathways for the recombination of Mg(BH$_4$)$_2$.

5.1   Structural characterization at room temperature

5.1.1   X-ray diffraction

Three different batches of Mg(BH$_4$)$_2$ (MKBB6388, 84096JM and 06496HMV) were obtained from Sigma Aldrich and had been found to contain different polymorphs. Therefore, it was necessary to first understand the nature of the starting materials. A comparison of room temperature XRD patterns of the different batches of the as-received Mg(BH$_4$)$_2$ is shown in **Figure 5.1**. The Mg(BH$_4$)$_2$ (06496HMV, May 2012) sample exhibited identical diffraction peaks to a single crystalline γ-phase with a cubic structure (space group *Ia*-3*d*) with no other phases present. The lattice parameter of γ-phase was refined to be *a* = 15.78(5) Å, which is similar to the value of *a* = 15.7575(16) Å reported by Filinchuk *et al.* (2011).

Sharp diffraction peaks and smooth background were observed for another batch of Mg(BH$_4$)$_2$ (84096JM, October 2011), suggesting an increased crystallinity of the sample. This was possibly due to the use of a different synthesis route (and/or synthesis conditions), which have affected the microstructure and/or phase content of the as-received materials. The XRD quantitative phase analysis (QPA) indicated that the sample consisted of

117

approximately 91.6 mol% γ-Mg(BH$_4$)$_2$ and 8.3 mol% α-Mg(BH$_4$)$_2$. The α-Mg(BH$_4$)$_2$ had a

hexagonal structure with lattice parameters *a* = 10.39(1) Å and *c* = 37.21(2) Å, which is

larger than the values of *a* = 10.3540(12) Å and *c* = 37.055(4) Å for the single crystal

material using synchrotron X-ray diffraction at -173 °C (Filinchuk *et al.*, 2009a).
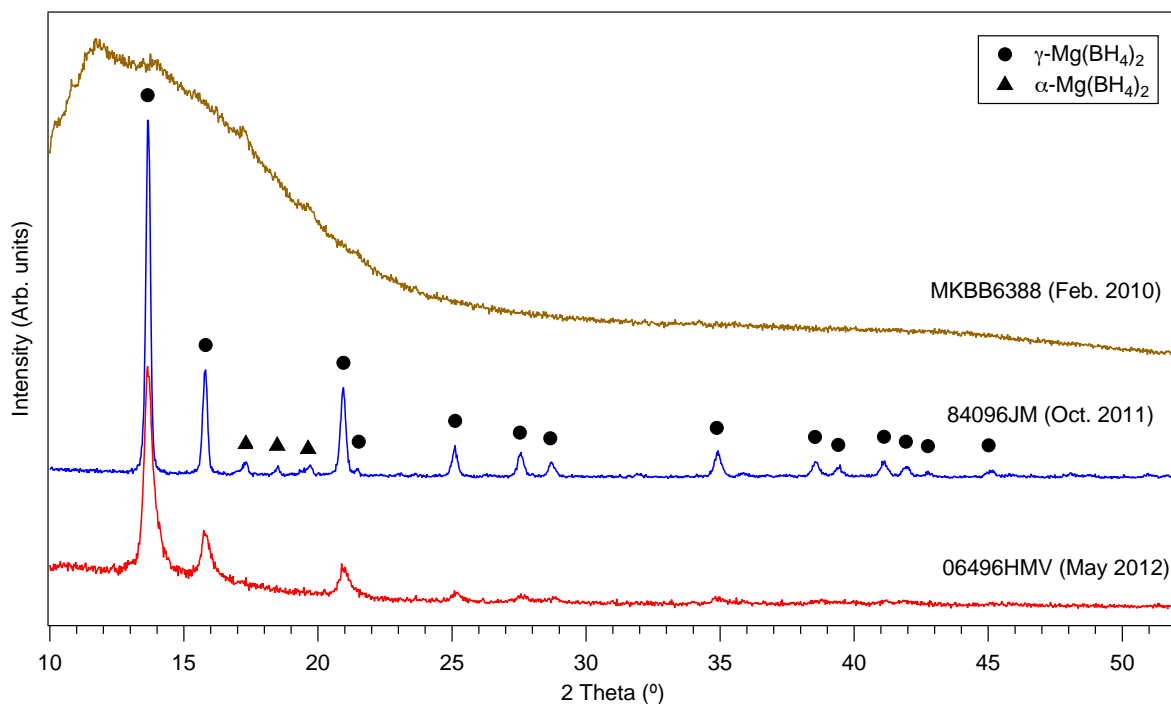
Figure 5.1 Ex situ XRD patterns of three different batches of as-received Mg(BH$_4$)$_2$ (MKBB6388, 84096JM and 06496HMV) at room temperature. The purchase date of the sample is quoted in the brackets after the batch number.

However, the sample with the batch number MKBB6388, was predominantly non-

crystalline or amorphous, showing a very broad intense background below 25° *2θ*. Several

reflections, at 11.8°, 13.9°, 17.2° and 19.6° *2θ*, are superimposed upon the noisy

background. These peaks are located at diffraction positions which are consistent with the

α-Mg(BH$_4$)$_2$ phase. Attempts to index these peaks did not succeed due to weak intensity in

a noisy background.

In order to better understand the nature of the amorphous Mg(BH$_4$)$_2$ phase, the Mg(BH$_4$)$_2$

(06496HMV, γ phase only) was milled in 100 bar H$_2$ for 2 h in an attempt to induce more

structural disorder into the sample. After milling, the intensity of the XRD reflections of γ-

Mg(BH$_4$)$_2$ was greatly reduced and a broad 'bump' centred at 17.2° *2θ* (d = 5.1 Å) was visible, relating to the amorphization of γ-Mg(BH$_4$)$_2$ (**Figure 5.2**). This amorphous 'bump' sat at a similar *d*-spacing (ca. 4.9 Å) as the amorphous-Mg(BH$_4$)$_2$ synthesised by ball-milling MgB$_2$ in H$_2$ (Pistidda *et al.*, 2010), and by ball-milling α/β-Mg(BH$_4$)$_2$ under Ar (Li *et al.*, 2007a; Bardaji *et al.*, 2011a); but was different from the diffraction bump observed for the as-received amorphous Mg(BH$_4$)$_2$ (MKBB6388), indicating different structural origins between these two batches. In addition, a small amount of Fe impurity originating from the milling media (stainless steel milling pot and balls), is present as an impurity in the milled γ-Mg(BH$_4$)$_2$ sample.
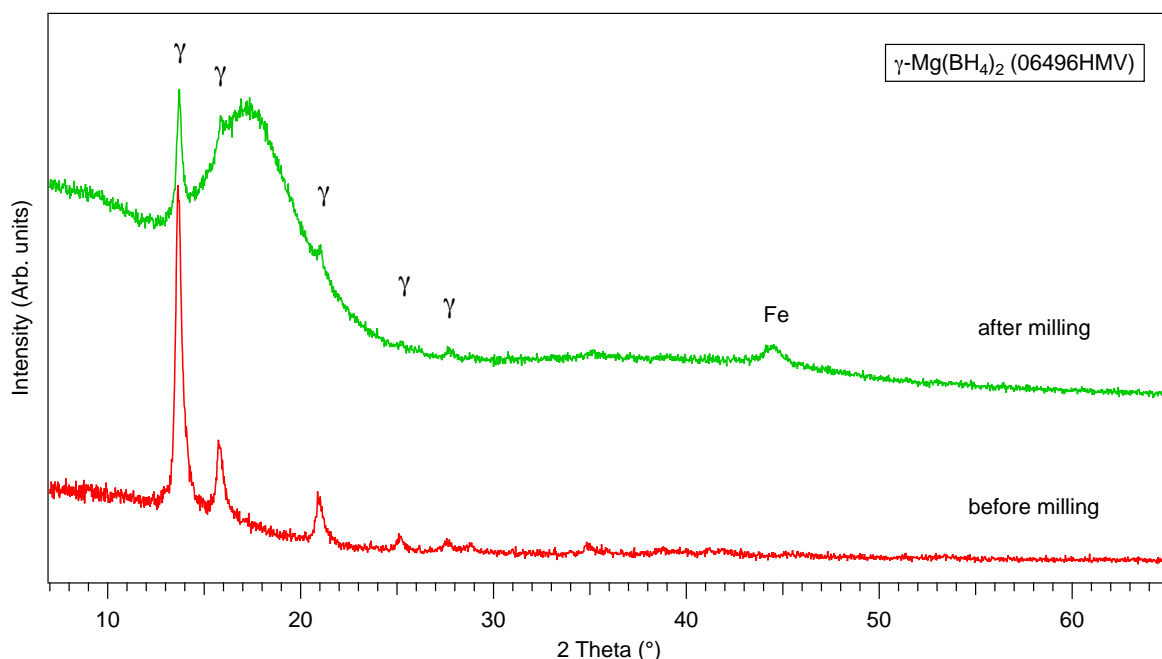
Figure 5.2 Room temperature XRD patterns of the γ-Mg(BH$_4$)$_2$ (06496HMV) as-received and after being ball-milled for 2 h in 100 bar H$_2$.

5.1.2 Vibrational spectra

The Raman and IR spectra of three different batches of Mg(BH$_4$)$_2$ and the milled γ-Mg(BH$_4$)$_2$ were compared in **Figure 5.3**. **Table 5.1** and **Table 5.2** list the Raman and IR peak positions, respectively, together with published data. The internal vibrational modes of Mg(BH$_4$)$_2$ could be divided into two main regions: [BH$_4$]$^-$ stretching modes (2200-2400 cm^{-1})

and bending modes (1100-1500 cm^{-1}), based on the published assignments by Filinchuk *et al.* (2009a) and Giannasi *et al.* (2010).
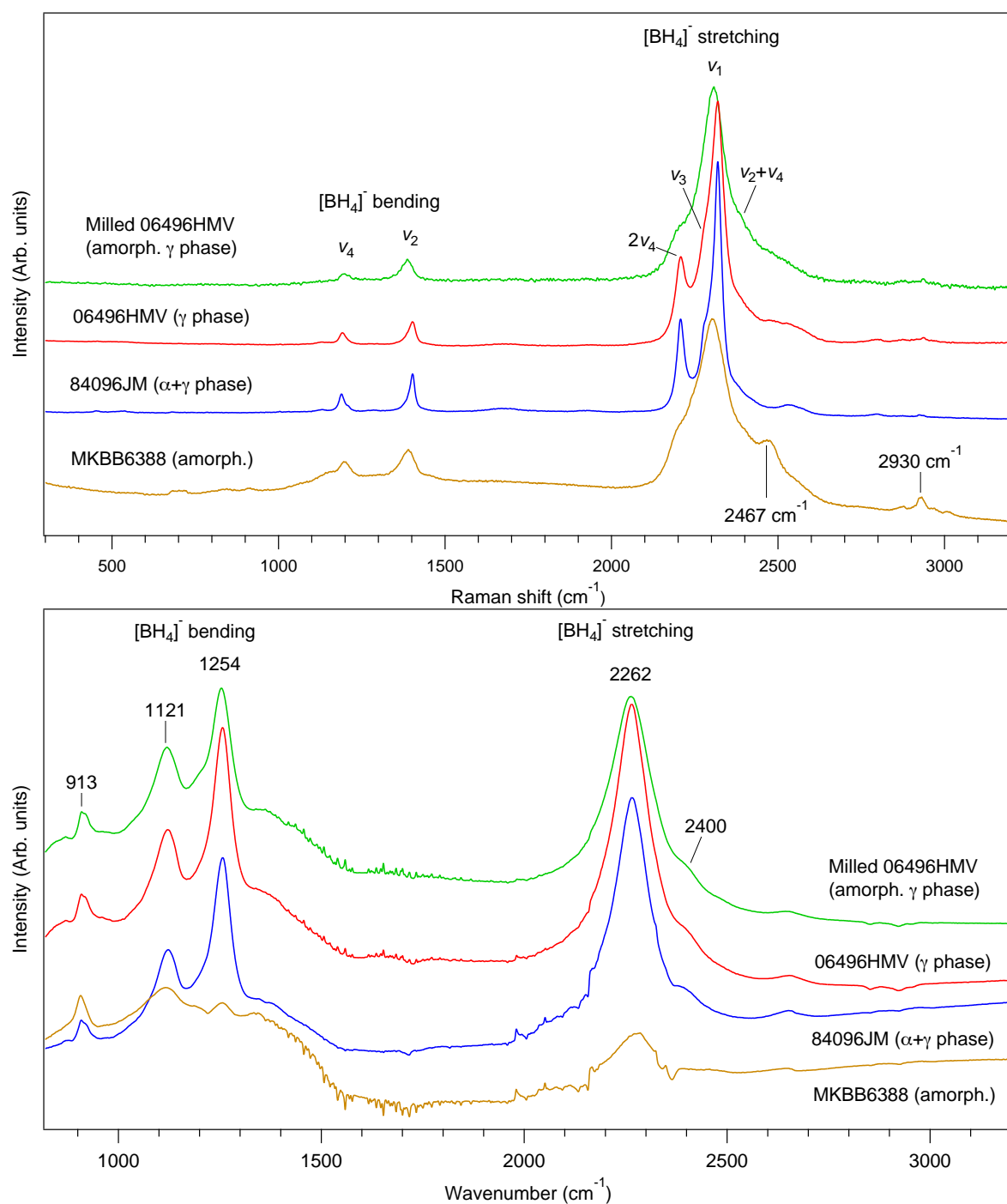
Figure 5.3 Raman (top) and IR (bottom) spectra of different batches of the as-received Mg(BH$_4$)$_2$ and the milled γ-Mg(BH$_4$)$_2$ (06496HMV) sample. The crystal structure corresponding to each sample obtained from the XRD data was quoted in the brackets after the batch number.

Table 5.1 Raman frequencies (cm^{-1}) of different batches of as-received Mg(BH$_4$)$_2$ and milled γ-Mg(BH$_4$)$_2$ (06496HMV), in comparison to the published data observed for α-Mg(BH$_4$)$_2$. The intensity of peaks was represented as: s = strong, m = medium, sh = shoulder.

	Raman (cm^{-1})				
	Milled 06496HMV (amorph. γ)	06496HMV (γ)	84096JM (α+γ)	MKBB6388 (amorph.)	α-Mg(BH$_4$)$_2$ *
v_2+v_4	2390			2392	2388	2400 w,sh
v_3						2330 sh
v_1	2305	2320	2319	2303	2305 s
v_3		2287	2284		
$2v_4$	2211	2206	2206	2219	2199 m
v_2	1386	1403	1401	1386	1395 m
v_4	1196	1193	1190	1198	1199 m

*Filinchuk *et al.* (2009a)

Table 5.2 IR frequencies (cm^{-1}) of different batches of as-received Mg(BH$_4$)$_2$ and milled γ-Mg(BH$_4$)$_2$ (06496HMV), in comparison to the published data observed for α-Mg(BH$_4$)$_2$. The intensity of peaks was represented as: s = strong, m = medium, w = weak, sh = shoulder.

IR (cm^{-1})				
Milled 06496HMV (amorph. γ)	06496HMV (γ)	84096JM (α+γ)	MKBB6388 (amorph.)	α-Mg(BH$_4$)$_2$ *
2400	2404	2399		2399 sh
2262	2265	2266	2275	2274 s
				1391 w
1254	1258		1258	1258 s
1121	1121	1120	1118	1104 m
				1032 sh
				1018 m
913	913	909	908	

* Filinchuk *et al.* (2009a)

The Raman spectra showed that the B-H stretching region of γ-Mg(BH$_4$)$_2$ was composed of the stretching symmetric v_1 and asymmetric v_3 modes, accompanied by the combination mode v_2+v_4 and the overtone mode $2v_4$. Compared to the vibrational assignment for α-Mg(BH$_4$)$_2$, the v_1 from γ phase was slightly shifted to a higher frequency at 2320 cm^{-1}, and the v_3 was shown as a shoulder only at 2287 cm^{-1}. The v_3 mode observed at 2330 cm^{-1} for the α phase, however, could not be identified for the γ phase. As for the bending region,

there was a maximum of only 8 cm^{-1} shift in peak positions between the γ and α phases. The high frequency of the symmetrical BH$_2$ bending mode v_2 at 1403 cm^{-1} was attributed to a bidentate bonding between [BH$_4$]$^-$ and Mg^{2+} ions, i.e. the movement of BH$_2$ bending directed towards the Mg^{2+} ions within deformed Mg-H$_2$BH$_2$-Mg fragments (Marks and Kolb, 1977; Filinchuk *et al.*, 2009a).

The IR spectra of the different Mg(BH$_4$)$_2$ samples only exhibit small shifts in wavenumber between the different polymorphs. The most intense stretching mode for the γ phase located at 2265 cm^{-1}, which was slightly reduced compared to that for the α phase at 2274 cm^{-1}. However, the bending modes at 1032 and 1018 cm^{-1} reported for the α phase (Filinchuk *et al.*, 2009a) was not observed in this work. The small spikes between 1400-1850 cm^{-1} and 1900-2200 cm^{-1} were due to H$_2$O and CO$_2$ respectively from the atmosphere. The origin of the peak at around 913 cm^{-1} is not clear.

There was very little difference in Raman and IR frequencies between the mixed α+γ phases sample (84096JM) and the pure γ-Mg(BH$_4$)$_2$ (06496HMV). The amorphous batch (MKBB6388), had vibrational frequencies very similar to the α-phase, suggesting that this batch might be the amorphous α-Mg(BH$_4$)$_2$ based material. However, peaks at 2467 and 2930 cm^{-1} were later confirmed as oxygen contamination, by comparing Raman spectra of a 06496HMV sample that was exposed to air. Therefore, this batch was not be further used in the thermal property study.

After ball milling of the γ-Mg(BH$_4$)$_2$, a slight shift and broadening were observed in the spectrum for the [BH$_4$]$^-$ anions. The v_1 at 2320 cm^{-1} was shifted to 2306 cm^{-1} which was at a similar frequency to that of the α-phase reported by Filinchuk *et al.* (2009a). The HWHM (half-width at half maximum) of the v_1 also broadened from 40 to 81 cm^{-1}. The v_4 at 1192 cm^{-1} and v_2 at 1401 cm^{-1} were shifted to 1197 and 1386 cm^{-1}, respectively, while the v_2 was also broadened from 15 to 28 cm^{-1}. Thus, ball milling induced an increase in defects and molecular disordering, and probably led to a transformation to α-phase based [BH$_4$]$^-$

arrangement in the local structure, giving a mixture of amorphous-Mg(BH$_4$)$_2$ and remnant crystalline γ-Mg(BH$_4$)$_2$. However, the similarity of the vibrational frequencies suggests that the different crystalline and amorphous Mg(BH$_4$)$_2$ polymorphs are very similar at a local level, despite the differences in long-range order.

5.2 Thermal decomposition

5.2.1 In situ XRD

The crystalline decomposition products of different Mg(BH$_4$)$_2$ polymorphs was investigated by in situ X-ray powder diffraction at variable temperatures. The samples were loaded into alumina or boron nitride sample crucibles and heated at 12 °C/min from 30 °C to 500 °C under ~2 bar helium flowing at 100 ml/min. The diffraction data in the range 10° to 65° 2θ (step size 0.03°) was collected isothermally at 25 °C intervals, with a data collection time of around 25 minutes per scan. This corresponds to an average heating rate of 1 °C/min.

5.2.1.1 γ-Mg(BH$_4$)$_2$

Figure 5.4 shows surface plots of in situ XRD patterns of crystalline γ-Mg(BH$_4$)$_2$ (06496HMV) during heating. At room temperature, diffraction from the γ-Mg(BH$_4$)$_2$ and the BN sample crucible were present in the pattern for the single-phase sample (06496HMV). With increasing temperature, the γ-phase transformed to a mixture of ε+β' phases at 175 °C, of which the ε-phase was metastable and strongly faded in intensity leaving single β'-phase at 225 °C. Due to the relatively low resolution of the lab-based in situ XRD, only three peaks at 18.0°, 19.7° and 21.9° 2θ originating from the ε-Mg(BH$_4$)$_2$ phase were observed; as a result, it was not possible to accurately index a structural solution. The β' phase had lattice parameters of a = 37.98(16) Å, b = 18.85(8) Å, c = 10.99(4) Å and V = 7865(57) Å^3, showing a similar but more disordered structure to the orthorhombic β-Mg(BH$_4$)$_2$ (space group Fddd) (Filinchuk et $al.$, 2009a). The observation of the ε and β'

phases was consistent with results reported by David *et al.* (2012) and Paskevicius *et al.* (2012) for γ-Mg(BH$_4$)$_2$.
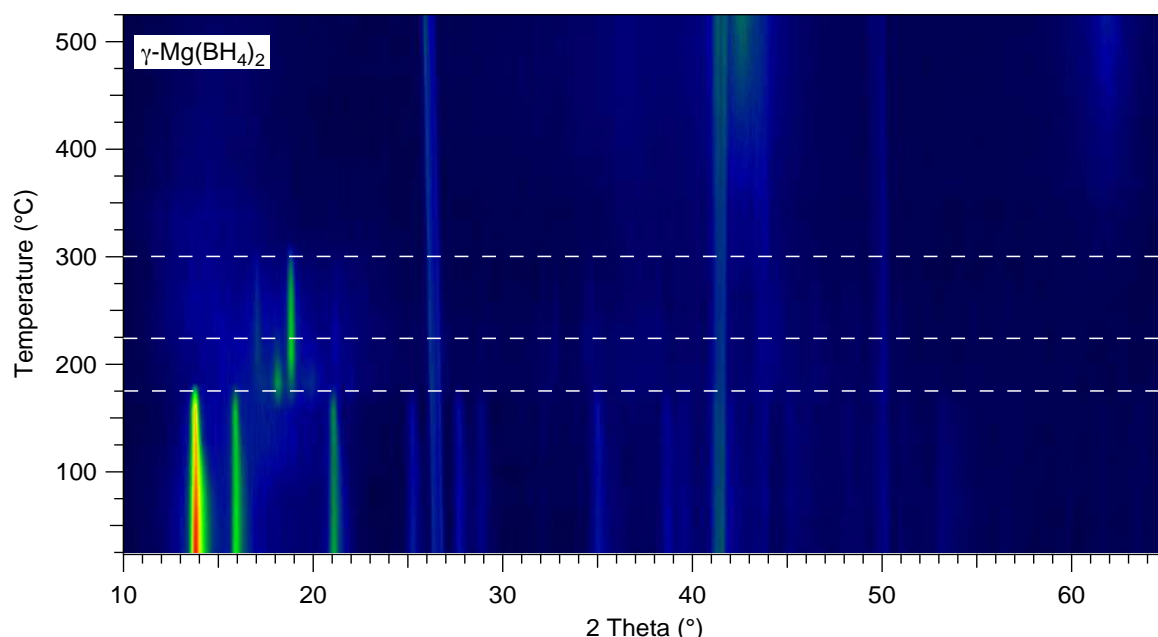
Figure 5.4 In situ XRD patterns of the crystalline γ-Mg(BH$_4$)$_2$ (06496HMV) heated under He (100 ml/min, ~2 bar) between 30 and 500 °C. A brighter colour corresponds to a higher diffraction intensity. The white dashed lines are given as a guide of the phase transition temperature for the eyes.

Figure 5.5 shows zoomed regions of the in situ XRD patterns on heating from 200 to 600 °C. A broad diffraction halo centred at around 17.4° 2θ (d = 5.1 Å) was seen at 200 °C, which might be due to overlapped diffractions from disordered β' and ε-Mg(BH$_4$)$_2$ phases. Diffractions from the β'-Mg(BH$_4$)$_2$ phase started to decrease from 250 °C and completely disappeared at 300 °C; this coincided with the appearance of two weak diffraction peaks at 42.7° and 61.9° 2θ due to MgO. The formation of MgO was believed to be a result of a reaction between Mg (formed during decomposition) and air in the experiment setup.
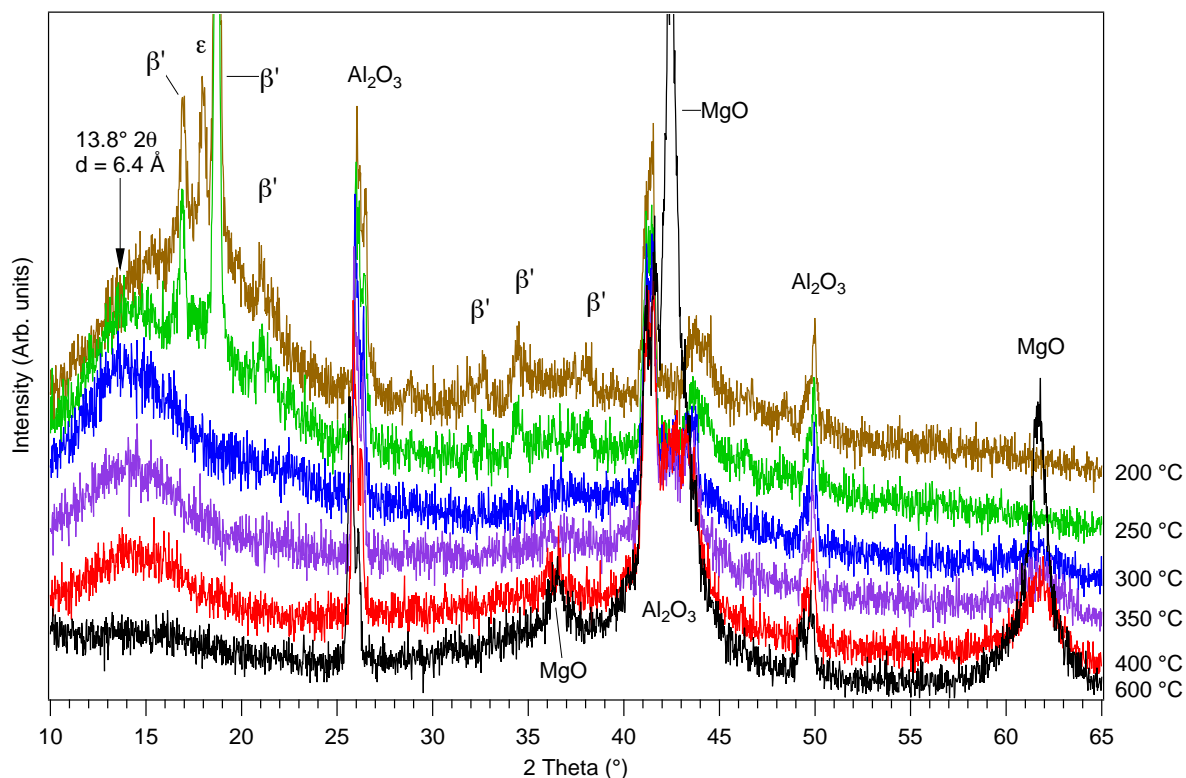
Figure 5.5 In situ XRD data highlighting changes in the low 2*θ* background during heating the crystalline γ-Mg(BH$_4$)$_2$ (06496HMV) under He (100 ml/min, ~2 bar) between 30 and 500 °C from 200 to 600 °C. The Al$_2$O$_3$ phase came from the sample holder.

Moreover, the diffraction halo at 17.4° 2*θ* (d = 5.1 Å) shifted to 13.8° 2*θ* (d = 6.4 Å) above 250 °C, and then gradually decreased in intensity. Paskevicius *et al.* (2012) claimed that the halo at *d* = 5.1 Å is due to a short-lived ionic melting of Mg(BH$_4$)$_2$, and that this is supported by a series of photographs of the melting sequence of γ-Mg(BH$_4$)$_2$. They also observed a similar halo shift (from d = 5.1 Å to > 6.3 Å) associated with a gradual decomposition process: unknown Mg-B-H phase(s) changing from an average composition of MgB$_2$H$_{5.3}$ at 325 °C, to MgB$_{2.9}$H$_{3.2}$ at 350 °C, and to MgB$_{4.0}$H$_{3.7}$ at 450 °C.

MgH$_2$ which was proposed to appear between 325 and 360 °C and decompose into Mg at 410 °C (Hanada *et al.*, 2008; Soloveichik *et al.*, 2009; Paskevicius *et al.*, 2012), was not observed in this work. This was possibly because that the Mg reacted with air to form MgO rather than with H$_2$ to form MgH$_2$. At 500 °C, Mg was observed as a small reflection at 36.2° 2*θ*, and was subsequently replaced by MgO.

5.2.1.2 α+γ-Mg(BH₄)₂

As for the sample starting with the α+γ-Mg(BH$_4$)$_2$ polymorphs (84096JM), the in situ XRD plots (**Figure 5.6**) showed that the γ phase firstly transformed to the ε+β' phases at 175 °C, while the α phase remained stable until 200 °C. The proportion of the ε phase largely reduced at 200 °C, leaving single β' phase between 225 and 300 °C. A small amount of MgO (represented by weak peak at 42.5° 2θ) started to form from 300 °C and rapidly increases in intensity above 400 °C with concurrent formation of a small amount of Mg at ~36.2° 2θ. The Mg and MgO phases were stable up to 500 °C. No diffraction peaks corresponding to MgH$_2$ or MgB$_2$ were observed during heating. Therefore, the overall decomposition process of this mixed phases sample, appeared to be the same as for the single-phase γ-Mg(BH$_4$)$_2$ sample.
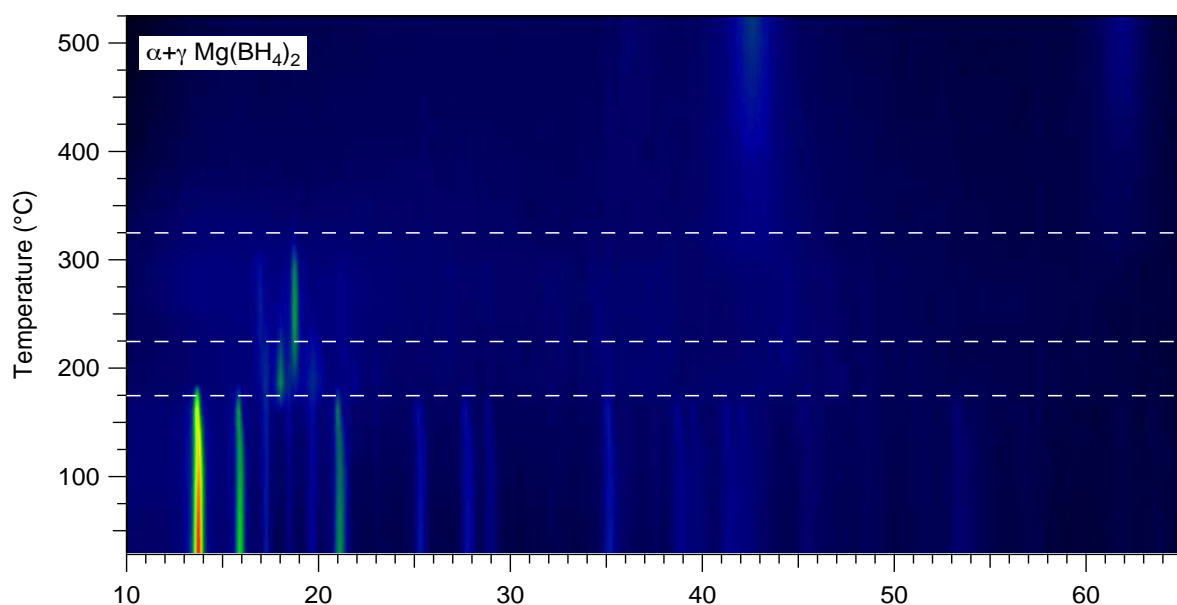
Figure 5.6 In situ XRD patterns of the crystalline α+γ-Mg(BH$_4$)$_2$ (84096JM) heated under He (100 ml/min, ~2 bar) between 30 and 500 °C. A brighter colour corresponds to a higher diffraction intensity. The white dashed lines are given as a guide of the phase transition temperature for the eyes.

5.2.1.3 Milled γ-Mg(BH$_4$)$_2$

For the γ-Mg(BH$_4$)$_2$ sample (06496HMV) that had been ball-milled for 2 h in 100 bar H$_2$, **Figure 5.7** showed that the amorphous Mg(BH$_4$)$_2$ was stable up to 125 °C. Recrystallization of the metastable ε-phase occurred at 150 °C, with the concurrent formation of a broad 'bump' (denoted here as unknown phase I) centered at around 18.5° 2θ (d = 4.8 Å). **Figure 5.8** shows zoomed regions of the in situ XRD patterns on heating from 200 to 600 °C. It was difficult to determine whether the unknown phase I was due to the formation of α, β or β' polymorphs and/or other amorphous compounds, as their diffraction peaks may be overlapping.
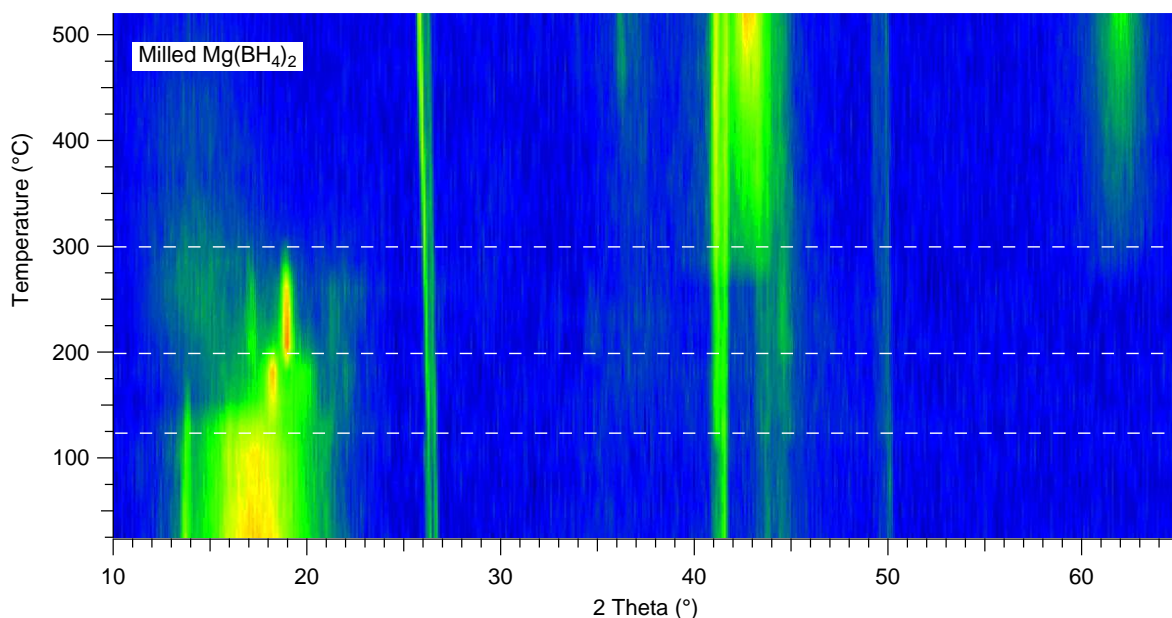
Figure 5.7 In situ XRD patterns of γ-Mg(BH$_4$)$_2$ (06496HMV) that had been ball-milled (for 2 h in 100 bar H$_2$), heated under He (100 ml/min, ~2 bar) between 30 and 500 °C. A brighter colour corresponds to a higher diffraction intensity. The white dashed lines are given as a guide of the phase transition temperature for the eyes.
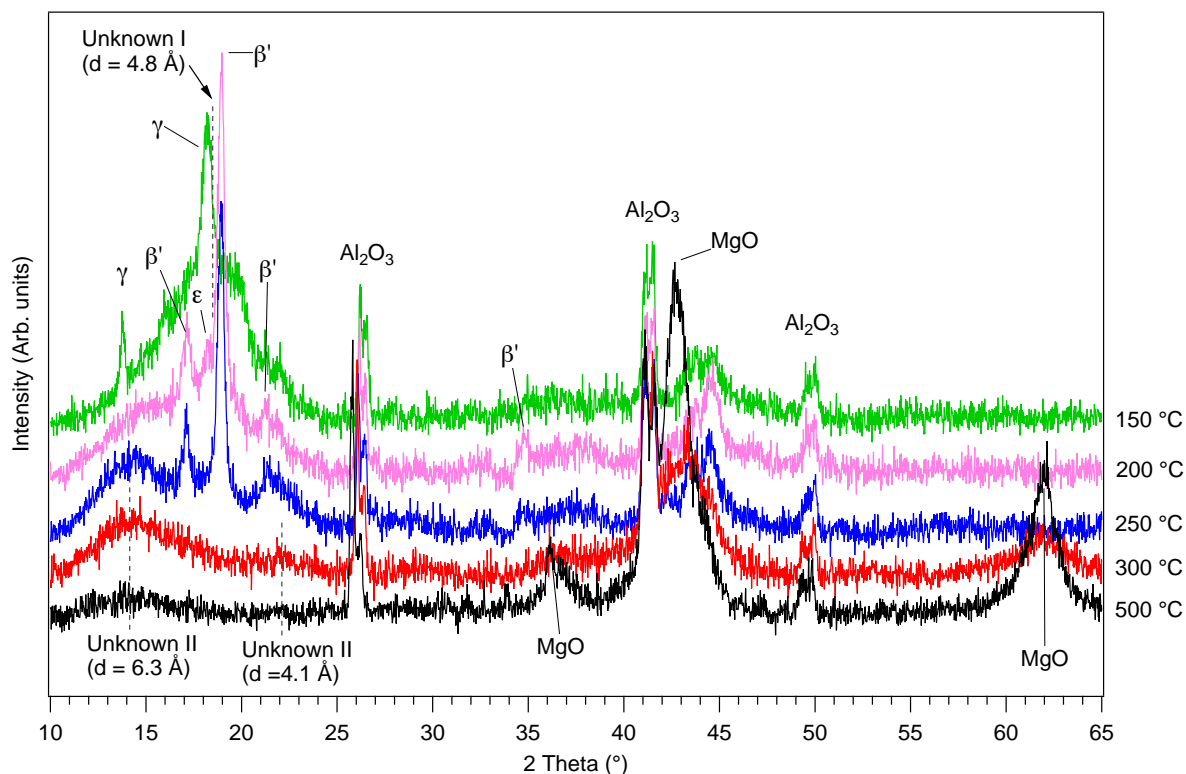
Figure 5.8 In situ XRD data highlighting changes in the low 2θ background during heating the milled γ-Mg(BH$_4$)$_2$ (06496HMV) under He (100 ml/min, ~2 bar) between from 150 to 500 °C.

The remaining γ-phase transformed to ε-phase between 150 and 175 °C, and subsequently to β'-Mg(BH$_4$)$_2$ at 200 °C. Two newly formed broad bumps centred at about 14.1° 2θ (d = 6.3 Å) and 21.7° 2θ (d = 4.1 Å) could also be distinguished, assigned as unknown phase II. This might be associated with the formation of the amorphous Mg-B-H compounds from the partially decomposed Mg(BH$_4$)$_2$. Both ε-Mg(BH$_4$)$_2$ and unknown phase I disappeared at 225 °C, leaving β'-Mg(BH$_4$)$_2$ and unknown phase II.

On heating to 275 °C, the intensity of reflections for the β' phase shrank rapidly and small diffractions from a very small amount of MgO appeared. The diffractions from β'-Mg(BH$_4$)$_2$ dissappeared at 300 °C, which might be due to decomposition and/or a molten transition. The diffraction peaks of unknown phase II were largely reduced at 325 °C, and became too weak to be observed above 450 °C. The MgH$_2$ which would be expected to form between 325 and 360 °C, was still absent. With increasing temperature to 425 °C, Mg was seen as a small reflection at 36.2° 2θ, and was subsequently replaced by MgO.

MgB$_2$ was not detected by in situ XRD measurements due to oxidation of Mg on the surface of the sample. **Figure 5.9** shows the ex situ XRD pattern of a milled γ-Mg(BH$_4$)$_2$ sample that had been heated to 600 °C in the in situ XRD cell and which was then ground in a mortar and pestle (inside an Ar glovebox). The phase abundances (excluding amorphous compounds) in the decomposed sample were estimated to be 62.4(5) wt% MgO, 36.1(5) wt% MgB$_2$ and 1.5(1) wt% Fe; this compares with an estimate of >98 wt% MgO for a powder sample that was collected from the top surface layer of the in situ XRD sample that had been heated to 600 °C. This confirms that MgB$_2$ was indeed formed from a reaction between Mg inside the bulk of the powder and a boron-containing decomposition product.
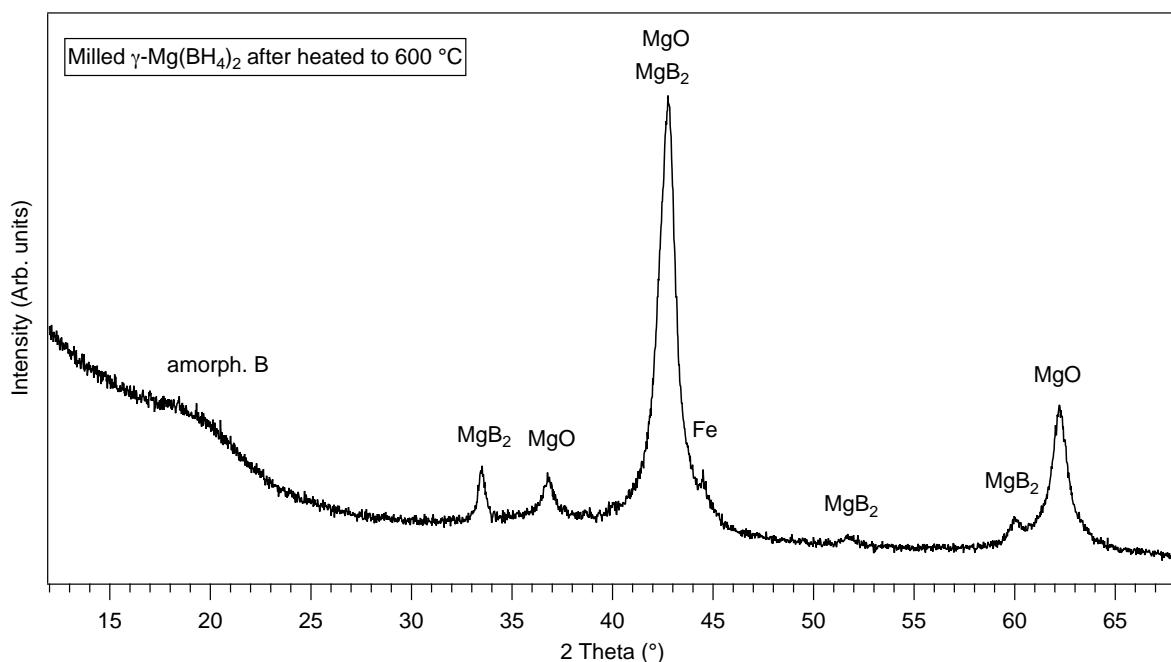
Figure 5.9 Ex situ room temperature XRD pattern of milled γ-Mg(BH$_4$)$_2$ after it had been heated to 600 °C in the in situ XRD cell (shown in **Figure 5.7**) and then ground under Ar in a pestle and mortar.

A broad 'bump' at ~20° 2θ (d = 4.4 Å), was consistent with the bump attributed to the amorphous boron from the decomposed LiBH$_4$ sample (see Figure 4.8, p113). Therefore, by using the in situ XRD cell, oxidation appears to have prevented some of the Mg from forming either MgH$_2$ or MgB$_2$, leading to amorphous B as a decomposition product.

5.2.2   In situ Raman spectroscopy

Temperature-dependent Raman measurements were performed using a 488 nm laser. The sample was placed into an Al crucible (inside an Ar glovebox) and heated at 2 °C/min under ~1 bar Ar flowing at 100 ml/min. The spectra were collected isothermally every 25 °C with a collection time of around 10 minutes per scan. Spectra were only selected for inclusion in figures when a phase transformation occurred or a significant vibrational change was observed.

5.2.2.1 γ-Mg(BH$_4$)$_2$

In situ Raman spectra of the crystalline γ-Mg(BH$_4$)$_2$ (06496HMV) during heating is presented in **Figure 5.10**; variations in Raman peak positions and widths of Raman shift of the [BH$_4$]$^-$ stretching mode v_1 (2320 cm^{-1}) are shown as red symbols in **Figure 5.11**. When the sample went through the transitions from γ to ε- and minor β- phases, no significant change in the [BH$_4$]$^-$ internal vibrations was observed. However, a slight shift to a lower frequency in peak position (e.g. ~4 cm^{-1} for v_1) occurred on heating to 200 °C, which was with concurrent thermal broadening. This suggested that the γ and ε-Mg(BH$_4$)$_2$ phases have very similar local [BH$_4$]$^-$ anion configurations.

At 225 °C where the sample contained only β'-phase, the v_1 mode rapidly decreased in frequency by about 15 cm^{-1}, with significantly broadening from 34 cm^{-1} to 62 cm^{-1} (HWHM, half width at half maximum). This might be related to a faster reorientational motion in the β'-phase which could result in an abrupt jump in the line width (Gomes *et al.*, 2002; Eagles *et al.*, 2012). Between 275 and 325 °C, the v_4 mode at ~1193 cm^{-1} became very weak leaving the v_2 mode at 1403 cm^{-1} in the [BH$_4$]$^-$ bending region, while the stretching vibrations exhibited a broad feature with reduced intensity. This could be explained by the partial decomposition and possible ionic molten state of the sample that was proposed by Paskevicius *et al.* (2012).

As the temperature increased to 400 °C, the [BH$_4$]$^-$ stretching modes were replaced by a broad bump centred at 2311 cm^{-1} with shoulders between 2150 and 2700 cm^{-1}. These new peaks are consistent with the characteristic Raman modes of the BH stretching from a number of [B$_x$H$_y$]$^{n-}$ species, e.g. [B$_3$H$_8$]$^-$, [B$_{10}$H$_{10}$]$^{2-}$ and [B$_{12}$H$_{12}$]$^{2-}$ (Tomkinson *et al.*, 1979; Leites, 1992), suggesting the presence of Mg-B-H compound(s). However, it was difficult to distinguish the nature of these compounds, as their Raman vibrations overlapped and were hidden by a relatively high fluorescent background. No Raman peak could be distinguished from the spectrum at 500 °C due to increased fluorescence.
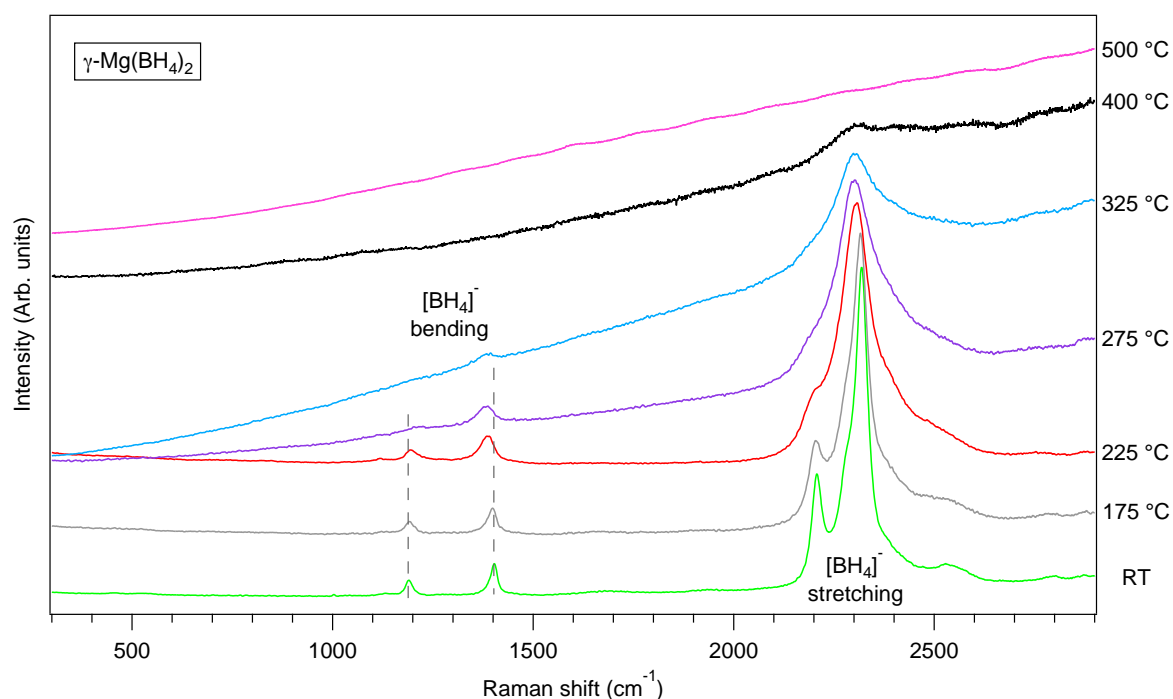
Figure 5.10 Raman spectra of the crystalline γ-Mg(BH$_4$)$_2$ (06496HMV) collected between room temperature and 500 °C. The intensity of all spectra were normalised in order for easy comparison, and the intensities of the spectra at 400 and 500 °C were multiplied by three times. Grey dashed lines between Raman peaks has been added as guides for the eye.
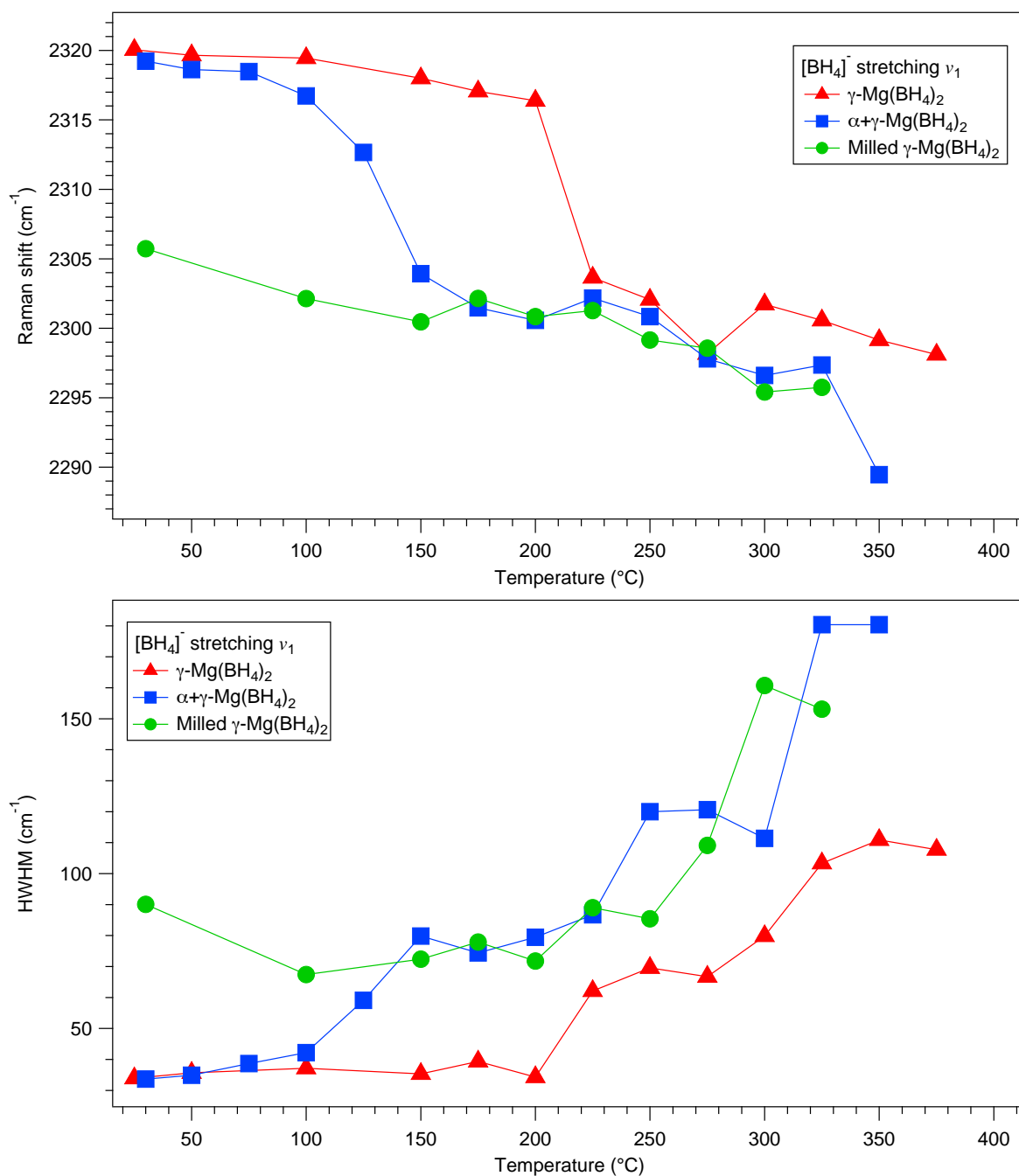
Figure 5.11 Variations of peak positions (top) and HWHM (half width at half maximum) (bottom, of Raman shift of the [BH$_4$]$^-$ stretching mode ν_1 of the crystalline γ-Mg(BH$_4$)$_2$, α+γ-Mg(BH$_4$)$_2$ and the milled γ-Mg(BH$_4$)$_2$ during heating. The trendline between symbols was a guide for eyes.

5.2.2.2 α+γ-Mg(BH$_4$)$_2$

For the crystalline α+γ-Mg(BH$_4$)$_2$ sample (84096JM), **Figure 5.12** shows that the [BH$_4$]$^-$

vibrations broaden and shift to lower frequencies from 125 °C: this is at a lower

temperature than that seen for the pure γ-Mg(BH₄)₂ sample. A new peak was found to form

at around 2473 cm^{-1} in the spectrum at 175 °C, and its origin is not clear.
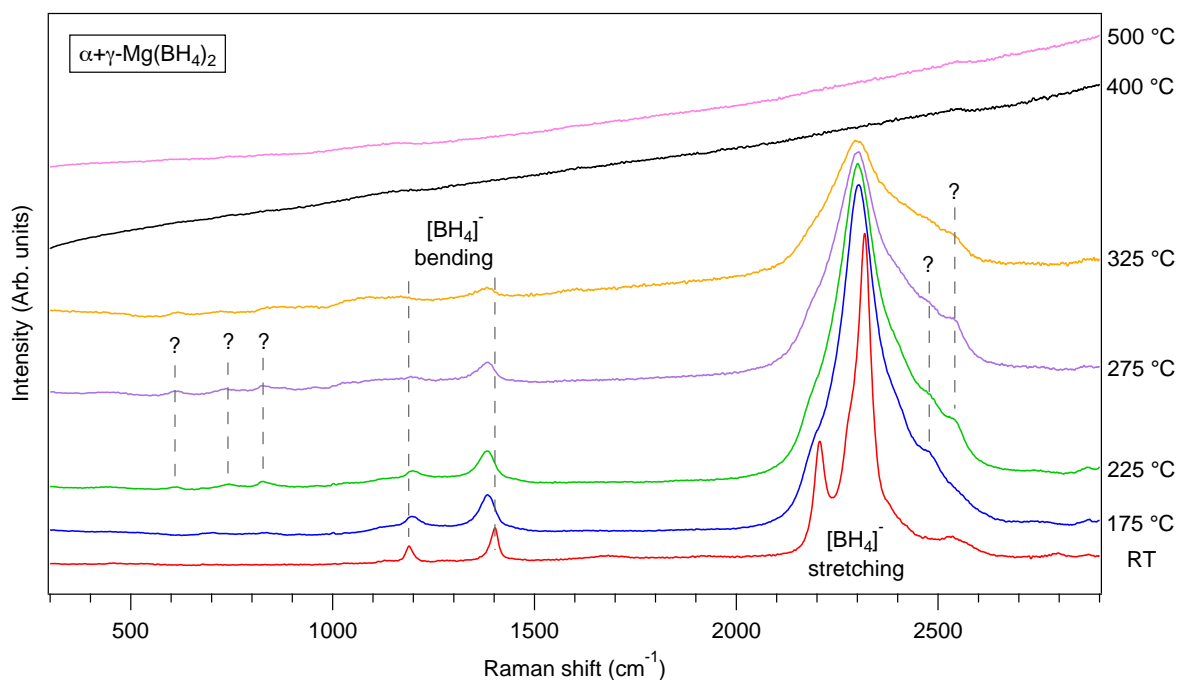
Figure 5.12 Raman spectra of the crystalline α+γ-Mg(BH₄)₂ collected between room temperature and 500 °C. The intensity of all spectra were normalised in order for easy comparison, and the intensities of the spectra at 400 and 500 °C were multiplied by three times. Grey dashed lines between Raman peaks have been added as guides for the eye.

Increasing temperature to 225-325 °C, a number of new peaks appeared at 609, 741, 827

and 2541 cm^{-1}; these are close to the wavenumbers of 620, 747, 838 and 2524 cm^{-1} for

solid K₂B₁₀H₁₀ (the vibrational assignment of K₂B₁₀H₁₀ will be discussed in detail in Section

7.1, Chapter 7). However, less-intense Raman active peaks (e.g. at 2495, 2460 and 1013

cm^{-1}) assigned for the K₂B₁₀H₁₀ were not seen in heated α+γ-Mg(BH₄)₂ samples, which

were possibly hidden by intense peaks from other compounds, such as the remnant [BH₄]$^{-}$

ions, in a strong fluorescence background. The formation of [B₁₀H₁₀]$^{2-}$ was found in the

partial decomposed α-Mg(BH₄)₂ after heating to 300-350 °C for 6-12 h (Chong *et al.*, 2011);

and was recently reported as a result of the reaction of Mg(BH₄)₂ and B₂H₆ gas at 100-

150 °C (Remhof *et al.*, 2014). No Raman peaks could be distinguished in the spectra at

400 and 500 °C due to a strong fluorescence background, although a "bump" might be present at around 2550 cm^{-1} if the baseline correction is altered.

5.2.2.3 Milled γ-Mg(BH$_4$)$_2$

In situ Raman spectra of the γ-Mg(BH$_4$)$_2$ (06496HMV) sample that had been ball-milled (for 2 h in 100 bar H$_2$), is shown in **Figure 5.13**. When heating the sample through the recrystallization and phase transitions to ε- and β'-phases, a constant decrease in the frequency of the [BH$_4$]$^-$ stretching mode v_1 (2305 cm^{-1}) was observed between room temperature and 325 °C. Simultaneously, the peak width (HWHM) decreased by around 23 cm^{-1} up to 100 °C, followed by small increase from 100 °C (67 cm^{-1}) to 250 °C (85 cm^{-1}). An abrupt rise of approximately 50 cm^{-1} in peak width occurred at 250-300 °C. Meanwhile, the v_4 mode at 1198 cm^{-1} became too weak to be seen in the [BH$_4$]$^-$ bending region above 275 °C leaving the v_2 at 1383 cm^{-1}. These changes are likely due to a higher local symmetry of the [BH$_4$]$^-$ ions in the β' phase.
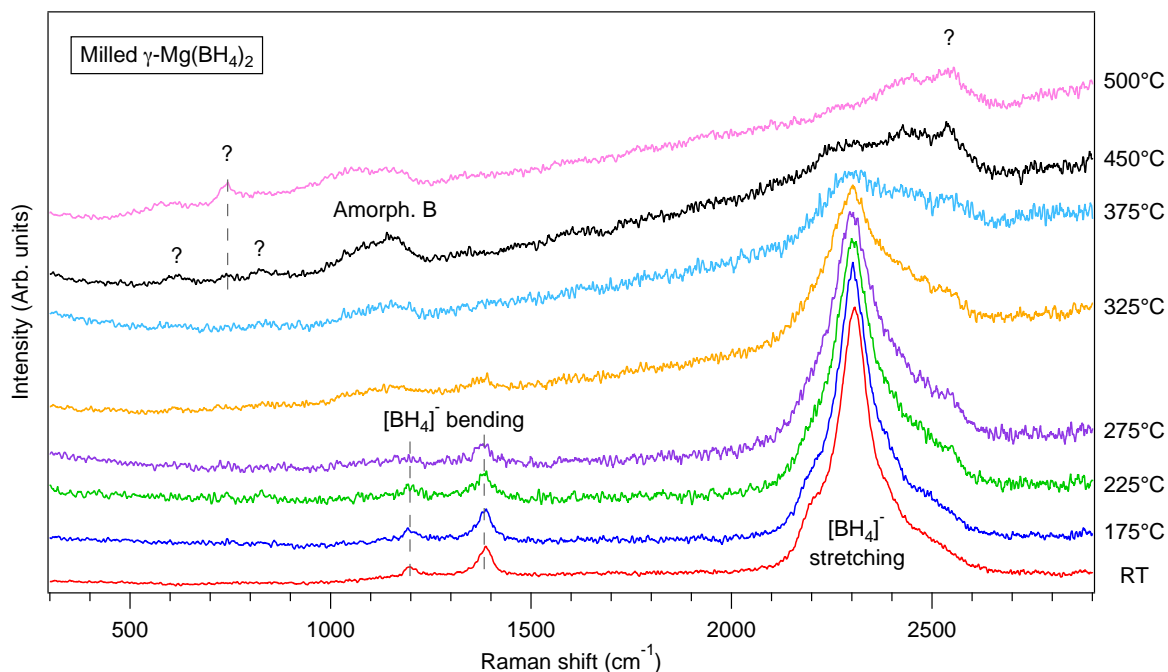
Figure 5.13 Raman spectra of the milled γ-Mg(BH$_4$)$_2$ collected up to 500 °C. The intensity of all spectra were normalised in order for easy comparison, and the intensities of spectra at 450 and 500 °C were further multiplied by three times. Grey dashed lines between Raman peaks have been added as guides for the eye.

At 325 °C, a broad hump appeared between 1000 and 1200 cm^{-1}, which was consistent with Raman vibrations for amorphous boron observed in the decomposition of LiBH$_4$ in the current (see Section 4.2) and previous studies (Orimo *et al.*, 2006; Reed and Book, 2011). Upon heating to 375 °C, several overlapped peaks forming a broad shoulder between 2200 and 2700 cm^{-1}, as well as peaks at 615, 742, 831 cm^{-1} were observed. Frequencies of these peaks were consistent with the characteristic Raman modes of the B-H bonding from the B-H stretching from some [B$_x$H$_y$]$^{n-}$ species, e.g. [B$_3$H$_8$]$^-$, [B$_{10}$H$_{10}$]$^{2-}$ and [B$_{12}$H$_{12}$]$^{2-}$, implying at least one Mg-B-H compound exists. However, it was not possible to rule out the presence of magnesium borates in the sample, as some strong B–O stretching modes might be masked by amorphous boron in the region 1000–1200 cm^{-1} (Li *et al.*, 1995). These new peaks in the Raman spectra appear in a similar temperature range to the amorphous unknown phase II in the in situ XRD measurement (**Figure 5.8**).

5.2.3   DSC-TGA-MS

The thermal properties of crystalline γ-Mg(BH$_4$)$_2$ (06496HMV), crystalline α+γ-Mg(BH$_4$)$_2$ (84096JM) and amorphous γ-Mg(BH$_4$)$_2$ (06496HMV that has been milled for 2 h in 100 bar H$_2$), were investigated by DSC and TGA-MS (mass spectrometry) measurements, as shown in **Figure 5.14**. The MS was set to monitor gaseous H$_2$ (*m/z* = 2), B$_2$H$_6$ (*m/z* = 26), dimethyl sulphide ((CH$_3$)$_2$S, *m/z* = 47) and dimethyl sulphoxide ((CH$_3$)$_2$SO, *m/z* = 63) release. All of the samples were heated at 2 °C/min under flowing Ar.

5.2.3.1 γ-Mg(BH$_4$)$_2$

The transformation of γ-Mg(BH$_4$)$_2$ to the ε- and β'- phases was shown as an endothermic peak at 168 °C with concurrent mass loss of 1.3 wt% H$_2$ up to 175 °C (**Figure 5.14** (top)). Small endothermic fluctuations with steady small increased H$_2$ slope were detected between 180 and 240 °C, which corresponds to the disappearance of the metastable ε-phase leaving single β'-phase in the X-ray diffraction patterns.
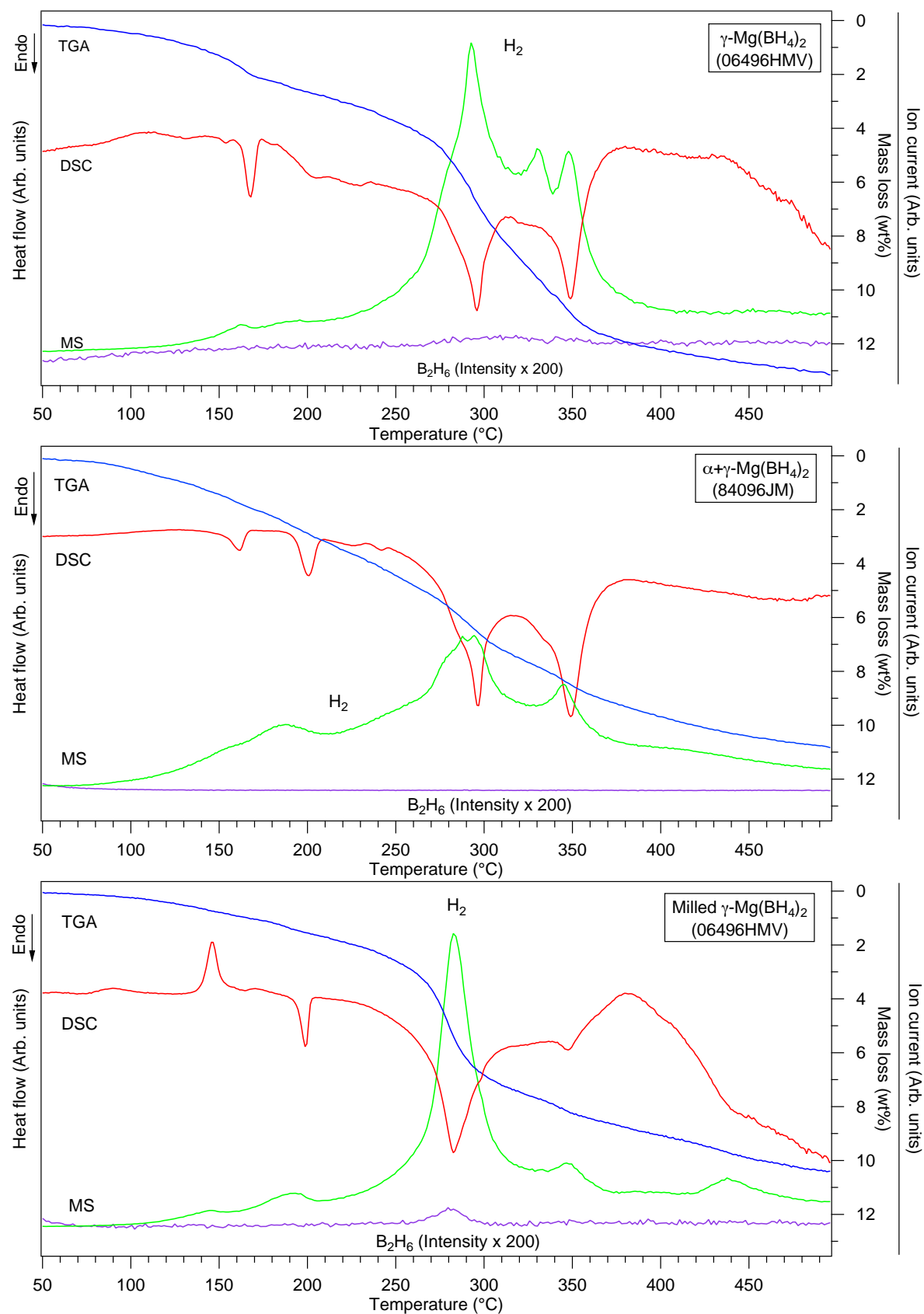
Figure 5.14 DSC, TGA–MS traces of crystalline γ-Mg(BH$_4$)$_2$, crystalline α+γ-Mg(BH$_4$)$_2$, and milled γ-Mg(BH$_4$)$_2$, respectively. The green and purple lines represent the signals for H$_2$ and B$_2$H$_6$ gases, respectively. The intensity of B$_2$H$_6$ was multiplied by 200.

The major desorption of β'-phase began at approximately 240 °C, and then reached a maximum at 293 °C with 5.7 wt% H$_2$ release up to 320 °C to form amorphous Mg(B$_x$H$_y$)$_n$ species and a small amount of Mg. Part of these amorphous Mg(B$_x$H$_y$)$_n$ species may rapidly decompose to Mg and/or MgH$_2$, giving the hydrogen peak at 331 °C with a 1.4 wt% weight loss. 1.2 wt% H$_2$ was then released between 340 and 380 °C, which is within the expected decomposition temperature range of MgH$_2$ (Hanada *et al.*, 2008; Paskevicius *et al.*, 2012). This indirectly confirmed the formation of MgH$_2$ during γ-Mg(BH$_4$)$_2$ decomposition, despite the lack of direct crystalline evidence from the in situ XRD data due to surface oxidation. A total amount of 12.2 wt% H$_2$ was released up to 500 °C with no detected diborane emission.

5.2.3.2 α+γ-Mg(BH$_4$)$_2$

For the α+γ-Mg(BH$_4$)$_2$ sample, the endothermic reaction corresponding to the phase change from γ to ε+β' could be distinguished at 161 °C. The reaction at 200 °C was responsible for the phase transition from α to β. The gradual transformation from ε to β' led to small thermal fluctuations between 215 and 245 °C in the DSC curve. A steady increasing slope was found in the hydrogen signal onset at approximately 90 °C forming a broad peak at 187 °C, leading to a weight loss of 3.6 wt%. This was due to the evaporation of a small amount of coordinated solvent (from the synthesis) (David *et al.*, 2012), which might explain the unknown peak at 2473 cm^{-1} in the Raman spectrum at 175 °C.

The decomposition of Mg(BH$_4$)$_2$ resulted in two H$_2$ peaks at 297 and 350 °C respectively, where the first peak was accompanied by a shoulder at 288 °C. However, the second desorption event during the pure γ-Mg(BH$_4$)$_2$ decomposition was absent in this sample. The desorption at 350 °C was consistent with the temperature of decomposition of MgH$_2$ into Mg, which corresponds well with the rapid growth of Mg(MgO) diffraction peaks in the in situ XRD measurements. A reduced weight loss of 10.8 wt% was found in the mixed phase sample at 500 °C. In light of the appearance of a series of unknown Raman peaks at 225-

325 °C, this suggests that there is a different reaction pathway leading to the formation of different amorphous phases.

5.2.3.3 Milled γ-Mg(BH$_4$)$_2$

After high-pressure ball-milling for 2 h in 100 bar H$_2$, the disordered γ-Mg(BH$_4$)$_2$ underwent an exothermic reaction due to recrystallization at 146 °C, with a simultaneous rise of 0.4 wt% in H$_2$ release between 130 and 160 °C. The endothermic peak at 200 °C, occurred at the same temperature as the α to β transformation in the α+γ-Mg(BH$_4$)$_2$ sample, although it was not possible to distinguish the α and β phases in the in situ XRD patterns due to overlapping diffraction peaks. A 0.8 wt% weight loss of H$_2$ is measured between 160 and 210 °C, which might correspond to the formation of intermediate Mg–B–H species, which was suggested by features in both the in situ XRD and Raman data.

The main H$_2$ desorption began at 240 °C forming a single H$_2$ peak at 280 °C; as a result, the formation of a small amount of Mg was observed in the XRD data. Notably, a very small rise in the diborane signal also appeared in this temperature range, which was not observed in the crystalline samples. The concurrent evolution of H$_2$ and B$_2$H$_6$ gases resulted in a weight loss of 5.9 wt% between 210 and 325 °C. The diborane might subsequently decompose to amorphous B (seen in Raman) and H$_2$; and/or react with Mg-B-H to form MgB$_{12}$H$_{12}$, or other Mg-B-H species (Gaines et al., 1963).

Upon further heating, an endothermic peak between 325 and 380 °C relating to a H$_2$ desorption of 1.2 wt% was observed, which was located at the expected decomposition temperature range of MgH$_2$ (Hanada et al., 2008; Paskevicius et al., 2012). A broad endothermic event appeared between 380 and 460 °C associated with another small increase in H$_2$ release of 1.3 wt% at 440 °C which was not seen in the crystalline γ-Mg(BH$_4$)$_2$ and α+γ-Mg(BH$_4$)$_2$ samples. This might be associated with the decomposition of some metastable Mg-B-H species (labelled as "unknown phase II" in the in situ XRD patterns), to form Mg(MgO) and amorphous B. A total mass loss of 10.0 wt% was observed

up to 500 °C, which was lower than the theoretical 14.9 wt% due to the formation of relatively stable Mg(B$_x$H$_y$)$_n$ compounds.

5.3   General discussion and conclusion

A detailed investigation of the structural and thermal properties of crystalline γ-Mg(BH$_4$)$_2$, α+γ-Mg(BH$_4$)$_2$, and ball-milled γ-Mg(BH$_4$)$_2$ has been performed. There were only small differences in the vibrational frequencies of the [BH$_4$]$^-$ ions for α-, γ- and ε-Mg(BH$_4$)$_2$, despite the β' polymorph exhibiting a simpler and broader vibrational feature due to its higher symmetry at the local level. By high-pressure (100 bar H$_2$) ball-milling of the crystalline γ-Mg(BH$_4$)$_2$, a disordered Mg(BH$_4$)$_2$ was produced which may have similar local ordering of the [BH$_4$]$^-$ ions to that which occurs in the α-Mg(BH$_4$)$_2$ polymorph. A bidentate coordination of Mg-H$_2$BH$_2$-Mg in Mg(BH$_4$)$_2$ gives a characteristic bending mode v_2 at higher frequencies of 1380 – 1410 cm^{-1}, compared to those vibrations in the region of 1280 – 1330 cm^{-1} observed for the ionic bonding between Li$^+$ and [BH$_4$]$^-$.

After going through a transformation from γ- to β'-phase via ε, the decomposition pathway of the crystalline γ-Mg(BH$_4$)$_2$ was from then on, similar to that reported for α-Mg(BH$_4$)$_2$ (Hanada *et al.*, 2008; Soloveichik *et al.*, 2009). The main decomposition proceeded via 3-steps between 240 and 400 °C, giving a total of 12.2 wt% H$_2$ evolution with the formation of Mg (MgO) and B at 500 °C. There was no diborane release detected throughout the decomposition process (for the TGA-MS system used in this study, in which the MS is connected to the TGA via a heated capillary tube). These observations suggest the following multi-step reaction pathway shown in Equation 5.1 to 5.4 (to be balanced).

$$\text{γ-Mg(BH}_4)_2 \rightarrow \text{ε-Mg(BH}_4)_2 + \text{β'-Mg(BH}_4)_2 \qquad\qquad 130\text{-}175\ °C \qquad (5.1)$$

$$\rightarrow \text{β'-Mg(BH}_4)_2 + \text{H}_2 \qquad\qquad 175\text{-}225\ °C \qquad (5.2)$$

$$\rightarrow \text{Mg/MgH}_2 + \text{metastable Mg-B-H (amorph.)} + \text{H}_2 \quad 225\text{-}400\ °C \qquad (5.3)$$

$$\rightarrow \text{Mg + B + stable Mg-B-H (amorph.)} + \text{H}_2 \qquad 400\text{-}500\ °C \qquad (5.4)$$
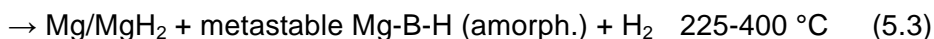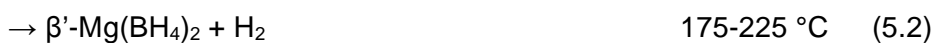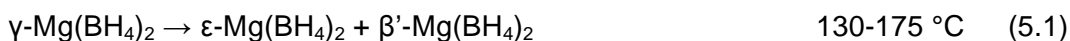
The α+γ-Mg(BH$_4$)$_2$ showed an onset desorption temperature as low as 90 °C, which may be attributed to the evaporation of a small amount of coordinated solvent (that presumably occurred during sample synthesis) (David *et al.*, 2012). The structural changes from the starting phases to ε-, β'- and β-phases occurred at similar temperatures to those observed for the single-phase γ- or α-Mg(BH$_4$)$_2$ sample. There were two major desorption reactions between 230 and 380 °C through the formation of Mg, MgH$_2$, B and a series of amorphous Mg-B-H compounds. One of these metastable compounds exhibited Raman active vibrations very similar to those for K$_2$B$_{10}$H$_{10}$, suggesting that it has a higher borane closo-structure. This type of closo-borane compounds appeared to be stable and led to a reduced weight loss of 10.8 wt% for the sample at 500 °C.

Unlike in the crystalline samples, the milled γ-Mg(BH$_4$)$_2$ decomposed via a different pathway after going through a series of structural changes from amorphous to ε-, β'-and possibly β-phases (Guo *et al.*, 2013). The sample began to dehydrogenate at 240 °C and released a small amount of the undesirable by-product of diborane gas during H$_2$ desorption at 280 °C. Various amorphous Mg-B-H compounds desorbed H$_2$ and/or interact with each other in multiple steps throughout the decomposition process, some of which then rapidly liberated H$_2$ at 430 °C. MgB$_2$ and possible Mg-B-H species were observed up to 600 °C. The formation of stable Mg-B-H species led to a reduction in the total mass loss of the milled sample from the maximum theoretical H$_2$ content of 14.9 wt%, to the experimentally observed 10.0 wt% at 500 °C. The overall decomposition pathway of the milled sample was proposed as shown in Equation 5.5-5.9 (to be balanced).

$$\text{amorph. Mg(BH}_4)_2 \rightarrow \text{Mg-B-H (amorph. I)} + \text{H}_2 \qquad\qquad (5.5)$$

$$\rightarrow \text{Mg-B-H (amorph. II)} + \text{Mg/MgH}_2 + \text{B}_2\text{H}_6 + \text{H}_2 \qquad (5.6)$$

$$\rightarrow \text{Mg-B-H (amorph. III)} + \text{Mg} + \text{B} + \text{H}_2 \qquad\qquad (5.7)$$

$$\rightarrow \text{MgB}_{12}\text{H}_{12}? + \text{Mg} + \text{B} + \text{H}_2 \qquad\qquad (5.8)$$

$$\text{Mg} + 2\text{B} \rightarrow \text{MgB}_2 \qquad > 500\ °\text{C} \qquad\qquad (5.9)$$
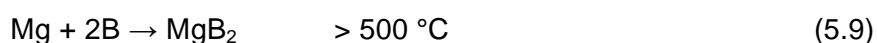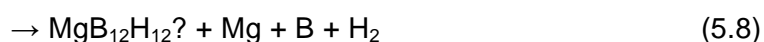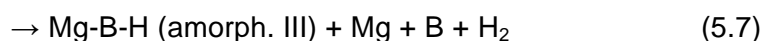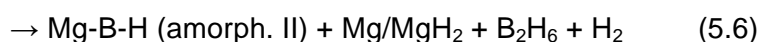
For potential use as a hydrogen storage medium, Mg(BH$_4$)$_2$ has a much lower desorption temperature (T$_{peak}$ 293 °C) than LiBH$_4$ (512 °C), and the subsequent reformation of Mg(BH$_4$)$_2$ from its main decomposition product (MgB$_2$) is more thermodynamically favourable than the formation of LiBH$_4$, (from LiH). But one of concerns for using Mg(BH$_4$)$_2$ is that diborane might be released as a by-product according to theoretical calculations (Chong *et al.*, 2011; Callini *et al.*, 2013). Diborane is a highly undesirable compound, as it is toxic to humans and PEM fuel cells; and it facilitates the formation of very stable compounds (e.g. [B$_{12}$H$_{12}$]$^{2-}$) that preclude the practical reformation of the borohydride (Friedrichs *et al.*, 2010c; Remhof *et al.*, 2014). Although the diborane desorption has not been detected in the decomposition of Mg(BH$_4$)$_2$, it may depend on the chemical state (e.g. oxidation) of the surface of the borohydride particles by lowering the mobility of borane species (Kato *et al.*, 2010). Some possible surface impurities (such as oxides or remnant solvent from synthesis) could trap the diborane and thereby promote further reactions. Various intermediates Mg-B-H subsequently form, resulting in a complex multi-step decomposition process. However, ball-milling resulted in the Mg(BH$_4$)$_2$ having a 'cleaner' surface with an increased surface area (and/or smaller particle size), thereby allowing the evolution of diborane.

Further studies into the surface chemistry of the Mg(BH$_4$)$_2$ powder would be useful, in order to try to control the reaction between Mg(B$_x$H$_y$)$_n$ and diborane, and so ultimately achieve reversibility at a reduced temperature and pressure.

6 Ca(BH₄)₂ and Eutectic 0.68LiBH₄+0.32Ca(BH₄)₂ Mixture

6.1 Ca(BH₄)₂

The crystal and vibrational structures of the room temperature polymorphs of $Ca(BH_4)_2$ including α, β and γ, were investigated. A study of the decomposition of $Ca(BH_4)_2$ under flowing argon was conducted using DSC, TPD-MS, in situ Raman and ex situ XRD up to 500 °C.

6.1.1 Structural characterisation at room temperature

Figure 6.1 shows the refined XRD data for $Ca(BH_4)_2$ purchased from Sigma-Aldrich (batch number 17696LKV). At room temperature, three distinct structures were identified and quantified as: 34.3(3) wt% orthorhombic α-$Ca(BH_4)_2$, 57.0(3) wt% tetragonal β-$Ca(BH_4)_2$, and 8.6(4) wt% orthorhombic γ-$Ca(BH_4)_2$. The refined lattice parameters for the α, β and γ-phases (**Table 6.1**) are in good agreement with room-temperature synchrotron XRD data by Lee *et al.* (2009b), Filinchuk *et al.* (2009b) and (Noritake *et al.*, 2010), respectively.

Table 6.1 Lattice parameters of α, β and γ-phases for as-received $Ca(BH_4)_2$.

Unit cell	α (*F2dd*) this work	α Lee *et al.* (2009b)	β (*P-4*) this work	β Filinchuk *et al.* (2009b)	γ (*Pbca*) this work	γ (Noritake *et al.*, 2010)
a (Å)	8.790(1)	8.772(6)	6.921(1)	6.9189(1)	7.528(3)	7.525(1)
b (Å)	13.136(2)	13.118(7)			13.114(5)	13.109(2)
c (Å)	7.500(1)	7.496(4)	4.349(1)	4.3471(1)	8.412(3)	8.403(1)
V (Å³)	866.0(2)	867(1)	208.4(1)	208.1	830.6(1)	828.92
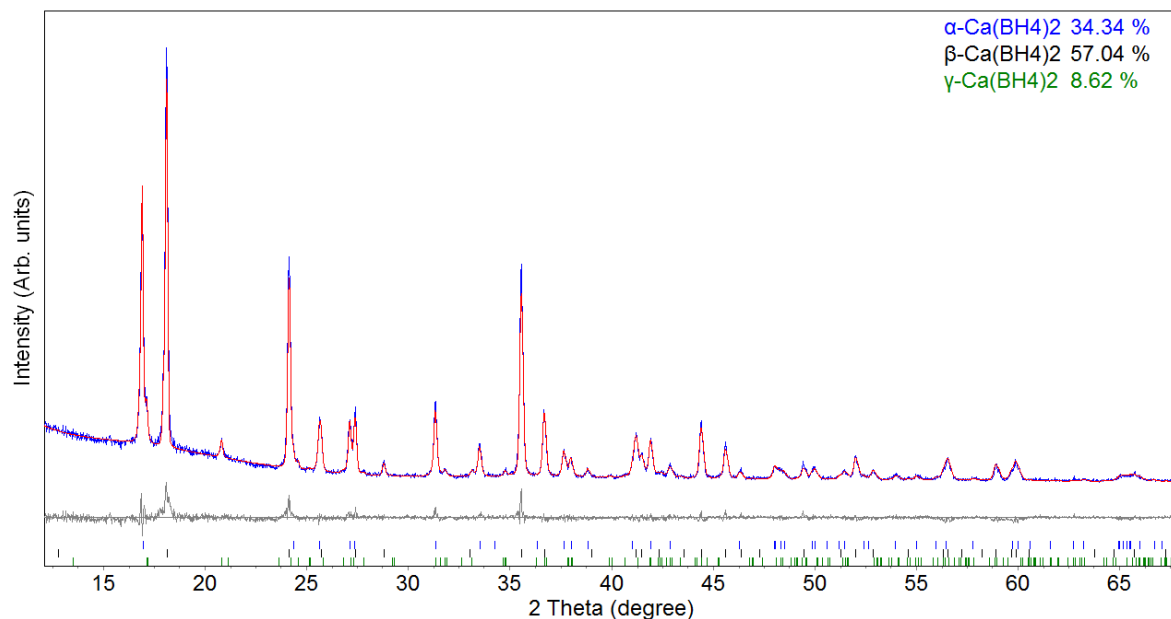
Figure 6.1 Rietveld refinement profile of X-ray diffraction data for as-received $Ca(BH_4)_2$, showing the observed data (Y_{obs}, black), the calculated fit to the data (Y_{calc}, red) and the difference (Y_{obs}-Y_{calc}, grey). Goodness-of-fit = 1.371.

The room temperature Raman spectrum of the as-received $Ca(BH_4)_2$ is shown in **Figure 6.2** , and the assignment of vibrations in comparison to the literature values is summarised in **Table 6.2**. There were five pure A_g and four B_{1g} Raman active modes observed for internal $[BH_4]^-$ vibrations in a region of 1000-2700 cm^{-1}, which are consistent with the theoretical predictions for the C_2 local symmetry for α-$Ca(BH_4)_2$ (Fichtner *et al.*, 2008). The Raman frequencies of the β-phase rich sample from this work are very close to those observed for a sample rich in the α-$Ca(BH_4)_2$ phase, reported by Llamas-Jansa *et al.* (2012). However, a larger proportion of β-phase led to the peak widths for the v_2 modes 1238 and 1325 cm^{-1}, increasing to 14 and 20 cm^{-1} (HWHM), respectively. These HWHM values lie in the range between 8 and 11 cm^{-1} for the pure α polymorph, and 21 and 26.5 cm^{-1} for the β polymorph (Fichtner *et al.*, 2008).
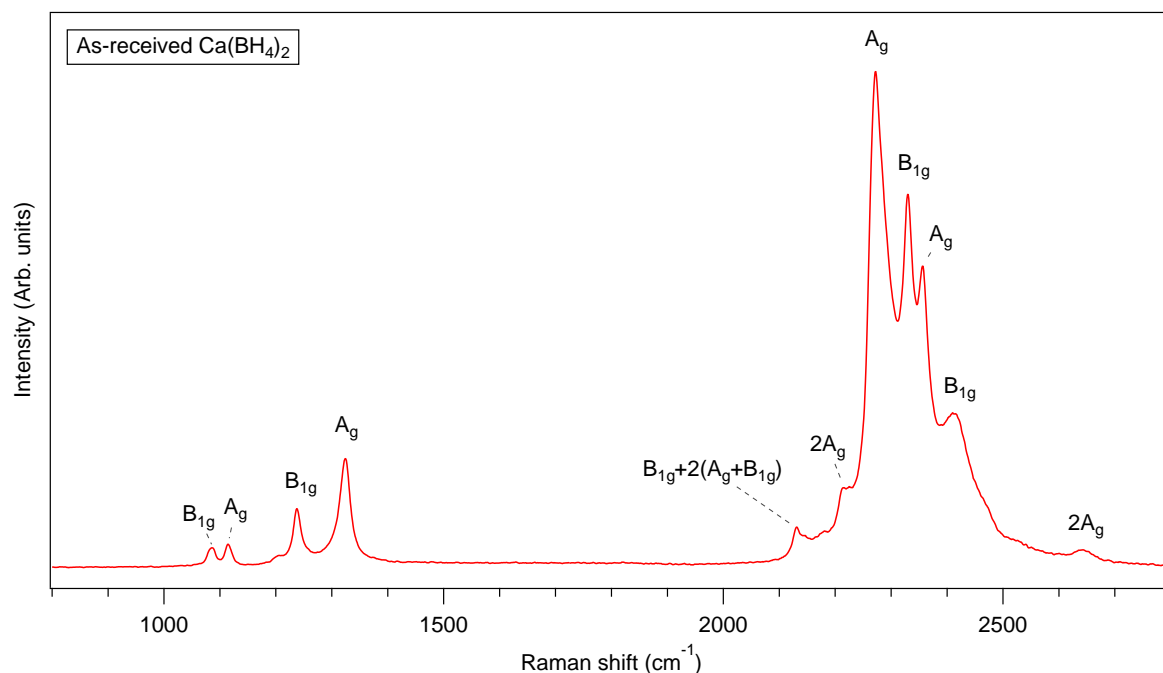
Figure 6.2 Raman spectrum of as-received Ca(BH$_4$)$_2$ at room temperature.

Table 6.2 Raman frequencies (cm^{-1}) of Ca(BH$_4$)$_2$ in different polymorphs mixtures.

Symmetry [b]		β$_{αγ}$	α [a]	α$_{βγ}$ [b]	β$_{92}$ [b]	γ$_α$ [b]
B$_{1g}$	v_4	1085 w	1089	1087		1096
A$_g$	v_4	1114 w	1117	1115	1101	
B$_{1g}$	v_4	1204 vw	1204	1203		
A$_g$	v_2	1237 m	1241	1238		1234
A$_g$	v_2	1324 m	1327	1325		1321
B$_{1g}$+2(A$_g$+B$_{1g}$)		2131 w		2133		
2A$_g$		2213 w		2214		
A$_g$	v_1	2272 vs	2273	2273	2274	2295
B$_{1g}$	v_3	2330 s	2332	2332		2330
A$_g$	v_3	2356 s	2356	2357	2368	2367
B$_{1g}$	v_3	2413 m	2415	2416		2404
A$_g$+2A$_g$		2524 w		2524	2532	
2A$_g$		2641 w		2647	2649	2653

Intensity: vs = very strong, s = strong, m = medium, w = weak, vw = very weak.
β$_{αγ}$ = α(34%)+β(57%)+γ(9%), this work; α$_{βγ}$ = α(67%)+β(23%)+γ(10%); γ$_α$ = α(8%) + γ(92%);
β$_{92}$ = β(92%) + (CaH$_2$+FeNi$_3$)(8%), synthesized from reactive milling in B$_2$H$_6$;
[a] (Fichtner *et al.*, 2008); [b] (Llamas-Jansa *et al.*, 2012);

6.1.2   **Thermal decomposition**

6.1.2.1 DSC-TPD-MS

The temperature-dependent reactions of $Ca(BH_4)_2$ were investigated using DSC, TPD-MS at a heating rate of 2 °C/min under flowing argon (100 ml/min), as shown in **Figure 6.3**. The H_2 signal from the mass spectrometer is stable until around 110 °C where a small rise corresponding to H_2 release might occur. This is possibly due to the evaporation of a small amount of remnant solvent (from the synthesis process). A small endothermic peak, with no corresponding H_2 evolution, was observed at 195 °C (inset in **Figure 6.3**). This might be attributed to the phase transformation from α to β polymorph, although it occurred at a higher temperature than the reported temperature of 140-170 °C (Rönnebro and Majzoub, 2007; Kim *et al.*, 2008). However, Nickels (2010) found that the phase transition temperature increased, with a higher ratio of β-phase in the starting material.
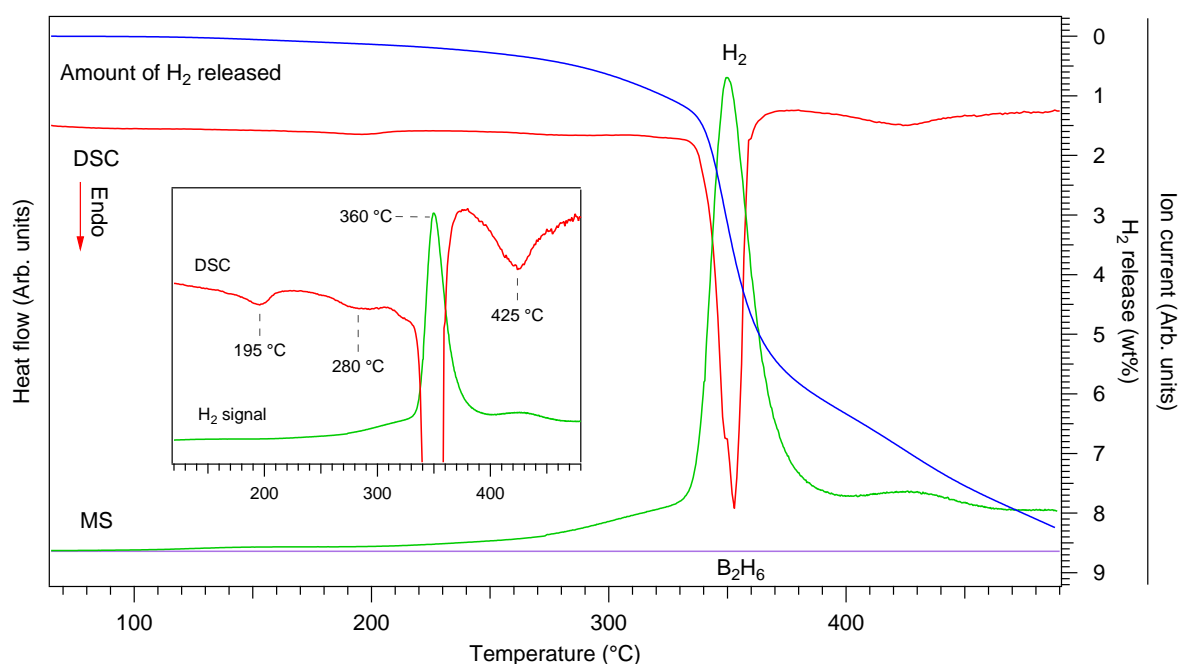
Figure 6.3 DSC, TPD-MS traces of $β_{αγ}$-$Ca(BH_4)_2$ with simulated gravimetric data for the amount of H_2 release. The green and purple lines represent the signals for H_2 and B_2H_6 gases, respectively.

A weak endothermic event centred at around 280 °C was observed. Around 1.0 wt% H_2 loss occurred between 285 and 335 °C: this may be explained by the partial decomposition

of β-Ca(BH$_4$)$_2$ into an intermediate CaB$_2$H$_x$ phase up to 335 °C, according to in situ XRD data in the same temperature range reported by Riktor *et al.* (2007) and Kim *et al.* (2012a).

The major H$_2$ desorption started at 345 °C and reached a maximum at 364 °C, resulting in 5.2 wt% H$_2$ release up to 415 °C. On further heating, an endothermic peak at 424 °C, corresponding to 1.9 wt% H$_2$ loss between 415 and 500 °C, could be distinguished. A total of the observed H$_2$ loss is 8.2 wt% H$_2$, which is lower than values of 9.6 or 8.7 wt% from the reactions (Equation 6.1 and 6.2) proposed by Miwa *et al.* (2006) and Kim *et al.* (2009), respectively.

$$Ca(BH_4)_2 \rightarrow {}^2\!/_3 CaH_2 + {}^1\!/_3 CaB_6 + {}^{10}\!/_3 H_2 \qquad 9.6 \text{ wt\% } H_2 \qquad (6.1)$$

$$Ca(BH_4)_2 \rightarrow CaH_2 + 2B + 3H_2 \qquad\qquad\quad 8.7 \text{ wt\% } H_2 \qquad (6.2)$$
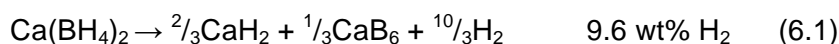
Figure 6.4 is an ex situ room temperature XRD pattern of the decomposed Ca(BH$_4$)$_2$ after the TPD-MS measurement to 500 °C. CaB$_6$, CaH$_2$ and CaO appeared as the major crystalline decomposition products. The formation of CaO is most likely due to the presence of oxygen (from the synthesis process) in the starting material, and has been reported for the Ca(BH$_4$)$_2$ decomposition in many other studies, e.g. Riktor *et al.* (2009), Kim *et al.* (2009), Llamas-Jansa *et al.* (2012); although no oxygen-containing phase could be seen in the as-received Ca(BH$_4$)$_2$. There was a large background with broad amorphous features between 16.2° and 21.4° 2θ (*d*-spacing = 5.5-4.1 Å). This bump is located at a similar diffraction position to the amorphous B observed in the decomposition of LiBH$_4$ and Mg(BH$_4$)$_2$ (Chapters 4.2, p111 and 5.2.1, p127, respectively).
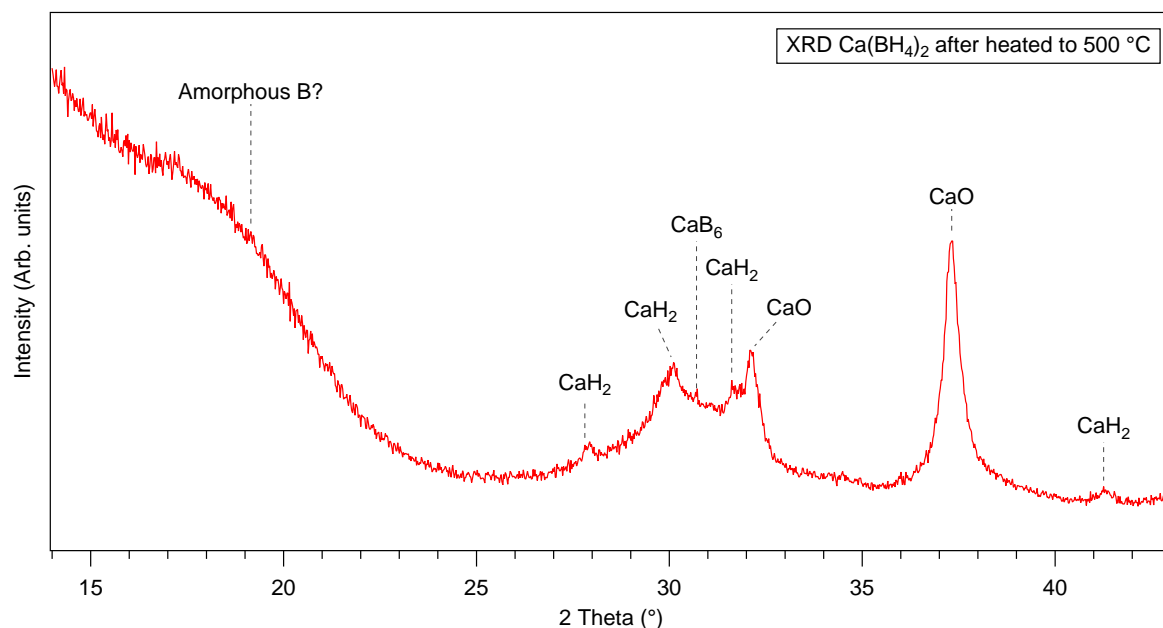
Figure 6.4 Ex situ room temperature XRD pattern of a Ca(BH$_4$)$_2$ sample which had been heated to 500 °C at 2 °C/min in a TPD-MS system under flowing Ar.

6.1.2.2 In situ Raman spectroscopy

In-situ Raman spectroscopy measurements were carried out, with samples heated up to 500 °C at 5 °C/min under Ar flowing at 100 ml/min (**Figure 6.5**). The Raman vibrations from [BH$_4$]$^-$ were thermally broadened at 150 °C. With increasing temperature to 250 °C where the phase transition α to β-phase is expected to complete, a significant broadening in peak width was observed for the [BH$_4$]$^-$ vibrations, i.e. the bending modes v$_2$ (1233 and 1322 cm^{-1}) increased to 56 and 54 cm^{-1} (compared to 14 and 20 cm^{-1}, respectively, at room temperature). This may be explained by the presence of some disorder due to reorientational motions of the [BH$_4$]$^-$ ion in the β phase, based upon vibrational (Fichtner *et al.*, 2008) and crystallographic (Buchter *et al.*, 2008b) studies of the Ca(BH$_4$)$_2$ phase transition.
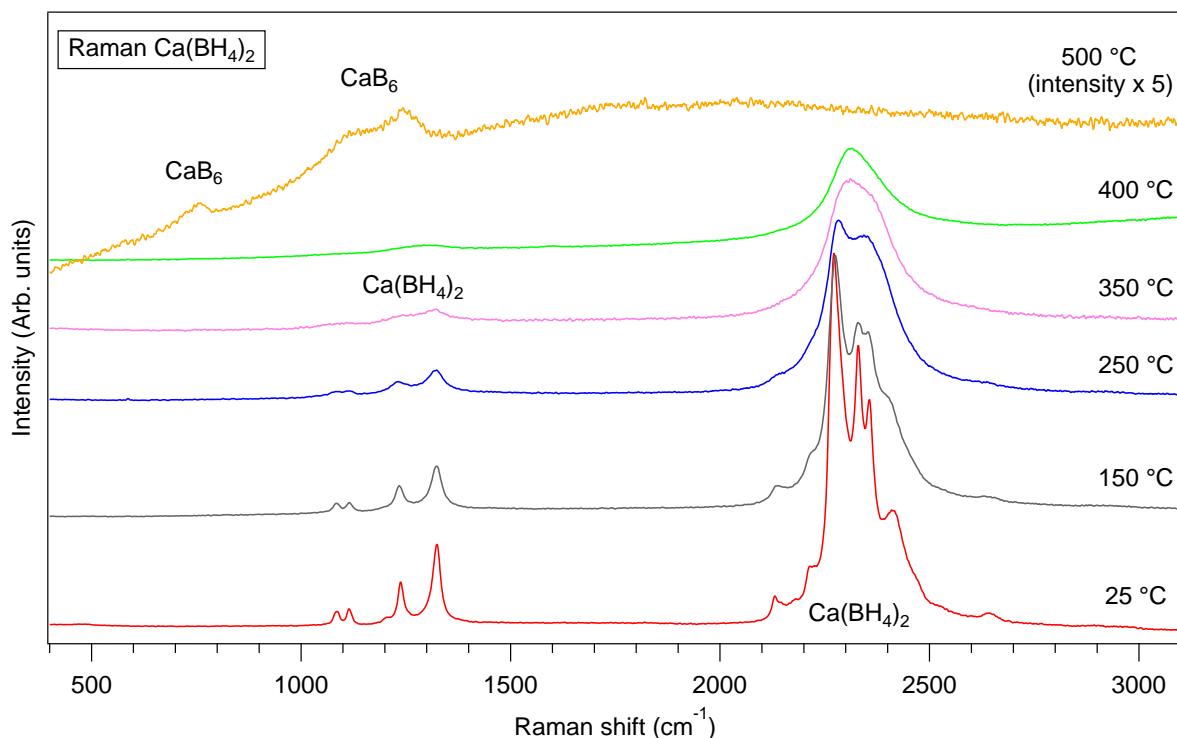
Figure 6.5 Raman spectra of β$_{\alpha\gamma}$-Ca(BH$_4$)$_2$ collected between 25 °C and 500 °C. The intensity of all the spectra were normalised in order for easy comparison, and the intensities of the spectrum at 500 °C was further multiplied by five times.

At 350 °C, the vibrations for [BH$_4$]$^-$ became simpler and decreased in intensity forming a single broad peak centred at approximately 2312 cm^{-1} in the B-H stretching region, whereas the bending modes v_2 could only just be distinguished at 1238 and 1319 cm^{-1}, respectively. The significant degradation of the [BH$_4$]$^-$ vibrations at 400 °C is due to the dissociation of Ca(BH$_4$)$_2$. No intermediate phase(s) (e.g. CaB$_{12}$H$_{12}$, and CaB$_2$H$_x$) proposed in earlier studies (Rönnebro and Majzoub, 2007; Riktor *et al.*, 2009) were observed during this in situ measurement. At 500 °C, CaB$_6$ appeared as Raman peaks at 760, 1113 and 1240 cm^{-1} respectively, possibly overlapping with a broad bump centered at approximate 1150 cm^{-1} due to amorphous B; meanwhile no Ca(BH$_4$)$_2$ was observed. CaH$_2$, which was expected as a final decomposition product based on the XRD results, was not found in the spectra, possibly due to a strong fluorescence effect.

Therefore, β$_{\alpha\gamma}$-Ca(BH$_4$)$_2$ decomposed via two competitive reactions (Equation 6.1 and 6.2) to form CaB$_6$, CaH$_2$ and amorphous B and 8.2 wt% H$_2$ at 500 °C with no intermediates such

as CaB$_2$H$_x$, CaB$_{12}$H$_{12}$ or B$_2$H$_6$ in situ observed, despite the MS data showing that the H$_2$ release occurs in multiple steps. These results are in good agreement with recent research showing that the starting polymorph may affect the amount of hydrogen released: 9.9 wt% from α-Ca(BH$_4$)$_2$, and 8.1 wt% from β- or γ$_α$-Ca(BH$_4$)$_2$ where CaH$_2$ and CaO were the only crystalline products observed in all the samples decomposed at 500 °C (Llamas-Jansa *et al.*, 2012).

6.2   0.68LiBH$_4$ + 0.32Ca(BH$_4$)$_2$ mixture

Mixed borohydride compounds offer the prospect of more favourable thermodynamic properties and lower decomposition temperatures, and so have been investigated as possible hydrogen storage media. In this work, a mixture of 0.68LiBH$_4$+0.32Ca(BH$_4$)$_2$ (both purchased from Sigma-Aldrich) was ball milled for 10 h under 1 bar Ar. The phase transformation and the decomposition mechanism of the mixture were investigated, utilising various techniques including in-situ XRD and Raman spectroscopy.

6.2.1   Structural characterisation of the milled sample

After ball-milling for 10 h, the X-ray diffraction peaks from the 0.68LiBH$_4$+0.32Ca(BH$_4$)$_2$ mixture were identified as: 39.9(6) wt% orthorhombic LiBH$_4$ (68.0 mol%) and 60.1(6) wt% α-Ca(BH$_4$)$_2$ (32.0 mol%), with no diffraction peaks corresponding to β or γ-Ca(BH$_4$)$_2$. The quantitative phase estimation is consistent with the molar ratio of the starting materials LiBH$_4$ (68 mol%) and Ca(BH$_4$)$_2$ (32 mol%). Furthermore, the refined lattice parameters for o-LiBH$_4$ [a = 7.183(2) Å, b = 4.439(1) Å, c = 6.820(2) Å and V = 217.4(1) Å^3] and α-Ca(BH$_4$)$_2$ [a = 8.785(1) Å, b = 13.140(2) Å, c = 7.515(2) Å and V = 867.5(3) Å^3] are very close to the values of the as-received o-LiBH$_4$ (Chapter 4.1.1) and the α polymorph in β$_{αγ}$-Ca(BH$_4$)$_2$ (Chapter 6.1.1, p147). Therefore, both qualitative and quantitative results indicate that a

physical mixture had been formed by high-energy ball-milling, with no evidence for the presence of a bimetallic borohydride and/or solid solution phase(s)
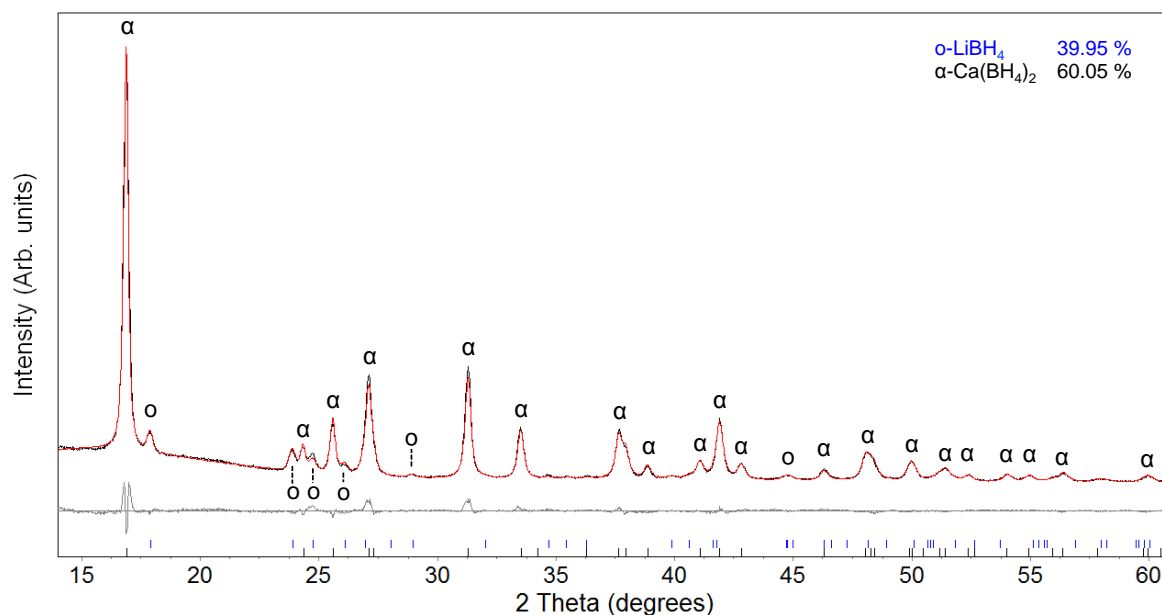
Figure 6.6 Rietveld refinement of XRD data for as-milled 0.68LiBH₄+0.42Ca(BH₄)₂, showing the observed data (Y_{obs}, black), the calculated fit to the data (Y_{calc}, red) and the difference (Y_{obs}-Y_{calc}, grey). Goodness-of-fit = 2.196.

Since the phase transformation from β- to α, γ-Ca(BH₄)₂ has been reported (Fichtner *et al.*, 2008; Buchter *et al.*, 2009) to only partially occur (depending on cooling rate), the presence of LiBH₄ (in the milled 0.68LiBH₄+0.32Ca(BH₄)₂ mixture) appears to have led to β, γ-Ca(BH₄)₂ completely transforming to α-Ca(BH₄)₂. A similar phenomenon was also observed for the LiBH₄-Mg(BH₄)₂ composite: the presence of LiBH₄ made the α-β transition of Mg(BH₄)₂ reversible (Bardaji *et al.*, 2011b).

Figure 6.7 shows the Raman spectrum of the as-milled 0.68LiBH₄+0.32Ca(BH₄)₂ sample, compared to the spectra for the LiBH₄ and Ca(BH₄)₂ starting materials. The Raman vibrations for the LiBH₄-Ca(BH₄)₂ sample simply consists of a combination of the Raman bands of the two single phases o-LiBH₄ and α-Ca(BH₄)₂, with no significant shifts in peak positions. This supports the XRD results, that the two borohydride compounds are a physical mixture after ball-milling. In addition, no evidence of oxides or borates is observed in the as-received or milled materials.
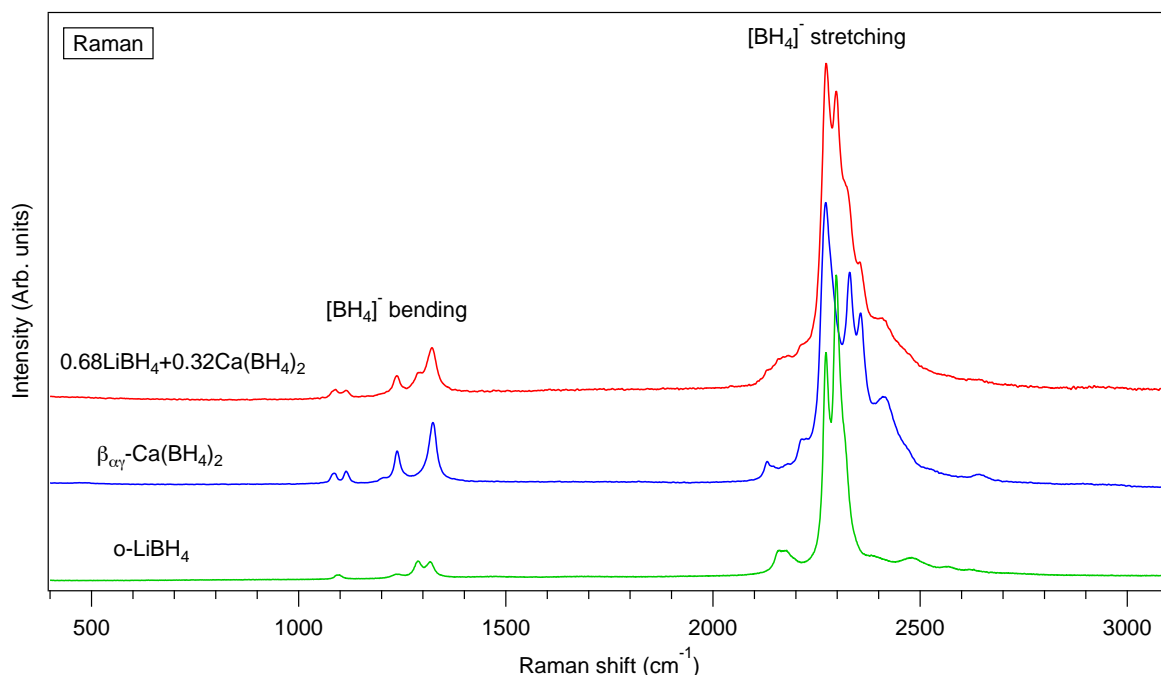
Figure 6.7 A comparison of Raman spectroscopy of the as-milled 0.68LiBH$_4$+0.32Ca(BH$_4$)$_2$ and the starting materials o-LiBH$_4$ and β$_{αγ}$-Ca(BH$_4$)$_2$.

6.2.2 Phase transformation up to eutectic point

The phase transformation of the milled 0.68LiBH$_4$+0.32Ca(BH$_4$)$_2$ mixture was monitored by in situ XRD during two consecutive heating-cooling cycles between 80 and 210 °C at a ramp rate of 12 °C/min under flowing helium. The sample was loaded into an Al$_2$O$_3$ crucible. The data was collected isothermally at 20 °C intervals, with a collection time of around 25 minutes per scan. This corresponds to an average ramp rate of 0.6 °C/min. The surface plot of the diffraction data is shown in **Figure 6.8**, and the abundance of each phase varied during the 1st heating cycle is shown in **Figure 6.9**.
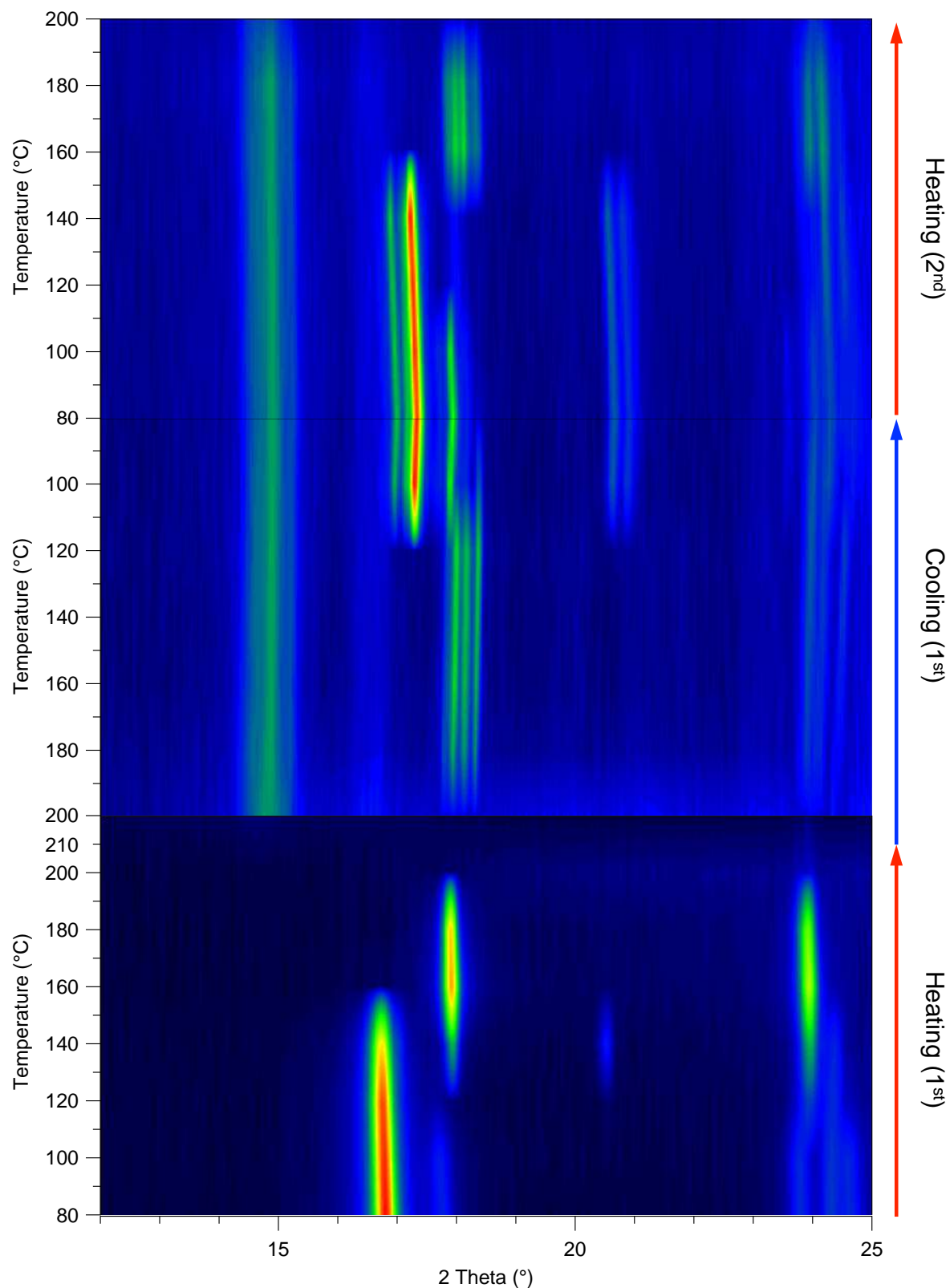
Figure 6.8 Surface plot of the in situ XRD data for 0.68LiBH$_4$+0.32Ca(BH$_4$)$_2$ heated and cooled between 80 and 210 °C at a ramp rate of 12 °C/min under flowing helium (100 ml/min). The pattern was isothermally collected at every 20 °C with a scanning time of ~25 min. The brighter colour represents the higher diffraction intensity.
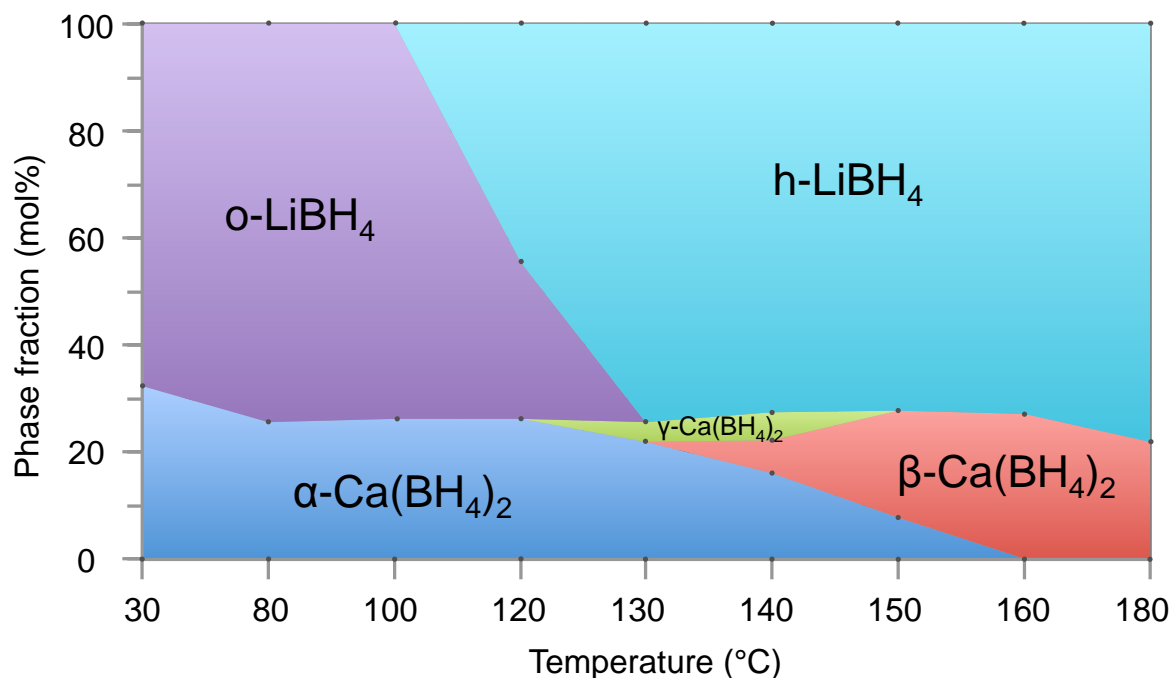
Figure 6.9 Phase fractions present in the 0.68LiBH$_4$+0.32Ca(BH$_4$)$_2$ mixture during heating in the 1st cycle. Grey dots represent data points.

On the first heating cycle, the molar fractions of each phase were slightly shifted to 73.3(7) mol% o-LiBH$_4$ and 26.7(10) mol% α-Ca(BH$_4$)$_2$ at 80 °C, and remained relatively stable on further heating. The phase transformation from o-LiBH$_4$ to h-LiBH$_4$ occurred between 100 and 120 °C. The α-Ca(BH$_4$)$_2$ partially transformed into to γ-Ca(BH$_4$)$_2$ (~3.6 mol%) at 130 °C, followed by the formation of a large amount of β-Ca(BH$_4$)$_2$ upon heating to 140 °C. Only X-ray diffraction peaks from o-LiBH$_4$ and β-Ca(BH$_4$)$_2$ were observed at 160 °C, with a molar fraction of 72.8(15) mol% and 27.2(13) mol%, respectively. No X-ray peaks are present at 200 and 210 °C, corresponding to the molten state of the sample.

On cooling, the sample recrystallized into h-LiBH$_4$, β-Ca(BH$_4$)$_2$ and an unknown phase at 180 °C. Diffraction peaks (e.g ~18.1° and 18.3° 2θ, at 180 °C) from this unknown phase started to decrease in intensity at 120 °C and disappeared at 100 °C, meanwhile h-LiBH$_4$ and β-Ca(BH$_4$)$_2$ transformed to o-LiBH$_4$ and α,γ-Ca(BH$_4$)$_2$, respectively. A significant amount of Ca$_3$(BH$_4$)$_3$(BO$_3$) was observed at ~14.8° 2θ after the 1st heating and remained stable after a further heating-cooling cycle. The formation of the oxide was believed to be due to reactions between the sample and the oxygen from the starting material and/or from a small

leak in the in situ XRD system. The formation of Ca$_3$(BH$_4$)$_3$(BO$_3$) was also observed by heating Ca(BH$_4$)$_2$ above 250 °C (Riktor et al., 2011).

During the 2nd heating cycle, the o-LiBH$_4$ changed to h-LiBH$_4$ between 100 and 120 °C, whereas the α-Ca(BH$_4$)$_2$ transformed to β-Ca(BH$_4$)$_2$ and an unknown phase upon heating to 140 °C. The X-ray diffraction peaks for this unknown phase are consistent with the unknown phase previously observed during cooling. Attempts to identify this unknown phase is still on-going; however, it does not appear to correspond to: LiBH$_4$; Ca(BH$_4$)$_2$; or known borohydride-borates, such as LiCa$_3$(BH$_4$)(BO$_3$)$_2$. A recent NMR study proposed that the 0.68LiBH$_4$+0.32Ca(BH$_4$)$_2$ mixture could form a solid solution between 140 and 170 °C (Lee et al., 2012), which is located in a similar temperature range as the unknown phase in this work. In which case, the unknown phase may tentatively be ascribed as a new, metastable solid solution. A complete transformation from γ to β-Ca(BH$_4$)$_2$ was observed at 160 °C. No X-ray diffraction peaks corresponding to borohydrides or unknown phases were observed above 200 °C, when the sample was melting.

DSC traces for the 0.68LiBH$_4$+0.32Ca(BH$_4$)$_2$ sample undergoing three consecutive heating-cooling cycles up to 210 °C, are shown in **Figure 6.10**. On the 1st heating cycle, the transformation from o- to h-LiBH$_4$ led to an endothermic peak at 114 °C, followed by a change from α-Ca(BH$_4$)$_2$ to γ- and β-Ca(BH$_4$)$_2$ at 139 and 150 °C, respectively. A strong endothermic peak responsible for the eutectic melting appeared at 204 °C, which agrees with a report by Lee et al. (2009a). The sample recrystallized from a molten state to h-LiBH$_4$, β-Ca(BH$_4$)$_2$ and an unknown phase was observed at 194 °C. No phase change occurred until 103 °C where the unknown disappeared leaving o-LiBH$_4$ and α,γ-Ca(BH$_4$)$_2$.
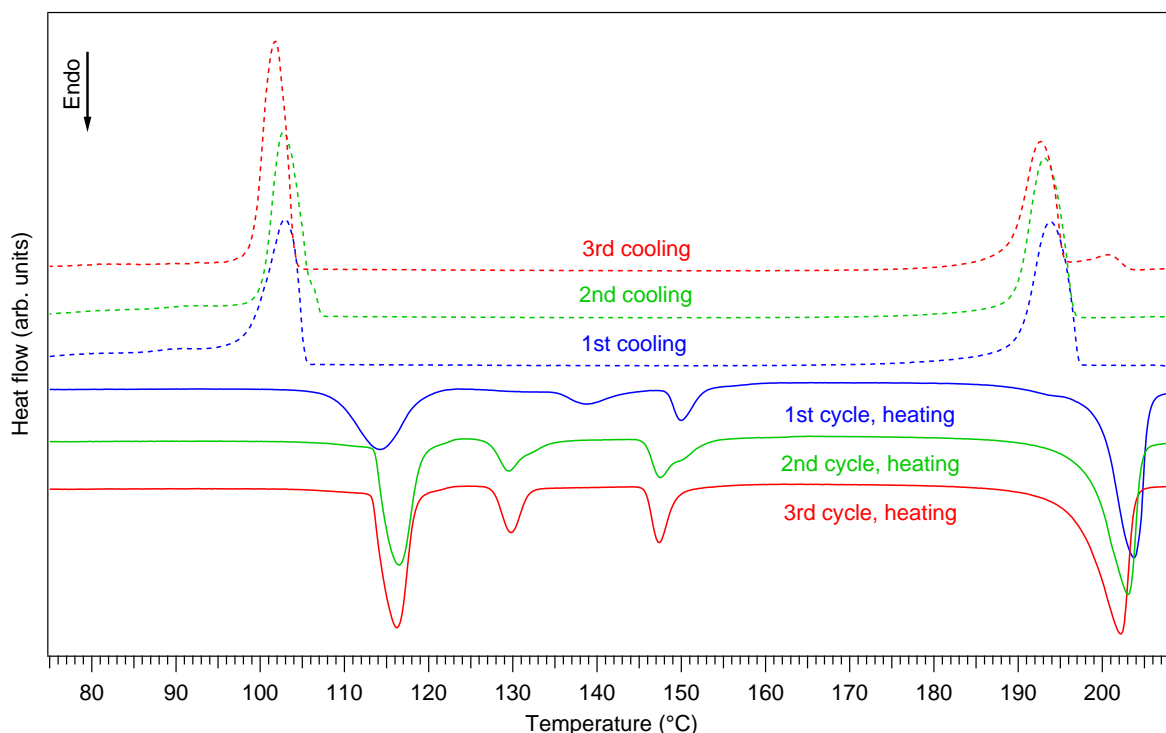
Figure 6.10 DSC traces of the 0.68LiBH$_4$+0.32Ca(BH$_4$)$_2$ sample going through three heating-cooling cycles at 2 °C/min between 70 and 210 °C (under 4 bar Ar flowing at 100 ml/min). The solid and dash lines represent the heating and cooling sequences, respectively. Data was offset in the y-axis to make it easier to compare.

In the following heating cycle, the LiBH$_4$ phase transition occurred at 116 °C, while the transformation from α-Ca(BH$_4$)$_2$ to β-Ca(BH$_4$)$_2$ and the unknown phase corresponded to an endothermic reaction at the lower temperature of 129 °C. The γ to β-Ca(BH$_4$)$_2$ transition was recorded at 147 °C. The eutectic melting point was slightly shifted by 1 °C to 203 and 202 °C respectively during the 2nd and 3rd heating cycle. This might be attributed to a slower dehydrogenation process and/or oxidation of the molten sample, leading to a small compositional shift. During all the cooling cycles, there were only two exothermic reactions corresponding to: eutectic solidification at 193 °C; and the phase transformation from h-LiBH$_4$, β-Ca(BH$_4$)$_2$ and the unknown phase to o-LiBH$_4$, α,γ-Ca(BH$_4$)$_2$ at 103 °C. Thus, the phase transition during cooling occurred in a different manner to the phase transition during heating; this is probably due to the formation of the unknown compound, suggesting a different reaction pathway.

6.2.3   Thermal decomposition

The decomposition reaction of the as-milled 0.68LiBH$_4$+0.32Ca(BH$_4$)$_2$ mixture was initially studied by DSC and the gaseous desorption products monitored by MS at a heating rate of 2 °C under flowing Ar (100 ml/min), as shown in **Figure 6.11**. There was no H$_2$ release detected when the sample was heated through a series of phase transitions to the eutectic melting point. The H$_2$ signal started to slowly rise from around 205 °C forming small peaks at 220 and 250 °C, which correspond to the appearance of small endothermic DSC peaks.
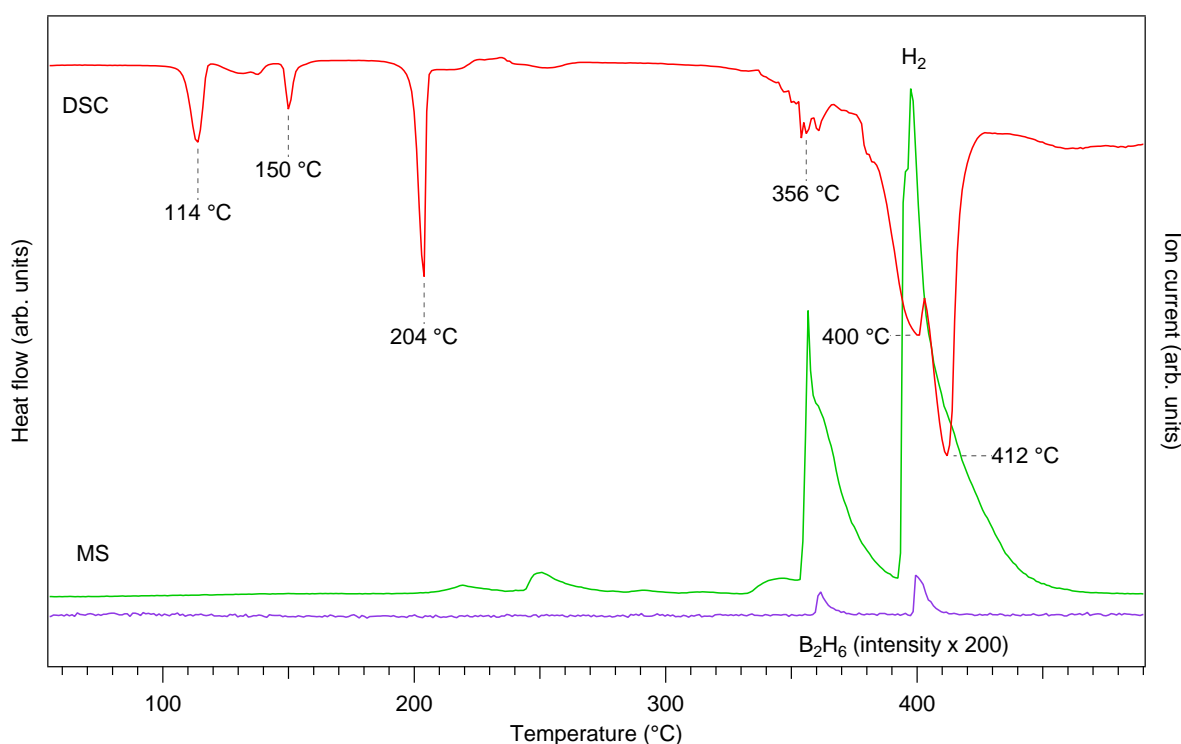
Figure 6.11 DSC, MS traces of the milled 0.68LiBH$_4$+0.32Ca(BH$_4$)$_2$ mixture (heating rate 2 °C/min under Ar flowing at 100 ml/min). The green and purple lines represent the signals for H$_2$ and B$_2$H$_6$ gases, respectively. The intensity of B$_2$H$_6$ signal was increased by 200 times.

The major dehydrogenation event of the mixture proceeds in multiple steps beginning at 333 °C and exhibiting the first peak at 356 °C: this can be related to the decomposition of Ca(BH$_4$)$_2$. Comparison to pure Ca(BH$_4$)$_2$ (see Section 6.1.2, p150), the Ca(BH$_4$)$_2$ in the mixture decomposed at a slightly lower temperature. On further heating to 375-430 °C, strong endothermic reactions were observed, which were responsible for the largest H$_2$ evolution peaking at 398 °C. The second desorption stage was believed due to the LiBH$_4$

decomposition, although it occurred at a much lower temperatures than the 480-530 °C range observed for pure $LiBH_4$ (see Chapter 4.2). In addition, the appearance of two small B_2H_6 peaks were also seen at 360 and 400 °C, which were not observed during the decomposition of pure $LiBH_4$ or pure $Ca(BH_4)_2$.

Figure 6.12 shows the in-situ Raman spectra of the $0.68LiBH_4+0.32Ca(BH_4)_2$ sample heated from 25 to 500 °C at a heating rate of 5 °C/min under Ar flowing at 100 ml/min. The phase change from o- to h-$LiBH_4$ led to a significant peak broadening and shift of the $[BH_4]^-$ vibrations at 150 °C due to an increased symmetry (see Chapter 4.1.2). It was difficult to distinguish the vibrational change for the α to β, γ-$Ca(BH_4)_2$ phase transition, since its vibrations were largely masked by broad BH signals from the h-$LiBH_4$ phase. After heating through the eutectic melting point, a further peak broadening was observed, e.g. the peak width (HWHM) of the $[BH_4]^-$ bending mode v_2 at 1308 cm^{-1} was increased from 102.8 cm^{-1} at 150 °C to 222 cm^{-1} at 250 °C. This significant broadening was a result of the complete freedom of the $[BH_4]^-$ species in the liquid form.

The $[BH_4]^-$ vibrations started to decrease in intensity at 350 °C, indicating partial decomposition of borohydride(s). A number of new Raman peaks at 2484, 956 and 756 cm^{-1} simultaneously formed: the peaks at 2484 and 756 cm^{-1} should be attributed to $Li_2B_{12}H_{12}$; and the peak at 956 cm^{-1} might possibly be attributed to the intermediate phase (e.g. CaB_2H_n) from the partially decomposed $Ca(BH_4)_2$ proposed by earlier work (Riktor *et al.*, 2009; Kim *et al.*, 2012b). However, this unknown 956 cm^{-1} peak did not agree well with the theoretical Raman spectrum for the CaB_2H_2 predicted by Vajeeston et al. (2011); and it was unlikely to be $CaB_{12}H_{12}$, as $Li_2B_{12}H_{12}$ is more thermodynamically stable (Ozolins *et al.*, 2009). The identification of this peak at 956 cm^{-1} is still on-going. The formation of amorphous boron was also observed at 350 °C, forming a broad bump centred at approximately 1150 cm^{-1}. The appearance of CaB_6, responsible for the Raman peaks at 1238 and 1115 cm^{-1} respectively, was seen upon heating to 400 °C. The unknown peak at 956 cm^{-1} disappeared at 500 °C, leaving peaks from $Li_2B_{12}H_{12}$, amorphous B and CaB_6.
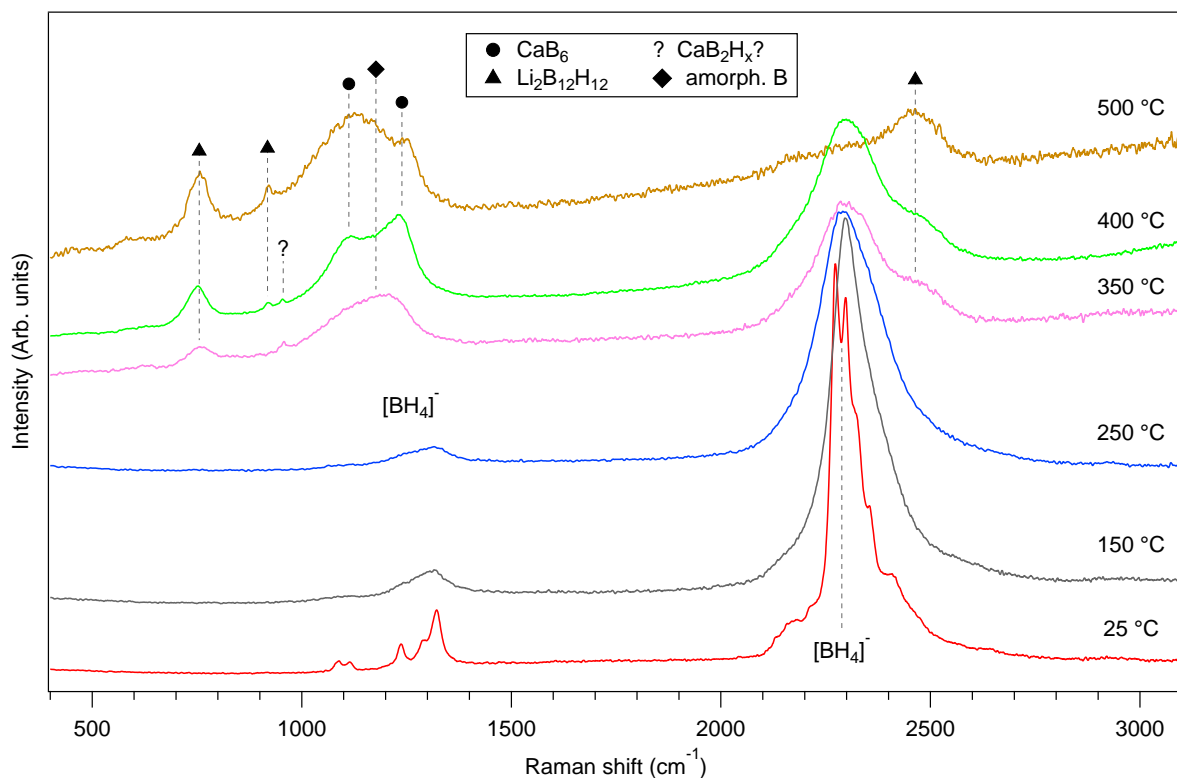
Figure 6.12 Raman spectra of the 0.68LiBH$_4$+0.42Ca(BH$_4$)$_2$ mixture collected between 25 °C and 500 °C. The intensity of all the spectra were normalised in order for easy comparison, and the intensities of the spectrum at 500 °C was further multiplied by three times.

6.3   General discussion and summary

As-received Ca(BH$_4$)$_2$, containing a mixture of α (34.3%), β (57.0%) and γ (8.6%) polymorphs, was investigated by XRD, Raman, DSC and TPD-MS. The structural refinement of the phases in the sample fitted well to the space groups *F2dd*, *P*-4 and *Pbca* for the α-, β- and γ-Ca(BH$_4$)$_2$ phases, respectively; the refined lattice parameters for these phases are in good agreement with the literature. There are nine Raman active bands observed for the internal [BH$_4$]$^-$ vibrations of β$_{αγ}$-Ca(BH$_4$)$_2$. The introduction of β and γ-Ca(BH$_4$)$_2$ led to some degree of broadening in the Raman peak width of the sample compared to those for the pure α-Ca(BH$_4$)$_2$, although no large frequency shift was detected.

When β$_{αγ}$-Ca(BH$_4$)$_2$ was heated under flowing argon, only vibrational broadening for the phase transformation from α, γ, to β polymorph was observed. With increasing temperature, the Ca(BH$_4$)$_2$ started to partially decompose at around 285 °C, and released 1 wt% H$_2$ up to

158

335 °C. The major dehydrogenation occurred in a single step, giving an intense H$_2$ peak at 364 °C. As a result, the Raman vibrations from Ca(BH$_4$)$_2$ greatly decreased in intensity, in conjunction with the release of 5.2 wt% H$_2$ up to 415 °C. A small rise in H$_2$ signal with 1.9 wt% H$_2$ loss was seen between 415 and 500 °C. After heating to 500 °C, CaB$_6$, CaH$_2$, CaO and possibly amorphous B were found to be the decomposition products of β$_{αγ}$-Ca(BH$_4$)$_2$, accompanied by a total H$_2$ evolution of 8.2 wt%. However, no intermediate phases such as CaB$_2$H$_x$ and CaB$_{12}$H$_{12}$ proposed by previous studies (Kim *et al.*, 2012a), were observed during the in situ Raman measurements.

After ball milling for 10 h, the 0.68LiBH$_4$+0.32Ca(BH$_4$)$_2$ sample consisted of a fine mixture of the two borohydride compounds: no new compounds or solid solutions were detected in the milled mixture, however, the presence of o-LiBH$_4$ appears to have promoted the transformation of β,γ-Ca(BH$_4$)$_2$ into α-Ca(BH$_4$)$_2$. With increasing temperature, the o-LiBH$_4$ transformed into h-LiBH$_4$, followed by a phase change from α to β-Ca(BH$_4$)$_2$ via the partial formation of the γ polymorph (Equation 6.3). A eutectic melting point appeared at 203 °C, leading to the appearance of a diffuse region (with no diffraction peaks) in the situ XRD patterns that is characteristic of an amorphous phase.

Reversible phase transformations between α, γ and β-Ca(BH$_4$)$_2$ were observed in subsequent heating-cooling cycles between room temperature and the eutectic melting point. An unknown phase, which may tentatively be ascribed to a new, metastable dual-cation borohydride, was formed when cooled from the eutectic melting point (Equation 6.4), and it participated in the reversible phase changes that occurred in the subsequent heating-cooling cycles (Equation 6.5). The identification of this undefined phase is ongoing, however, it does not appear to correspond to: LiBH$_4$; Ca(BH$_4$)$_2$; or known borohydride-borates, such as LiCa$_3$(BH$_4$)(BO$_3$)$_2$, Ca$_3$(BH$_4$)$_3$(BO$_3$) etc.

1st heating: o-LiBH$_4$ → h-LiBH$_4$ → liquid

α-Ca(BH$_4$)$_2$ → (partial γ) → β-Ca(BH$_4$)$_2$ → liquid   (6.3)

1st cooling: liquid → h-LiBH$_4$ + β-Ca(BH$_4$)$_2$ + unknown phase

→ o-LiBH$_4$ + α,γ-Ca(BH$_4$)$_2$ (6.4)

2nd heating: o-LiBH$_4$ + α,γ-Ca(BH$_4$)$_2$ → h-LiBH$_4$ + α,γ-Ca(BH$_4$)$_2$

→ β,γ-Ca(BH$_4$)$_2$ + h-LiBH$_4$ + unknown phase

→ β-Ca(BH$_4$)$_2$ + unknown phase

→ liquid   (6.5)
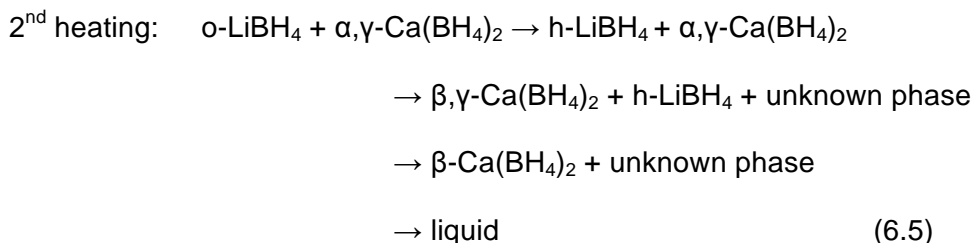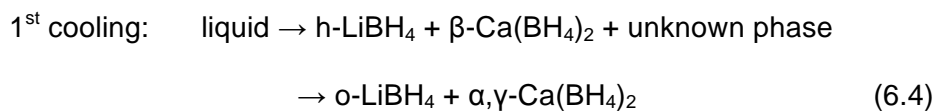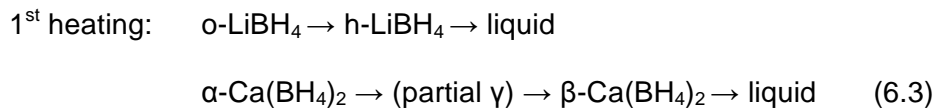
(to be balanced)

The decomposition mechanism was studied using in situ Raman spectroscopy. Upon heating to the eutectic point, the Raman peaks of [BH$_4$]$^-$ bands became extremely broad, suggesting an increased rotational freedom of the [BH$_4$]$^-$ ions in the liquid. The major decomposition of the 0.68LiBH$_4$+0.32Ca(BH$_4$)$_2$ mixture started at about 330 °C, which was 10 °C and 150 °C lower than those of single-phase Ca(BH$_4$)$_2$ and LiBH$_4$, respectively. The Raman peaks corresponding to amorphous boron, Li$_2$B$_{12}$H$_{12}$ and an unknown peak at 956 cm^{-1} were present at 350 °C. The formation of amorphous boron and Li$_2$B$_{12}$H$_{12}$ occurred in a similar temperature range to those observed in a recent NMR study (Yan *et al.*, 2013a). The intensity of CaB$_6$ increased with the concurrent disappearance of the unknown peak at 500 °C. Only Raman peaks from CaB$_6$, Li$_2$B$_{12}$H$_{12}$ and amorphous boron were observed in the Raman spectrum at 500 °C. To the best of my knowledge, this was the first time in situ Raman spectra have been obtained showing the decomposition reactions for a LiBH$_4$-Ca(BH$_4$)$_2$ eutectic mixture. The reaction pathway after the eutectic melting point was proposed as follows:

h-LiBH$_4$ + β-Ca(BH$_4$)$_2$ → Li$_2$B$_{12}$H$_{12}$ + amorph. B + [B$_x$H$_y$]$^{n-}$?

→ Li$_2$B$_{12}$H$_{12}$ + amorph. B + CaB$_6$ (6.6)
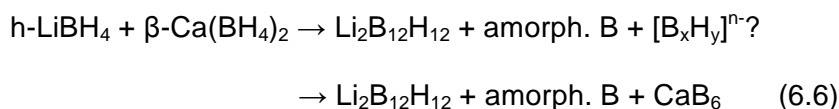
Ca(BH$_4$)$_2$ – either as a pure compound or as a component within a eutectic LiBH$_4$-Ca(BH$_4$)$_2$ mixture – showed a higher desorption temperature and smaller H$_2$ capacity than Mg(BH$_4$)$_2$. There is no evidence for the formation of CaB$_{12}$H$_{12}$ during the decomposition of Ca(BH$_4$)$_2$ (pure or mixture), only CaB$_6$ and CaH$_2$ phases under the conditions used: this should make it more thermodynamically favourable for rehydrogenation.

In the future, the structural determination based on solid solution and/or new dual Li-Ca cation borohydrides needs to be carried out, in order to identify the unknown phase observed in the phase transitions. Samples using isotopic-labeled borohydrides, might help to identify the unknown peak appeared in in situ Raman spectra during the decomposition. Ex situ solution- and/or solid-state NMR on the decomposed unknown intermediates or products may also help to identify the [B$_x$H$_y$]$^{n-}$ species and interpret the decomposition mechanisms. On the other hand, further study of the controlling re/dehydrogenation conditions (e.g. temperature, heating rate and back-pressure) could also be useful, particularly given a recent report on how such conditions may affect the kinetics and reversibility of the system (Yan *et al.*, 2013a).

7 $M(\mathrm{BH_4})_n$ / $M\mathrm{H_n}$ + $\mathrm{B_2H_6}$

Diborane plays an important role in the H_2 sorption mechanisms of borohydrides, as previously discussed. The focus of this chapter is to investigate the effect of diborane on the decomposition and formation of borohydrides by heating metal borohydrides (or hydrides) to various temperatures in a gaseous diborane-hydrogen atmosphere. The diborane gas source was achieved by heating a ball-milled $2\mathrm{NaBH_4}+\mathrm{ZnCl_2}$ mixture to about 100 °C (see Chapter 3.1.2). It is re-iterated (Chapter 3) that diborane is a toxic gas, and so a detailed Risk Assessment must be performed and any necessary safety precautions put in place, before it is used.

The resulting products from the solid-gas reactions were characterised using ex situ XRD and Raman spectroscopy. Raman-active vibrations of commercial crystalline $\mathrm{K_2B_{12}H_{12}}$ and $\mathrm{K_2B_{10}H_{10}}$ were assigned, to try to better understand the vibrational structures of $M_n\mathrm{B_{12}H_{12}}$ and $M_n\mathrm{B_{10}H_{10}}$ (M = Li, Na, Mg, or Ca; n = 1 or 2). This chapter demonstrated the solvent-free synthesis of $\mathrm{LiBH_4}$ and $\mathrm{NaBH_4}$ by gas-solid reactions of LiH/NaH with $\mathrm{B_2H_6}$ and H_2. A $\mathrm{Li_2B_{12}H_{12}}$ or $\mathrm{Na_2B_{12}H_{12}}$ passivation layer on the surface of the new-formed borohydride powders (i.e. forming a core-shell structure) was suggested as the limiting step for full hydrogenation. Additionally, diborane and/or its adducts were found to be associated with the formation of higher boranes (e.g. $[\mathrm{B_{12}H_{12}}]^{2-}$) during the decomposition of $\mathrm{LiBH_4}$, $\mathrm{Mg(BH_4)_2}$ and $\mathrm{Ca(BH_4)_2}$, leading to poor reversibility. These studies provide new insights into the H_2 cycling mechanism(s) of metal borohydrides.

7.1 Vibrational modes of $K_2B_{12}H_{12}$ and $K_2B_{10}H_{10}$

Due to an absence of a detailed vibration analysis of $M_2B_{12}H_{12}$ and $M_2B_{10}H_{10}$ (M = Li, Na, Mg, Ca) in the literature, vibrational spectroscopy was performed on commercial crystalline $K_2B_{12}H_{12}$ and $K_2B_{10}H_{10}$ samples to try to gain a better understanding of the vibrational modes of the $[B_{10}H_{10}]^{2-}$ and $[B_{12}H_{12}]^{2-}$ anions. **Figure 7.1** and **Figure 7.2** show a comparison of Raman and IR spectra of solid $K_2B_{12}H_{12}$ and $K_2B_{10}H_{10}$; and **Table 7.1** summarises the corresponding vibrational assignments based on previous studies (Leites *et al.*, 1982; Leites *et al.*, 1983; Cyvin *et al.*, 1986).

The $[B_{12}H_{12}]^{2-}$ icosahedron with the point group I_h, exhibits 66 fundamental vibrations:

$$\Gamma_{vib} = 2A_g + F_{1g} + 2G_g + 4H_g + 3F_{1u} + 2F_{2u} + 2G_u + 2H_u$$

of which only the A_g and H_g vibrations are Raman active and only F_{1u} is IR active (Leites *et al.*, 1982). As a result, there were two symmetric modes A_g and four degenerate modes H_g expected in the Raman spectrum, whereas three triply degenerate modes F_{1u} were in the IR spectrum. The crystalline $K_2B_{12}H_{12}$ (cubic, space group $Fm3$ with four molecules per unit cell), exhibits a lower symmetry with point group of T_h (Wunderlich and Lipscomb, 1960). This could lead to increased active vibrations and splitting modes in the spectra, e.g. the v_4 of the H_g at 955 cm^{-1} has split into two individual components v_4 at 951 cm^{-1} and v_4' at 976 cm^{-1}. However, upon transition from an aqueous solution of $K_2B_{12}H_{12}$ to a crystalline solid-state, the vibrational spectra showed that the internal $[B_{12}H_{12}]^{2-}$ vibrations did not change significantly.
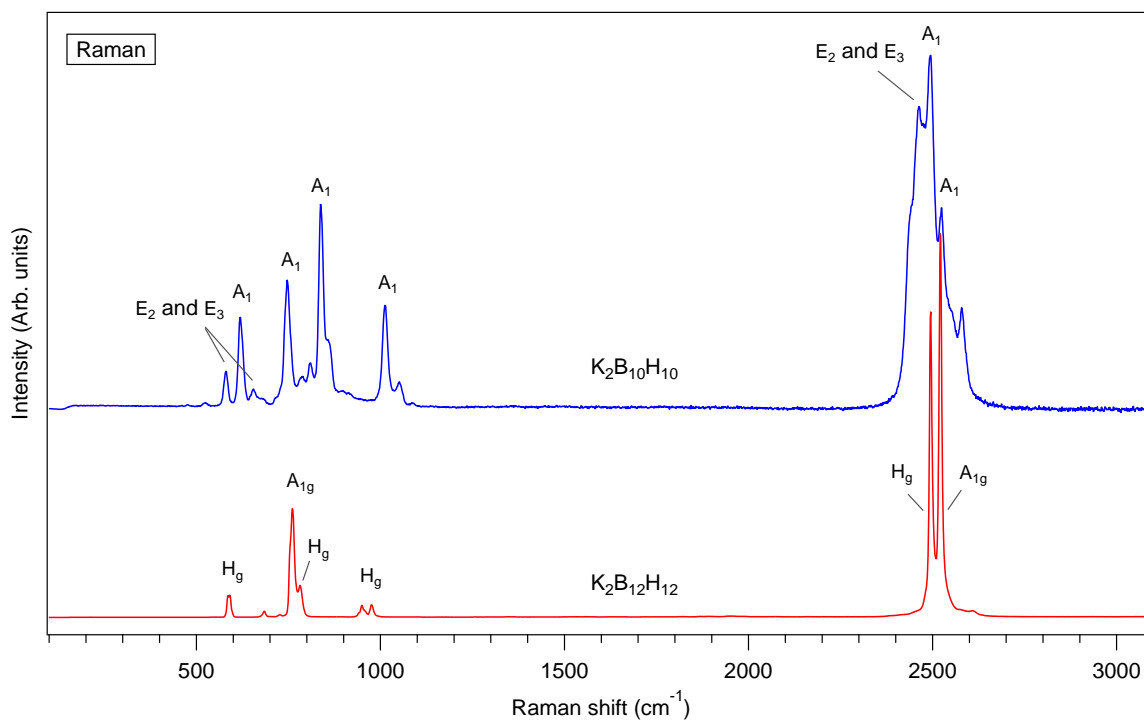
Figure 7.1 Comparison of the Raman spectra of $K_2B_{10}H_{10}$ and $K_2B_{12}H_{12}$ (Data was collected at room temperature in reference Reed and Book (2011))
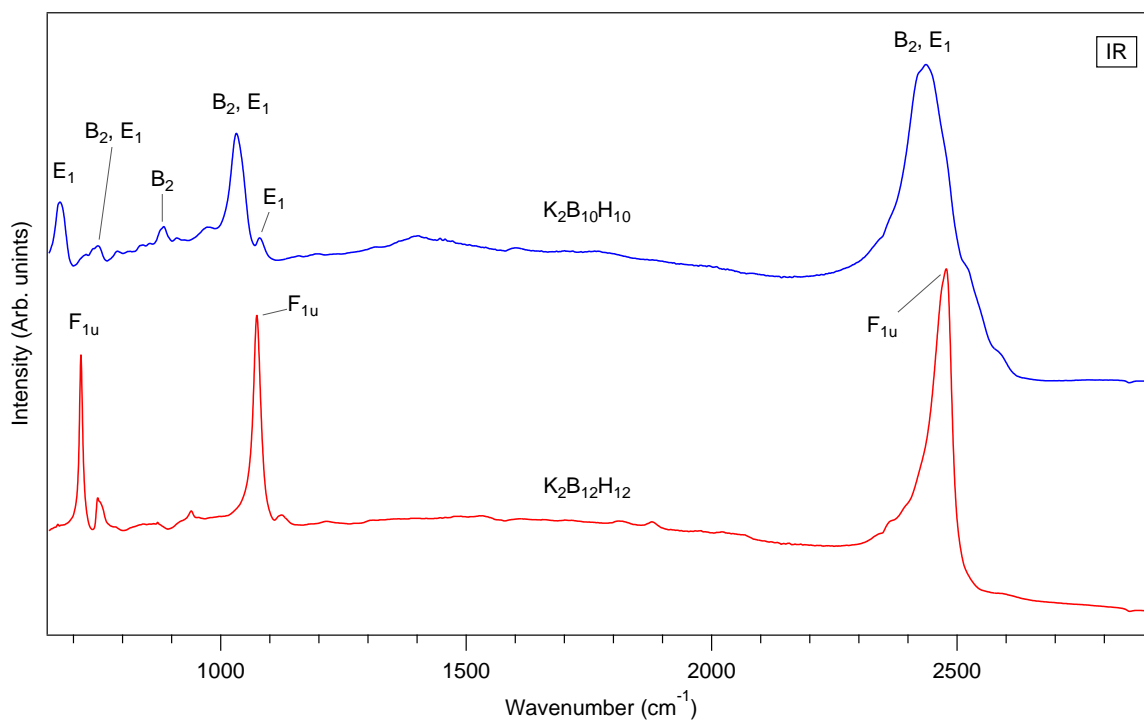
Figure 7.2 Comparison of the IR spectra of $K_2B_{10}H_{10}$ and $K_2B_{12}H_{12}$ at room temperature.

Table 7.1 Assignment of Raman active modes for $K_2B_{12}H_{12}$ and $K_2B_{10}H_{10}$ in solid and H_2O solution, respectively, together with the proposed assignment from the literature. (s = strong; m = medium; w = weak; sh = shoulder; B_v = vertex B atom, B_e = equatorial B atom)

$K_2B_{12}H_{12}$						$K_2B_{10}H_{10}$				
Symmetry Mode		Solid	H_2O solution [a]	Intensity	Bonding type [b]	Symmetry Mode	Solid	H_2O solution [c]	Intensity	Bonding type [c]
A_{1g} (Raman)	v_1	2521	2517	s	BH stretch		2524	2515	m	B_v-H
	v_2	760	745	s	BB stretch		2495	2483	m	B_e-H
H_g (Raman)	v_3	2495	2470	m	BH stretch	A_1 (Raman)	1013	1002	m	mainly B-B
	v_4	951	955	w	BH stretch + BBH bend		838	836	s	mainly B-B
	v_4'	976		w			747	741	s	mainly B-B
	v_5	781	770	m	BB stretch + BBH bend		620	614	m	mainly BBH
	v_6	589	580	m	mainly BB stretch	E_3 (Raman)		933	w	
						E_2 and E_3 (Raman)	2460	2452	m	B_eH
							859	853	w, sh	
							785	755	w, sh	
							657	647	w	
							580	573	w	
							524	515	w	
F_{1u} (IR)	v_7	2476	2485	s	mainly BH stretch	B_2, E_1 (IR)	2435	2467	m	B_e-H
	v_8	1073	1072 *	m	BB stretch + BBH bend		1029	1030	s	
	v_9	715	719 *	m			746	736 *	w	
						B_2 (IR)	881	883 *	w	
						E_1 (IR)	1077	1080 *	m	
							672	664 *	w	

[a] (Leites *et al.*, 1982), [b] (Cyvin *et al.*, 1986), [c] (Leites *et al.*, 1983);   * Data was collected from the solid sample in original paper.

In this work, it was not possible to measure the external vibrations due to the type of Raman system used: the holographic notch filters prevented measurements being made < 100 cm^{-1}. Future options to make such measurements could include: Raman spectroscopy using low wavenumber filters (e.g. "Eclipse" form Renishaw), and inelastic neutron scattering (INS) measurements (e.g. the TOSCA instrument at ISIS, Rutherford Appleton Laboratories).

Unlike the icosahedral $[B_{12}H_{12}]^{2-}$ in which all the BH and BB bonds and the BBH angles are equivalent, the $[B_{10}H_{10}]^{2-}$ anions (symmetry group D_{4d}) have a more complex vibrational structure since all the ν_{BH}, ν_{BB} and δ_{BBH} coordinates are not equivalent and each set are being subdivided into subsets (Leites et $al.$, 1983).

In this work, all six vibrations of A_1 modes of solid $K_2B_{10}H_{10}$ were assigned. A_1 modes at 2524 and 2495 cm^{-1} were due to the vibrations of the vertex and equatorial BH bonds, respectively (Muetterties et $al.$, 1964); while peaks at 1010, 838 and 747 cm^{-1} were predominantly attributed to the vibrations of the different types of BB bonds but also involve the ν_{BH} and possibly the δ_{BBH} coordinates (Leites et $al.$, 1983). Only 6 out of 13 expected depolarized Raman bands (E_2 and E_3) and 6 out of 12 IR vibrations (B_2 and E_1), were observed due to overlapping at similar frequencies. In addition, a lower symmetry of the crystalline sample led to the occurrence of numbers of new bands in the mode region of 500-1100 cm^{-1}, e.g. unassigned peaks at 787, 810 and 1050 cm^{-1}, as shown in **Figure 7.1**.

7.2 $LiBH_4$ + B_2H_6

Since the formation of $Li_2B_{12}H_{12}$ and possibly B_2H_6 were proposed to be an undesirable by-product during $LiBH_4$ decomposition (see Chapter 4.2), it is necessary to better understand the formation mechanisms of these compounds and the effect on the decomposition mechanism of borohydrides. Thus, $LiBH_4$ were heat-treated in a mixed B_2H_6/H_2 atmosphere for 40 h at 150, 160 and 200 °C, respectively.

7.2.1 Ex situ XRD

Figure 7.3 shows the ex situ XRD results of the resulting products after the reaction between $LiBH_4$ and B_2H_6. At 150 °C, the X-ray diffraction peaks for $Li_2B_{12}H_{12}$ and unreacted o-$LiBH_4$ and a small amount of $Li_2B_{10}H_{10}$ were observed. With increasing temperature to 160 °C, the phase abundance of $Li_2B_{10}H_{10}$ increased relative to $Li_2B_{12}H_{12}$, leaving only $Li_2B_{10}H_{10}$ with residual $LiBH_4$ present at 200 °C. The crystal structure of $Li_2B_{12}H_{12}$ was refined to be in a cubic arrangement (space group Pa-3) with lattice parameter of a = 9.597(1) Å, which is in good agreement with the published data (Her *et al.*, 2008).
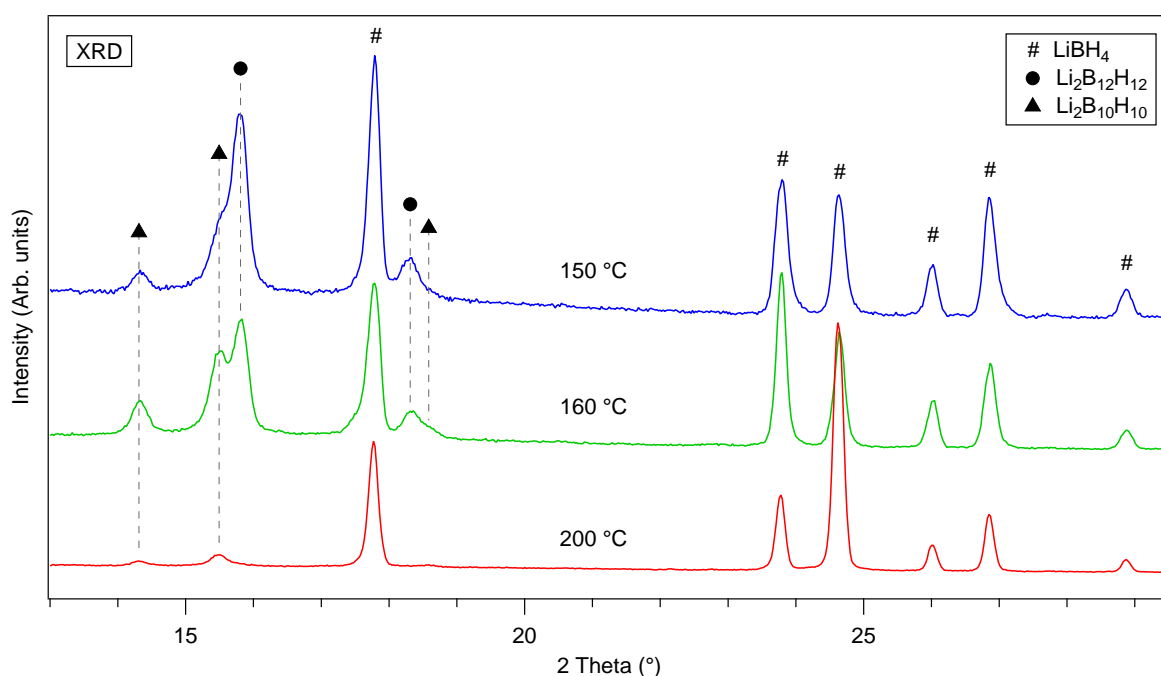
Figure 7.3 ex situ XRD patterns measured at room temperature for the $LiBH_4$ samples after being exposed to B_2H_6 for 40 h at 150, 160 and 200 °C, respectively.

The diffraction peaks observed for $Li_2B_{10}H_{10}$ are consistent with those for the anhydrous $Li_2B_{10}H_{10}$ synthesized by Johnson and Brody (1982), but do not match the theoretical structure of tetragonal (space group I442) proposed by Ohba *et al.* (2006) based on DFT calculations. Due to the lack of a crystal structure determination for $Li_2B_{10}H_{10}$, it was difficult to perform quantitative phase analysis to accurately estimate the abundance of each phase in the sample.

7.2.2 Raman spectroscopy

Figure 7.4 shows the ex situ Raman spectra of samples which had been heated to 150, 160 and 200 °C in a B_2H_6/H_2 atmosphere. For the sample treated at 150 °C, vibrational peaks were from $Li_2B_{12}H_{12}$ and a small amount of $Li_2B_{10}H_{10}$. In order to better understand the vibrations of higher boranes, $Li_2B_{12}D_{12}$ and a small amount of $Li_2B_{10}D_{10}$ was also produced by heating $LiBD_4$ to 150 °C for 40 h in a B_2D_6/D_2 atmosphere (provided by heating a ball-milled $2NaBD_4+ZnCl_2$ mixture to about 100 °C): the Raman spectrum of the $LiBD_4+B_2D_6$ after the reaction is shown in **Figure 7.5**.

Seven internal vibration bands originated from $Li_2B_{12}H_{12}$ were observed between 2400-2600 cm^{-1} and 500-1000 cm^{-1}, whereas four Raman bands from $Li_2B_{12}D_{12}$ were located between 600-800 cm^{-1} and 1800-2000 cm^{-1}. **Table 7.2** summarizes the assignment of the vibrations of $Li_2B_{12}H_{12}$ ($Li_2B_{12}D_{12}$), in accordance with the vibrations of solid $K_2B_{12}H_{12}$.

Table 7.2 Raman modes of $Li_2B_{12}H_{12}$ ($Li_2B_{12}D_{12}$) after being exposed to a B_2H_6/H_2 (B_2D_6/D_2) atmosphere at 150 °C, in comparison with those for solid $K_2B_{12}H_{12}$ ($K_2B_{12}D_{12}$) (s = strong; m = medium; w = weak).

Symmetry Mode		$Li_2B_{12}H_{12}$	$K_2B_{12}H_{12}$	$Li_2B_{12}D_{12}$	$K_2B_{12}D_{12}$ *	Li H/D	K H/D *	Vibrations *
A_{1g}	v_1	2529	2521 s	1904	1899 m	1.33	1.32	BH stretch
	v_2	749	760 s	719	713 s	1.04	1.04	BB stretch
H_g	v_3	2474	2495 m	1853	1854 m	1.34	1.33	BH stretch
	v_4	943	951 w		891 w			BH stretch + BBH bend
	v_4'	973	976 w					
	v_5	764	781 m	609	616 s	1.25	1.25	BB stretch + BBH bend
	v_6	580	589 m		531 w			mainly BB stretch

* (Leites *et al.*, 1982)
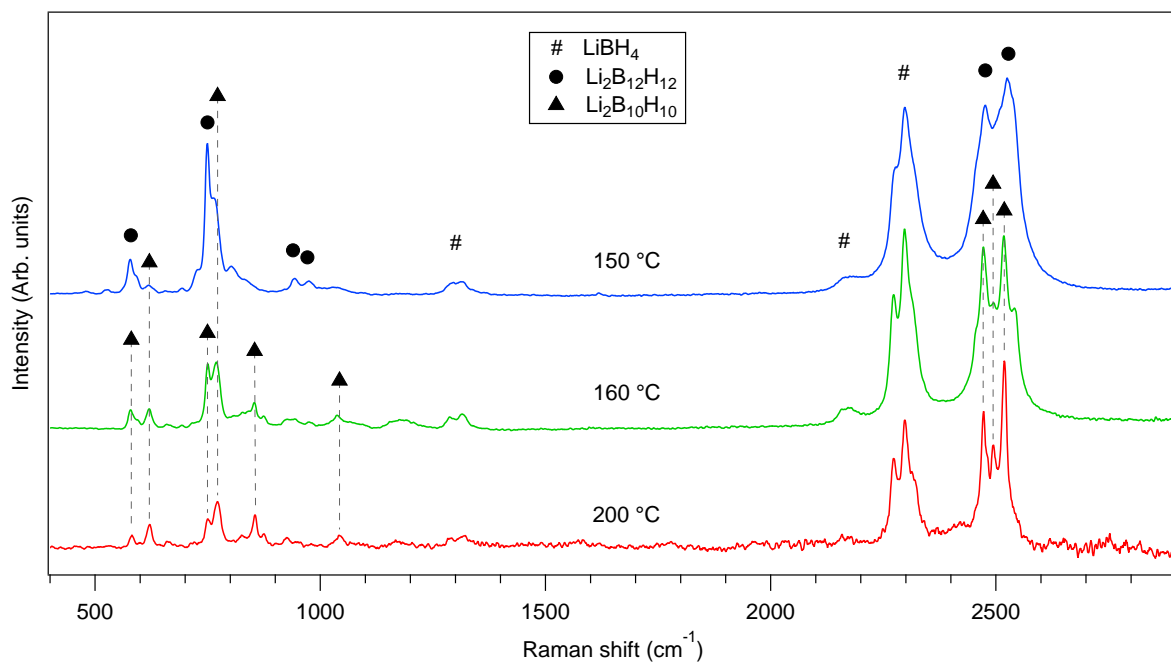
Figure 7.4 Room temperature Raman spectra of the samples of LiBH$_4$ exposed to B$_2$H$_6$ for 40 h at 150, 160 and 200 °C, respectively.
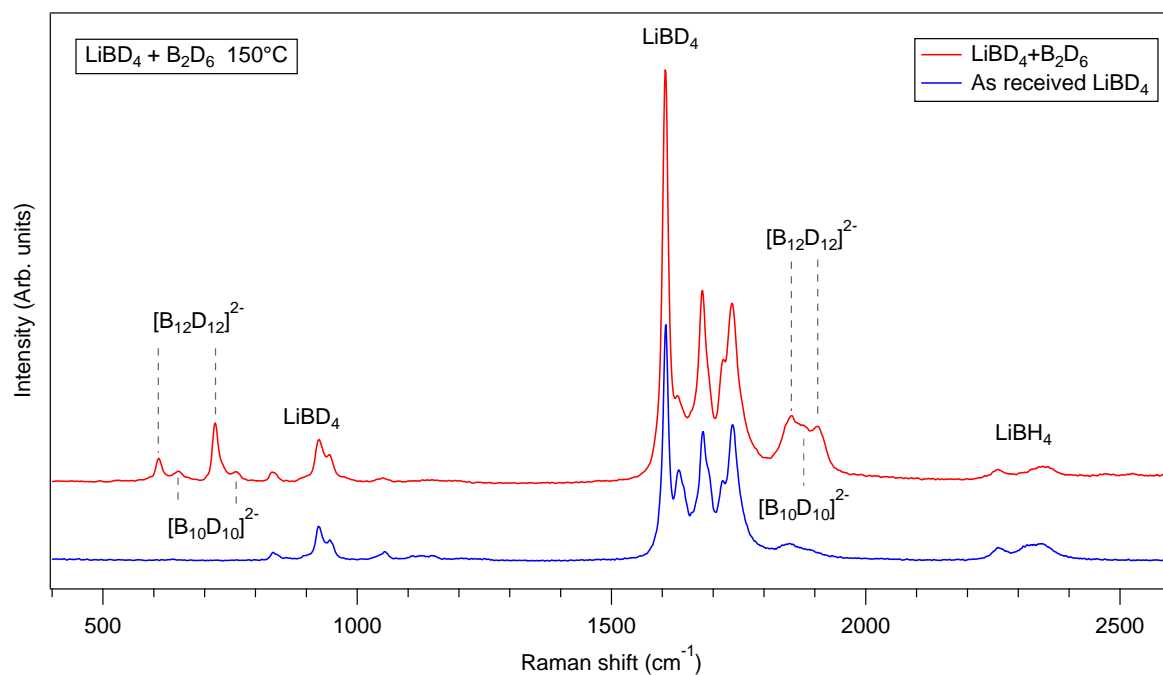
Figure 7.5 Raman spectra of LiBD$_4$ before and after exposure to B$_2$D$_6$ for 40 h at 150 °C.

The v_1 (A_{1g}) and v_3 (H_g) modes appear to mainly originate from BH stretching, as their H/D isotopic ratios of 1.33 and 1.34 respectively, are very close to the value of 1.36 that would be expected if only H and D atoms are involved. The close agreement of the H/D ratio for v_2

(1.04) indicates that only a single B-B unit participates in the vibration (i.e. close to the ideal H/D ratio of 1), with little or no effect on the BH stretch force constant. The v_5 mode, with an intermediate H/D value of 1.25, involves movements of both H and B atoms against the stretching and bending force constants (Muetterties *et al.*, 1962). In general, the vibrational assignment of $Li_2B_{12}H_{12}$ was consistent with results from previous studies (Leites *et al.*, 1982; Cyvin *et al.*, 1986).

Furthermore, the v_1 at 2529 cm⁻¹ and v_3 at 2474 cm⁻¹ from $Li_2B_{12}H_{12}$ exhibit notable peak broadening with half-width half maximum (HWHM) of 49 and 54 cm⁻¹, due to the formation of a small amount of $Li_2B_{10}H_{10}$ whose vibrational bands (at ~2519 and 2473 cm⁻¹) overlap with those of $Li_2B_{12}H_{12}$. With increasing reaction temperature to 160 °C, the peak intensity of $Li_2B_{12}H_{12}$ (e.g. v_2 at 749 cm⁻¹, v_4 at 943 cm⁻¹ and v_6 at 580 cm⁻¹) decreased. Vibrations from $Li_2B_{10}H_{10}$ were predominant in the spectrum at 200 °C, and only the v_2 mode could be confirmed for $Li_2B_{12}H_{12}$ due to low peak intensities of the other vibrations and to $Li_2B_{10}H_{10}$ bands overlapping. For all three samples after the reaction, residual $LiBH_4$ was observed in the Raman spectra in the form of $[BH_4]^-$ stretching bands at 2200-2400 cm⁻¹ and bending bands at 1200-1400 cm⁻¹. The change in abundance of each phase in the Raman spectra as a function of temperature is in good agreement with results from the XRD measurements.

Table 7.3 lists the vibrational frequencies of $Li_2B_{10}H_{10}$ ($Li_2B_{10}D_{10}$) in accordance to the vibrations of solid $K_2B_{10}H_{10}$. The Raman spectrum for the $LiBH_4$+B_2H_6 sample heated to 200 °C has peaks at 2519, 2495, 1043, 855, 751 and 622cm⁻¹ which may be attributed to the A_1 modes of $[B_{10}H_{10}]^{2-}$ anion, whereas the peaks at 2473, 771 and 582 cm⁻¹ are due to the E_2 and E_3 modes. Only two A_1 and one E_2+E_3 mode were observed for $Li_2B_{10}D_{10}$ in the $LiBD_4$+B_2D_6 sample heated at 150 °C, due to the weak intensity Raman peaks (with respect to the relatively noisy spectrum background). The isotopic ratios are close to values for the $K_2B_{10}H_{10}$, supporting the assignments.

Table 7.3 Assignment of Raman vibrations of: $\mathrm{Li_2B_{10}H_{10}}$ from a $\mathrm{LiBH_4}$ sample exposed to $\mathrm{B_2H_6}/\mathrm{H_2}$ at 150 °C; and $\mathrm{Li_2B_{10}D_{10}}$ from $\mathrm{LiBD_4}$ exposed to $\mathrm{B_2D_6}/\mathrm{D_2}$ at 150 °C (s = strong; m = medium; w = weak; sh = shoulder; $\mathrm{B_v}$ = vertex B atom, $\mathrm{B_e}$ = equatorial B atom)

Symmetry Mode	$\mathrm{Li_2B_{10}H_{10}}$	$\mathrm{K_2B_{10}H_{10}}$	$\mathrm{Li_2B_{10}D_{10}}$	$\mathrm{K_2B_{10}D_{10}}$ *	Li H/D	K H/D *	Vibrations *
A_1 (Raman)	2519	2524 m		1898			$\mathrm{B_v}$-H
	2495	2495 m	1877	1862	1.33	1.33	$\mathrm{B_e}$-H
	1043	1013 m		970			mainly B-B
	855	838 s	762	756	1.12	1.11	mainly B-B
	751	747 s		610			mainly B-B
	622	620 m		540			mainly BBH
E_2 and E_3 (Raman)	2473	2460 m		1840			$\mathrm{B_e}$-H
	771	785 w,sh	649	658	1.19	1.15	
	582	580 w		531			

* (Leites *et al.*, 1983)

Therefore, both the Raman spectra and XRD patterns demonstrate the formation of $\mathrm{Li_2B_{12}H_{12}}$ and $\mathrm{Li_2B_{10}H_{10}}$ by the reaction of $\mathrm{LiBH_4}$ with $\mathrm{B_2H_6}$ between 150 and 200 °C. This result agrees well with the reaction proposed by Friedrichs *et al.* (2010c). Furthermore, to the best of my knowledge, this is the first time that crystalline and vibrational evidence has shown the formation of $\mathrm{Li_2B_{10}H_{10}}$ via the reaction of diborane gaseous reaction with $\mathrm{LiBH_4}$: the study by (Friedrichs *et al.*, 2010c) only reported the formation of amorphous $\mathrm{Li_2B_{10}H_{10}}$. The predominant formation of either $\mathrm{Li_2B_{12}H_{12}}$ or $\mathrm{Li_2B_{10}H_{10}}$ is temperature-dependent competitive reactions: $\mathrm{Li_2B_{10}H_{10}}$ formed and appeared to be more stable than $\mathrm{Li_2B_{12}H_{12}}$ at higher temperatures (up to 200 °C).

In terms of thermal decomposition of $\mathrm{LiBH_4}$, the formation of $\mathrm{Li_2B_{12}H_{12}}$ as a reaction product has been demonstrated upon heating to around 350 °C (Ohba *et al.*, 2006; Orimo *et al.*, 2006; Reed and Book, 2009) and was suggested as a result of the reaction of $\mathrm{B_2H_6}$ and $\mathrm{LiBH_4}$ (Friedrichs *et al.*, 2010c). However, as $\mathrm{B_2H_6}$ is unstable at high temperatures (> 250 °C) and its thermolysis is at the basis of a very rich chemistry (Soderlund *et al.*, 2005), it is still not clear whether other higher boranes (including ionic and neutral compounds, e.g. $\mathrm{BH_4^-}$, $\mathrm{B_{10}H_{14}}$ etc.) play a role in the decomposition of $\mathrm{LiBH_4}$.

7.3   LiH + B_2H_6

Figure 7.6 is the XRD refinement file on the LiH sample after being exposed to a B_2H_6/H_2 gas mixture at 120 °C for 40 h. The reaction products were identified and quantified to be: 29(1) wt% LiH, 67(1) wt% LiBH$_4$, and 4(1) wt% Li$_2$B$_{12}$H$_{12}$. These values are close to those reported by (Friedrichs *et al.*, 2009a) for a LiH sample after diborane absorption at 150 °C: 25.9 wt% LiH, 72.2 wt% LiBH$_4$ and 1.9 wt% Li$_2$B$_{12}$H$_{12}$. The lattice parameters for orthorhombic LiBH$_4$ were determined to be *a* = 7.166(9) Å, *b* = 4.434(6) Å, *c* = 6.821(9) Å and *V* = 216.7(5) Å^3, which is consistent with the parameter reported for pure LiBH$_4$ (Soulié *et al.*, 2002).

LiH	29.04 %
o-LiBH4	66.83 %
Li2B12H12	4.13 %
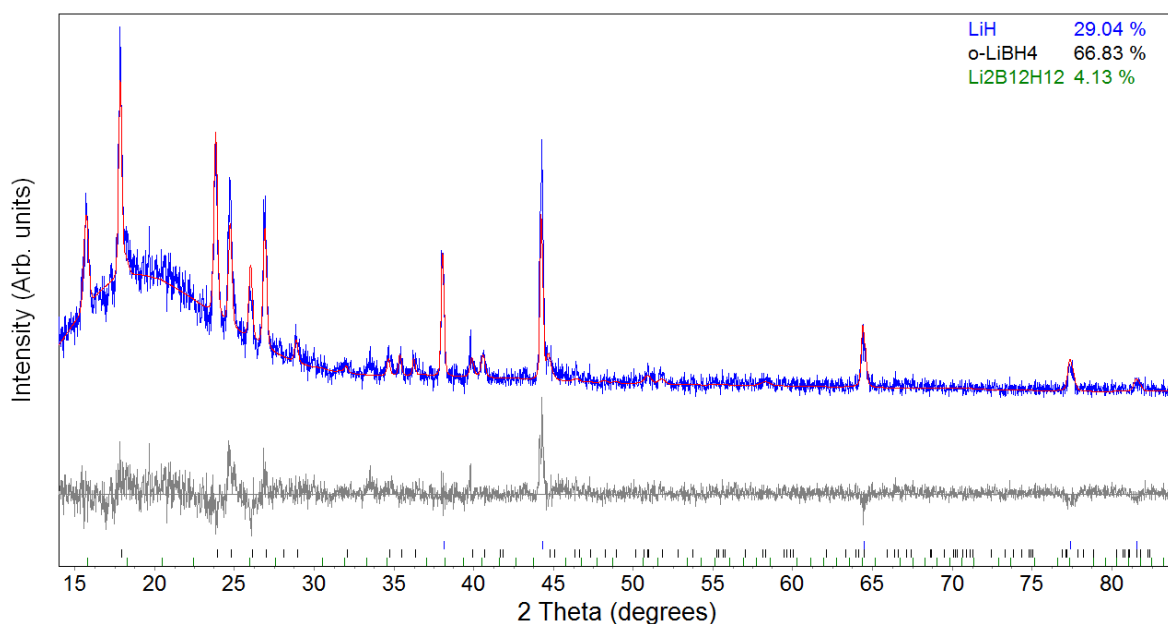
Figure 7.6 Rietveld refined XRD pattern of the reaction products of LiH that had been heated in B_2H_6 /H$_2$ to 120 °C for 40 h. Blue: raw data; Red: calculated data, Grey: difference curve (observed – calculated). Goodness of fit = 1.181.

Figure 7.7 is the room-temperature ex situ Raman spectrum of the newly formed LiBH$_4$ by heating LiH in B_2H_6 at 120 °C. The vibrational bending and stretching modes of o-LiBH$_4$ could be identified between 1250-1350 cm^{-1} and 2100 and 2400 cm^{-1}, respectively: the wavenumbers are consistent with those for the [BH$_4$]$^-$ anion for pure LiBH$_4$ (see Chapter 4.1.2). The LiH emitted broad Raman bands centered at around 506 and 1108 cm^{-1}, and

172

possibly a shoulder between 2000-2130 cm^{-1}, which is also observed in as-received LiH material. In addition, a small amount of Li$_2$B$_{12}$H$_{12}$ also appeared, giving Raman active modes of A$_{1g}$ modes v_1 (2524 cm^{-1}) and v_2 (748 cm^{-1}) and of H$_g$ modes v_3 (2486 cm^{-1}) and v_6 (579 cm^{-1}). The formation of Li$_2$B$_{12}$H$_{12}$ was possibly a result of the newly formed LiBH$_4$ subsequently reacting with excess B$_2$H$_6$.
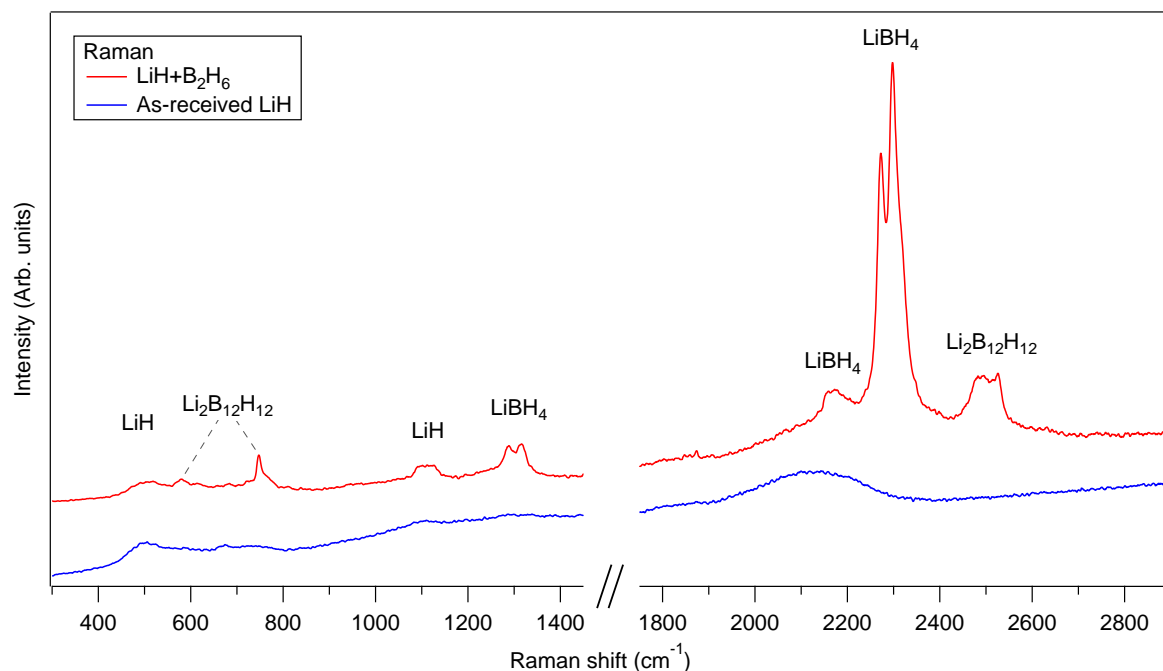
Figure 7.7 Room temperature Raman spectra of as-received LiH and LiH that had been heated in B$_2$H$_6$/H$_2$ to 120 °C for 40 h.

Residual LiH indicates that this reaction with diborane stopped after about 46 mol% of LiH was consumed, yielding LiBH$_4$. Therefore, the reaction was not only taking place on the surface of the LiH, but also in the bulk of the material. However, the B$_2$H$_6$ may then further react with the newly formed LiBH$_4$ to produce a layer of Li$_2$B$_{12}$H$_{12}$ on the surface.

Gremaud *et al.* (2011) recently demonstrated that [BH$_4$]$^-$ ions were formed from the splitting of B$_2$H$_6$, replacing the H$^-$ ions of LiH to form LiBH$_4$. Thus, the diffusion of [BH$_4$]$^-$ and Li$^+$ to exchange H$^-$ with LiH inside of the bulk material, could be the limiting steps for the LiH+B$_2$H$_6$ reaction, rather than the formation of the B-H bond. By using SEM secondary electron images and TEM-EELS, Friedrichs *et al.* (2010a) found that a boron-containing shell

(thickness ~3 μm) was formed on the surface of the LiD powder (particle size 30-100 μm) after reaction with B_2D_6. As $LiBH_4$ has been known to possess a high ion mobility in the hexagonal phase above 118 °C (Matsuo *et al.*, 2007), the $LiH+B_2H_6$ reaction probably stopped due to the $Li_2B_{12}H_{12}$ passivation layer which impeded both $[BH_4]^-$ species migrating into the particles and Li^+ diffusing towards the exterior (as sketched in **Figure 7.8**).
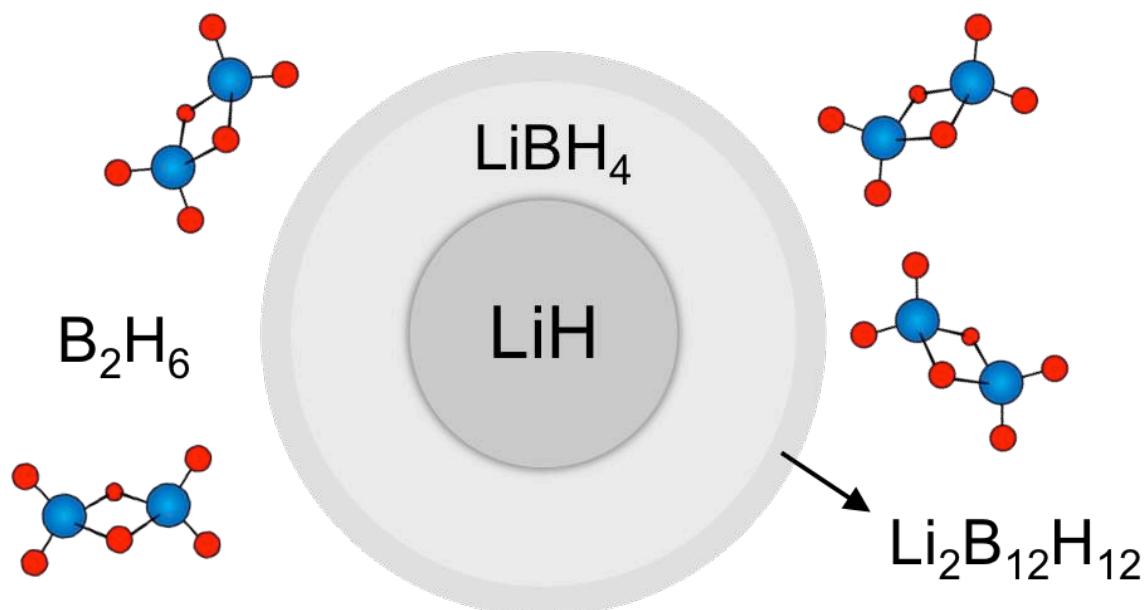
Figure 7.8 Sketch of the core shell structure of $LiBH_4$ and $Li_2B_{12}H_{12}$ which form due to surface reactions between B_2H_6 + LiH and B_2H_6 + the newly formed $LiBH_4$, respectively.

7.4 Reaction of B_2H_6 and other borohydrides / hydrides

An initial investigation into the effect of B_2H_6 on $M(BH_4)_x$ or MH_x (where M = Na, Mg or Ca; x = 1 or 2) has also been carried out at various temperatures.

7.4.1 $NaBH_4$ or NaH + B_2H_6 / H_2

After exposing $NaBH_4$ to a B_2H_6/H_2 gaseous mixture at 150 or 200 °C, no new compounds formed according to the XRD (**Figure 7.9**) and Raman (**Figure 7.10**) results, and the starting cubic $NaBH_4$ phase in the samples appears to have maintained its crystallinity. The lattice parameter of the cubic $NaBH_4$ phase was a = 6.166(1) Å before and after the B_2H_6/H_2 heat-treatment.
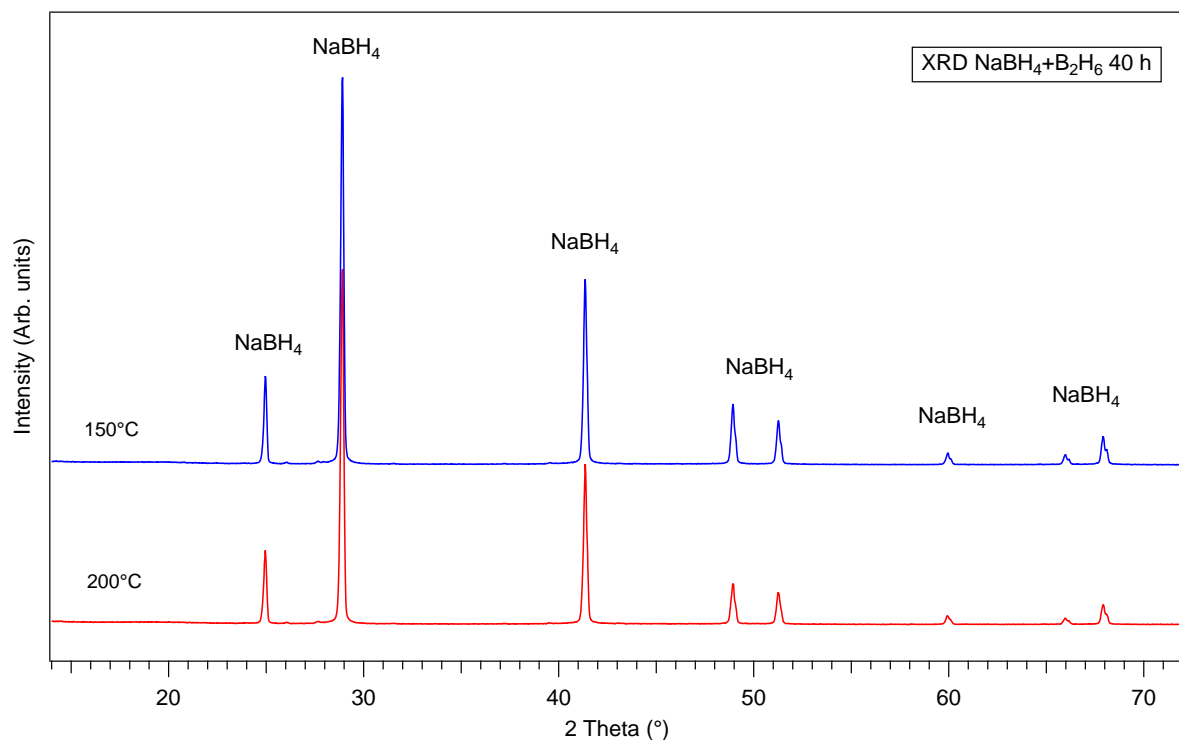
Figure 7.9 Ex situ room temperature XRD patterns of $NaBH_4$ that had been exposed to B_2H_6/H_2 at 150 and 200 °C for 40 h.
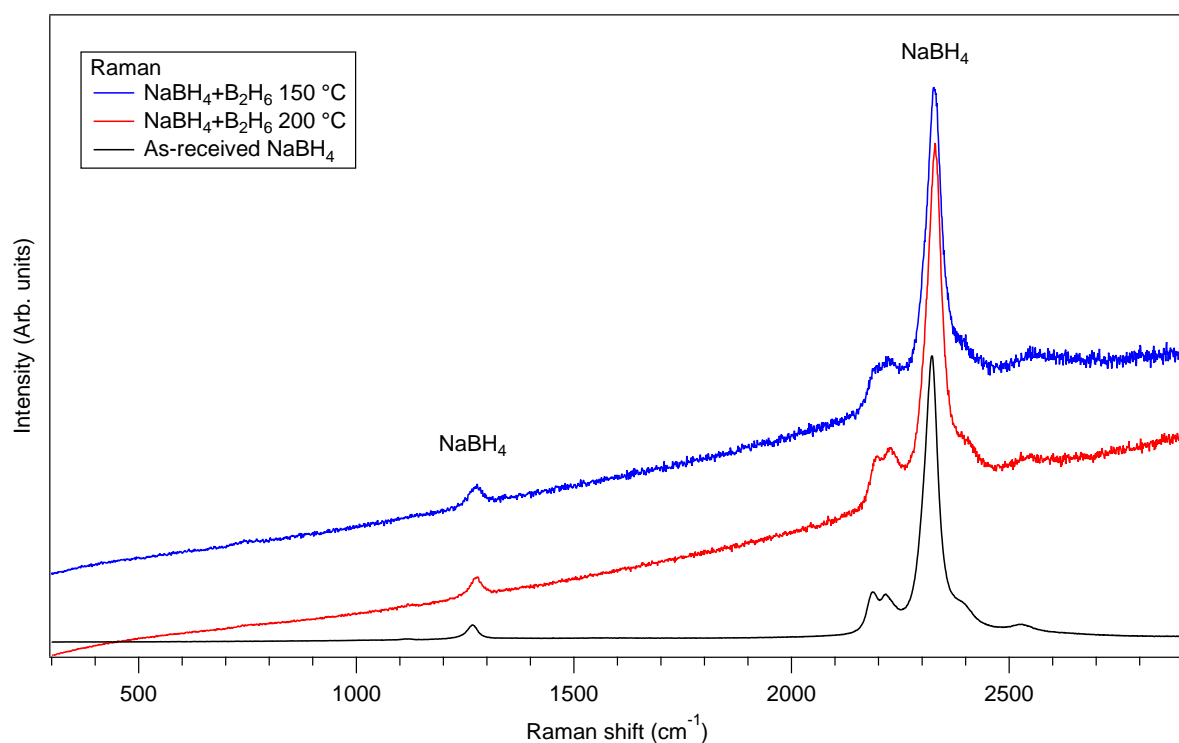
Figure 7.10 Ex situ room temperature Raman spectra of as received $NaBH_4$ and of $NaBH_4$ samples that had been exposed to B_2H_6/H_2 for 40 h at 150 °C and 200 °C. The intensity of the spectrum for as-received $NaBH_4$ is multiplied by 0.5 times, to make comparison easier.

However, a yield of approximately 7 mol% $NaBH_4$ and 0.6 mol% $Na_2B_{12}H_{12}$ were synthesised through the reaction between NaH and B_2H_6. A small diffraction at 15.3° 2θ (d = 5.8 Å) was observed in the XRD data (**Figure 7.11**), which was consistent with the most intense diffraction peak for the pure $Na_2B_{12}H_{12}$ (Her *et al.*, 2009).
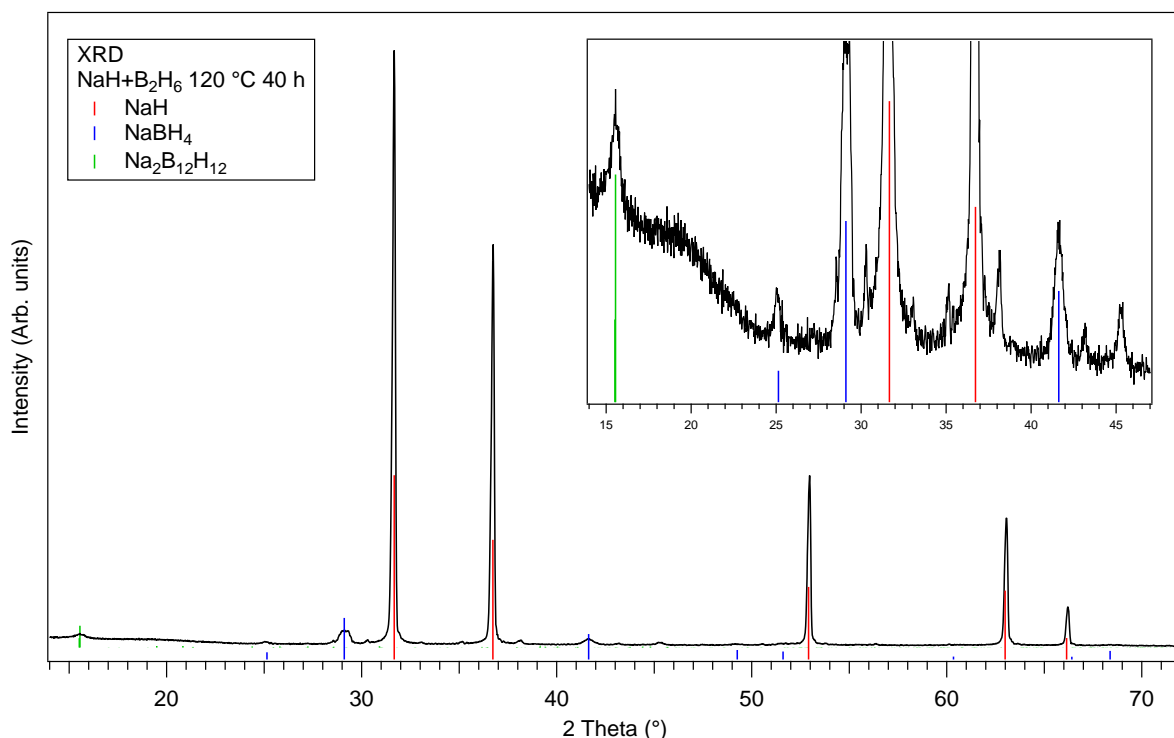
Figure 7.11 Ex situ room temperature XRD pattern of NaH that had been heated in B_2H_6/H_2 to 120 °C for 40 h. The inset window shows the part of the pattern between 14 and 47° 2θ in more detail. Vertical bars (|) are the Bragg positions for the pure compounds from the Inorganic Crystal Structure Database (ICSD Web, 2013).

Furthermore, Raman peaks at 2524 and 746 cm^{-1} are very close to the frequencies for the A_{1g} modes of pure $K_2B_{12}H_{12}$, and the peaks at 2458, 980, 944 and 579 cm^{-1} belong to the H_g modes, as shown in **Figure 7.12**. $Na_2B_{12}H_{12}$ has been reported to be stable up to 587 °C (Udovic *et al.*, 2014). Since no higher borane compound was found in the $NaBH_4$+B_2H_6 samples heated to 150 and 200 °C, it is unlikely that $Na_2B_{12}H_{12}$ was formed via the newly formed $NaBH_4$ from the reaction of NaH+B_2H_6 at 120 °C. Indeed, $Na_2B_{12}H_{12}$ could not be formed during the thermal decomposition of $NaBH_4$ but rather NaB_3H_8 (Caputo *et al.*, 2010). However, in this work, NaB_3H_8 might have only appeared as an intermediate and

subsequently reacted with B_2H_6 to form $NaB_{12}H_{12}$, which explains the absence of this compound in both Raman [i.e. at 2435 cm^{-1} (very strong, broad), 2146 cm^{-1} (medium, broad), 810 cm^{-1} (medium, broad) for aqueous $[B_3H_8]^-$ (Tomkinson *et al.*, 1979)] and XRD patterns [e.g. intense peaks at 22.6°, 24.7° and 27.2° 2θ (Dunbar *et al.*, 2013)]. Therefore, the formation of $Na_2B_{12}H_{12}$ (possibly via NaB_3H_8) and $NaBH_4$ are competing reactions when heating NaH in B_2H_6/H_2.
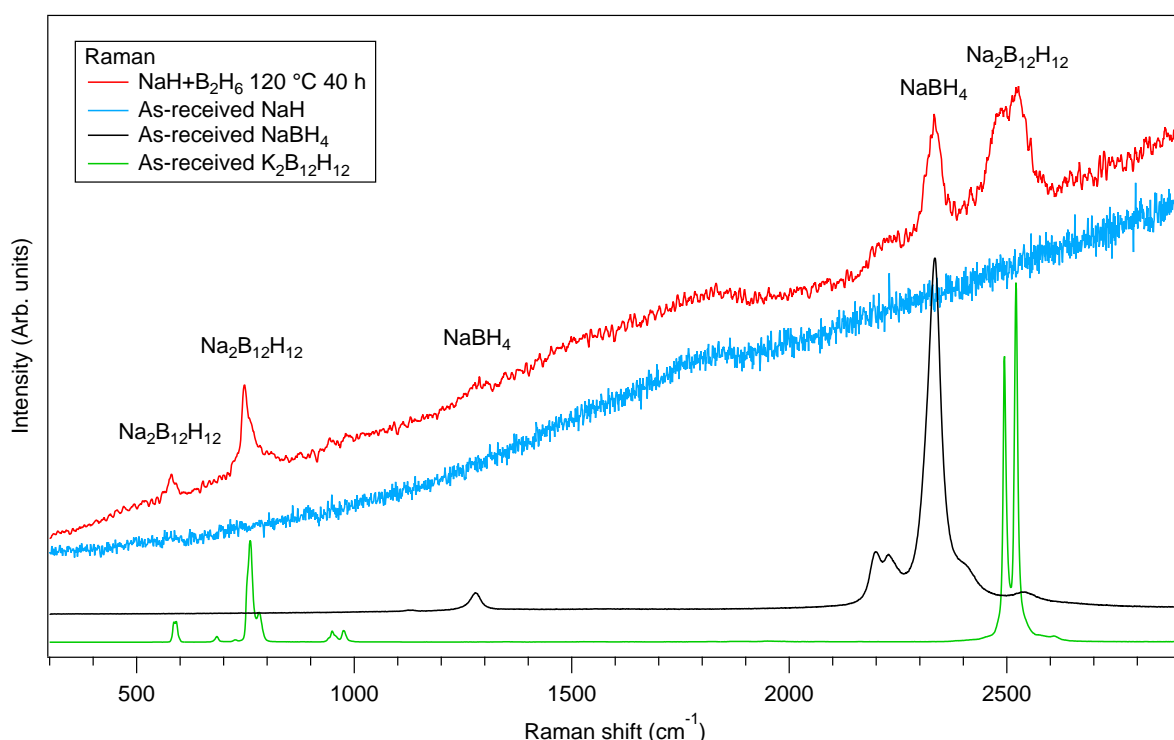
Figure 7.12 Ex situ room temperature Raman spectrum NaH that had been heated to 120 °C in B_2H_6/H_2 for 40 h, compared with the Raman spectra for pure NaH, $NaBH_4$ and $K_2B_{12}H_{12}$. All the spectra were normalised in intensity to allow easier comparison.

7.4.2 Mg(BH$_4$)$_2$ or MgH$_2$ + B$_2$H$_6$ / H$_2$

After exposing samples of $Mg(BH_4)_2$ to a B_2H_6/H_2 atmosphere at 150 and 200 °C, Raman spectra (**Figure 7.13**) showed peaks at 2542, 830, 742 and 612 cm^{-1} which are at similar frequencies to the unknown peaks observed during the heating of the γ-$Mg(BH_4)_2$ samples (**Figure 5.10**, p135). The peaks at 2542, 742 and 612 cm^{-1} are at similar frequencies to those found for $[B_{10}H_{10}]^{2-}$, as discussed for the $Li_2B_{10}B_{10}$ and $K_2B_{10}H_{10}$ compounds in

previous sections. Although a recent study by (Remhof *et al.*, 2014) showed that $Mg(B_3H_8)_2$, $MgB_{10}H_{10}$ and $MgB_{12}H_{12}$ were observed after milling $Mg(BH_4)_2$ in B_2H_6 at 100-150 °C, it was difficult to assign the unknown Raman peaks in this work to those compounds due to the relatively high fluorescence background in the Raman spectra.
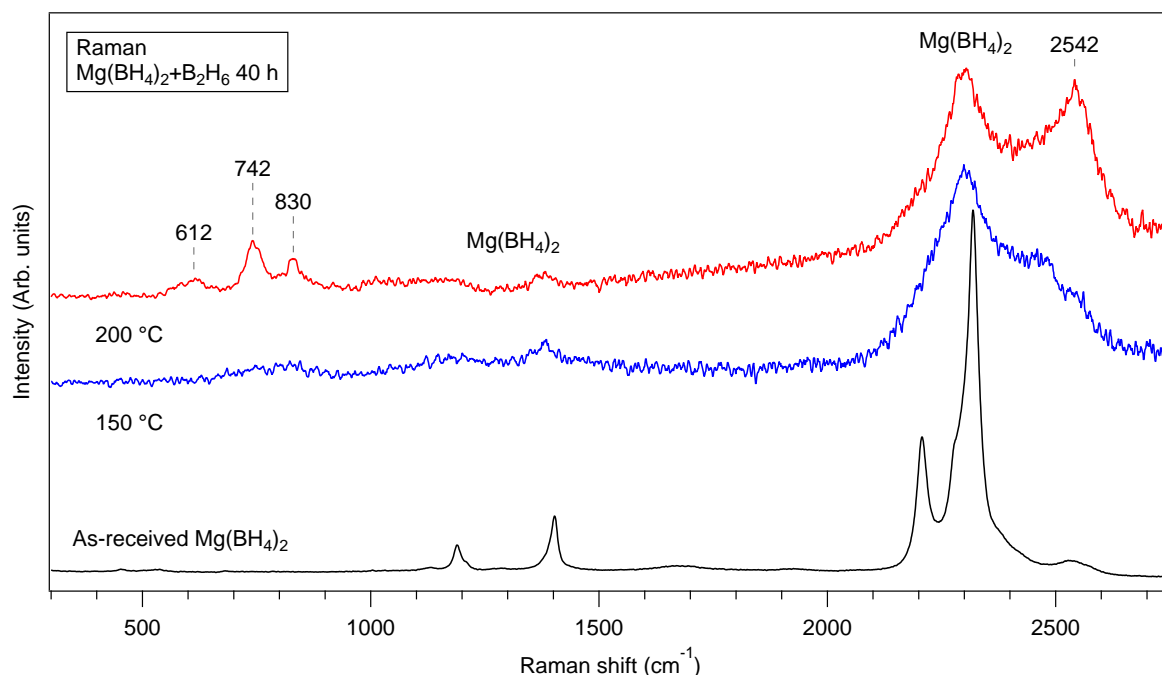
Figure 7.13 Ex situ room temperature Raman spectra of $Mg(BH_4)_2$ that had been heated in B_2H_6/H_2 to 150 and 200 °C for 40 h, compared to the spectra for as-received $Mg(BH_4)_2$. In order to allow an easier comparison, the intensities of all the spectra were normalised, and the intensity of the $Mg(BH_4)_2$ spectrum was also multiplied by 0.5 times. The grey dashed line above Raman peaks is added a a guide for the eye.

There was no crystalline (**Figure 7.14**) or vibrational (**Figure 7.15**) evidence for the formation of $Mg(BH_4)_2$ by heating either as-received or milled MgH_2 in a B_2H_6/H_2 atmosphere to between 120 and 200 °C, compared to the yield of 73% $Mg(BH_4)_2$ formed by milling MgH_2 in B_2H_6 for 145 h reported by (Remhof *et al.*, 2014). This might be due to the slow diffusion rate of atomic H through the MgH_2 layer to exchange with $[BH_4]^-$ clusters from the absorbed B_2H_6.
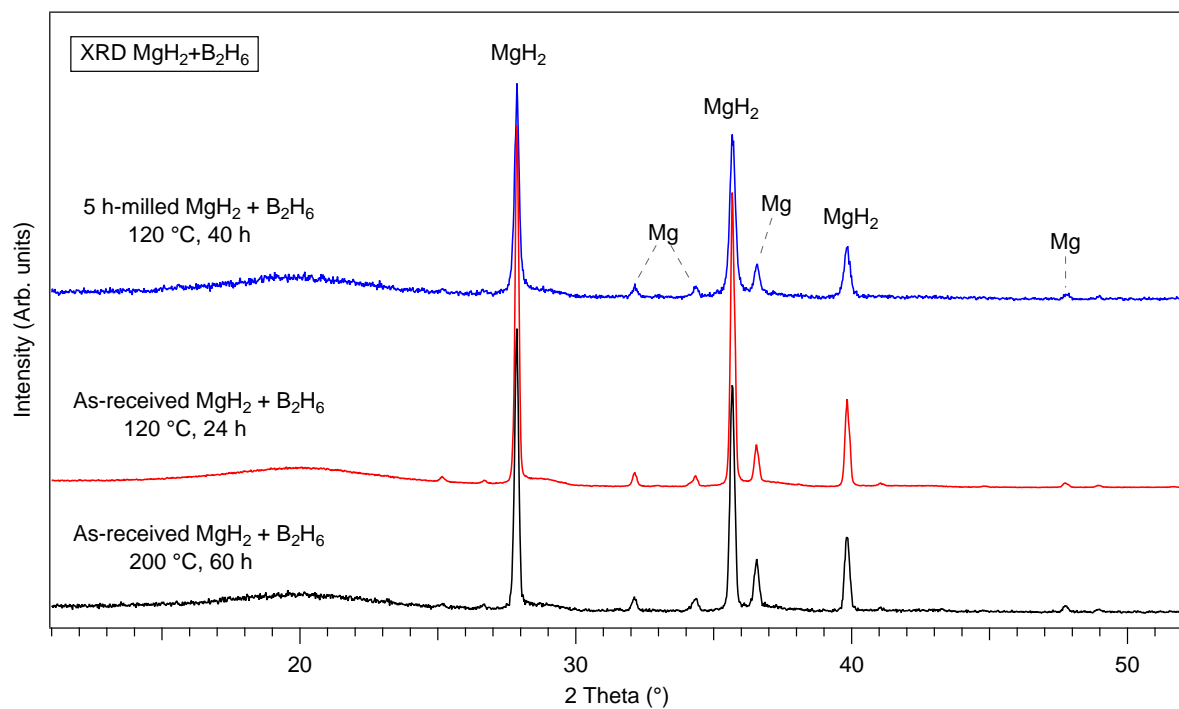
Figure 7.14 Ex situ room temperature XRD patterns of MgH_2 heated in $\mathrm{B}_2\mathrm{H}_6/\mathrm{H}_2$ to 120-200 °C for 24-60 h.
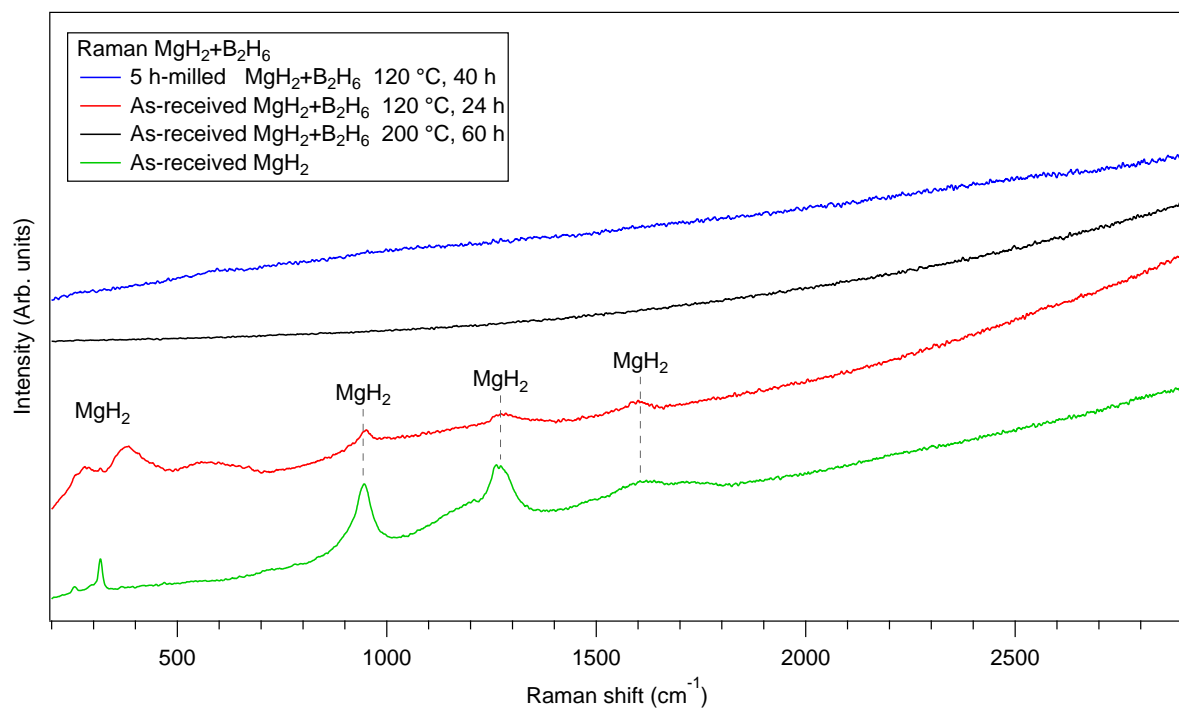
Figure 7.15 Ex situ room temperature Raman spectra of MgH_2 heated in $\mathrm{B}_2\mathrm{H}_6/\mathrm{H}_2$ to 120-200 °C for 24-40 h, compared with the spectra for as-received MgH_2. All the spectra were normalised in order to allow easier comparison.

179

7.4.3   Ca(BH₄)₂ + B₂H₆ / H₂

For $Ca(BH_4)_2$ heated in B_2H_6/H_2 for 40 h at 120 °C, the starting α- and β-$Ca(BH_4)_2$ phases remained as the only crystalline phases according to the XRD pattern (**Figure 7.16**), whereas the sample heated to 200 °C contained β-$Ca(BH_4)_2$ phase and a broad diffraction centered at 10.5° 2θ (d = 8.4 Å). As discussed in Chapter 6, it is known that an irreversible transformation from the α- to the β-phase occurs in $Ca(BH_4)_2$ at around 180 °C.
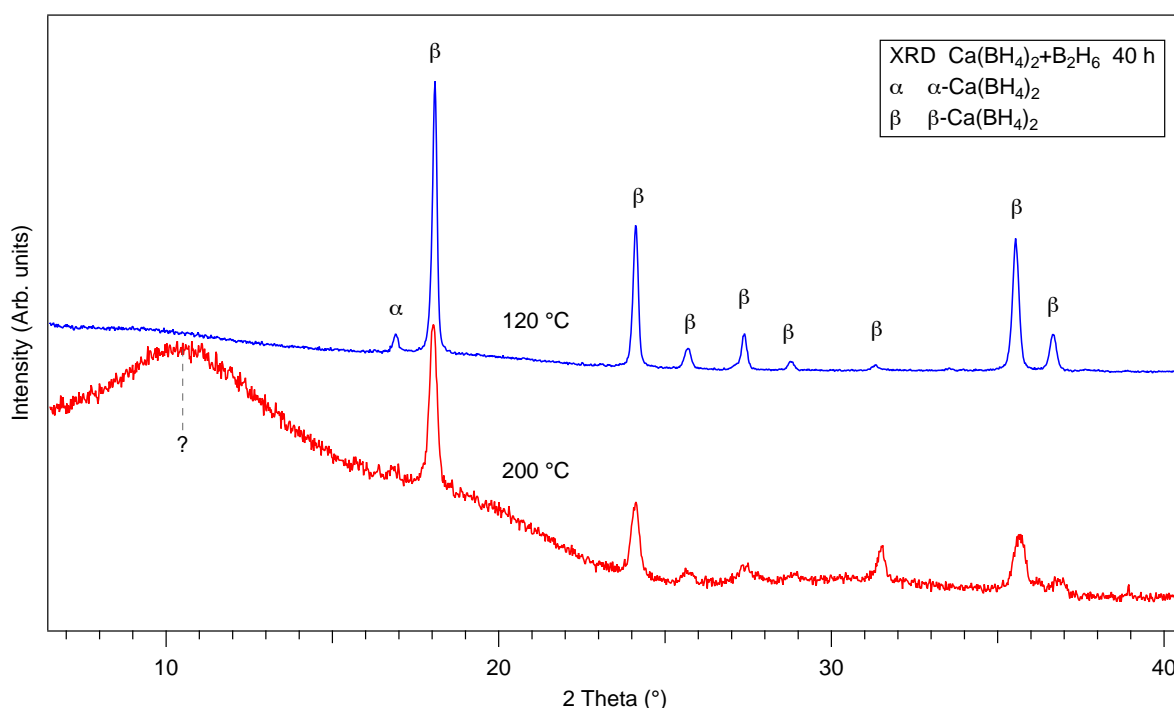
Figure 7.16 Ex situ room temperature XRD patterns of $Ca(BH_4)_2$ that had been heated in B_2H_6/H_2 for 40 h at 120 and 200 °C .

The Raman spectra (**Figure 7.17**) however, gave more information on the reaction products: showing peaks at 2570, 997, 885, 741,709 (shoulder), 577 cm^{-1} at 120 °C, of which 997, 885 and 709 cm^{-1} disappeared at 200 °C, and suggesting at least two intermediates formed during the reaction. There was high similarity between peaks at 2570, 741, and possibly 577 cm^{-1} to the calculated frequencies for $CaB_{12}H_{12}$ (Reed, 2011). The peak at 855 cm^{-1} was potentially fitted with the calculated Raman mode for CaB_2H_2 which was proposed as

an intermediate during $Ca(BH_4)_2$ decomposition (Vajeeston *et al.*, 2011). The Raman results might explain the formation of amorphous bump in XRD pattern.
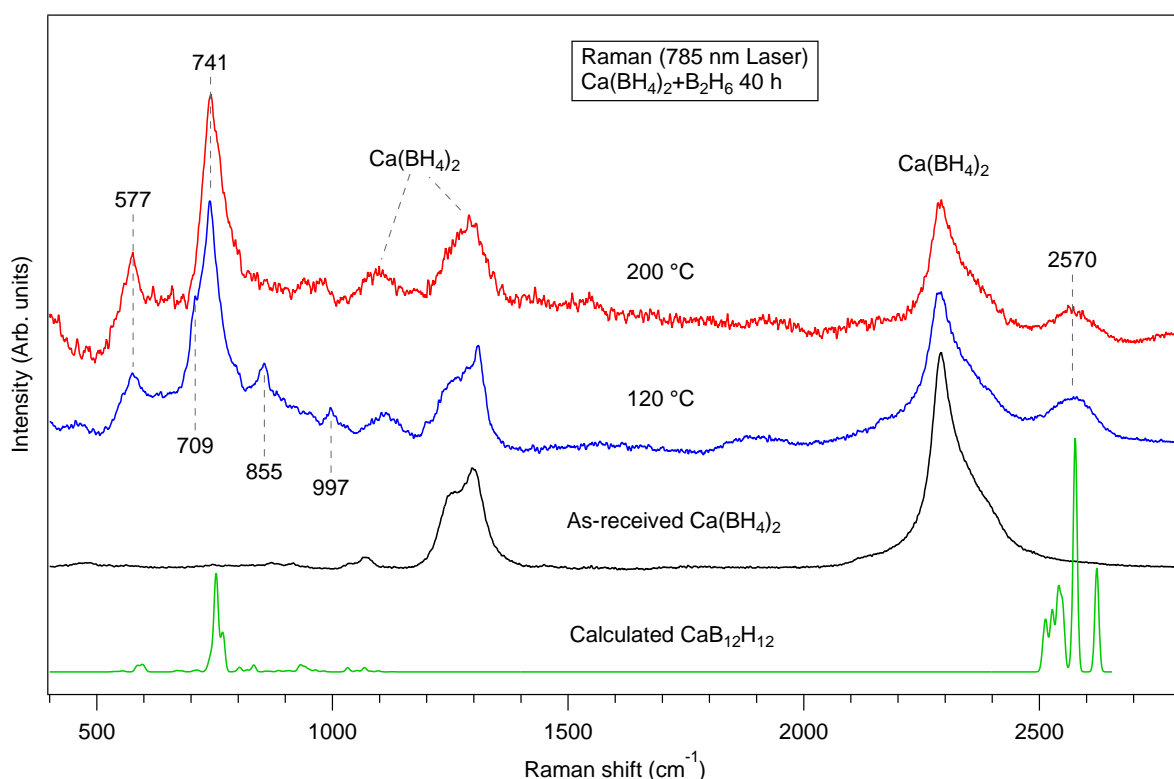
Figure 7.17 Ex situ room temperature Raman spectra of $Ca(BH_4)_2$ that has been heated in B_2H_6/H_2 for 40 h at 120 and 200 °C, compared to the measured spectrum for as-received $Ca(BH_4)_2$ and the calculated spectrum for $CaB_{12}H_{12}$. To allow an easier comparison the intensity of all the spectra were normalised and the intensity of the $Ca(BH_4)_2$ spectrum was also multiplied by 0.5 times. The grey dashed lines over the Raman peaks are given as a guide for the eye.

7.5   General discussion and conclusions

In this work, the vibrational structures of commercial crystalline $K_2B_{12}H_{12}$ and $K_2B_{10}H_{10}$ have been studied using Raman and IR spectroscopies, and the assignment of the observed bands is in good agreement with literature data: this is a useful data resource to help better understand the vibrational patterns of other analogue closo-dodecaborate, e.g. $Li_2B_{12}H_{12}$ and $MgB_{12}H_{12}$.

The resulting products after the reaction between $M(BH_4)_n$ / MH_n (M = Li, Na, Mg, or Ca; n = 1 or 2) and B_2H_6, are summarised in **Table 7.4**.

Table 7.4 Summary of the resulting products from the reaction between B_2H_6 and $M(\text{BH}_4)_x$/ $M\text{H}_x$ (M = Na, Mg, Ca; x = 1 or 2). All the samples were treated for 40 h, except for MgH_2 which was held for 24 h, 40 h and 60 h. "—" indicates that no sample was made.

Starting material	Reaction temperature and products		
	120 °C	150 °C	200 °C
LiBH_4	—	o-LiBH_4, $\text{Li}_2\text{B}_{12}\text{H}_{12}$, $\text{Li}_2\text{B}_{10}\text{H}_{10}$	o-LiBH_4, $\text{Li}_2\text{B}_{10}\text{H}_{10}$, a small amount of $\text{Li}_2\text{B}_{12}\text{H}_{12}$
LiH	LiH, o-LiBH_4, $\text{Li}_2\text{B}_{12}\text{H}_{12}$	—	—
NaBH_4	—	NaBH_4	NaBH_4
NaH	NaH, NaBH_4, $\text{Na}_2\text{B}_{12}\text{H}_{12}$	—	—
$\text{Mg(BH}_4)_2$	—	$\text{Mg(BH}_4)_2$, amorph. phase	$\text{Mg(BH}_4)_2$, amorph. $\text{MgB}_{10}\text{H}_{10}$?
MgH_2 (as-received/ 5 h-milled)	MgH_2, Mg (from starting material)	MgH_2, Mg (from starting material)	MgH_2, Mg (from starting material)
$\text{Ca(BH}_4)_2$	α+β-$\text{Ca(BH}_4)_2$, amorph. $\text{CaB}_{12}\text{H}_{12}$? & CaB_2H_2?	—	β-$\text{Ca(BH}_4)_2$, amorph. $\text{CaB}_{12}\text{H}_{12}$?

Higher borane compounds of (partially) crystalline $\text{Li}_2\text{B}_{12}\text{H}_{12}$ and $\text{Li}_2\text{B}_{10}\text{H}_{10}$ could be produced by reacting LiBH_4 powder with gaseous B_2H_6 between 150 and 200 °C; and $\text{Li}_2\text{B}_{10}\text{H}_{10}$ appeared to be more stable than $\text{Li}_2\text{B}_{12}\text{H}_{12}$ at higher temperatures. Both these compounds showed a similar vibrational structure to those of crystalline $\text{K}_2\text{B}_{12}\text{H}_{12}$ and $\text{K}_2\text{B}_{10}\text{H}_{10}$. In addition, solvent-free LiBH_4 with a yield of 46 mol%, has been successfully synthesised by exposing LiH to B_2H_6, although a tiny amount of undesirable $\text{Li}_2\text{B}_{12}\text{H}_{12}$ (0.4 mol%) was also formed as a by-product on the surface of the LiBH_4 powder. The formation of $\text{Li}_2\text{B}_{12}\text{H}_{12}$ was probably due to a subsequent reaction between the newly formed LiBH_4 and B_2H_6 to form a passivation layer of $\text{Li}_2\text{B}_{12}\text{H}_{12}$ on the surface of the LiBH_4 powder: this impeded the further absorption of B_2H_6 by LiH. By combining the results from previous studies (Gremaud *et al.*, 2011), the reactions of LiH/LiBH_4 and B_2H_6 in a temperature region of 120-200 °C could be proposed as follows:

$$B_2H_6 \rightarrow [BH_2]^+ + [BH_4]^- + B_xH_y \qquad\qquad (7.1)$$

$$LiH + [BH_2]^+ + [BH_4]^- \rightarrow LiBH_4 + BH_3 \qquad\qquad (7.2)$$

$$LiBH_4 + B_xH_y \rightarrow Li_2B_{12}H_{12} + H_2 \qquad 120\text{-}200\ ^\circ C \quad (7.3)$$

$$\rightarrow Li_2B_{12}H_{12} + H_2 \qquad 150\text{-}200\ ^\circ C \quad (7.4)$$
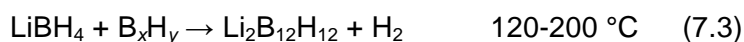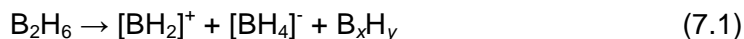
(*to be balanced*)

With respect to the decomposition process of $LiBH_4$, the formation of $Li_2B_{12}H_{12}$ was observed upon heating to 450 °C (see Section 4.2, p111-113). This can be now explained by the reaction between diborane (or similar borane species) with the remnant bulk $LiBH_4$ to form $Li_2B_{12}H_{12}$ and possibly $Li_2B_{10}H_{10}$. Since $Li_2B_{12}H_{12}$ or other higher *closo*-boranes are too stable (and may therefore be considered undesirable impediments to achieving reversibility in $LiBH_4$), controlling B_2H_6 might be the key to allowing hydrogen cycling of $LiBH_4$ under more moderate conditions (of temperature and pressure).

$NaBH_4$ with a yield of 7 mol% was synthesised via the reaction of NaH and B_2H_6, although 0.6 mol% $NaB_{12}H_{12}$ was also present as a stable by-product. Unlike the formation of $Li_2B_{12}H_{12}$, the $Na_2B_{12}H_{12}$ was probably formed via the reaction of absorbed diborane with the newly formed intermediate NaB_3H_8 rather than a reaction between diborane and $NaBH_4$ (Caputo *et al.*, 2010). However, it is not clear if the formation of $NaBH_4$ itself originated from the diborane-absorption of NaH and/or NaB_3H_8. The possible reaction pathway could be given as below:

$$NaH + B_2H_6 \rightarrow NaBH_4 + BH_3? \qquad\qquad (7.5)$$

$$NaH + B_2H_6 \rightarrow NaB_3H_8? + H_2 \qquad\qquad (7.6)$$

$$(or\ Na_3H_8 + B_2H_6 \rightarrow NaBH_4 + B_2H_6) \qquad\qquad (7.7)$$

$$NaB_3H_8? + B_2H_6 \rightarrow Na_2B_{12}H_{12} + H_2 \qquad\qquad (7.8)$$
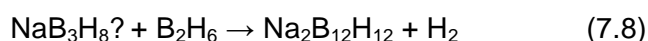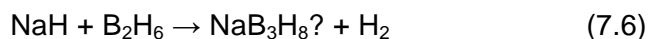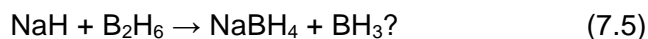
(*to be balanced*)

For the alkaline earth metal borohydride system, there were more amorphous borane species observed in the reaction of B_2H_6 and $Mg(BH_4)_2$/$Ca(BH_4)_2$, which agrees with the

theoretical studies proposing possible intermediates phase due to competing reaction pathways with similar reaction enthalpies of $[B_{12}H_{12}]^{2-}$ and other borane species (Ozolins *et al.*, 2009; Li *et al.*, 2010b). These results also verify that the formation of amorphous Mg-B-H species from the milled γ-Mg(BH$_4$)$_2$ (Section 5.2.1.3, p126) was due to the reaction between the released B_2H_6 (or its analogues) with the remaining material. Attempts to synthesise Mg(BH$_4$)$_2$ by heating either as-received or milled MgH$_2$ in B_2H_6/H$_2$ at 120-200 °C for 24-60 h were not successful: this is possibly due to poor diffusion of atomic H inside the bulk material.

Future H/D isotope labelling of the reaction reactants (e.g. LiBH$_4$+B_2D_6) could be a useful method of trying to trace the H or D atoms in the borane or borohydride products by Raman spectroscopy. This may lead to a better understanding of the mechanism(s) of solid-gas reactions between metal borohydride/hydride and diborane.

8   Mg-Ti-B Hydride System

A systemic study of Mg-B-Ti hydride thin films with varying ternary compositions by Amieiro-Fonseca *et al.* (2011), concluded that there is an optimum composition of $Mg_{0.36}B_{0.58}Ti_{0.06}$ that can store up to 10.6 wt% H_2 with an onset hydrogen desorption temperature of 260 °C and partial reversibility under moderate conditions (10 bar H_2 at room temperature). The presence of B-H bonding in the Raman spectrum suggested the possible formation of a metal borohydride. Therefore, the aim of this work is to try to produce this target composition in the form of bulk powder by reactive planetary ball-milling of MgH_2 and B with a range of Ti-based compounds, under 100 bar H_2. The spectroscopic and hydrogen sorption properties of the Mg-B-Ti-H composites produced were investigated.

8.1   Sample preparation

Magnesium hydride (MgH_2, purity 95%) was obtained from Goldschmidt, while titanium powder (Ti, purity 97%), titanium (II) hydride (TiH_2), titanium (III) chloride ($TiCl_3$, purity > 99%), and amorphous boron (B, purity 95-97%) were sourced from Sigma-Aldrich Company Ltd. All the powders were stored and characterised in an inert atmosphere to try to prevent exposure to air and moisture. The room temperature XRD patterns of the as-received B, Ti, TiH_2 and $TiCl_3$ can be found in Appendix A.

The milling conditions for each sample containing MgH_2 with or without a certain amount of amorphous B and TiX (TiX = Ti, TiH_2, $TiCl_3$), is summarised in **Table 8.1**. All the samples were loaded into a high pressure milling pot (evico-magnetics) and milled at 200 rpm with a

ball to powder ratio of 40:1, with 15 min periods of milling followed by 15 min rest periods (to try to prevent excessive over-heating).

The TiX additive was introduced into the samples via 3 different approaches:

1) all three reagents were mixed together and milled for 2 h, represented as $0.36MgH_2+0.58B+0.06TiX$;

2) MgH_2 and B were initially milled for 1 h, followed by the addition of TiX and a further 1 h milling, denoted as $(0.36MgH_2+0.58B)+0.06TiX$;

3) MgH_2 and TiX were milled for 1 h and then added with B for another 1 h milling, which is $(0.36MgH_2+0.06TiX)+B$.

Samples were examined using in/ex situ XRD, Raman spectroscopy, DSC, TGA-MS, and manometric analyser (HTP) in order to study their structural and hydrogen storage properties as a function of temperature. In this chapter, the samples will be represented by the abbreviations listed in **Table 8.1**, e.g. $MgH_2+B+TiH_2$ short for $0.36MgH_2+0.58B+0.06TiH_2$.

Table 8.1 Milling conditions for MgH_2-B-TiX (TiX = Ti, TiH_2 or $TiCl_3$) samples.

Sample stoichiometry	Atmosphere	Milling time	Abbreviation
MgH_2	$H_2 - 100$ bar	2 h	MgH_2 (2 h, H_2)
$0.4MgH_2 + 0.6B$	Ar – 1 bar	2 h	MgH_2+B (2 h, Ar)
$0.4MgH_2 + 0.6B$	$H_2 - 100$ bar	2 h	MgH_2+B (2 h, H_2)
$0.4MgH_2 + 0.6B$	$H_2 - 100$ bar	20 h	MgH_2+B (20h, H_2)
$0.36MgH_2 + 0.58B + 0.06Ti$	$H_2 - 100$ bar	2 h	MgH_2+B+Ti (2 h)
$0.36MgH_2 + 0.58B + 0.06Ti$	$H_2 - 100$ bar	20 h	MgH_2+B+Ti (20 h)
$(0.36MgH_2 + 0.58B) + 0.06Ti$	$H_2 - 100$ bar	2 h	$(MgH_2+B)+Ti$
$(0.36MgH_2 + 0.06Ti) + 0.58B$	$H_2 - 100$ bar	2 h	$(MgH_2+Ti)+B$
$0.36MgH_2 + 0.58B + 0.06TiH_2$	$H_2 - 100$ bar	2 h	$MgH_2+B+TiH_2$
$(0.36MgH_2 + 0.58B) + 0.06TiH_2$	$H_2 - 100$ bar	2 h	$(MgH_2+B)+TiH_2$
$(0.36MgH_2 + 0.06TiH_2) + 0.58B$	$H_2 - 100$ bar	2 h	$(MgH_2+TiH_2)+B$
$0.36MgH_2 + 0.58B + 0.06TiCl_3$	$H_2 - 100$ bar	2 h	$MgH_2+B+TiCl_3$
$(0.36MgH_2 + 0.58B) + 0.06TiCl_3$	$H_2 - 100$ bar	2 h	$(MgH_2+B)+TiCl_3$
$(0.36MgH_2 + 0.06TiCl_3) + 0.58B$	$H_2 - 100$ bar	2 h	$(MgH_2+TiCl_3)+B$

8.2 XRD of as-milled samples

8.2.1 Pure MgH$_2$ and MgH$_2$-B binary mixtures

Figure 8.1 is a comparison of XRD patterns for MgH$_2$ before and after ball milling. The as-received MgH$_2$ consisted of 93.9(1) wt% α-MgH$_2$ (tetragonal, space group $P4_2/mnm$) and 6.1(1) wt% Mg (hexagonal, $P6_3/mmc$). After milling for 2 h in 100 bar H$_2$, the XRD reflections from α-MgH$_2$ were significantly reduced in intensity and became broader. The diffraction broadening has been suggested to be an indication of a reduction in crystallite size (Varin *et al.*, 2006). It was unable to estimate crystallite size by the diffraction peak width using the Scherrer equation; as the particle size and morphology study (i.e. SEM images) and XRD instrumental line broadening correction, were not performed by this work. Small reflections originating from γ-MgH$_2$ (orthorhombic, *Pbcn*) were also observed.
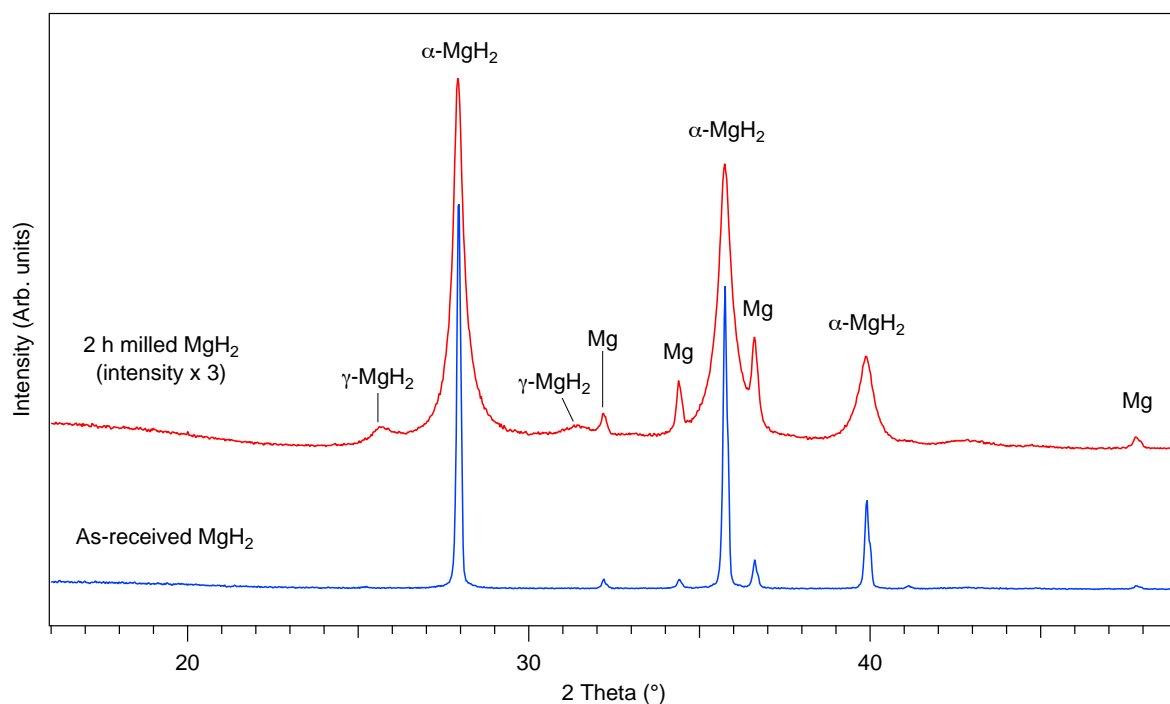
Figure 8.1 XRD patterns of as-received MgH$_2$ and milled MgH$_2$ in 100 bar H$_2$ for 2 h.

The quantitative phase analysis of the XRD data showed that the milled MgH$_2$ contained 88.0(6) wt% α-MgH$_2$, 5.0(3) wt% γ-MgH$_2$ and 6.0(4) wt% Mg. The total amount of α- and γ-

MgH_2 phases was consistent with the amount of α-MgH_2 in the as-received material, indicating a stress-induced transformation. This transformation has been commonly reported for milled MgH_2 (Varin *et al.*, 2006).

In order to understand the effect of amorphous boron on MgH_2, $0.4MgH_2+0.6B$ samples were milled in 1 bar Ar for 2 h, and in 100 bar H_2 for 2 and 20 h. XRD patterns for the milled binary $0.4MgH_2+0.6B$ samples are shown in **Figure 8.2**. Reflections are seen for α- and γ-MgH_2, Mg, B and a small amount of MgO. In addition, some small peaks between 10 and 25° 2θ are consistent with β-rhombohedral boron, indicating that the as-purchased "amorphous boron" exhibited some degree of crystallinity (even after milling).
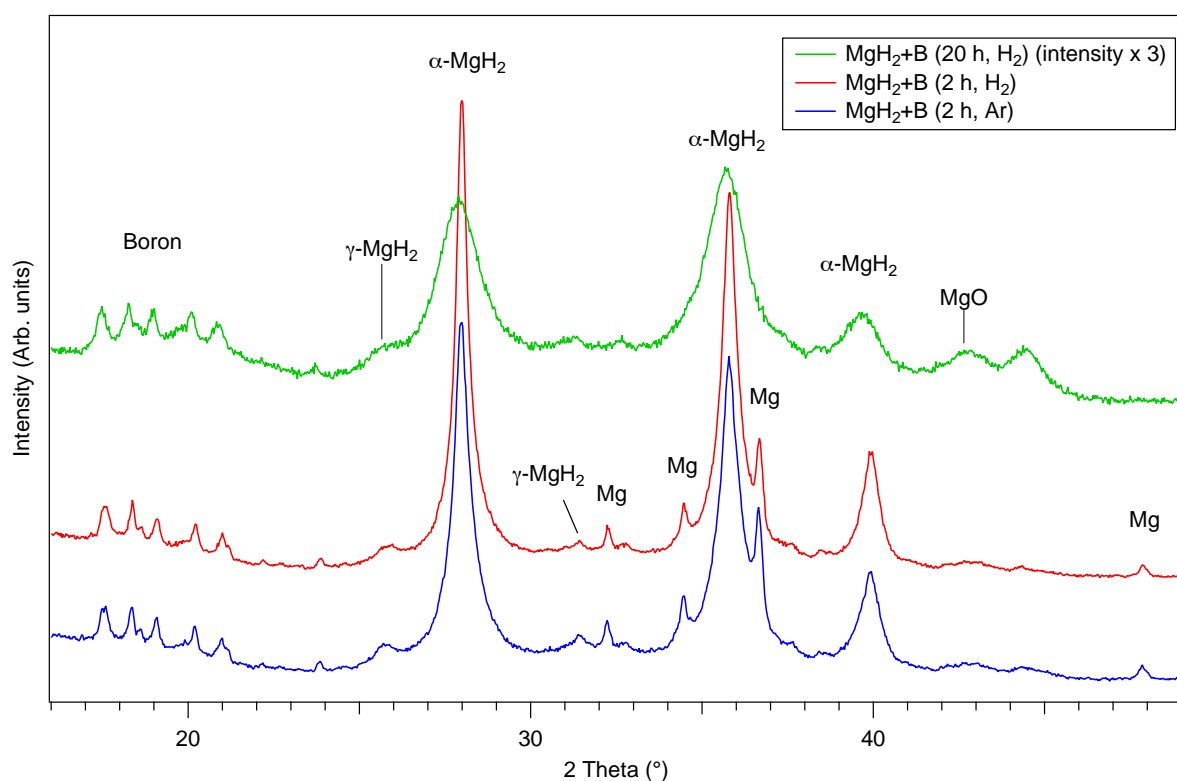
Figure 8.2 XRD patterns of $0.4MgH_2+0.6B$ after milling in 1 bar Ar for 2 h, and in 100 bar H_2 for 2 and 20 h.

No noticeable difference between the XRD diffraction patterns of the 2 h-milled samples was observed, except that the α-MgH_2 diffraction peaks in the MgH_2+B (2 h, Ar) sample are slightly broader and weaker in intensity. The lattice parameters of the α-MgH_2 and Mg phases were refined using Topas software, and are compared in **Table 8.2**. This shows that

there is no significant change in the lattice parameters of the MgH_2 and Mg phases, due to either: the atmosphere (Ar or H_2) during the 2 h milling, or to the addition of boron.

However, after increasing the milling time to 20 h there is a large reduction in diffraction intensities and a broadening in peak width, which should be related to a decreased crystallite size and the introduction of increased disorder into the structure. The Mg phase is difficult to distinguish as its diffraction peaks overlap with broad MgH_2 peaks. A considerable amount of MgO (~10 wt%) was also found, since milling for a long duration led to the increased production of fresh Mg powder surface.

Table 8.2 Lattice constants of MgH_2 and Mg phases in MgH_2 and MgH_2-B samples.

Samples	MgH_2			Mg		
	a (Å)	c (Å)	V (Å^3)	a (Å)	c (Å)	V (Å^3)
As received MgH_2	4.519 (0)	3.023 (0)	61.75 (1)	3.213 (0)	5.216 (1)	46.63 (1)
MgH_2 (2h, H_2)	4.523 (1)	3.024 (1)	61.87 (4)	3.214 (1)	5.218 (2)	46.69 (3)
MgH_2+B (2h, Ar)	4.520 (2)	3.021 (2)	61.71 (7)	3.213 (2)	5.215 (3)	46.61 (6)
MgH_2+B (2h, H_2)	4.520 (2)	3.021 (2)	61.74 (7)	3.213 (2)	5.215 (3)	46.63 (6)
MgH_2+B (20h, H_2)	4.541 (21)	3.034 (14)	62.54 (65)			

8.2.2 MgH_2-B-Ti ternary mixtures

The XRD analysis showed that the four milled MgH_2-B-Ti samples contained α, γ-MgH_2, Mg, B, and bct TiH_x (space group $I4/mmm$) phases (**Figure 8.3**). The starting material, α-Ti (hcp, $P6_3$mmc), mostly hydrided into a bct TiH_x phase, leaving only a weak α-Ti peak at 38.4° 2θ in the (MgH_2+B)+Ti and (possibly) MgH_2+Ti+B samples. For the MgH_2+B+Ti (20 h) sample, the pattern is dominated by diffraction peaks from the TiH_x phase, whilst the α-MgH_2 phase appears as broad and less intense "bumps". This large decrease in intensity of the MgH_2 phase is consistence with the X-ray peaks observed for the MgH_2 phase in the MgH_2+B (20 h, H_2) mixture.
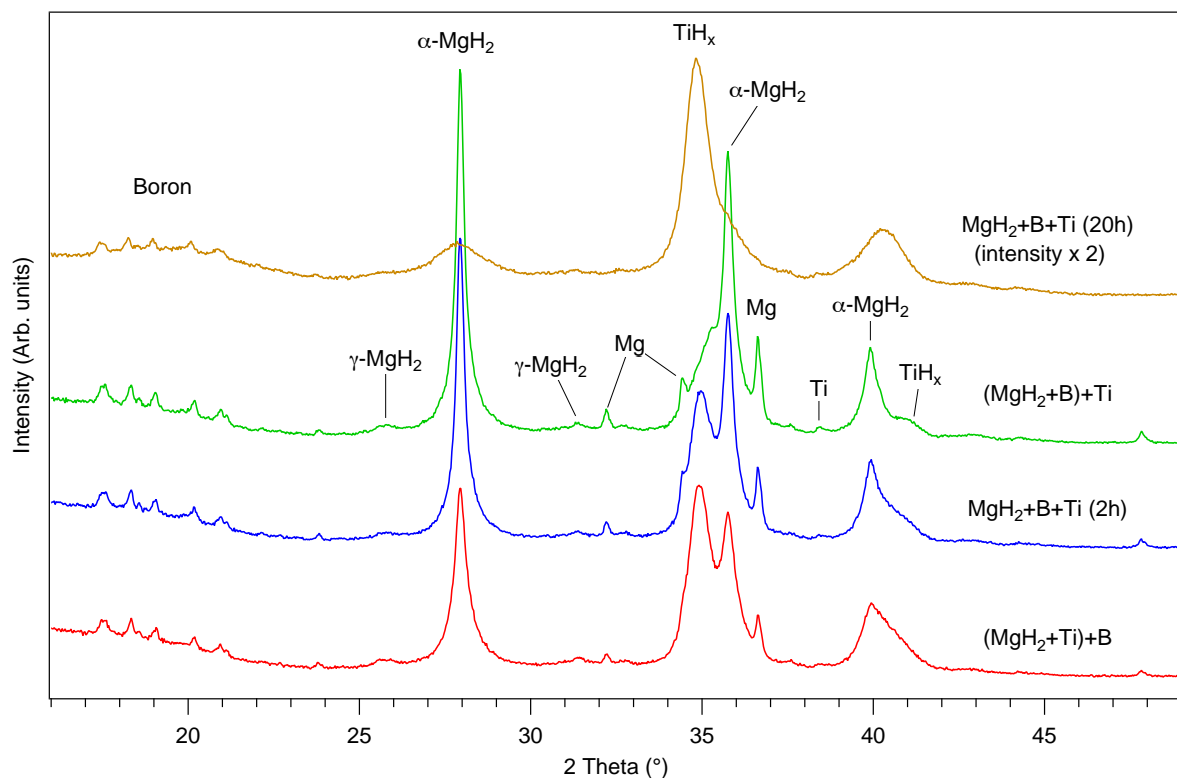
Figure 8.3 XRD patterns of MgH_2-B-Ti mixtures which were milled in 100 bar H_2: 0.36MgH_2-0.58B-0.06Ti milled for 2 h ["MgH_2+B+Ti (2h)"]; 0.36MgH_2-0.58B-0.06Ti milled for 20 h ["MgH_2+B+Ti (20h)"]; 0.36MgH_2-0.58B milled for 1 h & then 0.06Ti was added and milled for a further 1 h ["(MgH_2+B)+Ti"]; 0.36MgH_2-0.06Ti milled for 1 h & then 0.58B was added and milled for a further 1 h ["(MgH_2+Ti)+B"].

Refined lattice parameters of α-MgH_2, Mg and bct TiH_x are summarised in **Table 8.3**. With respect to MgH_2 and Mg phases, small decreases in both lattice parameters (up to 0.6% compared to those from MgH_2-B samples) and diffraction intensities are seen for the MgH_2+B+Ti and (MgH_2+Ti)+B samples. This reduction was also observed by Cuevas *et al.* (2012) who milled Mg and Ti powder in 80 bar H_2; which was explained by the dissolution of Ti atoms into the Mg and MgH_2 lattice (Liang and Schulz, 2003; Song *et al.*, 2004; Ponthieu *et al.*, 2013). In this work, there was up to 1.2 ± 0.2 at% Ti dissolved in MgH_2, and up to 2.3 ± 0.7 at% Ti in Mg according to Vegard's Law. The parameters for γ-MgH_2 are not given, as the intensities of the diffraction peaks are too low to allow an accurate structural refinement.

Table 8.3 Lattice parameters of α-MgH$_2$, Mg and tetragonal TiH$_x$ phases in the milled MgH$_2$, MgH$_2$-B-Ti and MgH$_2$-B samples.

Samples	α-MgH$_2$ V (Å^3)	Mg V (Å^3)	TiH$_x$ V (Å^3)
MgH$_2$ (2 h, H$_2$)	61.87 (4)	46.69 (3)	
MgH$_2$+B (2 h, H$_2$)	61.74 (7)	46.63 (6)	
MgH$_2$+B (20 h, H$_2$)	62.54 (65)		
(MgH$_2$+B)+Ti	61.80 (7)	46.63 (6)	43.57 (7)
MgH$_2$+B+Ti (2 h)	61.54 (6)	46.42 (4)	44.06 (5)
(MgH$_2$+Ti)+B	61.38 (6)	46.36 (7)	44.17 (7)
MgH$_2$+B+Ti (20 h)	62.15 (24)		44.63 (18)

It should be noted that, for all the 2 h milled samples, the refinement shows a better fit using the bct TiH$_x$ structure (Jaffe, 1956), rather than the fcc TiH$_2$ (space group *Fm-3m*) which was usually formed by the direct hydrogenation of Ti at high temperatures (e.g. 400 °C) (Lewkowicz, 1996). The formation of the bct TiH$_x$ phase was also observed by Zhang and Kisi (1997) who ball milled Ti powder under 2 bar H$_2$ for up to 3 h. Moreover, the cell volume of the bct TiH$_x$ phase increased during milling, which may be related to the amount of hydrogen absorbed by the TiH$_x$. For the MgH$_2$+B+Ti (20 h) sample, a mix of bct and fcc TiH$_x$ phases were identified. The lattice parameter of the fcc TiH$_x$ phase was refined to be $a =$ 4.455(6) Å, which is in good agreement with $a =$ 4.450(1) Å for the as-received fcc TiH$_2$ compound.

Therefore, the hydrogenation of α-Ti in the MgH$_2$-B-Ti mixture appears to have been a gradual process. The milling continuously creates fresh Ti surface and introduces lattice defects which may promote increased hydrogen diffusion within the bulk material. With increasing milling time, the crystallite size decreased, resulting in an increased hydrogenation rate; this has been explained in terms of shorter diffusion distances for hydrogen through the TiH$_x$ phase, due to the increased volume of grain boundaries and smaller grains introduced after ball-milling (Zhang and Kisi, 1997). When the H concentration is above > 1 at% (x > 0.01 in TiH$_x$, the bct TiH$_x$ was preferably formed. Full

hydrogenation to fcc TiH_2 phase could be achieved by a long milling duration (at least 20 h). This might explain why only single fcc TiH_2 phase was formed by milling MgH_2-Ti mixture for 20 h (Liang *et al.*, 1999) or 60 h (Charbonnier *et al.*, 2004). The addition of B appears to slow down the formation of TiH_x. However, there is no crystalline or vibrational evidence to indicate the formation of a B-H bond-containing compound after ball-milling MgH_2-B-Ti in H_2.

8.2.3 MgH_2-B-TiH_2 ternary mixtures

Good fits of the XRD data of the 2 h-milled $(MgH_2+B)+TiH_2$, $MgH_2+B+TiH_2$ and $(MgH_2+TiH_2)+B$ samples were obtained using α-MgH_2, Mg, fcc-TiH_2 and bct-TiH_2 phases (**Figure 8.4**), in addition to partially crystalline boron. A small amount of γ-MgH_2 phase might be present as a small hump at ~25.6° *2θ*. For all samples, approximately 80% of the starting material fcc TiH_2 (space group *Fm-3m*) transformed to a bct structure after milling. However, the fcc Mg-Ti-H hydrides produced from a Ti-rich MgH_2+xTiH_2 ($x > 0.1$) mixture milled for 200 h by Asano and Akiba (2009) was not observed in this work. Broader and less intense feature was observed for diffractions from α-MgH_2 and TiH_x phases from the $(MgH_2+TiH_2)+B$ sample, suggesting an increased structural disordering. The XRD refinement only showed small differences in the lattice parameters of the α-MgH_2 and Mg phases among three MgH_2-B-TiH_2 samples (**Table 8.4**): the cell volumes for the Mg phase were between 46.53-46.58 $Å^3$ which are very close to those for the MgH_2-B samples (V_{Mg} = 46.57-46.69 $Å^3$) if refinement errors are taken into account. Thus, it is unlikely that solid solutions of Mg(Ti) or Mg(Ti)H_2 were formed.

The cell volumes of fcc-TiH_2 in the milled samples were slightly reduced compared to the 88.25(4) $Å^3$ for the starting TiH_2 compound. The lattice parameters of the tetragonal TiH_x phase were larger in the $MgH_2+B+TiH_2$ and $(MgH_2+TiH_2)+B$ samples, than in $(MgH_2+B)+TiH_2$. This is possibly due to the formation of coherent interface interactions between $TiH_2(111)$-$MgH_2(110)$ which had been found in the Mg-Ti-H thin films and milled powders (Borsa *et al.*, 2007; Hao and Sholl, 2012; Ponthieu *et al.*, 2013). The formation of

this interface led the fcc TiH_2 phase to deform into a bct structure, in order to minimise lattice strain (Tao *et al.*, 2011).
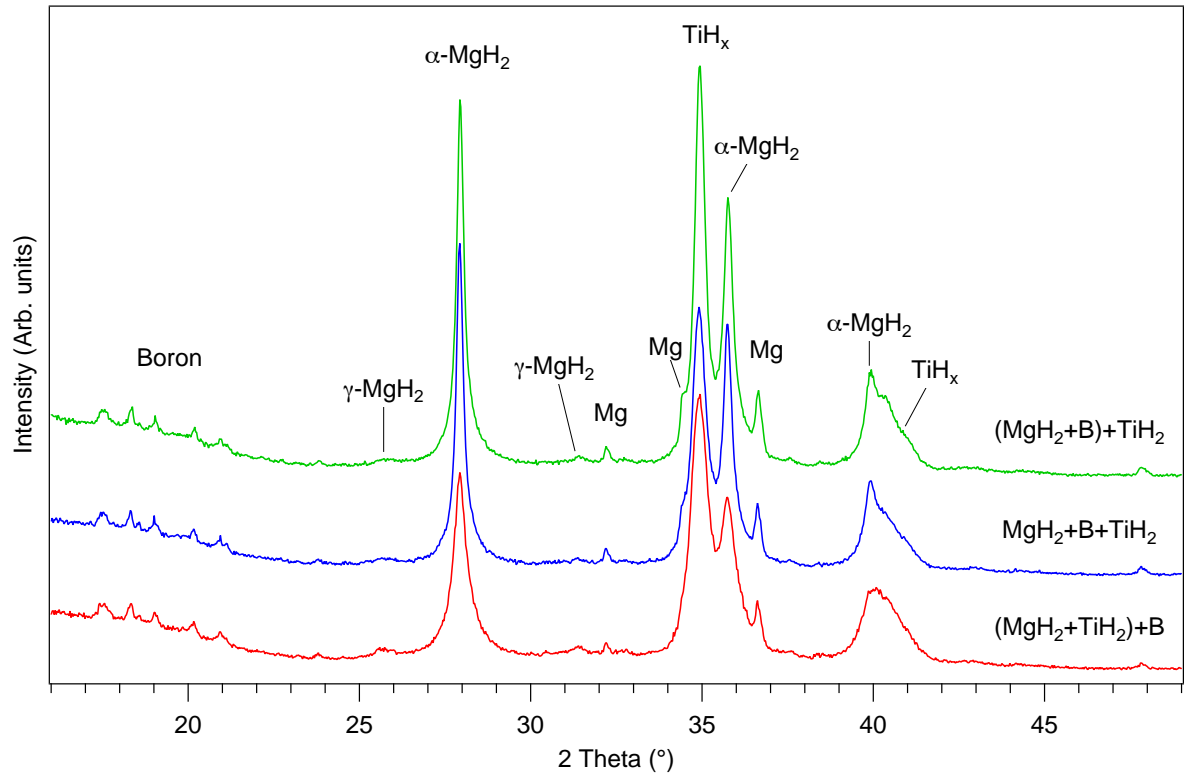
Figure 8.4 XRD patterns of MgH_2-B-TiH_2 mixtures which were milled in 100 bar H_2: 0.36MgH_2-0.58B-0.06TiH_2 milled for 2 h ["MgH_2+B+TiH_2"]; 0.36MgH_2-0.58B milled for 1 h & then 0.06TiH_2 was added and milled for a further 1 h ["(MgH_2+B)+TiH_2"]; 0.36MgH_2-0.06TiH_2 milled for 1 h & then 0.58B was added and milled for a further 1 h ["(MgH_2+TiH_2)+B"].

Table 8.4 Lattice parameters of α-MgH_2, Mg and tetragonal TiH_x phases in the milled MgH_2, MgH_2-B, MgH_2-B-TiH_2 samples.

Samples	α-MgH$_2$ V (Å^3)	Mg V (Å^3)	fcc TiH$_2$ V (Å^3)	tet. TiH$_x$ V (Å^3)
MgH$_2$ (2h, H$_2$)	61.87 (4)	46.69 (3)		
MgH$_2$+B (2h, H$_2$)	61.74 (7)	46.63 (6)		
(MgH$_2$+B)+TiH$_2$	61.66 (7)	46.53 (6)	87.88 (13)	44.13 (5)
MgH$_2$+B+TiH$_2$	61.78 (6)	46.58 (5)	87.95 (13)	44.31 (5)
(MgH$_2$+TiH$_2$)+B	61.72 (9)	46.54 (6)	87.85 (18)	44.36 (7)

8.2.4   MgH$_2$-B-TiCl$_3$ ternary mixtures

The X-ray diffraction patterns of the three milled MgH$_2$-B-TiCl$_3$ samples show the presence of α-MgH$_2$, Mg and partial crystalline B phases (**Figure 8.5**). No diffraction peaks corresponding to TiCl$_3$ were observed. This may be because ball-milling has led to the introduction of either: a disordered TiCl$_3$ structure whose X-ray peaks cannot be identified within the noise of the background of the diffractions pattern (Miyaoka *et al.*, 2000); or a new amorphous compound. In addition, XRD refinement shows that for all three samples, the cell volumes of the α-MgH$_2$ phase was 61.73 Å^3 and those for Mg were between 46.55-44.57 Å^3; these values are very close to those for the MgH$_2$-B samples (V_{Mg} = 46.57-46.69 Å^3) if refinement errors are taken into account (**Table 8.5**). This indicates that no solid solution, e.g. MgH(Cl)$_2$ and Mg(Ti) was formed in the Mg-containing phase.
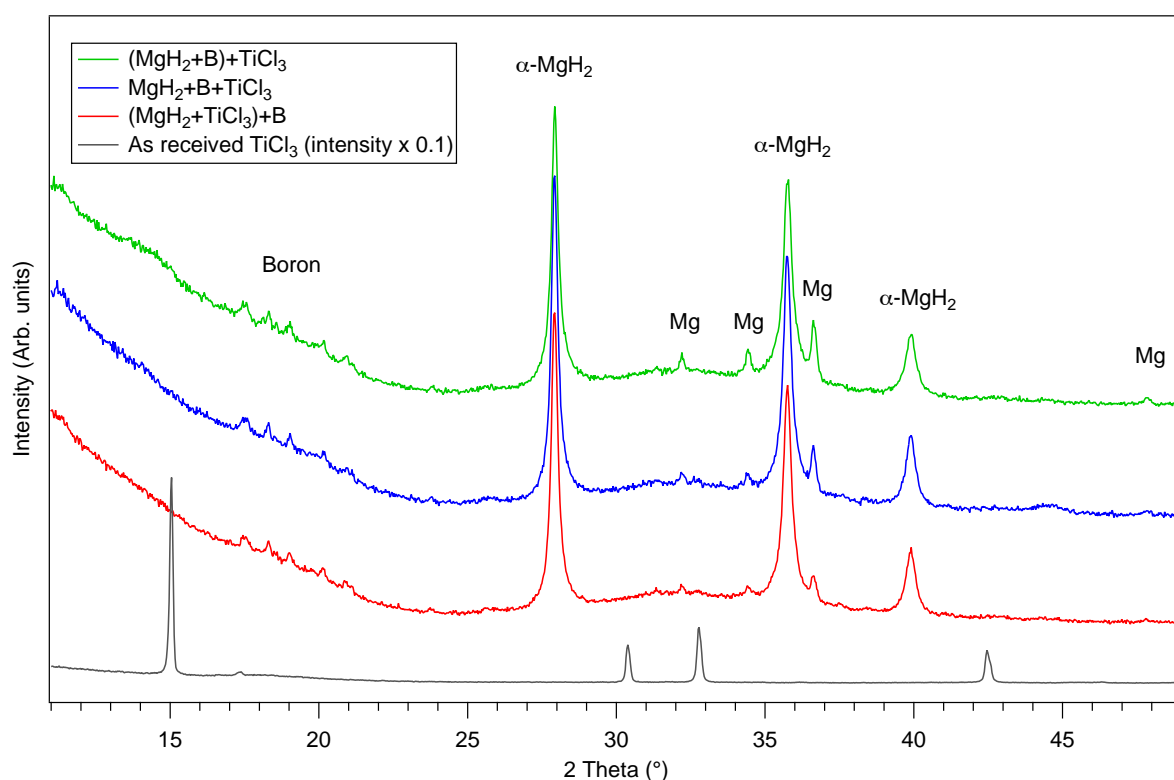
Figure 8.5 XRD patterns of as-received TiCl$_3$ and of MgH$_2$-B-TiCl$_3$ mixtures which were milled in 100 bar H$_2$: 0.36MgH$_2$-0.58B-0.06TiCl$_3$ milled for 2 h ["MgH$_2$+B+TiCl$_3$"]; 0.36MgH$_2$-0.58B milled for 1 h & then 0.06TiCl$_3$ was added and milled for a further 1 h ["(MgH$_2$+B)+TiCl$_3$"]; 0.36MgH$_2$-0.06TiCl$_3$ milled for 1 h & then 0.58B was added and milled for a further 1 h ["(MgH$_2$+TiCl$_3$)+B"].

Table 8.5 Lattice parameters of α-MgH$_2$ and Mg phases in the milled MgH$_2$, MgH$_2$-B and MgH$_2$-B-TiCl$_3$ samples.

Samples	MgH$_2$			Mg		
	a (Å)	c (Å)	V (Å^3)	a (Å)	c (Å)	V (Å^3)
MgH$_2$ (2h, H$_2$)	4.523 (1)	3.024 (1)	61.87 (4)	3.214 (1)	5.218 (2)	46.69 (3)
MgH$_2$+B (2h, H$_2$)	4.520 (2)	3.021 (2)	61.74 (7)	3.213 (2)	5.215 (3)	46.63 (6)
(MgH$_2$+B)+TiCl$_3$	4.520 (4)	3.022 (2)	61.73 (11)	3.211 (3)	5.211 (4)	46.55 (8)
MgH$_2$+B+TiCl$_3$	4.519 (2)	3.022 (1)	61.73 (6)	3.212 (2)	5.213 (3)	46.57 (5)
(MgH$_2$+TiCl$_3$)+B	4.520 (1)	3.022 (1)	61.73 (4)	3.212 (1)	5.211 (3)	46.56 (4)

8.3   Thermal properties

8.3.1   Pure MgH$_2$ and MgH$_2$-B mixtures

The thermal properties of as-received/milled pure MgH$_2$, MgH$_2$+B (2 h, Ar or H$_2$) and MgH$_2$+B (20 h, H$_2$) samples were investigated using DSC and TGA-MS (**Figure 8.6**). The as-received MgH$_2$ started to decompose at 390 °C and reached a maximum at 400 °C. A total amount of 6.68 wt% H$_2$ was released at 430 °C, which was lower than the theoretical maximum of 7.67 wt%. This reduced capacity is possibly due to the formation of thin MgO/Mg(OH)$_2$ layers on the Mg/MgH$_2$ surface when storing for long durations, which is difficult to be quantitated by XRD.

After milling for 2 h, the pure MgH$_2$ showed a reduced onset and peak decomposition temperatures at 310 °C and 330 °C, with almost no reduction in H$_2$ capacity (6.65 wt% H$_2$ released at 430 °C). The H$_2$ capacity of the milled MgH$_2$ will be used as a benchmark in the following studies of the binary and ternary systems. In addition, both DSC and MS traces show that the milled MgH$_2$ decomposed in two-steps, giving the most intense peak at 335 °C and a broad shoulder between 345 and 380 °C. This has been reported to correspond to the decomposition of α-MgH$_2$ and γ-MgH$_2$, respectively (Varin *et al.*, 2006).
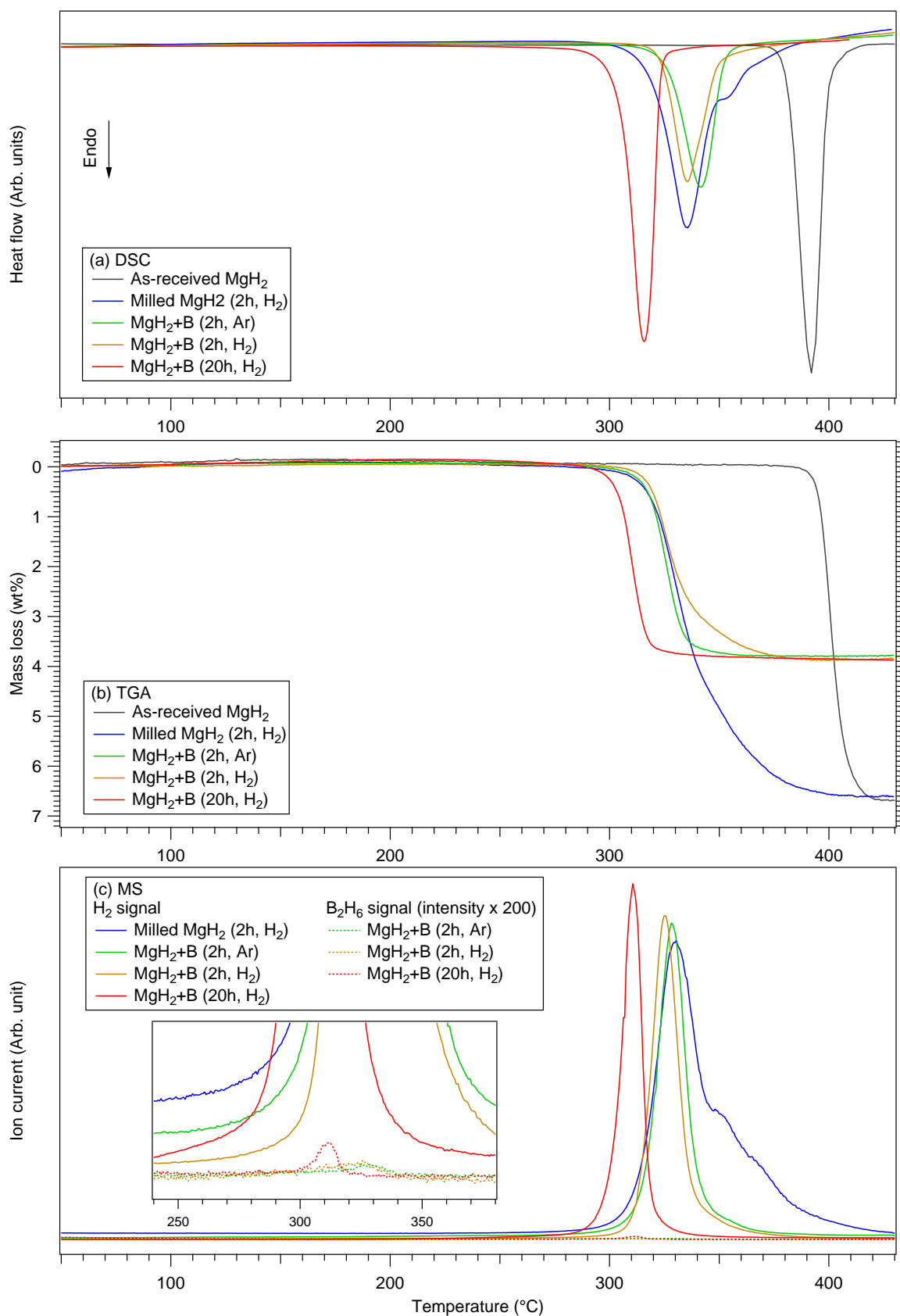
Figure 8.6 (a) DSC, (b) TGA and (c) MS traces for as-received/milled MgH$_2$, and milled MgH$_2$+B (2 h, Ar), MgH$_2$+B (2 h, H$_2$) and MgH$_2$+B (20 h, H$_2$). All measurements were performed at a heating rate of 2 °C/min under flowing Ar. The intensities of the B$_2$H$_6$ MS signal were multiplied by 200.

DSC and TGA-MS data of the MgH_2-B samples milled for 2 h in Ar or 100 bar H_2 show that a single-step dehydrogenation event occurs between 290 and 370 °C which is in a similar temperature range to the decomposition of milled MgH_2. The TGA-MS shows that the MgH_2+B (2 h, Ar) starts to dehydride at 310 °C and reaches a maximum desorption at 328 °C, releasing a total weight loss of 3.86 wt% between 250 and 430 °C; i.e. 93.7 % of maximum H_2 capacity of the milled MgH_2 was achieved by the MgH_2+B (2 h, Ar) sample.

The MgH_2+B (2 h, H_2) sample showed that the dehydrogenation occurred with an onset temperature of 300 °C and peaked at 315 °C. A total weight loss of 3.90 wt% is measured between 250 and 430 °C, i.e. 94.7 % of maximum H_2 capacity of the milled MgH_2 was gained which is slightly higher than for the MgH_2+B sample milled in Ar. For both the 2 h milled MgH_2-B samples, extremely small fluctuations in the B_2H_6 MS signals were observed at around 325 °C where the major dehydrogenation occurs.

With increasing milling duration, the MgH_2+B (20 h, H_2) mixture exhibits the lowest dehydrogenation temperature with an onset at around 295 °C and a maximum at 310 °C. A rise in the B_2H_6 signal was detected simultaneously with the H_2 peak. A total weight loss of 3.99 wt% was observed upon heating to 430 °C, which was higher than for the 2 h samples possibly due to evolution of B_2H_6 gas. This suggests that boron might react with H_2/MgH_2 to form a small amount of amorphous B-H containing compound(s) during long duration ball-milling under high-pressure hydrogen. However, no vibrations corresponding to B-H bonding could be observed in the Raman spectra for any of the MgH_2-B samples.

To sum up, the presence of B might destablise the MgH_2 phase, leading to: the decomposition of a small amount of the MgH_2 phase during milling resulting in a lower gravimetric H_2 capacity; and, an improvement in the dehydrogenation kinetics of the MgH_2, shown by the sharp single-step H_2 desorption peaks. Amorphous B-H-containing compounds might be formed when the milling time is increased from 2 to 20 h.

8.3.2 MgH$_2$-B-Ti ternary system

8.3.2.1 DSC-TGA-MS

The DSC, TGA-MS traces for the Mg-B-Ti ternary samples are presented in **Figure 8.7**. The dehydrogenation of (MgH$_2$+B)+Ti starts at around 280 °C and reaches a maximum at 330 °C followed by a sluggish shoulder up to 400 °C; this corresponded to H$_2$ releases of 2.54 wt% and 0.43 wt% between 270-350 °C and 350-400 °C, respectively. A total amount of 3.06 wt% H$_2$ desorption was measured at 430 °C, compared to the 3.4 wt% expected for the complete decomposition of milled MgH$_2$, i.e. only 90.2 % of the expected H$_2$ capacity is obtained for the MgH$_2$ phase.

The MgH$_2$+B+Ti (2 h) sample also exhibits a two-stage desorption: the first desorption peak is at 323 °C leading to 2.13 wt% mass loss at 345 °C, whereas the second desorption peak centred at 350 °C. A total amount of 2.97 wt% H$_2$ is observed for MgH$_2$+B+Ti (2 h) at 430 °C. For (MgH$_2$+Ti)+B, significant hydrogen evolution starts at around 270 °C and reaches a maximum at 309 °C with a weight loss of 2.04 wt% for the first desorption stage up to 324 °C, followed by the second desorption centred at 351 °C with a 0.71 wt% weight loss. A total amount of 2.89 wt% H$_2$ is released up to 430 °C. There is no signal corresponding to diborane release detected for any of the 2 h milled MgH$_2$-B-Ti samples during heating.

All of the 2 h milled MgH$_2$-B-Ti samples desorb H$_2$ in 2 steps. The addition of Ti reduces the decomposition temperature of the MgH$_2$ phase: (MgH$_2$+B)+Ti releases the most amount of H$_2$, while the (MgH$_2$+Ti)+B gives the least amount.

With increasing milling time to 20 h, the desorption temperature of the MgH$_2$+B+Ti (20 h) sample is significantly reduced to a temperature range between 170 and 250 °C, and the total mass loss of H$_2$ is increased to 3.71 wt% at 430 °C. The narrow single-step hydrogen peak at 226 °C suggests faster sorption kinetics. No diborane release was detected.
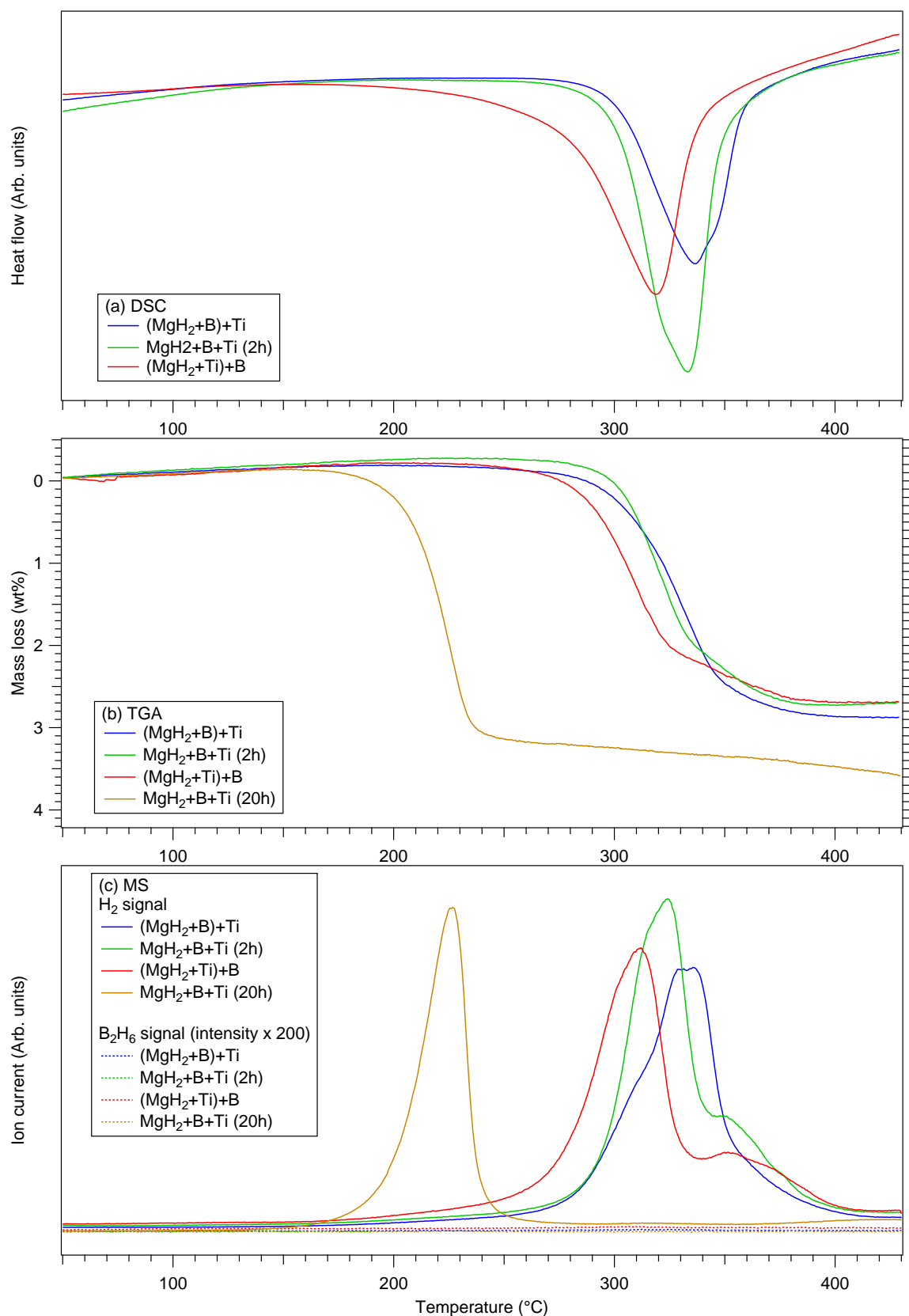
Figure 8.7 (a) DSC, (b) TGA and (c) MS measurements of MgH_2-B-Ti which had been milled in 100 bar H_2 for 2 h or 20 h with the addition of B and Ti (for the milling conditions shown in Table 8.1). All measurements were performed at a heating rate of 2 °C/min under flowing Ar. The intensities of the B_2H_6 MS signal were multiplied by 200.

8.3.2.2 In situ XRD

The decomposition mechanisms of $(MgH_2+B)+Ti$ and $(MgH_2+Ti)+B$ were investigated by in situ XRD, in which samples were heated at 12 °C/min in He flowing at 100 ml/min. Data was collected isothermally (with a collection time of ~25 min) in 10 °C intervals between 250 and 430 °C. This corresponds to an average heating rate of 0.8 °C/min.

For the $(MgH_2+B)+Ti$ sample as shown in **Figure 8.8**, the α-MgH_2 diffraction peaks begin to decrease at 320 °C and are no longer observed above 380 °C, with a concurrent increase in the intensity of the Mg peaks. The temperature range for the MgH_2 decomposition agrees well with the H_2 peak observed at 330 °C in the TGA-MS. The TiH_x diffractions are shifted to higher 2θ angles above 310 °C without a significant decrease in intensities, indicating that TiH_x gradually loses hydrogen which corresponds to a reduction in unit cell size. When H concentration is below 46 at% (i.e. $x <$ ~0.85 in TiH_x) according to the Ti-H phase diagram (Predel, 1996), there is a β-Ti(H) solid solution. At 420 °C, a small amount of hexagonal α- and cubic β-Ti(H) solid solutions mixture were found at 39.6° and 37.5° 2θ, respectively: at this temperature the H concentration should be less than ~33 at% ($x < 0.5$ in TiH_x). Therefore, the H_2 shoulders in the MS trace may be attributed to the dehydrogenation of the TiH_x compound. The partial decomposition of TiH_2 was also seen in studies by Shao *et al.* (2011). The oxidation of Mg to MgO is observed on heating to 290 °C, probably due to a leak in the system. The partially crystalline boron is stable throughout the measurements in both samples.

For the $(MgH_2+Ti)+B$ sample, the α-MgH_2 phase starts to decrease at 310 °C and disappears at 380 °C (**Figure 8.9**). The TiH_x diffractions start to shift to a higher 2θ at 310 °C, followed by the appearance of α-Ti(H) solid solution and an abrupt growth of β-Ti(H) solid solution on further heating to 430 °C.
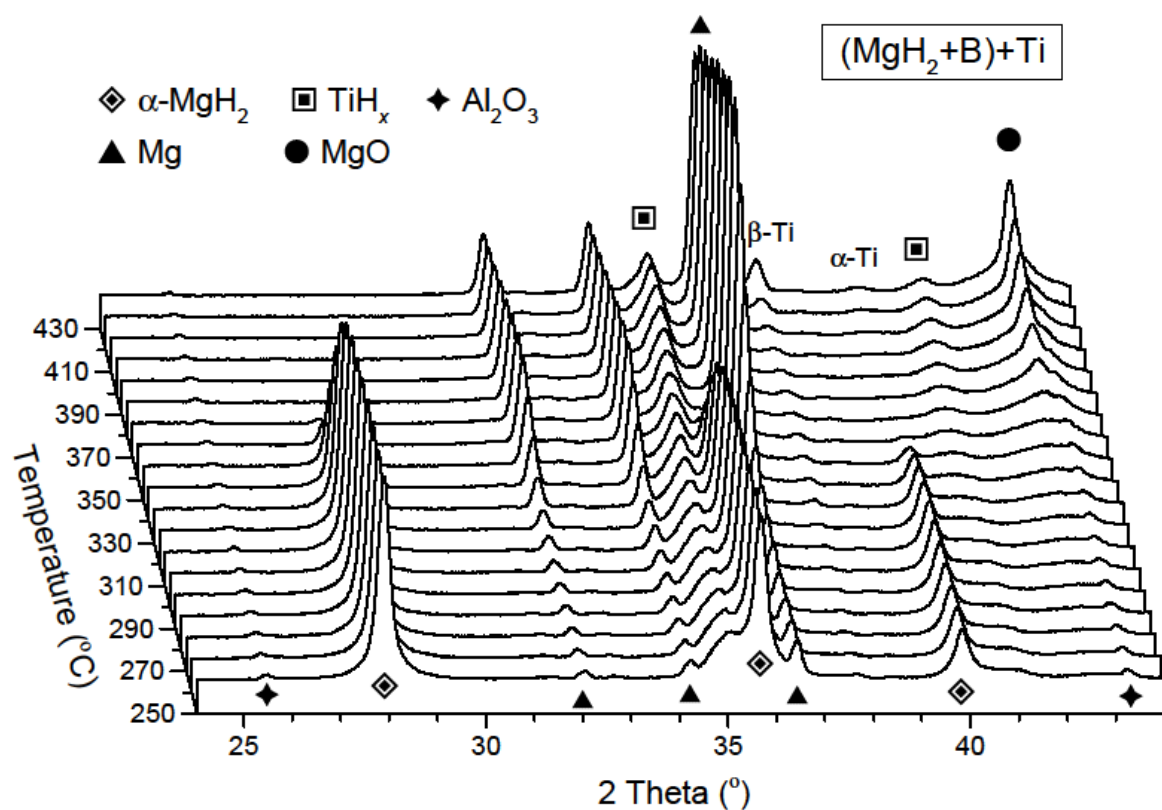
Figure 8.8 In-situ XRD of milled $(MgH_2+B)+Ti$ heated under flowing He (100 ml/min).
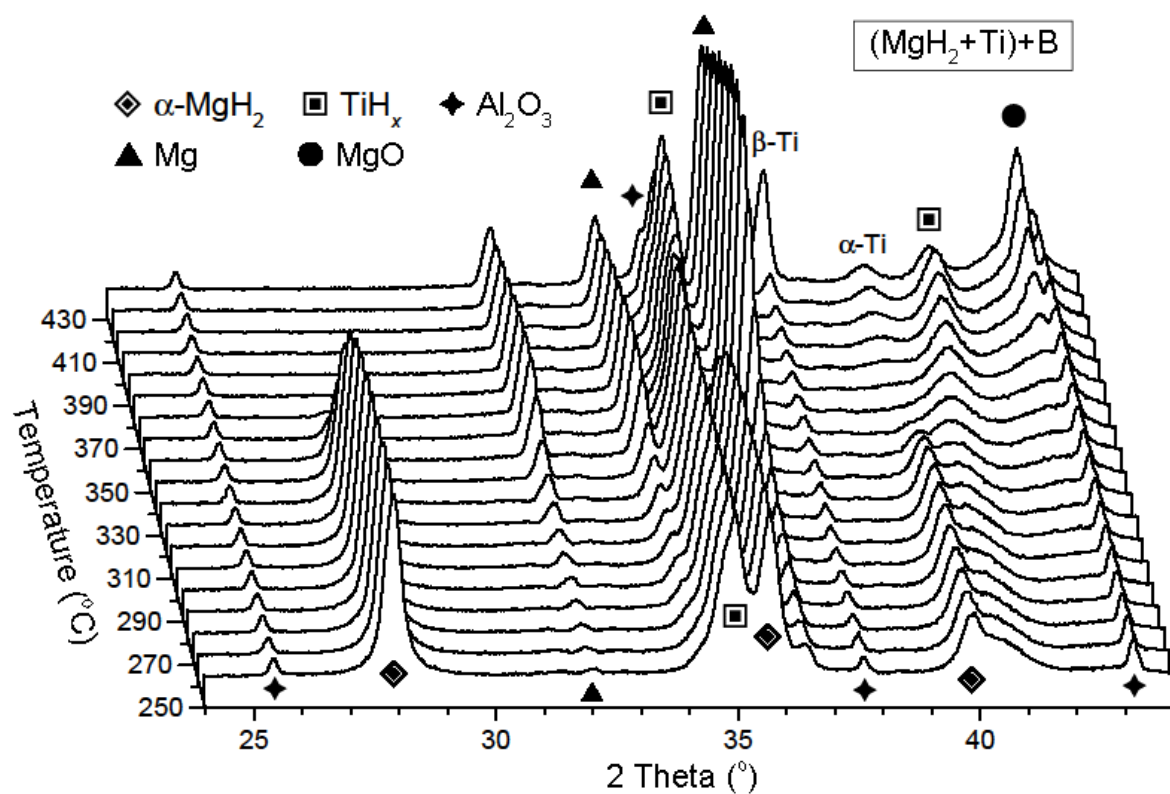
Figure 8.9 In-situ XRD of milled $(MgH_2+Ti)+B$ heated under flowing He (100 ml/min).

The unit cell volumes of the MgH_2 and TiH_x phases between 250 and 430 °C are shown in **Figure 8.10**. The cell volume of MgH_2 in both samples, increases almost linearly with temperature until decomposition is completed at 370 °C.
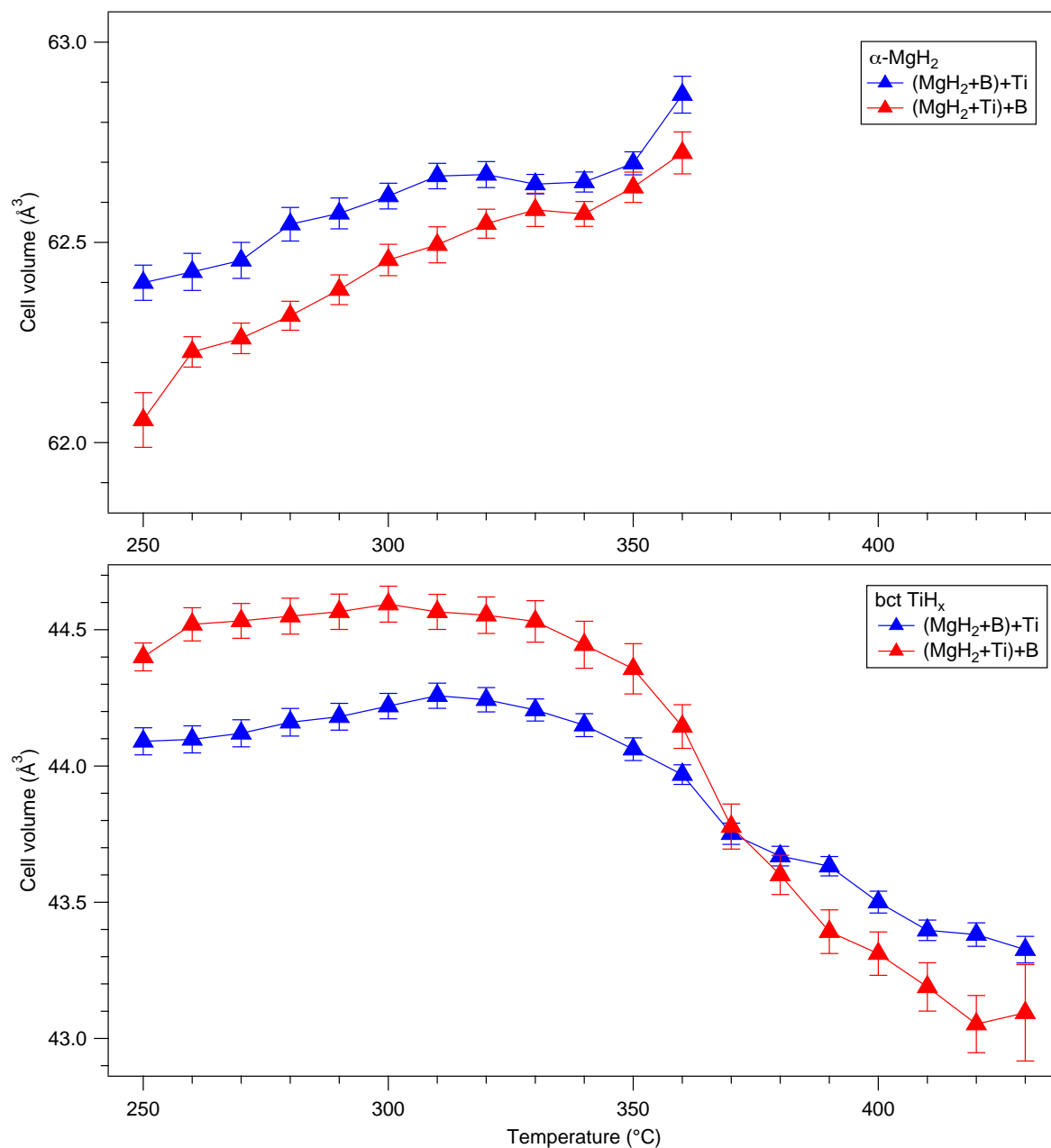
Figure 8.10 Unit cell volume of MgH_2 and TiH_x phases in the milled $(MgH_2+B)+Ti$ and $(MgH_2+Ti)+B$ samples with increasing temperature (from Figures 8.8 and 8.9).

The cell volume of TiH_x in both samples shows gradual thermal expansion until 300 °C, followed by a significant contraction on further heating. The TiH_x phase in the $(MgH_2+Ti)+B$ sample contracts more rapidly above 360 °C and becomes smaller than TiH_x in the

(MgH$_2$+B)+Ti sample at 430 °C. This is because more hydrogen is released from TiH$_x$ in the (MgH$_2$+Ti)+B sample during the second desorption stage, compared to the (MgH$_2$+B)+Ti sample. As a result, a relative higher phase abundance of Ti(H) solid solutions is found in the (MgH$_2$+Ti)+B.

8.3.3   MgH$_2$-B-TiH$_2$ ternary mixtures

8.3.3.1 DSC-TGA-MS

The DSC, TGA-MS measurements for the three MgH$_2$-B-TiH$_2$ samples are shown in **Figure 8.11**. For the (MgH$_2$+B)+TiH$_2$ and MgH$_2$+B+TiH$_2$ samples, the H$_2$ signal showed that the dehydrogenation proceeded in a single step starting at 275 and 260 °C and reaching maximums at 323 and 308 °C, leading to mass losses of 3.67 wt% and 3.68 wt% at 430 °C, respectively. It should be noted that these values are higher than the 3.37 wt% expected if H$_2$ is only released from the MgH$_2$ phase. Since neither diborane release nor B-H bonding were detected by MS and Raman spectroscopy respectively, the TiH$_x$ phase (bct and/or fcc polymorphs) is most likely to be responsible for the additional H$_2$ release. However, DSC traces show there are two overlapping endothermic events between 260 and 400 °C, of which the first corresponds well with the major dehydrogenation event. The second endothermic reaction is not accompanied by any significant hydrogen evolution, and so may be attributed to a titanium hydride phase transition and/or a reaction between the decomposed product and/or remained phases.

For the (MgH$_2$+TiH$_2$)+B sample, both DSC and the MS H$_2$ traces show multi-step dehydrogenation peaking at 300 °C with shoulders at 270 and 288 °C. The total mass loss, however, is reduced to 3.48 wt%, which is the lowest among the three samples. No diborane release was detected during heating.
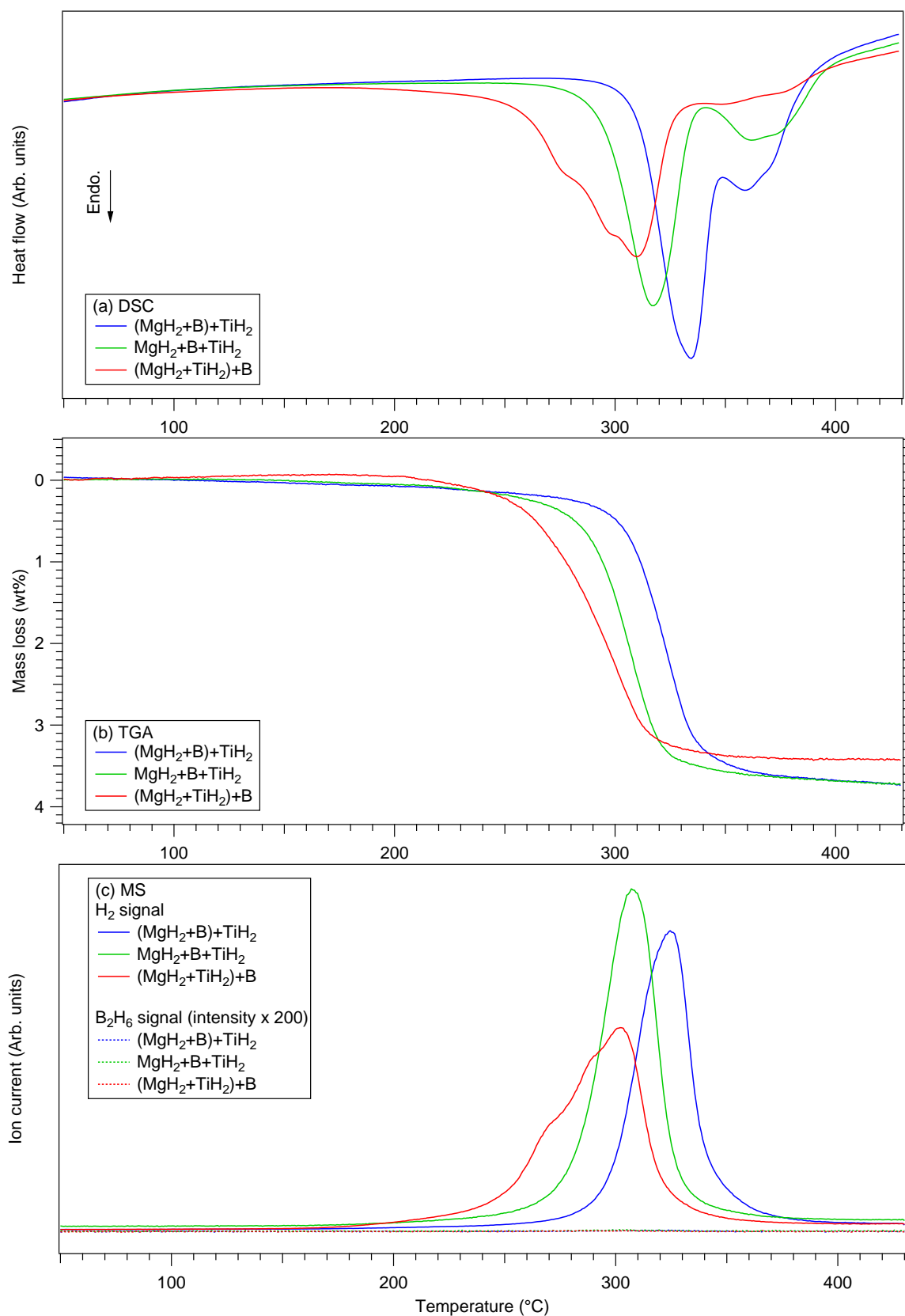
Figure 8.11 (a) DSC, (b) TGA and (c) MS measurements of MgH_2-B-TiH_2 which had been milled in 100 bar H_2 for 2 h with the addition of B and TiH_2 (for the milling conditions shown in Table 8.1). All measurements were performed at a heating rate of 2 °C/min under flowing Ar. The intensities of the B_2H_6 MS signals were multiplied by 200.

8.3.3.2 In situ XRD

In order to study decomposition reactions, phase changes and any other temperature-dependent crystalline transformations in the milled $(MgH_2+B)+TiH_2$ and $(MgH_2+TiH_2)+B$ samples, in situ XRD patterns were collected every 10 °C isothermally from 250 to 440 °C in helium flowing at 100 ml/min. With increasing temperature from 30 to 250 °C, the diffraction peaks agree well with α-MgH_2, Mg, TiH_x (a mixture of cubic and tetragonal polymorphs) phases in both the $(MgH_2+B)+TiH_2$ and $(MgH_2+TiH_2)+B$ samples (Al_2O_3 is due to the sample crucible).

In the $(MgH_2+B)+TiH_2$ sample (Figure 8.12), the peaks for α-MgH_2 start to decrease at 340 °C and disappear at 380 °C, with concurrent growth of the Mg diffraction peaks. The disappearance of the MgH_2 phase agrees well with the temperature range of the principal hydrogen desorption peak observed by TGA-MS. At 350 °C, diffraction peaks for TiH_x gradually shift to higher angles, followed by a decrease in intensity at 440 °C. A notable diffraction peak growth of the α and β-Ti(H) solid solutions is seen on further heating to 420 °C. The oxidation of Mg to MgO, leads to a small drop in intensity in the Mg peaks above 390 °C.

The $(MgH_2+TiH_2)+B$ sample shows (Figure 8.13) similar structural changes, but at different temperatures: the TiH_x peaks start to shift to higher 2θ values at 330 °C, before the disappearance of the α-MgH_2 phase at 370 °C. MgO and a small amount of α-Ti(H) phases are also observed above 390 °C. The decomposition of TiH_x and subsequently MgH_2 correspond well with the multi-step desorption process observed by TGA-MS. Unlike in the $(MgH_2+B)+TiH_2$, $(MgH_2+B)+Ti$ and $(MgH_2+Ti)+B$ samples where the TiH_x diffraction peaks are still present at 430-440 °C, in the $(MgH_2+TiH_2)+B$ sample the bct TiH_x phase disappears at 420 °C, while the β-Ti(H) (H concentration < ~33 at%, i.e. $x < 0.5$ in TiH_x) phase simultaneously increases in intensity.
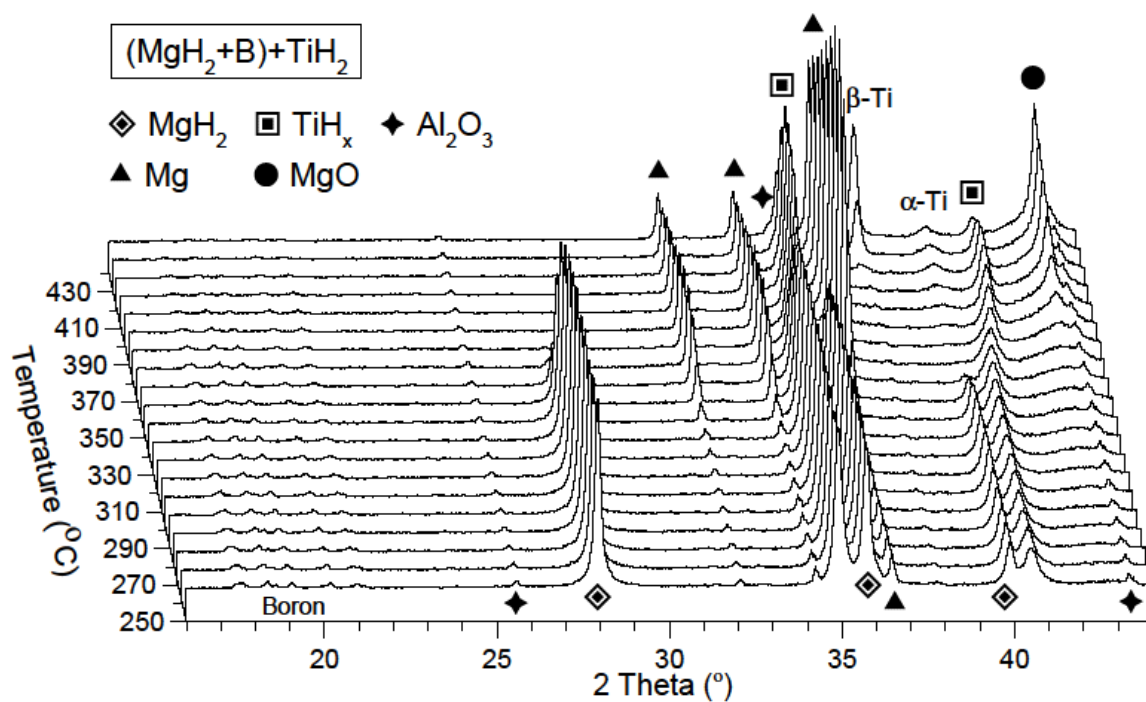
Figure 8.12 In situ XRD data for milled (MgH$_2$+B)+TiH$_2$ heated from 250 to 440 °C
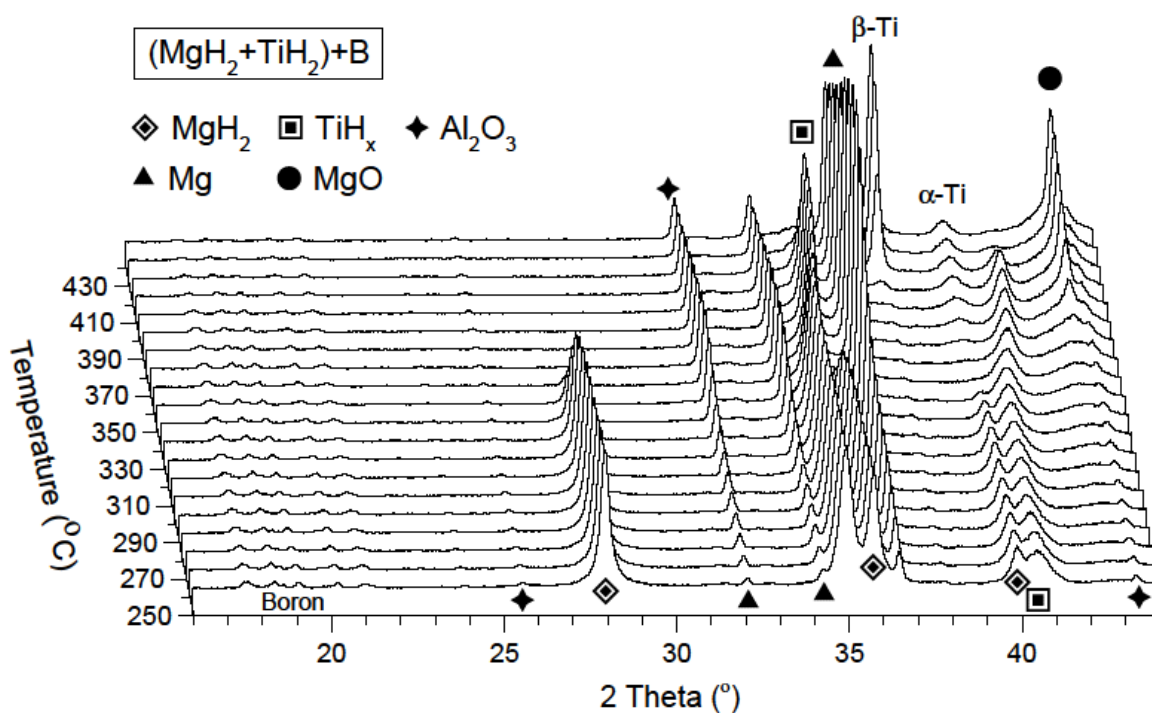
Figure 8.13 In situ XRD data for milled (MgH$_2$+TiH$_2$)+B heated from 250 to 440 °C.

The unit cell volumes of the MgH_2 and TiH_x phases in the $(MgH_2+B)+TiH_2$ and $(MgH_2+TiH_2)+B$ samples between 250 and 430 °C, are shown in **Figure 8.14**. It should be noted that the cell volumes of the α-MgH_2 phases gradually decrease from 340 °C, which was not observed for the MgH_2-B-Ti samples whose MgH_2 phases simply underwent thermal expansion until they decomposed (**Figure 8.10**). The cell volumes of both bct and fcc TiH_x phases start to contract at about 340 °C. In addition, the bct TiH_x phase in $(MgH_2+TiH_2)+B$ decomposes at a slightly faster rate than bct $TiHx$ in $(MgH_2+B)+TiH_2$, and the XRD peaks can no longer be refined above 420 °C.

Figure 8.15 shows ex situ room temperature XRD patterns for $(MgH_2+B)+TiH_2$ and $(MgH_2+TiH_2)+B$ samples that were heated to 440 °C as part of the in situ XRD measurements. Mg, α-Ti, TiH_x, and a small amount of MgO and TiO_2 are observed as decomposition products. The disappearance of β-Ti is due to the eutectic phase transformation to α-Ti and fcc-TiH_x at around 300 °C (San-Martin and Manchester, 1987). The cell volume of the partially decomposed fcc TiH_x phase is approximately 3% smaller than the volume of the as-received fcc-TiH_2, thus giving an approximate value of x of 1.6. No crystalline boron was observed in either sample after heating.
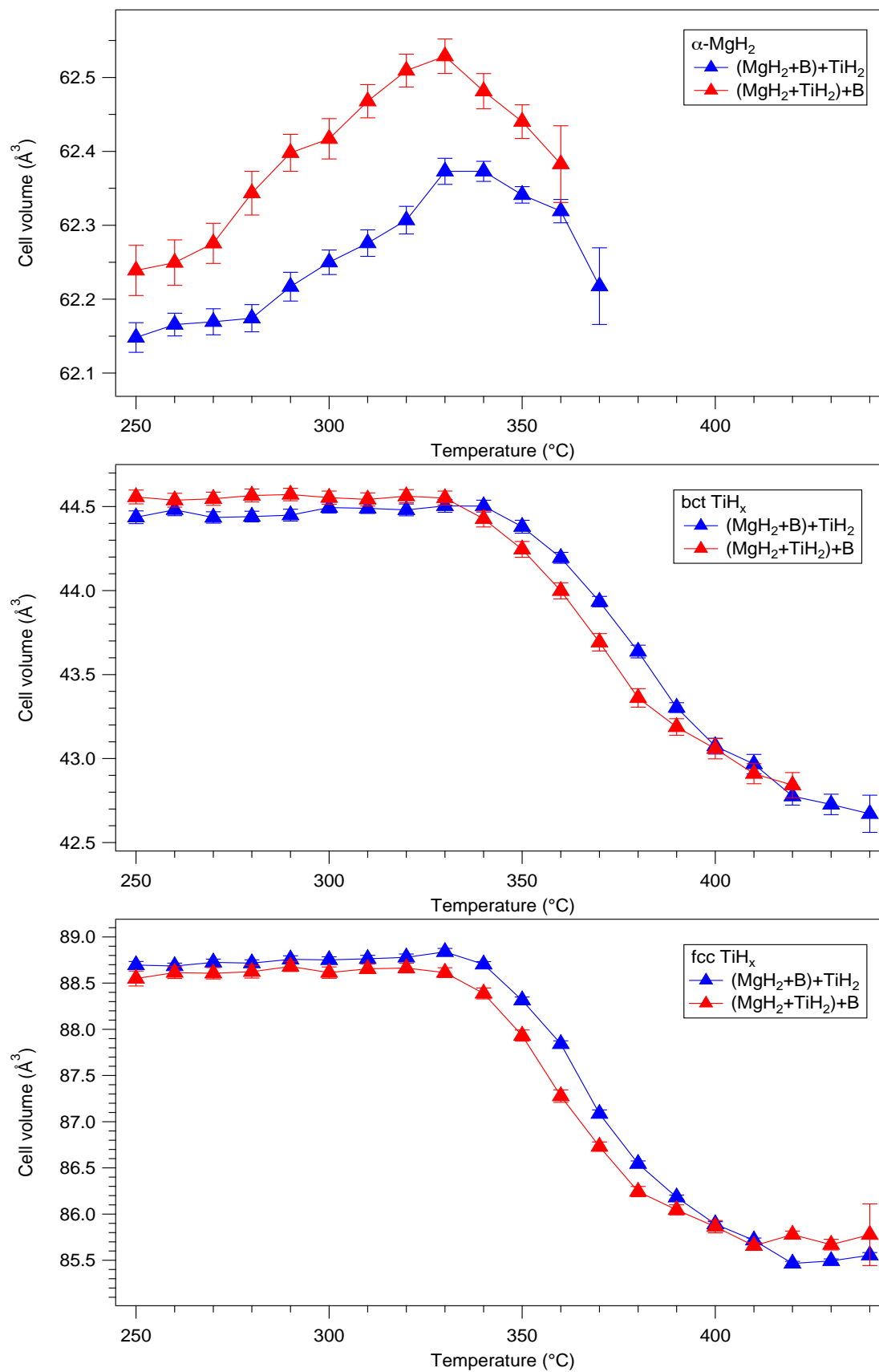
Figure 8.14 Cell volumes of the α-MgH$_2$, bct TiH$_x$ and fcc TiH$_x$ phases in the milled (MgH$_2$+B)+TiH$_2$ and (MgH$_2$+TiH$_2$)+B samples as they are heated from 250 to 440 °C.
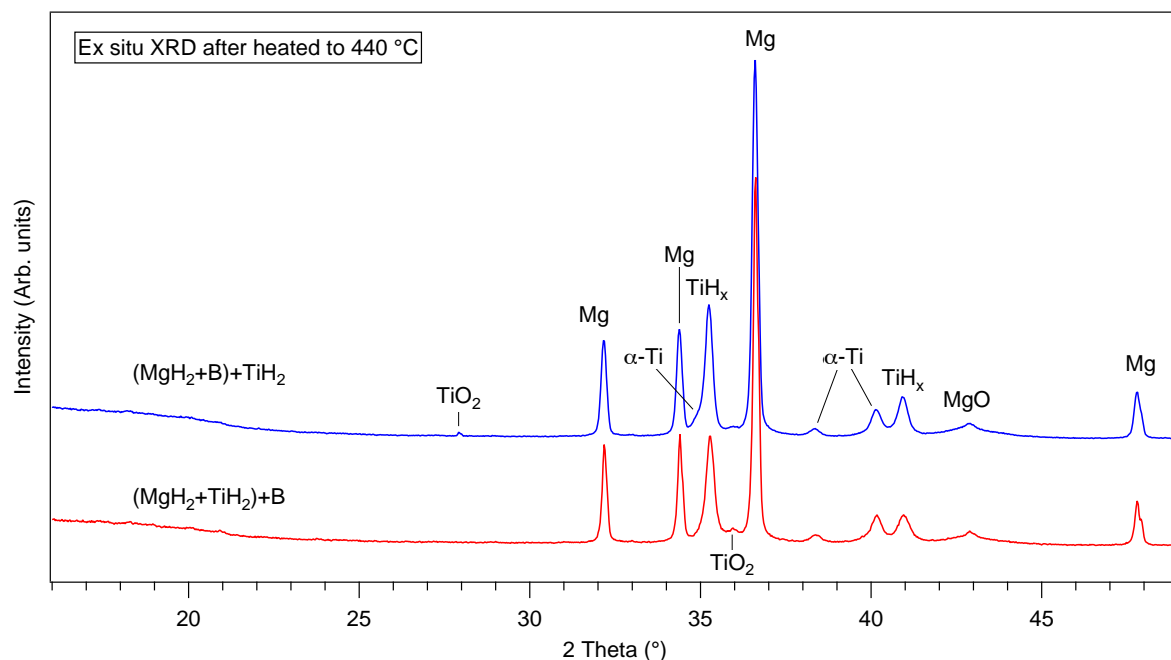
Figure 8.15 Ex situ room temperature XRD patterns of milled $(MgH_2+B)+TiH_2$ and $(MgH_2+TiH_2)+B$ samples after being heated to 440 °C in in situ XRD measurements (Figures 8.13 and 8.14).

To sum up, both MgH_2 and fcc TiH_2 phases were destabilised by ball milling the MgH_2-B-TiH_2 mixtures and the fcc TiH_2 was partially transformed into a bct structure. Higher H_2 capacities were observed for this ternary composition, compared with the milled MgH_2-B and MgH_2-B-Ti samples. The MgH_2 phase decomposed through a second-order reaction, indicating that Ti and TiH_2 additions have a different destabilization effect in the Mg-B-Ti-H system. There is no evidence for the formation of a B-H bond-containing compound, under the experimental conditions used.

8.3.4 MgH_2-B-$TiCl_3$ ternary mixtures

8.3.4.1 DSC-TGA-MS

The DSC, TGA-MS measurements of the three different milled MgH_2-B-$TiCl_3$ samples are shown in **Figure 8.16**. The onset hydrogen desorption temperatures of all the samples are significantly reduced to below 100 °C, although dehydrogenation does not finish until 350 °C.
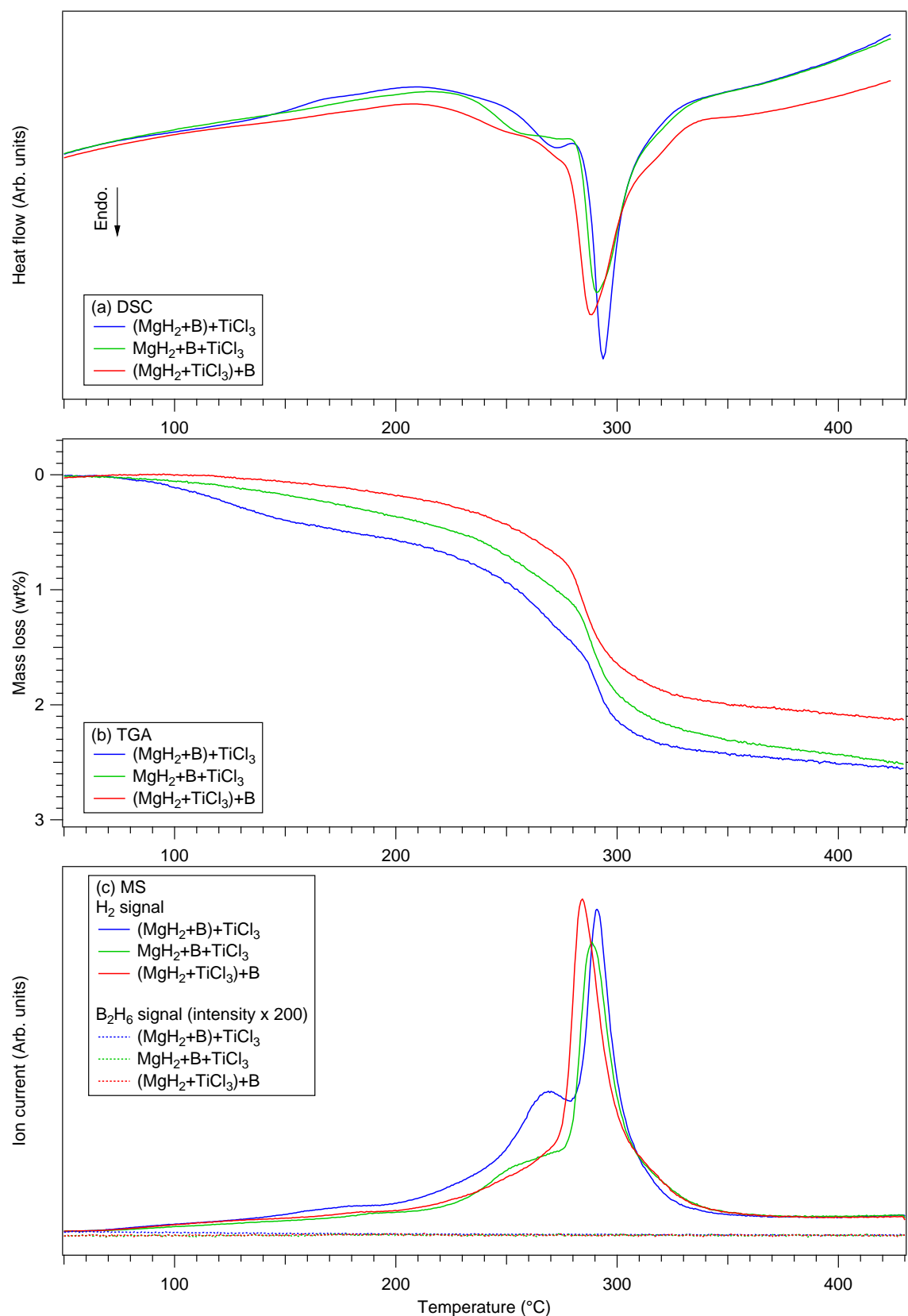
Figure 8.16 (a) DSC, (b) TGA and (c) MS measurements of MgH_2-B-$TiCl_3$ which had been milled in 100 bar H_2 for 2 h with the addition of B and TiH_2 (for the milling conditions shown in Table 8.1). All measurements were performed at a heating rate of 2 °C/min under flowing Ar. The intensities of the B_2H_6 MS signals were multiplied by 200.

For the (MgH$_2$+B)+TiCl$_3$ sample, desorption occurs in three steps starting at 70 °C. The first desorption stage has a gradually sloping MS H$_2$ signal and corresponds to weight loss of 0.65 wt% at 220 °C. The second and third stages appear as two hydrogen peaks at 268 and 289 °C, corresponding to H$_2$ releases of 0.81 wt% and between 220-280 °C and 280-340 °C, respectively. The total weight loss at 430 °C is 2.55 wt% H$_2$, with no diborane emission detected.

In contrast, the MgH$_2$+B+TiCl$_3$ and (MgH$_2$+TiCl$_3$)+B samples release less hydrogen during the first and second desorption steps, which agrees well with smaller slopes observed for their MS H$_2$ signals. The major desorptions for MgH$_2$+B+TiCl$_3$ and (MgH$_2$+TiCl$_3$)+B occur at 287 and 283 °C and resulting in total weight losses of 2.50 and 2.14 wt% at 430 °C, respectively (no diborane release was detected).

8.3.4.2 In situ XRD

In situ XRD measurements were performed on the MgH$_2$-B-TiCl$_3$ samples between 30 and 440 °C in flowing helium. Patterns were collected isothermally at 20 °C intervals with a heating rate of 12 °C/min. Samples were loaded in Al$_2$O$_3$ crucibles and therefore small peaks due to the crucible are observed in all patterns.

When the (MgH$_2$+B)+TiCl$_3$ and (MgH$_2$+TiCl$_3$)+B samples are heated from 30 °C, X-ray diffraction peaks for α-MgH$_2$, Mg and partially crystalline B are observed (**Figure 8.17** and **Figure 8.18**). No peaks for any Ti-containing compounds can be observed: this may be because any Ti-containing phase(s) were highly dispersed throughout the MgH$_2$ matrix by the ball milling process (Ma *et al.*, 2007). At 240 °C, diffractions from MgCl$_2$ appear with a concurrent decrease in the diffraction peak intensity of the α-MgH$_2$ phase. This occurs in the same temperature range as the second and third desorption events in the DSC-TGA-MS measurements.
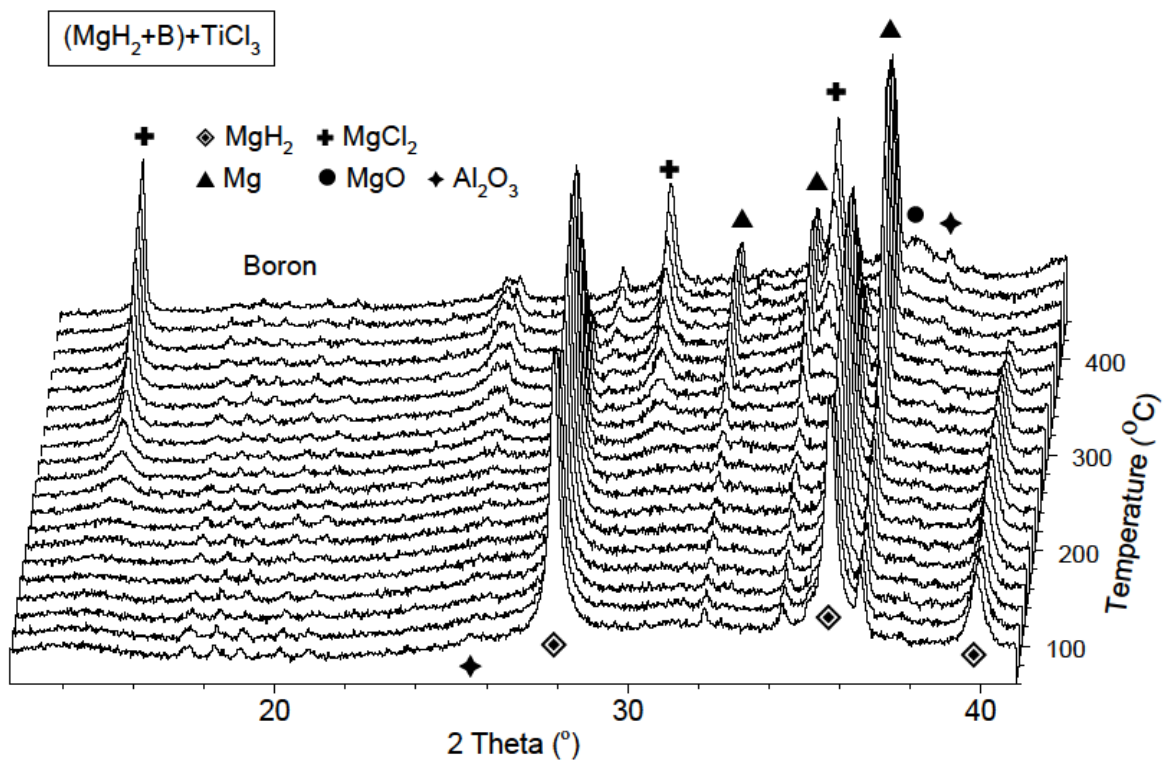
Figure 8.17 In-situ XRD of milled $(MgH_2+B)+TiCl_3$ heated at 12 °C/min from 60 to 440 °C. The patterns were taken every 20 °C, under 2 bar flowing He (100 ml/min).
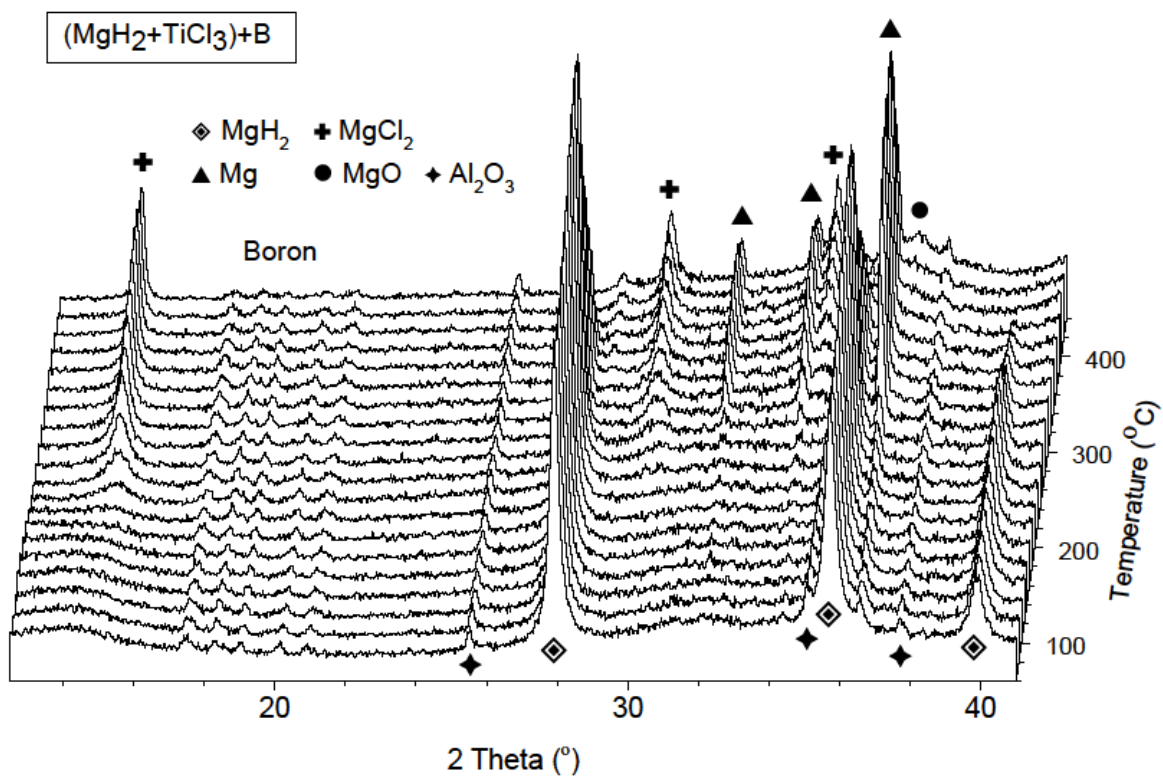
Figure 8.18 In-situ XRD of milled $(MgH_2+TiCl_3)+B$ heated at 12 °C/min from 60 to 440 °C. The patterns were taken every 20 °C, under 2 bar flowing He (100 ml/min).

Although no crystalline Ti-containing phase(s) can be detected, the formation of $MgCl_2$ and H_2 is most likely due to the reaction of $TiCl_3$ and MgH_2 to form TiH_2, $MgCl_2$ and H_2 during the first desorption step. Such a reaction corresponds to Equation 8.1, which was proposed by Ma *et al.* (2007) for the milled $MgH_2+0.04TiX_3$ (*X* = F or Cl) system. Diffraction peaks for α-MgH_2 phase do not completely disappear until 400 °C, leaving $MgCl_2$, Mg, B and MgO in the pattern at 440 °C. Diffraction peaks for boron appeared to be present throughout the heating process.

$$MgH_2 + {}^2\!/_3 TiCl_3 \rightarrow {}^2\!/_3\ TiH_2 + MgCl_2 \qquad (8.1)$$
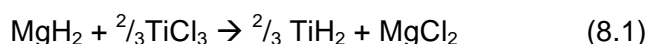
8.4   General discussion and conclusion

Prompted by a report of an interesting composition obtained in a thin-film form via Physical Vapour Deposition (PVD) (Amieiro-Fonseca *et al.*, 2011), attempts were made in this work to produce Mg-B-Ti-H ternary hydrides in a bulk powder form, by ball-milling mixtures of $0.4MgH_2+0.6B$, and $0.36MgH_2+0.58B+0.06TiX$ (TiX = Ti, TiH_2 or $TiCl_3$) in 100 bar H_2. The TiX or B compounds were added to MgH_2 after a milling time of 0 or 1 h, with a total milling time of 2 or 20 h. The structural and vibrational characterisation show no direct evidence of the formation of any B-H containing compounds in any of the samples.

After milling in 100 bar H_2, the decomposition temperature of MgH_2 decreased from 400 to 330 °C, due to improved sorption resulting from the reduced grain and particle size. This improvement in H_2 sorption kinetics occurred without a decrease in gravimetric H_2 capacity. The addition of boron to MgH_2 did not affect the decomposition temperature but reduced the H_2 capacity by 3-7 wt%. A small amount of B_2H_6 release was only detected for the MgH_2+B (20 h) sample, suggesting that boron might react with H_2/MgH_2 to form a small amount of amorphous B-H containing compound(s) after long duration milling under high-pressure hydrogen.

For the MgH_2-B-Ti samples, the hydrogenation of hcp α-Ti was a gradual process. The

hydrogen initially dissolved into the hcp Ti phase as α solid solution (H concentration < 1 at%, i.e. x < 0.01 in TiH$_x$). After further milling, bct TiH$_x$ formed, with the amount of hydrogen absorbed depending on the milling duration. In addition, the substitution of up to 1.2 at% Ti into Mg and 2.3 at% Ti into MgH$_2$, appears to take place according to the change in lattice parameters for each phases. With increasing milling duration (at least 20 h), full hydrogenation to fcc TiH$_2$ phase could be achieved. However, the addition of B appears to slow down the formation of TiH$_x$.

As for hydrogen storage properties, the hydrogen desorption temperature is reduced by up to 20 °C for the 2 h milled samples, although the H$_2$ capacities decrease to 2.9-3.1 wt%. With a longer milling time, the 20 h sample shows a significant reduction in H$_2$ desorption temperature of about 105 °C, corresponding to a H$_2$ capacity of 3.7 wt%. A stronger bonding between Ti and H led some of the hydrogen from MgH$_2$ to react with Ti to form titanium hydrides (i.e. coherent interface between MgH$_2$ and TiH$_x$), resulting in a reduction in the hydrogen capacities for the 2 h MgH$_2$-B-Ti samples (i.e. compared to the H$_2$ capacity expected for fully decomposed MgH$_2$).

In milled MgH$_2$-B-TiH$_2$, neither fcc Mg-Ti-H hydrides (Asano and Akiba, 2009) nor substitution of Ti into the MgH$_2$ phase were observed. The formation of a coherent interface between the MgH$_2$ and TiH$_2$ phases due to milling, leads to the original fcc TiH$_2$ being largely transformed to a bct TiH$_x$ structure, in order to mininise its lattice strain. On heating, the hydrogen capacity increases to a maximum of 3.68 wt% due to the partial decomposition of the titanium hydrides; and the H$_2$ peak temperature is reduced to 300 °C compared to the milled MgH$_2$ and MgH$_2$-B-Ti samples. The in situ XRD measurements indicate that the TiH$_2$ additive has a different thermal destablisation effect: MgH$_2$ liberated hydrogen atoms from the lattice sites leading to gradual contraction in the lattice parameters, whereas the lattice parameters of the MgH$_2$ from MgH$_2$-B-Ti samples underwent only linear thermal expansion until complete decomposition at 370 °C. In addition, the titanium hydride phases partially decompose to Ti and TiH$_{1.6}$ starting at 320 °C,

which compares with an onset desorption of 450 °C for TiH_2 (finishing at around 800 °C) (Kennedy and Lopez (2003).

For the milled MgH_2-B-$TiCl_3$ samples, the Ti-containing compound is thought to be highly dispersed throughout the MgH_2 matrix (Ma *et al.*, 2007), and hence can be considered to be amorphous. The addition of $TiCl_3$ leads to the largest reduction in hydrogen desorption temperature of all the samples, giving onset and peak temperatures of 70 and 284 °C, respectively. However, the H_2 capacity of the composite is reduced to 2.55 wt%, due to the abundance of $TiCl_3$. It is thought that the MgH_2 reacts with $TiCl_3$ to form $MgCl_2$, TiH_2 and H_2. However, no Ti-containing compound was observed during in situ XRD up to 400 °C. The resulting products and hydrogen capacities of the milled MgH_2, $0.4MgH_2$-$0.6B$, $0.36MgH_2$-$0.58B$-$0.06TiX$ samples, are compared in **Table 8.6**.

However, amorphous boron appears to be stable in all the MgH_2-B-TiX samples and appears not to have an effect on the decomposition process. With regard to the synthesis of new Mg-B-Ti-H ternary hydrides containing high hydrogen capacity (> 10 wt%), even a long milling duration seemed to not be sufficient to produce a bulk material with the target composition. It might be because the energy barrier of the B-B bonds in the icosahedral clusters of the starting elemental boron is too large to break (using the milling conditions in this work), since each atom is connected to five other atoms via covalent bonds in an icosahedral unit (Barkhordarian *et al.*, 2008). Thus, not only milling conditions and the composition of starting materials, but also the boron source needs to be modified.

Table 8.6 The resulting products and hydrogen capacity of the milled MgH$_2$, 0.4MgH$_2$-0.6B, 0.36MgH$_2$-0.58B-0.06TiX samples. The expected H$_2$ capacity was calculated by assuming H$_2$ is released from only milled MgH$_2$. The R$_{obs./expect}$ is as a ratio of "Total mass loss" and "Expected H$_2$ capacity". If R$_{obs./expect}$ > 1, there is H released from compound(s) in addition to MgH$_2$.

Starting material	Resulting compounds	H$_2$ peak (°C)	Total mass loss (wt%)	Expected H$_2$ capacity (wt%)	Ratio obs./expect
As received MgH$_2$	α-MgH$_2$, Mg	400	6.68		
MgH$_2$ (2 h, H$_2$)	α, γ-MgH$_2$, Mg	330	6.68	6.68	1
MgH$_2$ + B (2 h, Ar)	α, γ-MgH$_2$, Mg, B	327	3.86	4.12	0.94
MgH$_2$ + B (2 h, H$_2$)	α, γ-MgH$_2$, Mg, B	325	3.90	4.12	0.95
MgH$_2$ + B (20h, H$_2$)	α, γ-MgH$_2$, Mg, B, amorph. B-H bond containing phase	310	3.99 (H$_2$, B$_2$H$_6$)	4.12	0.97
(MgH$_2$ + B) + α-Ti	α, γ-MgH$_2$, Mg, B, α-Ti, bct TiH$_x$	330	3.06	3.39	0.90
MgH$_2$ + B + α-Ti (2h)	α, γ-MgH$_2$, Mg(Ti), B, α-Ti?, bct TiH$_x$	320	2.97	3.39	0.88
(MgH$_2$ + α-Ti) + B	α-Mg(Ti)H$_2$, γ-MgH$_2$, Mg(Ti), B, bct TiH$_x$	309	2.89	3.39	0.85
MgH$_2$ + B + α-Ti (20h)	α-Mg(Ti)H$_2$?, γ-MgH$_2$, Mg(Ti), B, bct TiH$_x$, fcc-TiH$_2$	226	3.71	3.39	1.09
(MgH$_2$ + B) + fcc-TiH$_2$	α, γ-MgH$_2$, Mg, B, bct TiH$_x$, fcc-TiH$_2$	323	3.67	3.37	1.09
MgH$_2$ + B + fcc-TiH$_2$	α, γ-MgH$_2$, Mg, B, bct TiH$_x$, fcc-TiH$_2$	308	3.68	3.37	1.09
(MgH$_2$ + fcc-TiH$_2$) + B	α, γ-MgH$_2$, Mg, B, bct TiH$_x$, fcc-TiH$_2$	300	3.48	3.37	1.03
(MgH$_2$ + B) + TiCl$_3$	α, γ-MgH$_2$, Mg, B, amorph.Ti-containing phase	291	2.55	2.52	1.01
MgH$_2$ + B + TiCl$_3$	α, γ-MgH$_2$, Mg, B, amorph.Ti-containing phase	288	2.50	2.52	0.99
(MgH$_2$ + TiCl$_3$) + B	α, γ-MgH$_2$, Mg, B, amorph.Ti-containing phase	284	2.14	2.52	0.85

9   Li-Mg Alloy

High-energy reactive milling of a Li-Mg alloy was carried out in 100 bar H_2, in an attempt to directly hydride an ordered Li-Mg alloy phase. Characterisation of the structural and thermal properties of ball-milled samples as a function of temperature, will be discussed in this chapter.

Prior to measurements or milling, the as-received Li-Mg alloy (obtained from Ilika plc) was gently polished using a SiC grinding paper (P800) in order to minimise the amount of oxide/hydroxide on the surface of the Li-Mg ribbon. The Ilika plc was unable to tell the composition of the alloy; but speculated that the alloy was synthesised via a combination of induction melting and cold-rolling (Shi *et al.*, 2001). Approximately 1 g of as-received Li-Mg alloy was loaded into a stainless steel milling vial (ball-to-powder weight ratio ~50:1). The vial was evacuated and charged with H_2 for five or more cycles, and then filled with 100 bar H_2. Planetary ball-milling was conducted at 200 rpm for 1, 2 and 5 h, in which each 15 min of milling was followed by a 15 min rest period to try to prevent any excessive temperature increase during ball-milling. The H_2 pressure was periodically checked during milling and was refilled to 100 bar if it had dropped. Samples were investigated by in/ex situ XRD and Raman spectroscopy, and DSC-TGA-MS measurements.

9.1   Structural characterisation

The Li-Mg alloy was received in the form of a soft, malleable ribbon (about 1 mm thick, and 5 mm wide), as shown in **Figure 9.1**. When the ribbon was gently polished, the light-gray surface oxide was removed, revealing a silvery-white coloured ribbon.

Li-Mg ribbon alloy   **5 h milled sample**

Figure 9.1 Li-Mg ribbon before and after milled for 5 h in 100 bar H_2.

Figure 9.2 shows XRD patterns of the Li-Mg alloy before and after milling in 100 bar H_2 for 1, 2 and 5 h. The XRD refinement indicates that the Li-Mg alloy ribbon has a bcc Li(Mg) solid solution structure (space group *Im*-3*m*) with a preferred plane orientation of (002). The lattice parameter of the alloy was refined as a = 3.5070(6) Å. According to the lattice parameter variation as a function of Li content (Herbstein and Averbach, 1956), the as-received Li-Mg alloy is most likely to have a stoichiometric composition of 97 at% Li and 3 at% Mg.

After ball-milling in 100 bar H_2, the Li-Mg ribbon changed into a brown powder for all 1, 2 and 5 h milled samples. The diffraction peaks for the bcc Li-Mg phase disappeared in the 2 and 5 h milled samples, but might still be present as a shoulder at 36.1° *2θ* in the 1 h sample. The formation of LiH (> 90 wt%) and α-Mg was observed in all the milled samples, in addition to a tiny amount of crystalline hexagonal α-MgH_2 (< 1 wt%) in the 1 and 5 h samples. This was the first report to demonstrate the large and fast hydrogenation of Li-Mg

alloy to form binary hydrides by high-energy reactive milling. Moreover, several small unknown peaks at 16.3, 26.1, 30.8, 33.2, 35.1 and 40.7° *2θ* appeared in the 2 h sample, of which the peak at 26.1° *2θ* was also observed in the 1 and 5 h samples. These unidentified peaks seem to not be associated with any known oxide, hydroxide, nitride or amide of Li, Mg or Fe, or to the ternary hydrides $LiMgH_3$ and Li_2MgH_4 from theoretical calculations (Vajeeston *et al.*, 2008; Li *et al.*, 2011a).
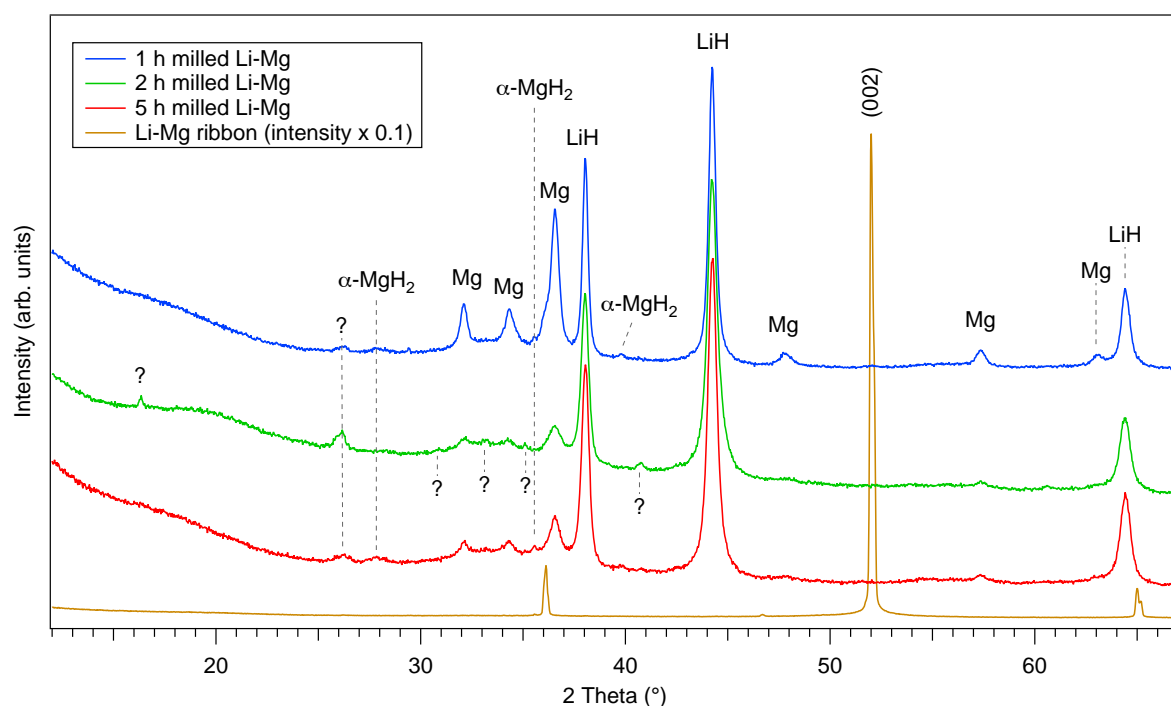
Figure 9.2 XRD patterns of Li-Mg ribbon samples before and after milling in 100 bar H_2.

The lattice parameters of the LiH and Mg phases present in the three milled samples are summarized in **Table 9.1**. The lattice parameters of LiH in the 1 and 2 h samples are similar to the as-purchased pure LiH compound, but appear to be slightly smaller (0.4 %) than those of the 5 h sample. Lattice parameters of the Mg phase tend to expand with increasing milling time, resulting in a larger *c/a* ratio as well as cell volume. This could be an indication that the Li atoms gradually separate from the alloy to form a hydride, leaving α-Mg with a small amount of Li in solution. The structural refinement for the MgH_2 phase is not given, as its diffraction peaks are too weak and the pattern background too noisy, to allow a proper

fitting. A precise determination of the relative phase abundance is not possible due to the presence of unknown/amorphous phase(s).

Table 9.1 Lattice parameters for LiH and Mg for the 1, 2 and 5 h milled Li-Mg samples.

Milling time	LiH		Mg			
	a (Å)	V (Å^3)	a (Å)	c (Å)	c/a ratio	V (Å^3)
1 h	4.082(3)	68.0(1)	3.204(2)	5.201(4)	1.623	46.2(1)
2 h	4.082(5)	68.0(2)	3.204(6)	5.234(12)	1.633	46.5(2)
5 h	4.087(6)	68.3(3)	3.207(5)	5.221(9)	1.628	46.5(2)
As-received LiH	4.083 (3)	68.1(1)				
Mg *			3.2094	5.2103	1.623	46.48

* reported by (Swanson and Tatge, 1953)

9.2   Thermal decomposition

9.2.1   DSC-TGA-MS

DSC-TGA-MS measurements of the milled Li-Mg samples are shown in **Figure 9.3**, and the reaction temperatures and weight losses are summarised in **Table 9.2**. For all samples, no endo/exothermic reactions due to dehydrogenation or phase change (including recrystallisation) was observed below 200 °C. The continuous endothermic dips in the DSC above 390 °C are probably due to an equipment fault.

Table 9.2 Summary of the TGA-MS profiles (Figure 9.3) for the milled Li-Mg samples

Milling Time (h)	1st H$_2$ desorption		2nd H$_2$ desorption		Total released H$_2$ at 450 °C (wt%)
	T_{peak} (°C)	H$_2$ (wt%) (240-350 °C)	T_{peak} (°C)	H$_2$ wt% (390-450 °C)	
1	284	0.09 (2)	425	0.08 (3)	0.17 (4)
2	284	0.32 (4)	415	0.02 (1)	0.34 (4)
5	290	0.36 (2)	425	0.05 (1)	0.41 (2)
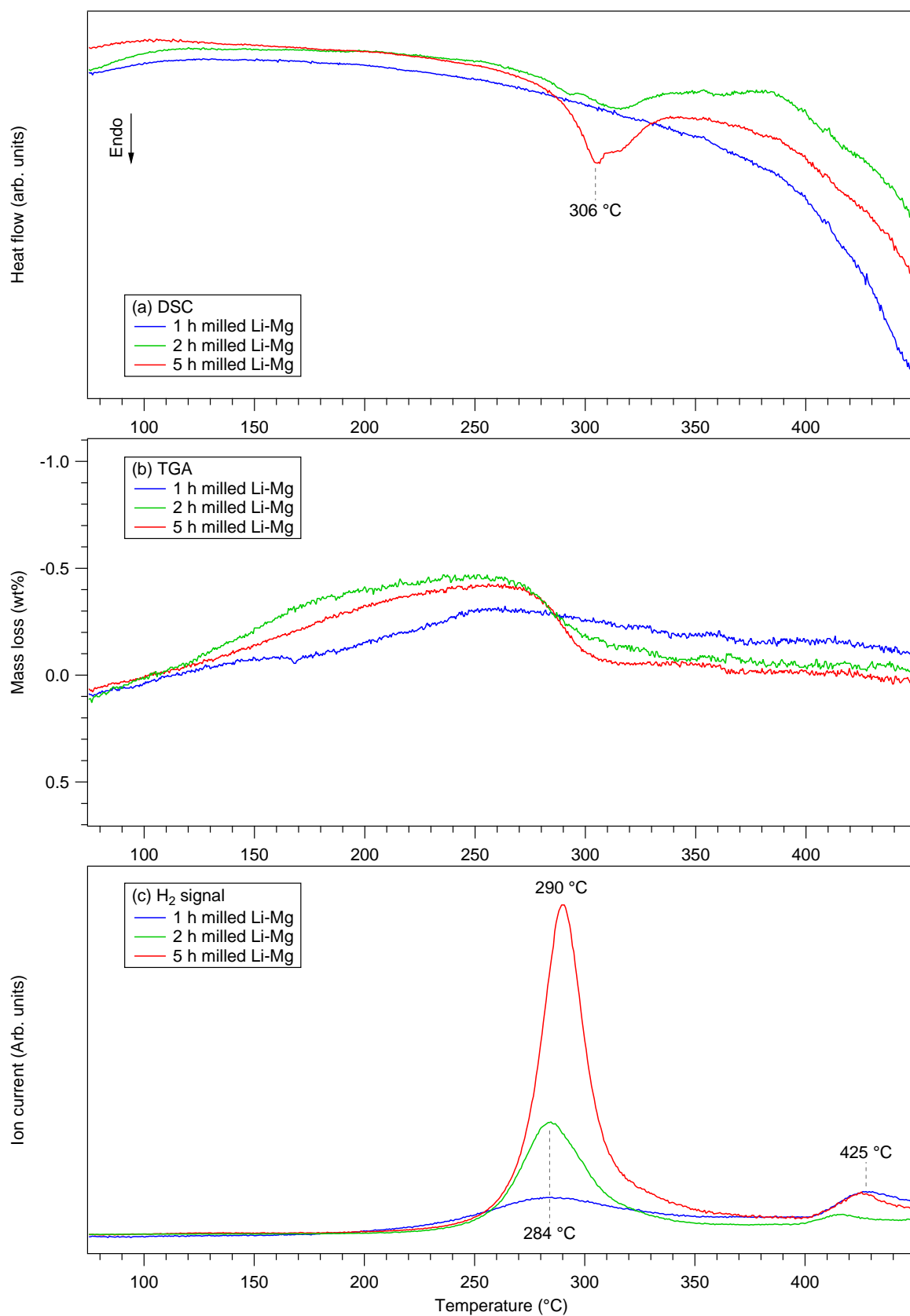
Figure 9.3 DSC-TGA-MS measurements of the milled Li-Mg alloy samples. The blue, green and red lines correspond to the samples milled in 100 bar H_2 for 1, 2 and 5 h, respectively.

When the 1 h sample is heated, no obvious DSC peak is observed, however small and broad rises in the MS H_2 signal are seen at 284 and 425 °C which corresponds to a total mass change of 0.17 wt% between 240 and 450 °C. For the 2 h sample, the DSC exhibits weak overlapping endothermic bumps centred at 293 and 316 °C, which corresponds to a 0.32 wt% H_2 release (240-350 °C). On further heating to 415 °C, a small H_2 peak appeared which gave an additional 0.02 wt% mass loss. The 5 h sample exhibits the strongest intensity endothermic DSC peak (306 °C) with a shoulder at 316 °C) with the release of the largest amount of 0.36 wt% H_2 (290 °C). A further desorption of 0.05 wt% H_2 is observed at 425 °C.

In addition, the 2 h sample was further heated to 600 °C and monitored by TGA and simultaneous MS traces for gaseous H_2 and H_2O (**Figure 9.4**). The H_2 signal largely increases from 470 °C, resulting in a total amount of 1.4 wt% H_2 released at 600 °C. This desorption may be associated with the decomposition of the LiH phase, although this is occurring at a significantly lower temperature than for milled LiH at ~650 °C (Yu *et al.*, 2006). No water peak was detected.
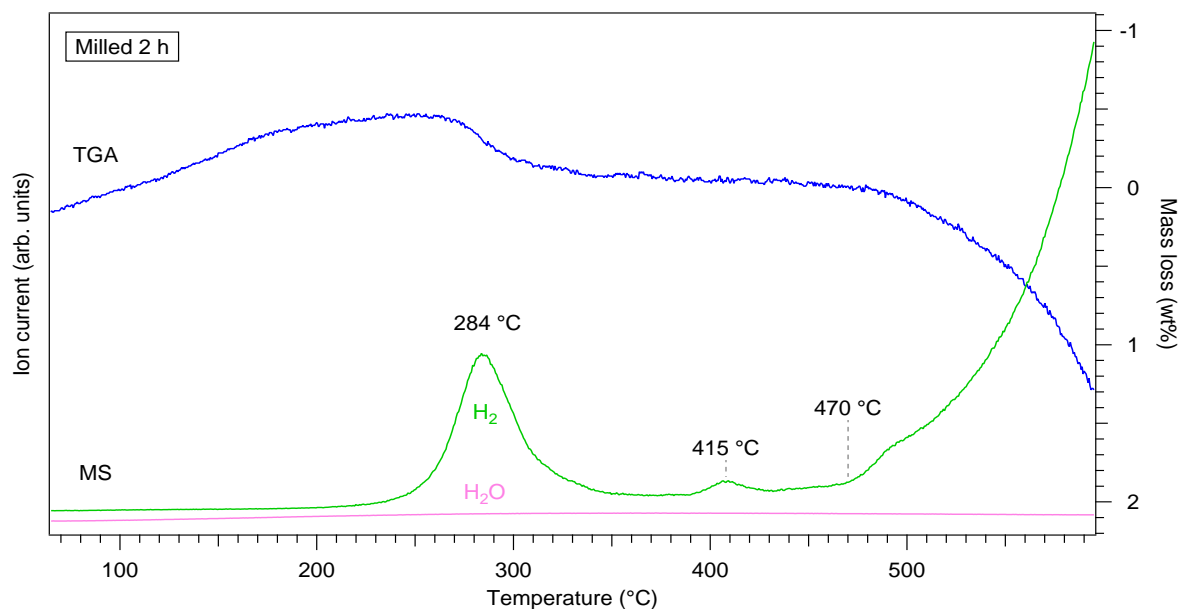
Figure 9.4 TGA and mass spectrometry of a Li-Mg alloy that had been milled for 2 h in 100 bar H_2. The sample was heated at 2 °C/min in 4 bar Ar flowing at 100 ml/min. MS traces for H_2 and H_2O were measured, and the intensity of the MS H_2O signal was multiplied by 300.

9.2.2   In situ XRD

The crystalline decomposition products of the 2 and 5 h milled samples formed during heating were studied by in situ XRD. The XRD patterns were isothermally collected every 25 °C (with a collection time of around 25 min per scan) from 30 °C to 450 °C at a heating rate of 12 °C/min under flowing He (100 ml/min). This corresponds to an average heating rate of 1 °C/min. **Figure 9.5** is a surface plot (view from the top) of the XRD patterns for the 5 h sample during heating; the normalized relative diffraction intensities of LiH, α-MgH$_2$ and Li-Mg solid-solutions (hcp-Mg or bbc-Li based) are shown in **Figure 9.6**.
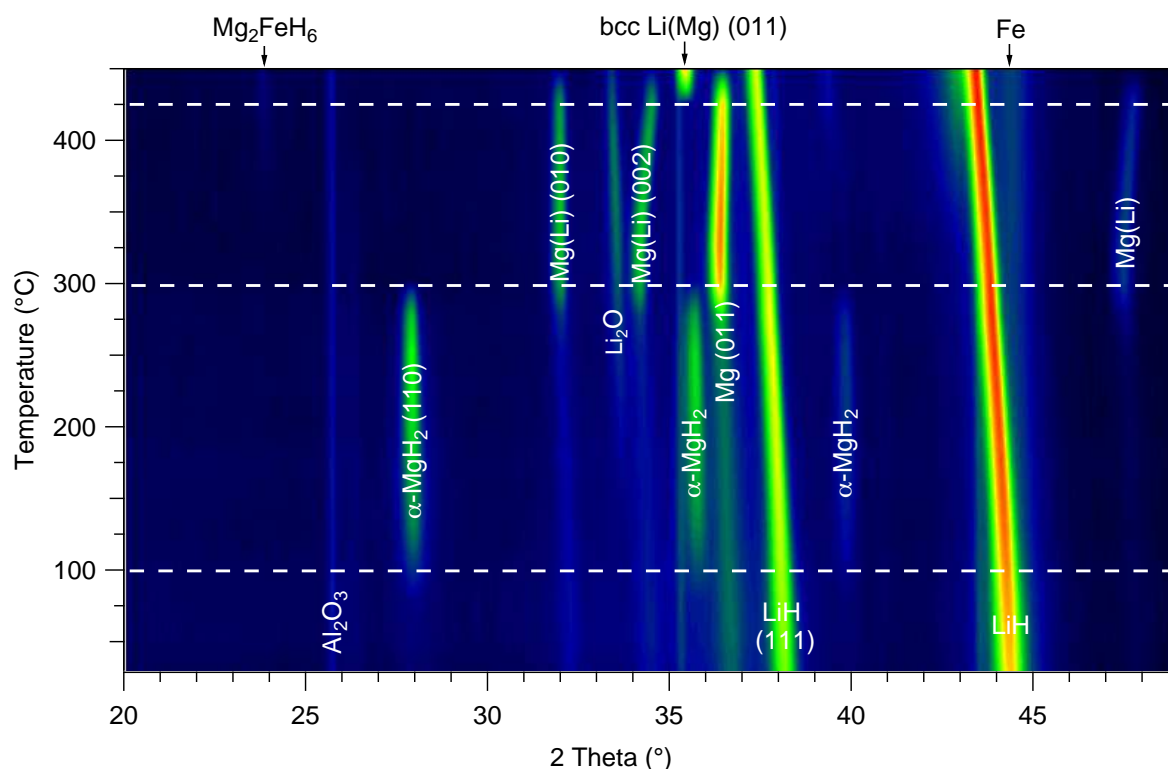
Figure 9.5 Surface plot of the in situ XRD patterns for Li-Mg that been milled for 5 h in 100 bar H$_2$. The sample was heated at 12 °C/min under flowing He. The width of the lines shows the width of the peaks and a brighter colour indicates a higher relative intensity. The white dashed lines are given as a guide of the reaction temperature for the eyes.
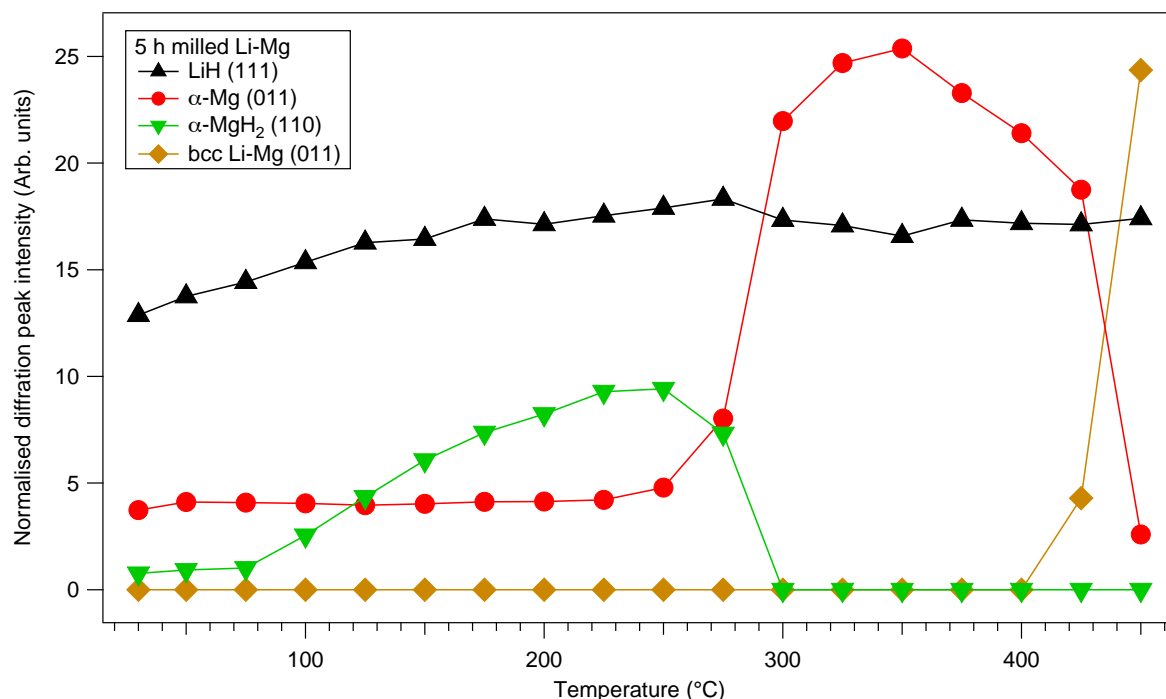
Figure 9.6 XRD intensities for LiH (111), α-MgH$_2$ (110), and solid solutions hcp Mg(Li) (011) and bcc Li(Mg) (011) phases. Data was taken from the in situ XRD measurements for heated 5 h milled Li-Mg (**Figure 9.5**) and then normalised.

At room temperature, the diffraction peaks for LiH, α-Mg and a small amount of α-MgH$_2$ and Al$_2$O$_3$ are observed. Al$_2$O$_3$ (i.e. at 25.6° and 35.2° *2θ*) is due to the sample holder. With increasing temperature, a gradual and steady rise in the diffraction intensity is seen for the LiH phase, which is attributed to some degree of lattice ordering. The abundance of crystalline α-MgH$_2$ abruptly increases from 1 wt% to 4.2 wt% between 100 °C and 225 °C. The formation of crystalline MgH$_2$ could be a result of either a reaction occurred within the sample, or recrystallization and grain growth of amorphous/nanocrystalline MgH$_2$, although no endothermic/exothermic event was observed in the DSC in this temperature range (**Figure 9.3**).

A small amount of Li$_2$O starts to appear (i.e. at 33.6 and 56.3° *2θ*) at 175 °C. The formation of oxides is believed to be due to a small leak in the in situ XRD during heating. Interestingly, Fe appears as a shoulder on the LiH X-ray peak at around 44.6° *2θ* with increasing temperature to 225 °C, and gradually becomes an individual peak on further heating. The impurity Fe originates from the stainless steel milling medium.

The MgH_2 diffraction peaks start to degrade at 275 °C and vanish at 300 °C, with simultaneous growth of the Mg phase. The decomposition of MgH_2 explains the major H_2 desorption event at 284 °C in the MS trace. On further heating, the diffraction positions of Mg shift to higher angles, in particular, there is a much larger shift for the (002) peak at ~34.4° 2θ; which is against thermal expansion to lower angles. At 450 °C, the hcp-Mg(Li) underwent a structural transition to bcc-Li(Mg). Diffraction peaks for MgO was present as a shoulder at 42.8° 2θ.

On the other hand, the impurity Fe reacted with the products Mg and H_2 from the MgH_2 decomposition, to form Mg_2FeH_6 (e.g. at ~23.8° and 39.7° 2θ) upon heating to 350 °C, which is stable upon cooling back to room temperature. The unknown diffraction peak at 26.1° 2θ disappears at 425 °C where the 2nd H_2 desorption (0.05 wt%) occurs.

As for lattice parameters, the cell volumes of the LiH expand almost linearly as a result of thermal expansion up to 450 °C (**Figure 9.7**). On the other hand, the cell volume of MgH_2 from the Li-Mg sample was 0.4% larger than those of as-received/milled pure MgH_2 (**Figure 9.8**). This could be an indication that the Mg^{2+} (r_{ionic} = 0.72 Å) was partially substituted by a larger Li^+ (r_{ionic} 0.76 Å) (Shannon, 1976), to form a bct-Mg(Li)H_2 solid solution. A rough estimation of the composition of the observed $Mg_{(1-x)}Li_xH_2$ phase using Vegard's law (Denton and Ashcroft, 1991) was x = ~0.04. For all samples, similar thermal expansions for the MgH_2 phase are seen up until complete decomposition at 300 °C.
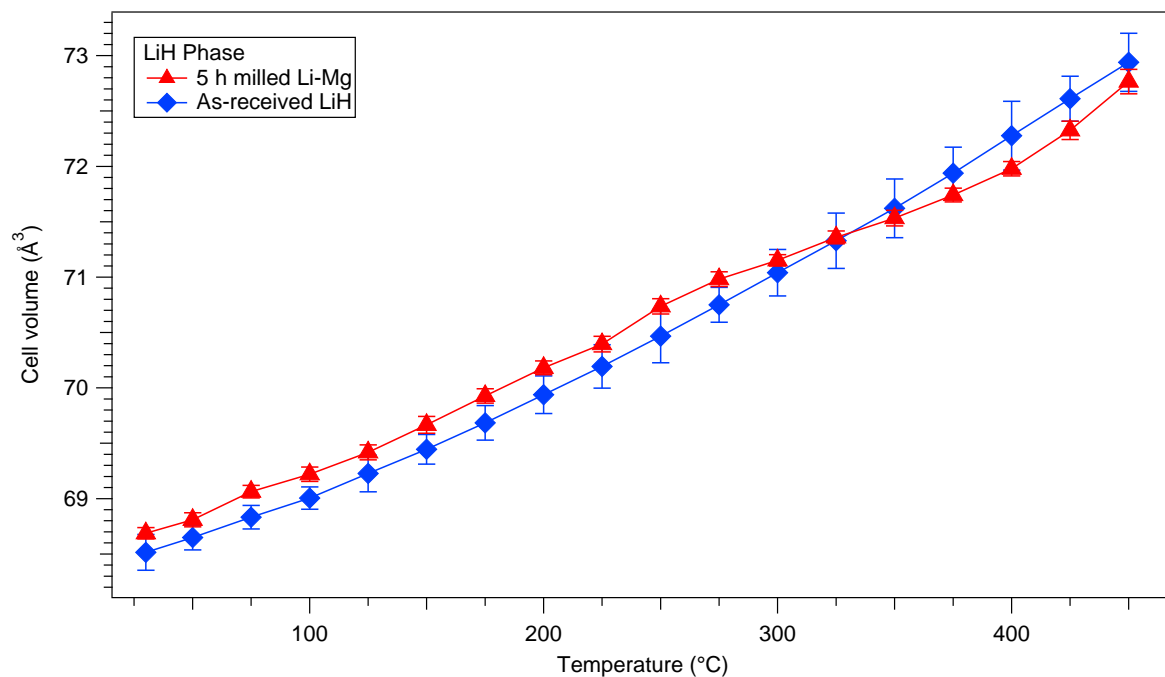
Figure 9.7 Unit cell volumes against temperature for the LiH phase found in: as-received LiH; and in Li-Mg samples that had been milled for 5 h in 100 bar H_2. Where error bars are not shown they are smaller than the data symbols. The solid lines are a guide for the eye.
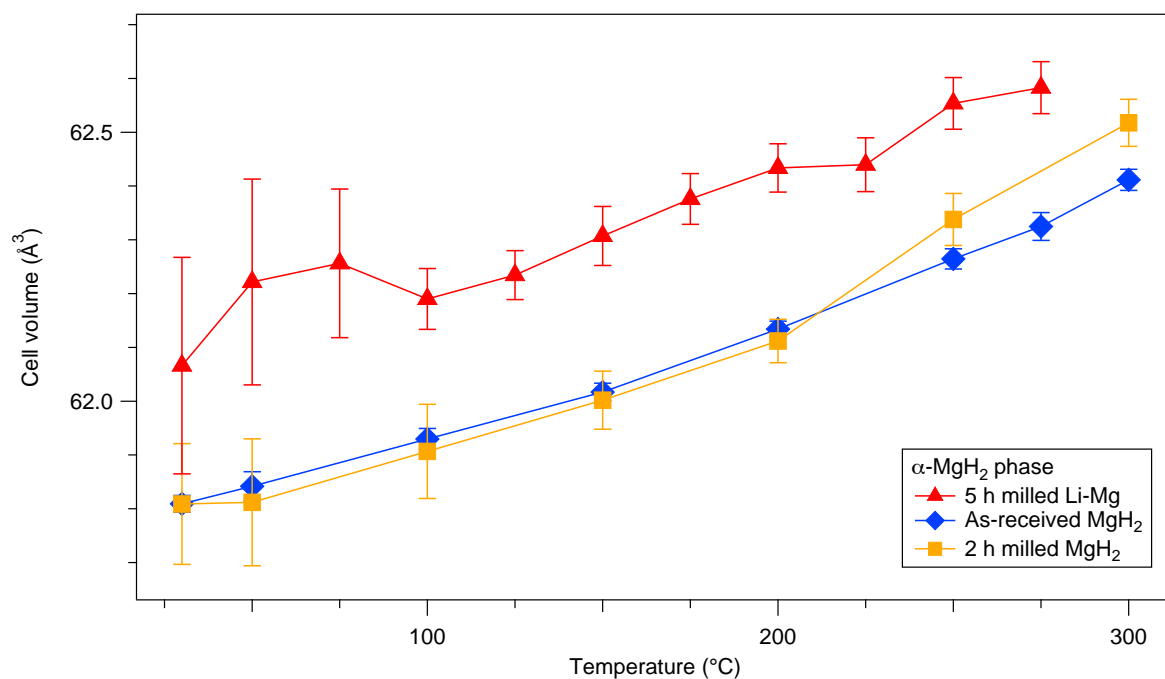
Figure 9.8 Unit cell volumes against temperature for the MgH_2 phase in: the as-received; and in Li-Mg alloy that had been milled in 100 bar H_2 for 2 h and for 5 h. Where error bars are not shown they are smaller than the data symbols. The solid lines are a guide for the eye.

In contrast, the variation of the α-Mg lattice parameters during heating is more complicated

(**Figure 9.9**). Between 30 and 300 °C, there is an overall increase in the lattice parameters

226

due to thermal expansion. A rapid reduction in the parameter *c* is observed above 325 °C, whereas the lattice parameter *a* remains at a value of ~3.2458(15) Å. This results in a smaller *c/a* ratio and significant contractions in cell volumes. As $Mg_{(1-x)}Li_xH_2$ (*x* = ~0.04) completely decomposes at 300 °C, the reaction product Li (r = 1.56 Å) subsequently dissolves into α-Mg (r = 1.60 Å) to form a hcp Mg(Li) solid solution. The degree of substitution increases rapidly on further heating. When the maximum solubility of Li in Mg is reached (~17 atom% Li at 450 °C ((Nayeb-Hashemi *et al.*, 1984), the hcp Mg(Li) transforms to a bcc phase.

Figure 9.10 shows in situ XRD patterns of the milled 5 h sample cooled from 450 to 30 °C at a rate of 12 °C/min, compared with the ex situ XRD pattern of the decomposed sample which had been ground in a mortar and pestle. During cooling, the Li-Mg alloy undergoes a partial phase transformation from bcc to hcp. By comparing in situ XRD patterns on cooling to 30 °C, a large reduction in the intensity of the oxide (Li_2O and MgO) diffraction peaks is observed in the ex situ pattern for the same decomposed sample. Therefore, the oxidation of the elemental Li and Mg was limited to the surface of the sample due to a leak in the in situ XRD system, and appeared not to affect the bulk of the material.
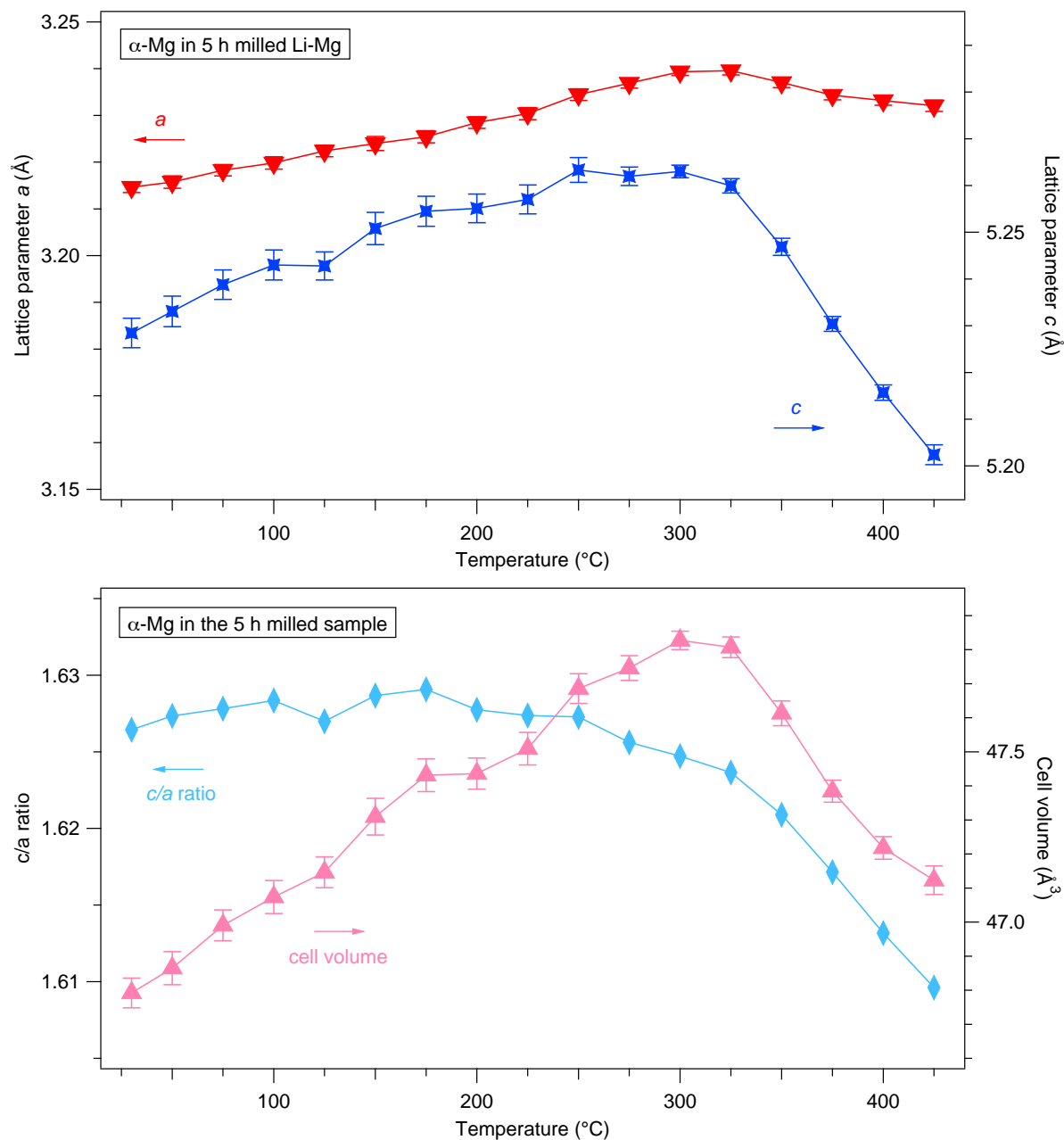
Figure 9.9 Lattice parameters *a*, *c* (top), cell volume and the *c*/*a* ratio (bottom) of the α-Mg phase in Li-Mg alloy that had been milled for 5 h in 100 bar H₂. Where error bars are not shown they are smaller than the data symbols. The solid lines are a guide for the eye.
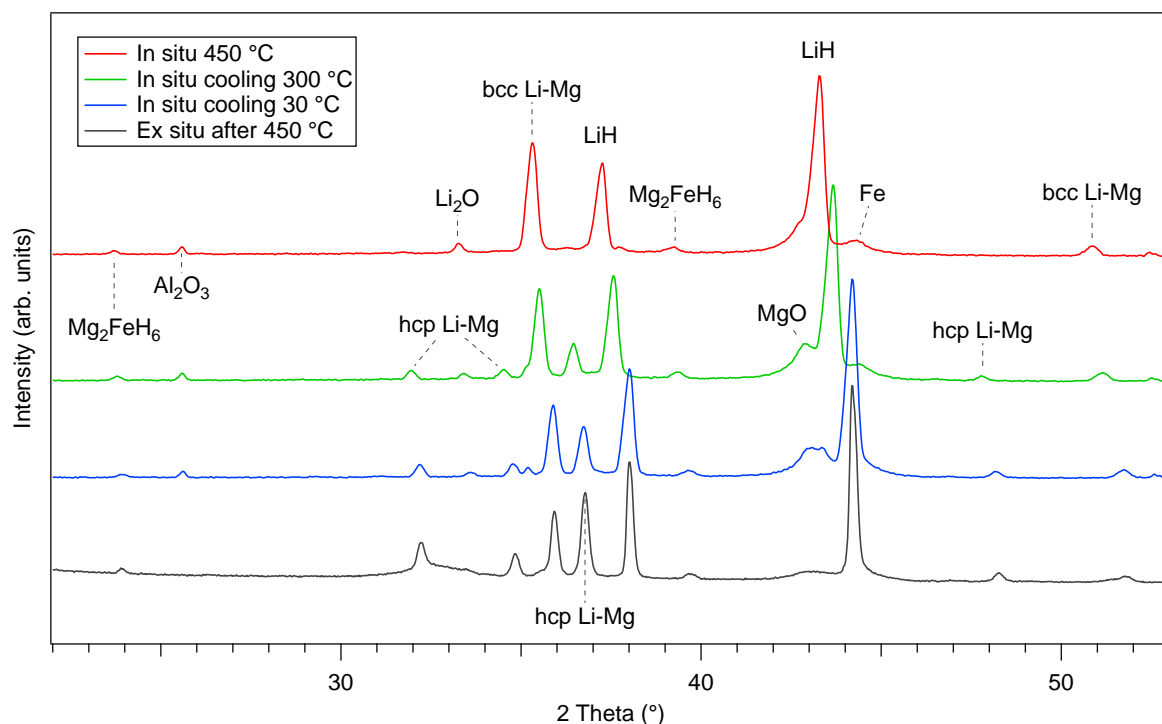
Figure 9.10 In situ XRD patterns of Li-Mg alloy that has been milled for 5 h in 100 bar H_2, measured under flowing He: at 450 °C; then cooled to 300; and finally cooled to 30 °C. Compared to an ex situ room temperature XRD pattern of the decomposed sample (obtained from the in situ XRD measurement) after it had been briefly ground in a mortar and pestle (in an argon glovebox).

9.3   General discussion and conclusions

The direct hydrogenation of a Li-rich Li-Mg ribbon into a powder containing LiH and $Mg_{(1-x)}Li_xH_2$ (x = ~0.04) phases has been demonstrated using high pressure reactive milling. The formation of LiH is thermodynamically and kinetically favorable. The yield of $Mg_{(1-x)}Li_xH_2$ was increased with increasing milling time. A small unknown peak at 26.1° *2θ* appeared in all the milled Li-Mg samples, which is not due to the known oxides, hydroxides, nitrides or amides of Li or Mg, or to the theoretical ternary hydrides $LiMgH_3$ and Li_2MgH_4 (Vajeeston *et al.*, 2008; Li *et al.*, 2011a). In situ XRD measurements showed the growth of crystalline $Mg_{(1-x)}Li_xH_2$ phase above 125 °C. However, it is not clear if the increased amount of $Mg_{(1-x)}Li_xH_2$ is due to the recrystallisation reaction or to the separation of metastable non-crystalline ternary Li-Mg hydrides, as no endo/exothermic events is observed in DSC-TGA-MS traces.

The decomposition of the hydrided Li-Mg samples occurs in three steps. The $Mg(Li)H_2$ decomposes into elemental Mg, Li and gaseous H_2 at ~284 °C, where Li subsequently substitutes for Mg to form a hcp Mg(Li) solid solution. The degree of the substitution increases and leads to a significant reduction in cell volume of hcp-Mg from 325 °C. The solubility of Li in hcp Mg (Li > 17 at% based on the Li-Mg phase diagram) reached at 450 °C, and hcp Li-Mg transforms to a bcc structure. The unknown diffraction peak at 26.1° *2θ* disappears at ~425 °C, which corresponds to a small evolution of H_2. However, the original of this unknown phase is not clear. In the final step, the presence of Mg destabilises the LiH, leading to a reduced H_2 desorption temperature from ~900 to 470 °C.

A small amount (< 0.6 mol%) of the impurity Fe reacts with the products Mg and H_2 from the MgH_2 decomposition, to form Mg_2FeH_6 upon heating to 350 °C, which is stable upon cooling to room temperature. The formation of Mg_2FeH_6 in a flowing helium atmosphere is possibly due to the reaction between Mg, Fe and atomic H migrating in the remnant hydride compounds (e.g. LiH and/or Li-Mg-H). This is different from the formation of Mg_2FeH_6 by the reaction of Mg and Fe via MgH_2 as an intermediate during heating in 100 bar H_2 (Polanski *et al.*, 2010). On the other hand, the stability of Mg_2FeH_6 is backpressure dependent, e.g. decomposed at 340 °C when heated in Ar (Polanski *et al.*, 2010), or at ~430 °C in 2 bar H_2 (Huot *et al.*, 1998). Thus, the thermal stability of Mg_2FeH_6 is probably improved by the presence of LiH and/or Li-Mg-H hydrides.

In future work, the effect of milling conditions (e.g. backpressure and milling time/speed) for Li-Mg alloy needs to be investigated, and optimized for a higher yield of Li-Mg-H. Studies on the vibrational structure, sorption kinetics and reversibility of the materials need to be carried out.

10 Conclusions and Future Work

Complex hydrides are a promising class of materials for hydrogen storage, which have been intensively studied during the past ten years. In this thesis, a family of alkali and alkaline metal borohydrides and Mg-based hydrides, have been investigated mainly by in situ XRD, Raman, DSC-TGA-MS measurements; with particular attention given to their structures, hydrogenation/dehydrogenation pathways and reactivity. The thermal decomposition of the metal borohydrides occurs via a wide range of reaction pathways, often in several steps, which may involve simultaneous – and in some cases coupled – competing reactions.

10.1 Borohydrides

10.1.1 Structure and phase transformation

Both the room temperature orthorhombic and high temperature hexagonal structures of $LiBH_4$ and $LiBD_4$ were observed. The Raman study indicates that the substitution of hydrogen for deuterium significantly affects the B-H bond vibrations, and results in frequency shifts between $LiBH_4$ and $LiBD_4$ due to the increased mass of deuterium compared to hydrogen. When going through the phase transition at 116 °C on heating, the local arrangement of tetrahedral $[BH_4]^-$ ($[BD_4]^-$) becomes more symmetrical and so leading to more reorientational freedom, thus inducing a dramatic broadening in the Raman line-width of the high-temperature phase.

Three different batches of as-received $Mg(BH_4)_2$ were characterised and were found to contain different polymorphs and compositions: the crystalline γ-$Mg(BH_4)_2$, $\alpha_{8\%}$+$\gamma_{92\%}$-$Mg(BH_4)_2$, and amorphous $Mg(BH_4)_2$, of which the batch of amorphous $Mg(BH_4)_2$ was later confirmed to contain a significant amount of oxygen contamination. Upon heating, the γ-$Mg(BH_4)_2$ transformed to β'-phase via the formation of a metastable ε-phase between 130 and 175 °C. There were only small differences in the vibrational frequencies of the $[BH_4]^-$ ions for α-, γ- and ε-$Mg(BH_4)_2$, despite the β' polymorph exhibiting a simpler and broader vibrational feature due to its higher symmetry at the local level. In addition, a disordered $Mg(BH_4)_2$ was produced by high-pressure ball-milling of the crystalline γ-$Mg(BH_4)_2$ in 100 bar H_2 for 2 h. This disordered $Mg(BH_4)_2$ may have similar local ordering of the $[BH_4]^-$ ions to that which occurs in the α-$Mg(BH_4)_2$ polymorph but different from the as-received amorphous $Mg(BH_4)_2$ batch.

As-received $Ca(BH_4)_2$ was found to contain a mixture of α (34.3%), β (57.0%) and γ (8.6%) polymorphs. The introduction of β and γ-$Ca(BH_4)_2$ led to some degree of broadening in the Raman peak width of the sample compared to those for the pure α-$Ca(BH_4)_2$, although no large frequency shift was detected. When $\beta_{\alpha\gamma}$-$Ca(BH_4)_2$ was heated under flowing argon, only vibrational broadening for the phase transformation from α, γ, to β polymorph was observed.

Ball milling of a mixture of $0.68LiBH_4$+$0.32Ca(BH_4)_2$ for 10 h did not yield new compounds or solid solutions; the presence of o-$LiBH_4$, however, appears to have promoted the transformation of β,γ-$Ca(BH_4)_2$ into α-$Ca(BH_4)_2$. With increasing temperature, the o-$LiBH_4$ transformed into h-$LiBH_4$, followed by a phase change from α to β-$Ca(BH_4)_2$ via the partial formation of the γ polymorph. A eutectic melting point appeared at 203 °C, leading to the appearance of a diffuse region (with no diffraction peaks) in the situ XRD patterns that is characteristic of an amorphous phase. Reversible phase transformations between α, γ and β-$Ca(BH_4)_2$ were observed in subsequent heating-cooling cycles between room temperature and the eutectic melting point. An unknown phase, which may tentatively be

ascribed to a new, metastable dual-cation borohydride, was formed when cooled from the eutectic melting point, and it participated in the reversible phase changes that occurred in the subsequent heating-cooling cycles. The identification of this undefined phase is ongoing, however, it does not appear to correspond to: $LiBH_4$; $Ca(BH_4)_2$; or known borohydride-borates, such as $LiCa_3(BH_4)(BO_3)_2$, $Ca_3(BH_4)_3(BO_3)$ etc.

The crystal structures of different polymorphs of borohydrides have been well reported by previous studies. The $[BH_4]^-$ ions of the investigated compounds are all nearly perfectly tetrahedral but the local orientation in the lattice may vary depending on the coordination (e.g. coordination number, metal-BH_4 bonding distance) between the metal and $[BH_4]^-$. This coordination can lead to a difference in the external vibrations of the different borohydrides including their various polymorphs, in the Raman spectra. However, it was difficult to fully detect the external modes (usually at low wavenumbers) as the Raman system used in this work could not measure below 100 cm^{-1}.

10.1.2 Thermal decomposition

The thermal decomposition of the metal borohydrides occurred via a range of reaction pathways, often in several steps, which may involve simultaneous and in some cases coupled competing reactions.

The first hydrogen desorption of $LiBH_4$ started at 312 °C, followed by the second larger stage peaked at 512 °C with the formation of LiH, amorphous boron, and amorphous B-H bond containing intermediate phases. One of these intermediates was most likely $Li_2B_{12}H_{12}$ and/or adducts $Li_2B_{12}H_{12-x}$, which appeared to be stable up to 600 °C. However, the presence of $Li_2B_{12}H_{12}$ only partially explains these unknown Raman peaks. No diborane evolution was observed during heating under 1 bar flowing argon, which may be because: B_2H_6 detection depends on the location of the detector within the TGA-MS system; and/or B_2H_6 evolution is sensitive to the reaction conditions such that is can be kinetically driven by a UHV environment.

After going through a transformation from β'-phase, the decomposition pathway of the crystalline γ-Mg(BH$_4$)$_2$ was from then on, similar to that reported for α-Mg(BH$_4$)$_2$. The main decomposition proceeded via 3-steps between 240 and 400 °C, giving a total of 12.2 wt% H$_2$ evolution with the formation of Mg (MgO) and B at 500 °C. There was no diborane release detected throughout the decomposition process (for the TGA-MS system used in this study, in which the MS is connected to the TGA via a heated capillary tube). In contrast, the milled γ-Mg(BH$_4$)$_2$ sample began to dehydrogenate at 240 °C and released a small amount of the undesirable by-product of diborane gas during H$_2$ desorption at 280 °C. Various amorphous Mg-B-H compounds desorbed H$_2$ and/or interact with each other in multiple steps throughout the decomposition process, some of which then rapidly liberated H$_2$ at 430 °C. MgB$_2$ and possible Mg-B-H species were observed up to 600 °C. The formation of stable Mg-B-H species led to a reduction in the total mass loss of the milled sample from the maximum theoretical H$_2$ content of 14.9 wt%, to the experimentally observed 10.0 wt% at 500 °C.

With increasing temperature, the Ca(BH$_4$)$_2$ started to partial decompose at around 285 °C, and released 1 wt% H$_2$ up to 345 °C. The major dehydrogenation occurred in a single step, giving an intense H$_2$ peak at 364 °C and released 5.2 wt% H$_2$ up to 415 °C. A small rise in H$_2$ signal with 1.9 wt% H$_2$ loss was seen between 415 and 500 °C. After heating to 500 °C, CaB$_6$, CaH$_2$, CaO and possibly amorphous B were found to be the decomposition products of β$_{αγ}$-Ca(BH$_4$)$_2$, accompanied by a total H$_2$ evolution of 8.2 wt%. However, no intermediate phases such as CaB$_2$H$_x$ and CaB$_{12}$H$_{12}$ proposed by previous studies, were observed during the in situ Raman measurements.

The major decomposition of the 0.68LiBH$_4$+0.32Ca(BH$_4$)$_2$ mixture started at about 330 °C, which was 10 °C and 150 °C lower than those of single-phase Ca(BH$_4$)$_2$ and LiBH$_4$, respectively. The formation of amorphous boron and Li$_2$B$_{12}$H$_{12}$ was observed at 350 °C. The intensity of CaB$_6$ increased with the concurrent disappearance of the unknown peak at 500 °C. Only Raman peaks for CaB$_6$, Li$_2$B$_{12}$H$_{12}$ and amorphous boron were observed in the

Raman spectrum at 500 °C.

A summary of the peak temperatures of the main decomposition and the reaction products of the investigated system in this work is shown in **Table 10.1**.

Table 10.1 Summary of decomposition temperatures, mass losses and reaction products. All measurements were performed under flowing Ar or He.

Samples	T_{peak} (°C)	Mass loss (wt%) (500 °C)	Observed products (500 °C)
o-LiBH$_4$	512	-	LiH, amorph B, Li$_2$B$_{12}$H$_{12}$, H$_2$
γ-Mg(BH$_4$)$_2$	293	12.2	Mg (MgO), amorph. Mg-B-H, H$_2$
Milled γ-Mg(BH$_4$)$_2$	280	10.0	Mg (MgO), amorph. B, MgB$_2$ MgB$_{12}$H$_{12}$, H$_2$, B$_2$H$_6$ (600 °C)
β$_{αγ}$-Ca(BH$_4$)$_2$	364	8.2	CaB$_6$, CaH$_2$, CaO, possibly amorph. B, H$_2$
0.68LiBH$_4$ + 0.32Ca(BH$_4$)$_2$	356 Ca(BH$_4$)$_2$ 398 LiBH$_4$	-	CaB$_6$, Li$_2$B$_{12}$H$_{12}$, amorph. B, H$_2$

10.1.3 Effect of diborane

It has been known that diborane plays an important role in the H$_2$ sorption mechanisms of some borohydrides: either a gaseous byproduct of the decomposition or in association to the formation of borane intermediates. This work demonstrates that [B$_{12}$H$_{12}$]$^{2-}$ could be formed by exposing LiBH$_4$, Mg(BH$_4$)$_2$, and Ca(BH$_4$)$_2$ in a mixture of H$_2$ and B$_2$H$_6$ gases, and [B$_{10}$H$_{10}$]$^{2-}$ was also formed in the case of LiBH$_4$ and possibly Mg(BH$_4$)$_2$. With respect to the decomposition process of borohydrides, diborane or similar borane species might be formed which will then react with the remnant materials to form Li$_2$B$_{12}$H$_{12}$ or other higher *closo*-boranes. As these compounds are relatively too stable (and may therefore be considered undesirable impediments to achieving reversibility), controlling B$_2$H$_6$ might be the key to allowing hydrogen cycling of borohydrides under more moderate conditions (of temperature and pressure).

Diborane was also used to understand the possible reversibility of borohydrides. LiBH$_4$

could be synthesised by the reaction of LiH and B_2H_6, with yields of 46 mol%. A small amount of $Li_2B_{12}H_{12}$ was also present as stable by-products. The formation of $Li_2B_{12}H_{12}$ was probably due to a subsequent reaction between the newly formed $LiBH_4$ and B_2H_6 to form a passivation layer of $Li_2B_{12}H_{12}$ on the surface of the $LiBH_4$ powder: this impeded the further absorption of B_2H_6 by LiH.

However, in the case of the sodium system, $Na_2B_{12}H_{12}$ could not be formed by exposing $NaBH_4$ to B_2H_6 and H_2 gases, which is consistent with there being no stable intermediates but rather having Na, B and H_2 present as the decomposition products of $NaBH_4$. On the other hand, it is interesting that 0.6 mol% $NaB_{12}H_{12}$ together with 7 mol% $NaBH_4$ was found in the NaH sample after exposing to B_2H_6 and H_2 gases. This suggests that $Na_2B_{12}H_{12}$ was probably formed via the reaction of B_2H_6 and the newly formed borane intermediate(s) (e.g. possibly NaB_3H_8) instead of $NaBH_4$. However, it is not clear if the formation of $NaBH_4$ originated from the diborane-absorption of NaH and/or $Na(B_xH_y)_n$ (e.g. NaB_3H_8).

Attempts to synthesise $Mg(BH_4)_2$ by heating either as-received or milled MgH_2 in B_2H_6/H_2 at 120-200 °C for 24-60 h were not successful, possibly due to poor diffusion of atomic H inside the bulk material.

10.2 Mg-B-Ti-H and Li-Mg-H hydride systems

Attempts to produce Mg-B-Ti-H ternary hydrides in a bulk powder form were made, by ball-milling mixtures of $0.4MgH_2+0.6B$, and $0.36MgH_2+0.58B+0.06TiX$ (TiX = Ti, TiH_2 or $TiCl_3$) in 100 bar H_2. However, there was no evidence of the synthesis of any new Mg-B-Ti-H ternary hydrides containing high hydrogen capacity (> 10 wt%). Amorphous boron appears to be stable in all the MgH_2-B-TiX (TiX = Ti, TiH_2 or $TiCl_3$) samples and not have an effect on the decomposition process. It was not possible to produce a bulk powder with the target composition even after ball-milling for 20 hours. This may be because the energy barrier of the B-B bonds in the icosahedral clusters of the starting elemental boron, is too large to

break (using the ball-milling conditions used in this work).

For the MgH_2-B-Ti samples, the α-Ti was hydrogenated to bct TiH_x after 2 h milling and to fcc TiH_2 after 20 h milling. The hydrogen desorption temperature is reduced by up to 20 °C for the 2 h milled samples, and the hydrogen capacities decrease to 2.9-3.1 wt%. This may be due to the stronger bonding between Ti and H leading to some of the hydrogen from the MgH_2 phase to react with Ti to form titanium hydrides, resulting in a reduction in the hydrogen capacities for the 2 h MgH_2-B-Ti samples (i.e. compared to the H_2 capacity expected for fully decomposed MgH_2). With increasing milling duration to 20 h, a large reduction in H_2 desorption temperature of about 105 °C was achieved, for MgH_2-B-Ti with a H_2 capacity of 3.7 wt%. But no thermodynamics improvement was observed: 78.9 kJ/mol H_2 by PCT measurements in comparison to 78.5 kJ/mol H_2 for as-received MgH_2.

The MgH_2-B-TiH_2 mixtures, show the formation of a coherent interface between the MgH_2 and TiH_2 phases leads to the transformation from the original fcc TiH_2 to a bct TiH_x structure in order to minimise its lattice strain after milling. Upon heating to 330 °C, MgH_2 liberated hydrogen leading to a gradual decrease in its lattice parameters. The Mg from the decomposition destabilised the titanium hydride phases, so that they started to decompose at 320 °C compared to the usual onset desorption of 450 °C for TiH_2. A maximum of 3.68 wt% hydrogen capacity was observed, which is the highest among all the Mg-B-TiX samples.

With the addition of $TiCl_3$, the onset desorption temperature of Mg-B-Ti-H system was reduced to 70 °C, although the desorption did not complete until 350 °C and the hydrogen capacity was lowered to 2.55 wt%. $TiCl_3$ reacts with MgH_2 to form more stable products of $MgCl_2$, TiH_2 and H_2, thereby giving a smaller desorption enthalpy.

Finally, the direct hydrogenation of a Li-rich Li-Mg ribbon into a powder containing LiH and $Mg_{(1-x)}Li_xH_2$ (x = ~0.04) phases has been demonstrated using high pressure reactive milling in 100 bar H_2. The formation of LiH is thermodynamically and kinetically favoured. The yield of $Mg_{(1-x)}Li_xH_2$ was increased with increasing milling time. A small unknown peak at 26.1° *2θ*

appeared in all the milled Li-Mg samples, which is not due to the known oxides, hydroxides, nitrides or amides of Li or Mg, or to the theoretical ternary hydrides $LiMgH_3$ or Li_2MgH_4. A significant proportion of the Mg-containing phases are amorphous or nanocrystalline after milling and only became visible in XRD patterns above 125 °C. However, it is not clear if the increased amount of $Mg_{(1-x)}Li_xH_2$ is due to the recrystallisation reaction or to the separation of metastable non-crystalline ternary Li-Mg hydrides.

The decomposition of the hydrided Li-Mg samples occurs in three steps. The $Mg(Li)H_2$ decomposes into elemental Mg, Li and gaseous H_2 at ~284 °C, where Li subsequently substitutes for Mg to form a hcp Mg(Li) solid solution. The hcp Li-Mg transforms to a bcc structure when reaching the solubility of Li in hcp Mg (Li > 17 at% based on the Li-Mg phase diagram) at 450 °C. The unknown diffraction peak at 26.1° 2θ disappears at ~425 °C, which corresponds to a small evolution of H_2. However, the original of this unknown phase is not clear. In the final step, the presence of Mg destabilises the LiH, leading to a H_2 desorption temperature that is reduced from ~900 to 470 °C. Although the dehydrogenation temperature of this Li-Mg-H composite is too high for mobile hydrogen storage, it may have properties that are of interest for other applications such as heat storage and electrodes in lithium batteries.

10.3 New knowledge

In addition to the detailed variable temperature structural and thermogravimetric studies in this thesis, a number of new discoveries have been made.

- In situ Raman measurements confirmed the formation of $Li_2B_{12}H_{12}$ ($Li_2B_{12}D_{12}$) during $LiBH_4$ ($LiBD_4$) decomposition at 500-600 °C, by comparing their H/D frequency ratio with data in the literature.

- Different decomposition behaviour was observed for as-received and high-pressure ball milled γ-$Mg(BH_4)_2$. The undesirable by-product of diborane was detected in the

decomposition of milled γ-Mg(BH$_4$)$_2$ for the first time.

- For the milled 0.68LiBH$_4$+0.32Ca(BH$_4$)$_2$ mixture, reversible phase transformations between α, γ and β-Ca(BH$_4$)$_2$ were observed in consecutive heating-cooling cycles between room temperature and the eutectic melting point. An unknown phase, which may tentatively be ascribed to a new, metastable dual-cation borohydride, was observed when cooled from the eutectic melting point. In situ Raman spectra on the decomposition of this eutectic mixture were obtained for the first time, and the reaction pathway was proposed.

- Raman vibrations of Li$_2$B$_{12}$H$_{12}$, Li$_2$B$_{10}$H$_{10}$, Li$_2$B$_{12}$D$_{12}$, Li$_2$B$_{10}$H$_{10}$, K$_2$B$_{12}$H$_{12}$, and K$_2$B$_{10}$H$_{10}$ are assigned.

- B$_2$H$_6$ and its analogues may play an important role in the formation of the stable closo-dodecaborate (e.g. Li$_2$B$_{12}$H$_{12}$ and MgB$_{12}$H$_{12}$) during the decomposition of LiBH$_4$, Mg(BH$_4$)$_2$ and Ca(BH$_4$)$_2$. A passivation layer of Li$_2$B$_{12}$H$_{12}$ formed on the surface of the powder by the reaction of LiH and B$_2$H$_6$, leads to an incomplete B$_2$H$_6$-absorption reaction between LiH and B$_2$H$_6$. NaBH$_4$ and a small amount of Na$_2$B$_{12}$H$_{12}$ can be formed by the gas-solid reaction between NaH and B$_2$H$_6$.

- Using amorphous boron as a boron source is not sufficient to produce a new Mg-B-Ti-H ternary hydride in a bulk form with the target composition even under a long milling duration (up to 20 h). However, a small amount of amorphous B-H-containing compound(s) might be yielded by milling the 0.4MgH$_2$+0.6B mixture in 100 bar H$_2$ for 20 h.

- The direct hydrogenation of a Li-rich Li-Mg alloy ribbon into a powder containing LiH and Mg$_{(1-x)}$Li$_x$H$_2$ (x = ~0.04) phases has been demonstrated using reactive milling: the formation of LiH is thermodynamically and kinetically favourable, and the yield of Mg$_{(1-x)}$Li$_x$H$_2$ increases with increasing milling time. Mg$_{(1-x)}$Li$_x$H$_2$ decomposed to hcp Li-Mg (Li < 17 at%) alloy and H$_2$ at ~ 284 °C. The unknown Li-containing phase disappeared at ~425 °C, which corresponded to a small evolution of H$_2$.

10.4 Borohydrides and Mg-based hydrides for hydrogen storage applications

The results presented in this dissertation illustrate the fascinating but also very complex chemistry of metal borohydrides in terms of crystal structure, microstructure and thermal stability. All of these borohydride materials show relatively high gravimetric H_2 capacities (at least 8.2 wt%), which are approaching the values necessary to meet the gravimetric system target (of 7.5 wt%) for an automotive hydrogen store. However, their high desorption temperature and sluggish hydrogen sorption kinetics means that a relatively energy-intensive on-board heating system would be needed, which would be inefficient and most likely unrealistic. The H_2 reversibility can be prevented from occurring by the formation of by-products (e.g. $[B_{12}H_{12}]^{2-}$ and sometimes B_2H_6) during the dehydrogenation process. In the case of $LiBH_4$ and $LiBH_4$-$Ca(BH_4)_2$, a molten state below the dehydrogenation temperature results in the material becoming very reactive and foaming: this issue would need to be overcome before such materials could be used in a storage system. The Mg-based hydride system presented in this dissertation has a much lower desorption temperature (down to T_{peak} = 226 °C) than as received MgH_2 powder, and exhibits fairly good reversibility under moderate conditions. However, slow sorption kinetics is still a primary issue for practical use.

For both borohydride-based and Mg hydrides-based storage systems, it is unlikely that hydrogen can be directly refuelled on-board. The "spent" media would need to be removed from the vehicle and then rehydrogenated either at the fuelling station or at another facility. In addition, this hydrogen storage method may also serve as a hydrogen delivery carrier by providing an alternative to transporting hydrogen as a gas or cryogenic liquid. Efforts to improve the hydrogen sorption kinetics and to optimise the reactor required for on-board hydrogen sorption (e.g. the volume, weight, and operation temperature/pressure) are therefore needed.

10.5 Future work

Knowledge of the structure and properties of metal borohydrides has increased tremendously in the past few years. However, much research is still needed to gain a better understanding of this complex system of compounds and to further tailor their properties to obtain materials suitable for hydrogen storage applications.

In this thesis, the structural and thermal properties of alkali and alkaline earth metal borohydrides has been investigated. Future work should focus on gaining a much greater understanding of the synthesis and decomposition pathways of all of these borohydrides, and thereby it may be possible to "tune" a more favourable reaction pathway (e.g. control the formation of stable intermediates by adjusting the dehydrogenation conditions) and so lower the temperature and pressure required to achieve reversibility. To achieve this, a combination of various characterisation techniques can be used, such as solid-state NMR, quantitative XRD and quantitative gaseous desorption measurements. In addition, H/D isotope labelling of the reaction reactants (e.g. $LiBH_4 + B_2D_6$) could be a particularly useful method to try to trace the H or D atoms in the borane or borohydride products by Raman spectroscopy.

Another important step is to study methods for retaining boron in a simple structure (e.g. lower borane or open-cage structure) in the solid state during decomposition. This is of great interest as it might be possible — by carefully designing novel composites with one or more small B-H containing compounds — of reacting with hydrogen at moderate conditions (of temperature and pressure) suitable for a reversible reaction. Furthermore, as the B-B bonds in the icosahedral clusters of the elemental boron are too stable to break (using the milling conditions used in this work), the approach to introduce the boron source is as important as the synthesis conditions (e.g. milling parameters and atmospheres).

Even though a wide range of metal borohydrides has been discovered, there is still great interest in the synthesis and characterization of novel compounds. The synthetic approach

includes a variety of reactions ranging from high temperature/pressure reactions of the elements/compounds to exchange reactions in solution or in solid state, and the product purification. The discovery of new materials may help to deduce trends and understand the complex chemistry, physics and structural topologies of the borohydrides system.

The possibility of forming a new Li-Mg-H ternary hydride, continues to be an interesting topic for applications such as heat storage and electrodes in lithium batteries, in addition to hydrogen storage. To follow up this dissertation, the composition of the starting Li-Mg alloy and milling conditions (e.g. backpressure and milling time/speed) needs to be optimised for a higher synthesis yield. Studies on the vibrational structure, sorption kinetics and reversibility of the materials need to be carried out.

Appendix A

Room temperature XRD patterns of as-received B, Ti, TiH$_2$, and TiCl$_3$
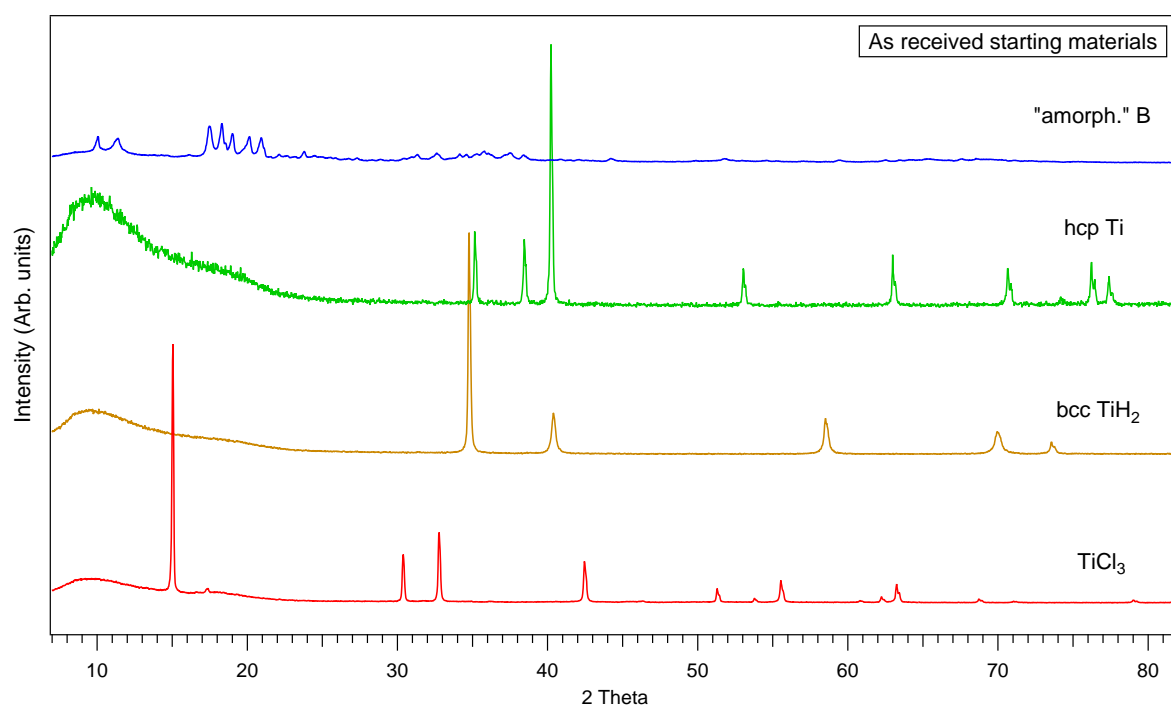
Figure A.1 XRD patterns of as-received Ti, TiH$_2$, TiCl$_3$ and amorphous B purchased from Sigma-Aldrich.

Appendix B

H$_2$ sorption properties of milled MgH$_2$-B, MgH$_2$-B-Ti and MgH$_2$-B-TiCl$_3$ systems

Hydrogen sorption measurements on the milled MgH$_2$+B (2 h, 20 h), MgH$_2$+B+Ti (2 h, 20 h) and MgH$_2$+B+TiCl$_3$ (2 h) samples were conducted using a Sievert's-PCT system, known as a Hiden Isochema HTPS-2 Volumetric System. This recorded the volume of hydrogen absorbed by materials as a function of set pressures up to 100 bar H$_2$ at different temperatures between 300 and 400 °C. Prior to measurements, an activation sequence (desorption-absorption-desorption) was performed on all the samples at 350 °C. The enthalpy and entropy of absorption and desorption were calculated from van't Hoff plots using plateau pressures from the PCT curves (**Figure B.1-B.3**). The observed H$_2$ capacities by TGA and PCT measurements, and the enthalpy and entropy of sorption reactions are summarised in .

The PCT results showed reduced H$_2$ capacities for the MgH$_2$+B (2, 20 h), MgH$_2$+B+Ti (2 h) and MgH$_2$+B+TiCl$_3$ (2 h) samples after the first desorption-absorption-desorption, whereas the capacity of the MgH$_2$+B+Ti (20 h) was increased to 4.1 wt%. However, PCT measurements on as-received/milled pure MgH$_2$, MgH$_2$+B+TiH$_2$ samples need to be carried out for comparison, and repeat measurements on all samples would be needed to ensure the data is accurate and reproducible.

Table B.1 Enthalpy and entropy data for sorption reactions of MgH_2+B, MgH_2+B+Ti and $MgH_2+B+TiCl_3$ samples.

Samples	Mass loss (wt%)		ΔH_{abs} (kJ/mol H_2)	ΔH_{des} (kJ/mol H_2)	ΔS_{abs} (J/mol K)	ΔS_{des} (J/mol K)
	TGA data (up to 430 °C)	PCT data (at 350 °C)				
$0.4MgH_2+0.6B$ (2 h)	3.90	4.1	-69.9 ± 1.3	88.8 ± 5.3	-128.0 ± 2.1	-155.7 ± 8.5
$0.4MgH_2+0.6B$ (20 h)	3.99 (H_2, B_2H_6)	3.1	-71.3 ± 0.7	87.3 ± 1.9	-129.4 ± 1.1	-152.3 ± 3.2
$0.36MgH_2+0.58B+0.06Ti$ (2 h)	2.97	2.0	-69.9 ± 5.7	73.6 ± 0.1	-128.4 ± 9.1	-132.1 ± 0.1
$0.36MgH_2+0.58B+0.06Ti$ (20 h)	3.71	3.1	-78.7 ± 2.8	78.9 ± 1.1	-140.7 ± 4.8	-139.8 ± 1.9
$0.36MgH_2+0.58B+0.06TiCl_3$ (2 h)	2.50	1.7	-81.2 ± 1.0	77.4 ± 1.8	-145.6 ± 1.8	-136.5 ± 3.1
Literature values						
As-received MgH_2 [a]	6.7 (330-370 °C)	5.9 (300 °C)		78.5		140.0
Mg+0.1Ti (300 bar, 20 h) [b]	5.5 (269-301 °C)	6.5 (300 °C)		77.4		137.5
$MgH_2+0.1TiH_2$ (138 bar, 4 h) [c]	6.2			68.2		127

[a] MgH_2 is purchased from Alfa (purity 98%) (Shao *et al.*, 2011).
[b] The Mg+0.1Ti mixture was milled under an initial H_2 pressure of 300 bar for 20 h, to form $MgH_2+0.1TiH_2$ as the resulting products. (Shao *et al.*, 2011)
[c] (Lu *et al.*, 2009)
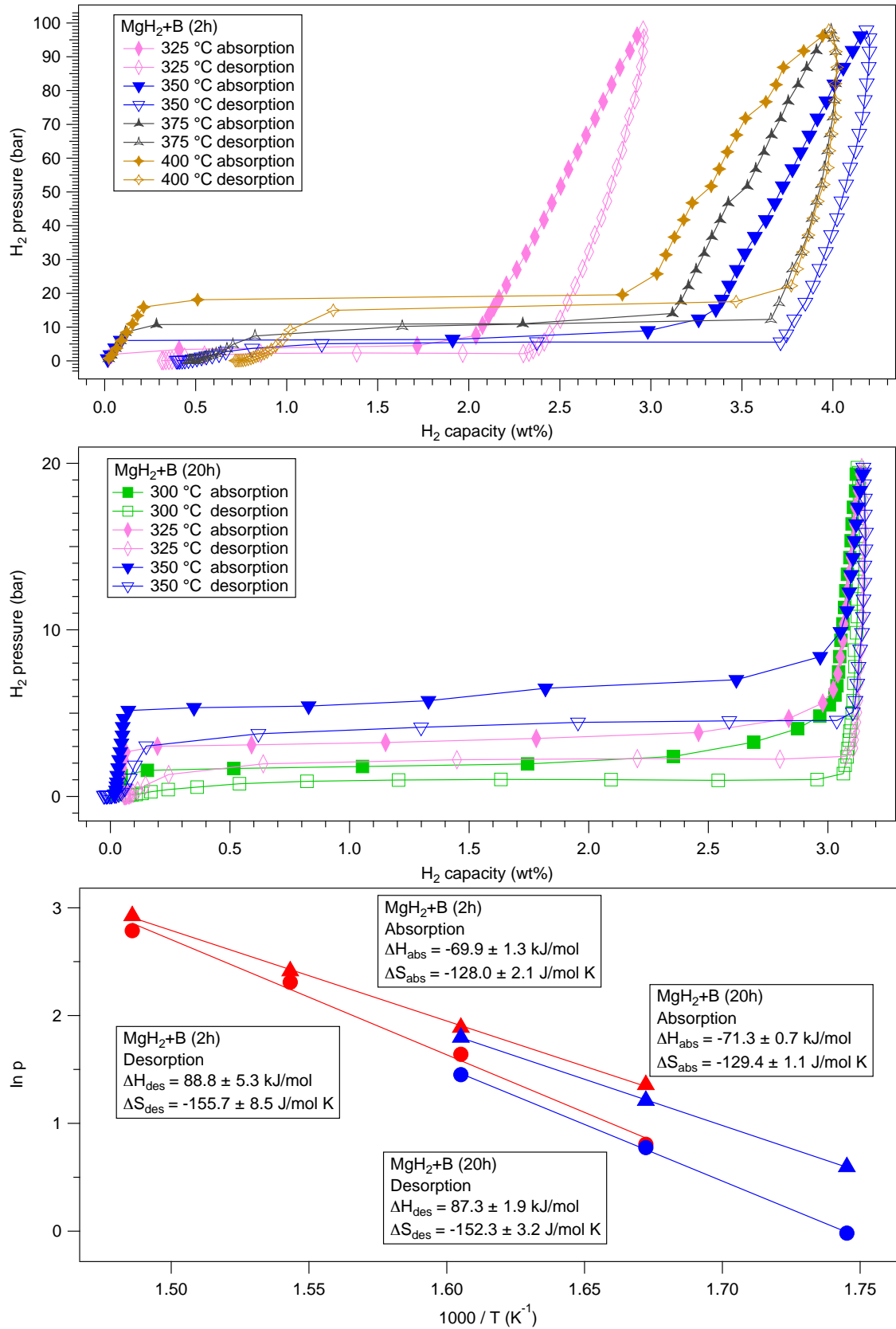
Figure B.1 PCT curves for hydrogen absorption and desorption in 0.4MgH$_2$+0.6B that had been milled in 100 bar H$_2$ for 2 h (top) and 20 h (middle). Bottom: van't Hoff plot for hydrogen absorptions and desorptions between 300 and 400 °C.
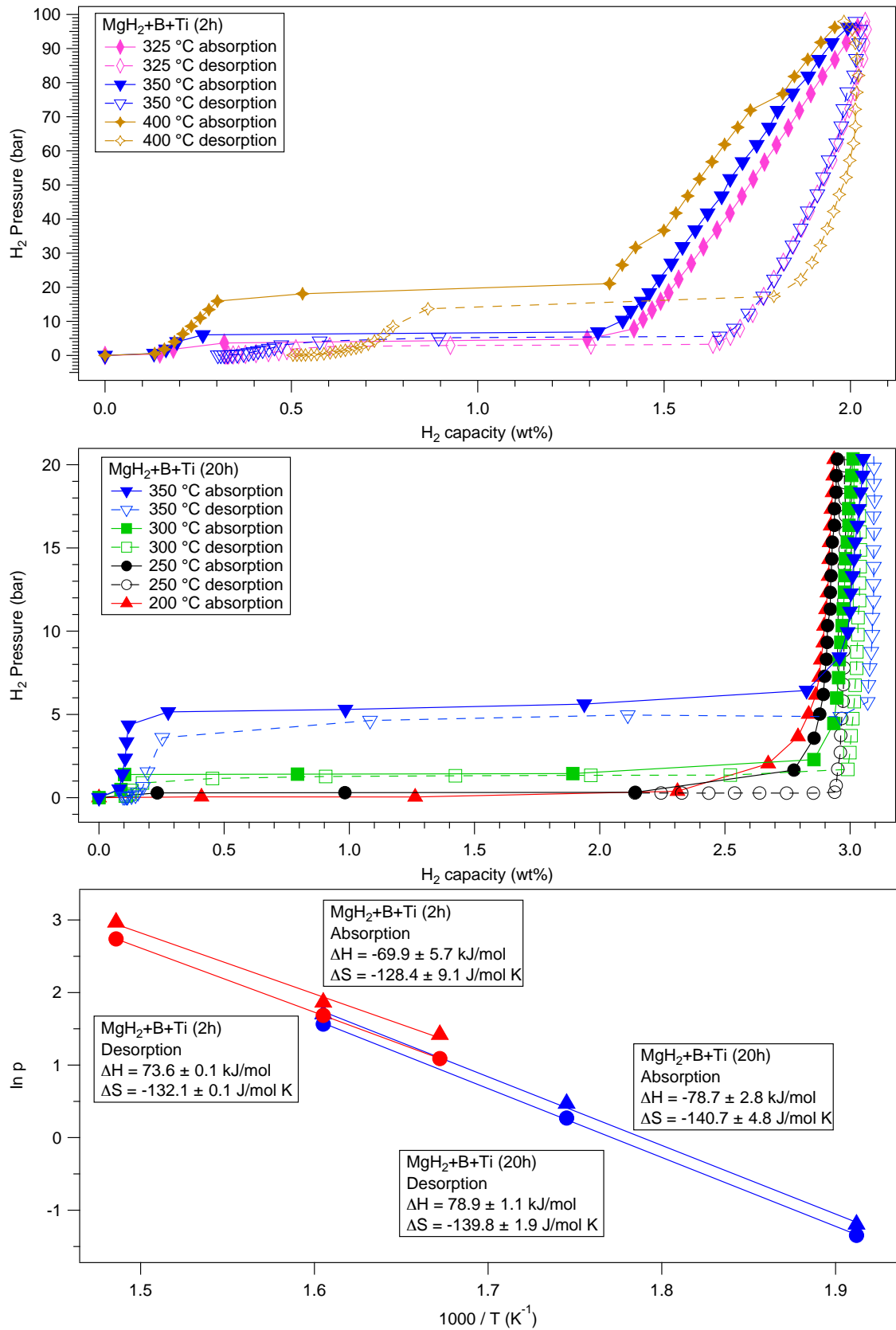
Figure B.2 PCT curves for hydrogen absorption and desorption of 0.36MgH₂+0.58B+0.06Ti that had been milled in 100 bar H₂ for 2 h (top) and 20 h (middle). Bottom: van't Hoff plot for hydrogen absorptions and desorptions between 300 and 400 °C.
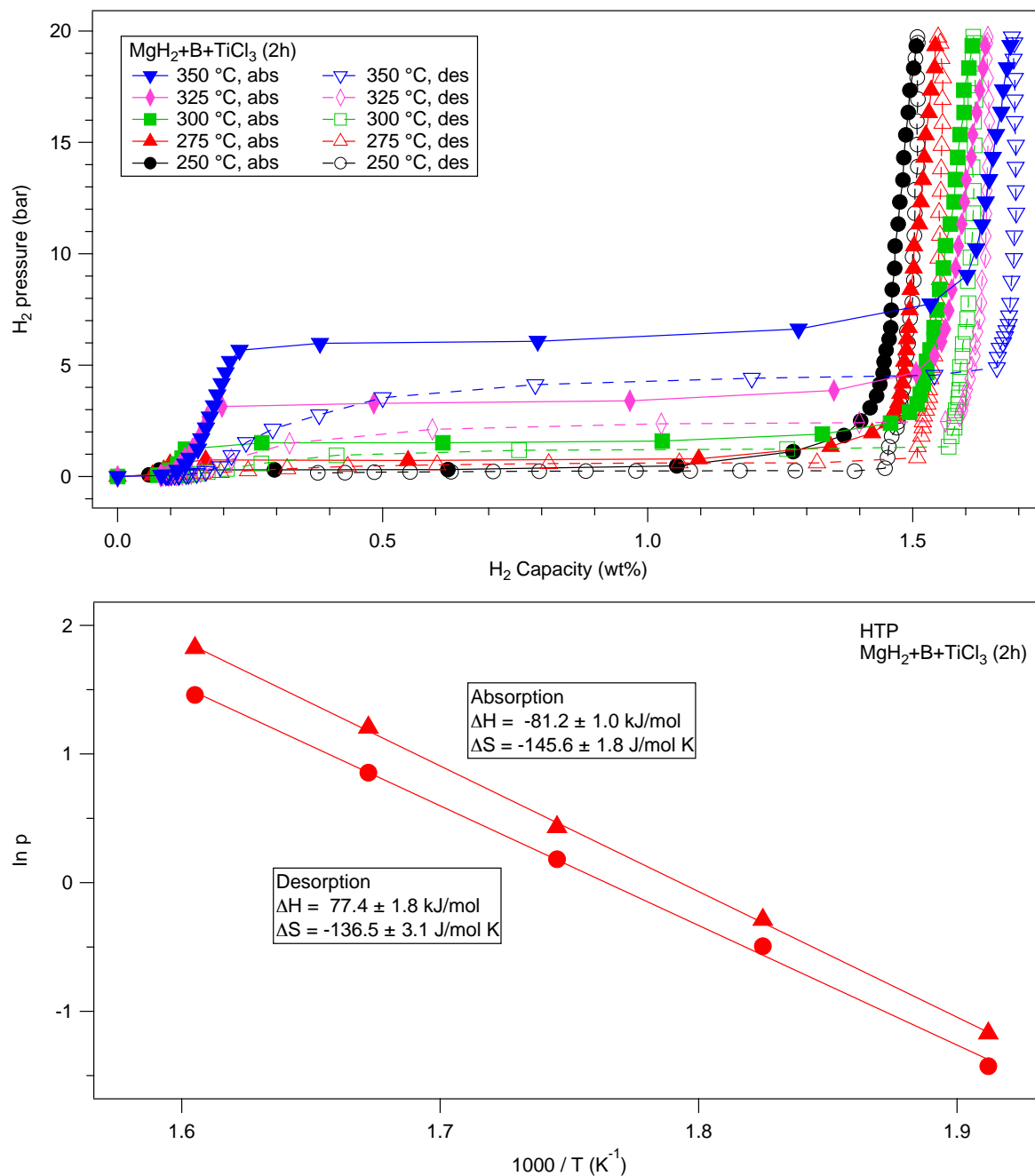
Figure B.3 Top: PCT curves for hydrogen absorption and desorption of $0.36MgH_2+0.58B+0.06TiCl_3$ that had been milled for 2 h in 100 bar H_2. Bottom: van't Hoff plot for hydrogen absorptions and desorptions between 300 and 400 °C.

References

Abrahams, S. C. & Kalnajs, J. (1954) The lattice constants of the alkali borohydrides and the low-temperature phase of sodium borohydride, **The Journal of Chemical Physics**, 22**,** 434-436.

Agresti, F. & Khandelwal, A. (2009) Evidence of formation of $LiBH_4$ by high-energy ball milling of LiH and B in a hydrogen atmosphere, **Scripta Materialia**, 60**,** 753-755.

Ahluwalia, R. K., Huaa, T. Q., Peng, J. K., Lasher, S., McKenney, K., Sinha, J. & Gardiner, M. (2010) Technical assessment of cryo-compressed hydrogen storage tank systems for automotive applications, **International Journal of Hydrogen Energy**, 35**,** 4171-4184.

Amieiro-Fonseca, A., Ellis, S. R., Nuttall, C. J., Hayden, B. E., Guerin, S., Purdy, G., Soulié, J. P., Callear, S. K., Culligan, S. D., David, W. I. F., Edwards, P. P., Jones, M. O., Johnson, S. R. & Pohl, A. H. (2011) A multidisciplinary combinatorial approach for tuning promising hydrogen storage materials towards automotive applications, **Faraday Discussions**, 151**,** 369-384.

Ampoumogli, A., Steriotis, T., Trikalitis, P., Bardaji, E. G., Fichtner, M., Stubos, A. & Charalambopoulou, G. (2012) Synthesis and characterisation of a mesoporous carbon/calcium borohydride nanocomposite for hydrogen storage, **International Journal of Hydrogen Energy**, 37**,** 16631-16635.

Aoki, M., Miwa, K., Noritake, T., Ohba, N., Matsumoto, M., Li, H. W., Nakamori, Y., Towata, S. & Orimo, S. (2008) Structural and dehydriding properties of $Ca(BH_4)_2$, **Applied Physics a-Materials Science & Processing**, 92**,** 601-605.

Asano, K. & Akiba, E. (2009) Direct synthesis of Mg-Ti-H FCC hydrides from MgH_2 and Ti by means of ball milling, **Journal of Alloys and Compounds**, 481**,** L8-L11.

Atkins, P., Overton, T., Rourke, J., Weller, M., Armstrong, F. & Hagerman, M. (2010) **Shriver and Atkins' Inorganic Chemistry**, Great Britain, Oxford University Press, 331.

Au, M., Jurgensen, A. & Zeigler, K. (2006) Modified lithium borohydrides for reversible hydrogen storage (2), **Journal of Physical Chemistry B**, 110**,** 26482-26487.

Banus, M. D. & Bragdon, R. W. (1955) **Method for preparing borohydrides of alkali metals**, US Patent 2720444.

Bardaji, E. G., Hanada, N., Zabara, O. & Fichtner, M. (2011a) Effect of several metal chlorides on the thermal decomposition behaviour of alpha-$Mg(BH_4)_2$, **International Journal of Hydrogen Energy**, 36**,** 12313-12318.

Bardaji, E. G., Zhao-Karger, Z., Boucharat, N., Nale, A., van Setten, M. J., Lohstroh, W., Rohm, E., Catti, M. & Fichtner, M. (2011b) $LiBH_4$-$Mg(BH_4)_2$: a physical mixture of metal borohydrides as hydrogen storage material, **Journal of Physical Chemistry C**, 115**,** 6095-6101.

Barkhordarian, G., Jensen, T. R., Doppiu, S., Bosenberg, U., Borgschulte, A., Gremaud, R., Cerenius, Y., Dornheim, M., Klassen, T. & Bormann, R. (2008) Formation of $Ca(BH_4)_2$ from hydrogenation of CaH_2+MgB_2 composite, **Journal of Physical Chemistry C**, 112**,** 2743-2749.

Barnes, P., Jacques, S. & Vickers, M. (2006) *Advanced Certificate in Powder Diffraction on the Web* [Online]. Birkbeck College, University of London. Available: http://pd.chem.ucl.ac.uk/pdnn/diff2/kinemat2.htm [Accessed 25th May].

REFERENCES

Bastide, J. P., Bonnetot, B., Letoffe, J. M. & Claudy, P. (1980) Polymorphism of magnesium hydride under high-pressure, **Materials Research Bulletin**, 15, 1215-1224.

Bateni, A., Scherpe, S., Acar, S. & Somer, M. (Year) Novel approach for synthesis of Magnesium Borohydride, Mg(BH$_4$)$_2$. **WHEC 2012 Conference Proceedings - 19th World Hydrogen Energy Conference,** Amsterdam. Elsevier Ltd., 26-33.

Berube, V., Radtke, G., Dresselhaus, M. & Chen, G. (2007) Size effects on the hydrogen storage properties of nanostructured metal hydrides: A review, **International Journal of Energy Research**, 31, 637-663.

Bevan, A. I., Zuttel, A., Book, D. & Harris, I. R. (2011) Performance of a metal hydride store on the "Ross Barlow" hydrogen powered canal boat, **Faraday Discussions**, 151, 353-367.

Bogdanović, B., Bohmhammel, K., Christ, B., Reiser, A., Schlichte, K., Vehlen, R. & Wolf, U. (1999) Thermodynamic investigation of the magnesium-hydrogen system, **Journal of Alloys and Compounds**, 282, 84-92.

Bogdanović, B. & Schwickardi, M. (1997) Ti-doped alkali metal aluminium hydrides as potential novel reversible hydrogen storage materials, **Journal of Alloys and Compounds**, 253-254, 1-9.

Borgschulte, A., Callini, E., Probst, B., Jain, A., Kato, S., Friedrichs, O., Remhof, A., Bielmann, M., Ramirez-Cuesta, A. J. & Zuttel, A. (2011a) Impurity gas analysis of the decomposition of complex hydrides, **Journal of Physical Chemistry C**, 115, 17220-17226.

Borgschulte, A., Gremaud, R., Zuttel, A., Martelli, P., Remhof, A., Ramirez-Cuesta, A. J., Refson, K., Bardaji, E. G., Lohstroh, W., Fichtner, M., Hagemann, H. & Ernst, M. (2011b) Experimental evidence of librational vibrations determining the stability of calcium borohydride, **Physical Review B**, 83.

Borgschulte, A., Züttel, A. & Wittstadt, U. (2008) Hydrogen production. **Hydrogen as a Future Energy Carrier**. Wiley-VCH Verlag GmbH & Co. KGaA.

Borsa, D. M., Gremaud, R., Baldi, A., Schreuders, H., Rector, J. H., Kooi, B., Vermeulen, P., Notten, P. H. L., Dam, B. & Griessen, R. (2007) Structural, optical, and electrical properties of MgyTi$_{1-y}$H$_x$ thin films, **Physical Review B**, 75, 205408.

Bortz, M., Bertheville, B., Bottger, G. & Yvon, K. (1999) Structure of the high pressure phase gamma-MgH$_2$ by neutron powder diffraction, **Journal of Alloys and Compounds**, 287, L4-L6.

Bowman, R. C. & Fultz, B. (2002) Metallic hydrides i: hydrogen storage and other gas-phase applications, **MRS Bulletin**, 27, 688-693.

Brinkman, N., Eberle, U., Formanski, V., Grebe, U.-D. & Matthe, R. (Year) Vehicle electrification - quo vadis? **33rd International Vienna Motor Symposium,** Vienna, Austria 186-215.

Broom, D. P. (2011) **Hydrogen storage materials: the characterisation of their storage properties**, London, Springer, p118.

Broom, D. P. & Thomas, K. M. (2013) Gas adsorption by nanoporous materials: Future applications and experimental challenges, **MRS Bulletin**, 38, 412-421.

Brown, H. C. (1975) **Organic synthesis via boranes**, New York, John Wiley & Sons, Inc.

Brown, H. C., Choi, Y. M. & Narasimhan, S. (1981) Convenient procedure for the conversion of sodium-borohydride into lithium borohydride in simple ether solvents, **Inorganic Chemistry**, 20, 4454-4456.

Buchter, F., Łodziana, Z., Mauron, P., Remhof, A., Friedrichs, O., Borgschulte, A., Züttel, A., Sheptyakov, D., Strässle, T. & Ramirez-Cuesta, A. J. (2008a) Dynamical properties and temperature induced molecular disordering of LiBH$_4$ and LiBD$_4$, **Physical Review B**, 78, 094302.

Buchter, F., Łodziana, Z., Remhof, A., Friedrichs, O., Borgschulte, A., Mauron, P., Züttel, A., Sheptyakov, D., Barkhordarian, G., Bormann, R., Chłopek, K., Fichtner, M., Sorby, M., Riktor, M., Hauback, B. & Orimo, S. (2008b) Structure of Ca(BD$_4$)$_2$ beta-phase from combined neutron and synchrotron X-ray powder diffraction data and density functional calculations, **Journal of Physical Chemistry B**, 112, 8042-8048.

REFERENCES

Buchter, F., Łodziana, Z., Remhof, A., Friedrichs, O., Borgschulte, A., Mauron, P., Züttel, A., Sheptyakov, D., Palatinus, L., Chłopek, K., Fichtner, M., Barkhordarian, G., Bormann, R. & Hauback, B. C. (2009) Structure of the Orthorhombic gamma-Phase and Phase Transitions of Ca(BD$_4$)$_2$, **Journal of Physical Chemistry C**, 113, 17223-17230.

Burstow, C. (2002) Magnesium: the impact of projected new supply on prices over the next five years, **Transactions of the Institution of Mining and Metallurgy Section C-Mineral Processing and Extractive Metallurgy**, 111, C62-C64.

Cahen, S., Eymery, J. B., Janot, R. & Tarascon, J. M. (2009) Improvement of the LiBH$_4$ hydrogen desorption by inclusion into mesoporous carbons, **Journal of Power Sources**, 189, 902-908.

Cakanyildirim, C. & Guru, M. (2008) Processing of LiBH$_4$ from its elements by ball milling method, **Renewable Energy**, 33, 2388-2392.

Callini, E., Borgschulte, A., Ramirez-Cuesta, A. J. & Züttel, A. (2013) Diborane release and structure distortion in borohydrides, **Dalton Transactions**, 42, 719-725.

Caputo, R., Garroni, S., Olid, D., Teixidor, F., Surinach, S. & Baro, M. D. (2010) Can Na$_2$B$_{12}$H$_{12}$ be a decomposition product of NaBH$_4$?, **Physical Chemistry Chemical Physics**, 12, 15093-15100.

Černý, R., Filinchuk, Y., Hagemann, H. & Yvon, K. (2007) Magnesium borohydride: Synthesis and crystal structure, **Angewandte Chemie-International Edition**, 46, 5765-5767.

Černý, R., Kim, K. C., Penin, N., D'Anna, V., Hagemann, H. & Sholl, D. S. (2010) AZn$_2$(BH4)$_5$ (A = Li, Na) and NaZn(BH$_4$)$_3$: Structural Studies, **Journal of Physical Chemistry C**, 114, 19127-19133.

Černý, R., Penin, N., D'Anna, V., Hagemann, H., Durand, E. & Ruzicka, J. (2011) Mg$_x$Mn$_{(1-x)}$(BH$_4$)$_2$ (x = 0-0.8), a cation solid solution in a bimetallic borohydride, **Acta Materialia**, 59, 5171-5180.

Černý, R., Penin, N., Hagemann, H. & Filinchuk, Y. (2009) The First Crystallographic and Spectroscopic Characterization of a 3d-Metal Borohydride: Mn(BH$_4$)$_2$, **Journal of Physical Chemistry C**, 113, 9003-9007.

Charbonnier, J., de Rango, P., Fruchart, D., Miraglia, S., Pontonnier, L., Rivoirard, S., Skryabina, N. & Vulliet, P. (2004) Hydrogenation of transition element additives (Ti, V) during ball milling of magnesium hydride, **Journal of Alloys and Compounds**, 383, 205-208.

Charkin, O. P., Bonakkorsi, R., Tomazi, Y., Zyubin, A. S. & Gorbik, A. A. (1987) Nonempirical calculation of structure and stability of calcium borohydride molecules taking into account electronic correlation in MP-4 approximation, **Zhurnal Neorganicheskoi Khimii**, 32, 2644-2648.

Chater, P. A. (2010) Mixed anion complex hydrides for hydrogen storage. **PhD thesis**, University of Birmingham.

Chen, C. P., Liu, B. H., Li, Z. P., Wu, J. & Wang, Q. D. (1993) The activation mechanism of mg-based hydrogen storage alloys, **Zeitschrift Fur Physikalische Chemie-International Journal of Research in Physical Chemistry & Chemical Physics**, 181, 259-267.

Chen, P., Xiong, Z., Luo, J., Lin, J. & Tan, K. L. (2002) Interaction of hydrogen with metal nitrides and imides, **Nature**, 420, 302-304.

Chen, Y. & Williams, J. S. (1995) Formation of metal-hydrides by mechanical alloying, **Journal of Alloys and Compounds**, 217, 181-184.

Chlopek, K., Frommen, C., Leon, A., Zabara, O. & Fichtner, M. (2007) Synthesis and properties of magnesium tetrahydroborate, Mg(BH$_4$)$_2$, **Journal of Materials Chemistry**, 17, 3496-3503.

Choi, Y. J., Lu, J., Sohn, H. Y., Fang, Z. Z. G. & Ronnebro, E. (2009) Effect of milling parameters on the dehydrogenation properties of the Mg-Ti-H System, **Journal of Physical Chemistry C**, 113, 19344-19350.

REFERENCES

Chong, M., Karkamkar, A., Autrey, T., Orimo, S., Jalisatgi, S. & Jensen, C. M. (2011) Reversible dehydrogenation of magnesium borohydride to magnesium triborane in the solid state under moderate conditions, **Chemical Communications**, 47, 1330-1332.

Chryssikos, G. D., Kamitsos, E. I., Patsis, A. P., Bitsis, M. S. & Karakassides, M. A. (1990) The devitrification of lithium metaborate: polymorphism and glass formation, **Journal of Non-Crystalline Solids**, 126, 42-51.

Coelho, A. (2007). TOPAS Academic Version 4.1., Program, Brisbane, Australia: Coelho Software.

Comănescu, C., Capurso, G. & Maddalena, A. (2012) Nanoconfinement in activated mesoporous carbon of calcium borohydride for improved reversible hydrogen storage, **Nanotechnology**, 23, 385401-385407.

Cuevas, F., Korablov, D. & Latroche, M. (2012) Synthesis, structural and hydrogenation properties of Mg-rich MgH_2-TiH_2 nanocomposites prepared by reactive ball milling under hydrogen gas, **Physical Chemistry Chemical Physics**, 14, 1200-1211.

Cyvin, S. J., Cyvin, B. N. & Mogstad, T. (1986) Normal coordinate analysis of icosahedral closoborate anions $B_{12}Y_{12}^{2-}$ (Y = H, D, F, Cl, Br, I), **Spectrochimica Acta Part a-Molecular and Biomolecular Spectroscopy**, 42, 985-989.

Dai, B., Sholl, D. S. & Johnson, J. K. (2008) First-principles study of experimental and hypothetical $Mg(BH_4)_2$ crystal structures, **Journal of Physical Chemistry C**, 112, 4391-4395.

David, W. I. F., Callear, S. K., Jones, M. O., Aeberhard, P. C., Culligan, S. D., Pohl, A. H., Johnson, S. R., Ryan, K. R., Parker, J. E., Edwards, P. P., Nuttall, C. J. & Amieiro-Fonseca, A. (2012) The structure, thermal properties and phase transformations of the cubic polymorph of magnesium tetrahydroborate, **Physical chemistry chemical physics**, 14, 11800-11807.

David, W. I. F., Shankland, K., McCusker, L. B. & Baerlocher, C. (2006) **Structure determination from powder diffraction data**, Oxford, New York, Oxford University Press.

Davis, R. L. & Kennard, C. H. L. (1985) Structure of sodium tetradeuteroborate, $NaBD_4$, **Journal of Solid State Chemistry**, 59, 393-396.

Denton, A. R. & Ashcroft, N. W. (1991) Vegard's law, **Physical Review A**, 43, 3161-3164.

Department of Energy & Climate Change. (2014) **Energy consumption in the UK** [Online]. Available: https://www.gov.uk/government/statistics/energy-consumption-in-the-uk [Accessed 16 August 2014].

Doppiu, S., Schultz, L. & Gutfleisch, O. (2007) In situ pressure and temperature monitoring during the conversion of Mg into MgH_2 by high-pressure reactive ball milling, **Journal of Alloys and Compounds**, 427, 204-208.

Dunbar, A. C., Macor, J. A. & Girolami, G. S. (2013) Synthesis and single crystal structure of sodium octahydrotriborate, NaB_3H_8, **Inorganic Chemistry**, 53, 822-826.

Duncan, J. L., McKean, D. C., Torto, I. & Nivellini, G. D. (1981) Diborane: infrared-spectra of gaseous and crystalline phases, and a complete vibrational assignment, **Journal of Molecular Spectroscopy**, 85, 16-39.

Durbin, D. J. & Malardier-Jugroot, C. (2013) Review of hydrogen storage techniques for on board vehicle applications, **International Journal of Hydrogen Energy**, 38, 14595-14617.

Eagles, M., Sun, B., Richter, B., Jensen, T. R., Filinchuk, Y. & Conradi, M. S. (2012) NMR investigation of nanoporous gamma-$Mg(BH_4)_2$ and its thermally induced phase changes, **Journal of Physical Chemistry C**, 116, 13033-13037.

Eberle, D. U. & von Helmolt, D. R. (2010) Sustainable transportation based on electric vehicle concepts: a brief overview, **Energy & Environmental Science**, 3, 689-699.

Eberle, U., Felderhoff, M. & Schüth, F. (2009) Chemical and physical solutions for hydrogen storage, **Angewandte Chemie International Edition**, 48, 6608-6630.

Eberle, U., Muller, B. & von Helmolt, R. (2012) Fuel cell electric vehicles and hydrogen infrastructure: status 2012, **Energy & Environmental Science**, 5, 8780-8798.

REFERENCES

Fang, Z. Z., Kang, X. D., Wang, P., Li, H. W. & Orimo, S. I. (2010) Unexpected dehydrogenation behavior of $LiBH_4/Mg(BH_4)_2$ mixture associated with the in situ formation of dual-cation borohydride, **Journal of Alloys and Compounds***, 491*, L1-L4.

Fichtner, M., Chlopek, K., Longhini, M. & Hagemann, H. (2008) Vibrational spectra of $Ca(BH_4)_2$, **Journal of Physical Chemistry C***, 112*, 11575-11579.

Fichtner, M., Zhao-Karger, Z., Hu, J., Roth, A. & Weidler, P. (2009) The kinetic properties of $Mg(BH_4)_2$ infiltrated in activated carbon, **Nanotechnology***, 20*, 204029.

Filinchuk, Y., Černý, R. & Hagemann, H. (2009a) Insight into $Mg(BH_4)_2$ with synchrotron x-ray diffraction: structure revision, crystal chemistry, and anomalous thermal expansion, **Chemistry of Materials***, 21*, 925-933.

Filinchuk, Y., Chernyshov, D. & Černý, R. (2008) Lightest borohydride probed by synchrotron X-ray diffraction: Experiment calls for a new theoretical revision, **Journal of Physical Chemistry C***, 112*, 10579-10584.

Filinchuk, Y. & Hagemann, H. (2008) Structure and properties of $NaBH_4$ center dot $2H_2O$ and $NaBH_4$, **European Journal of Inorganic Chemistry,** 3127-3133.

Filinchuk, Y., Richter, B., Jensen, T. R., Dmitriev, V., Chernyshov, D. & Hagemann, H. (2011) Porous and dense magnesium borohydride frameworks: synthesis, stability, and reversible absorption of guest species, **Angewandte Chemie-International Edition***, 50*, 11162-11166.

Filinchuk, Y., Ronnebro, E. & Chandra, D. (2009b) Crystal structures and phase transformations in $Ca(BH_4)_2$, **Acta Materialia***, 57*, 732-738.

Fischer, A., Kostler, H. & Schlapbach, L. (1991) Hydrogen in magnesium alloys and magnesium interfaces - preparation, electronic-properties and interdiffusion, **Journal of the Less-Common Metals***, 172*, 808-815.

Fischer, P. & Züttel, A. (2004) Order-disorder phase transition in $NaBD_4$, **Material Science Forum***,* 443-444**,** 287-290.

Fournier, V., Marcus, P. & Olefjord, I. (2002) Oxidation of magnesium, **Surface and Interface Analysis***, 34*, 494-497.

Friedlmeier, G. & Groll, M. (1997) Experimental analysis and modelling of the hydriding kinetics of Ni-doped and pure Mg, **Journal of Alloys and Compounds***, 253*, 550-555.

Friedrich, K. A., Büchi, F. N., Li, Z. P., Kiesgen, G., Leinhos, D. C., Rottengruber, H. S., Bowman, R. C. & Ratnakumar, B. V. (2008) Applications. **Hydrogen as a Future Energy Carrier**. Wiley-VCH Verlag GmbH & Co. KGaA.

Friedrichs, O., Borgschulte, A., Kato, S., Buchter, F., Gremaud, R., Remhof, A. & Züttel, A. (2009a) Low-temperature synthesis of $LiBH_4$ by gas-solid reaction, **Chemistry-a European Journal***, 15*, 5531-5534.

Friedrichs, O., Buchter, F., Borgschulte, A., Remhof, A., Zwicky, C. N., Mauron, P., Bielmann, M. & Zuttel, A. (2008) Direct synthesis of $LiBH_4$ and $LiBD_4$ from the elements, **Acta Materialia***, 56*, 949-954.

Friedrichs, O., Kim, J. W., Remhof, A., Buchter, F., Borgschulte, A., Wallacher, D., Cho, Y. W., Fichtner, M., Oh, K. H. & Zuttel, A. (2009b) The effect of Al on the hydrogen sorption mechanism of $LiBH_4$, **Physical Chemistry Chemical Physics***, 11*, 1515-1520.

Friedrichs, O., Kim, J. W., Remhof, A., Wallacher, D., Hoser, A., Cho, Y. W., Oh, K. H. & Zuttel, A. (2010a) Core shell structure for solid gas synthesis of $LiBD_4$, **Physical Chemistry Chemical Physics***, 12*, 4600-4603.

Friedrichs, O., Remhof, A., Borgschulte, A., Buchter, F., Orimo, S. I. & Züttel, A. (2010b) Breaking the passivation-the road to a solvent free borohydride synthesis, **Physical Chemistry Chemical Physics***, 12*, 10919-10922.

Friedrichs, O., Remhof, A., Hwang, S. J. & Züttel, A. (2010c) Role of $Li_2B_{12}H_{12}$ for the Formation and Decomposition of $LiBH_4$, **Chemistry of Materials***, 22*, 3265-3268.

REFERENCES

Frommen, C., Aliouane, N., Deledda, S., Fonnelop, J. E., Grove, H., Lieutenant, K., Llamas-Jansa, I., Sartori, S., Sorby, M. H. & Hauback, B. C. (2010) Crystal structure, polymorphism, and thermal properties of yttrium borohydride Y(BH$_4$)$_3$, **Journal of Alloys and Compounds**, 496, **710-716.**

Gaines, D. F., Tebbe, F. & Schaeffer, R. (1963) Convenient preparations of solutions containing triborohydride ion, **Inorganic Chemistry**, 2, **526-528.**

Garroni, S., Milanese, C., Pottmaier, D., Mulas, G., Nolis, P., Girella, A., Caputo, R., Olid, D., Teixdor, F., Baricco, M., Marini, A., Suriñach, S. & Baró, M. D. (2011) Experimental Evidence of Na$_2$[B$_{12}$H$_{12}$] and Na Formation in the Desorption Pathway of the 2NaBH$_4$+MgH$_2$ System, **The Journal of Physical Chemistry C**, 115, **16664-16671.**

Garroni, S., Minella, C. B., Pottmaier, D., Pistidda, C., Milanese, C., Marini, A., Enzo, S., Mulas, G., Dornheim, M., Baricco, M., Gutfleisch, O., Suriñach, S. & Baró, M. D. (2013) Mechanochemical synthesis of NaBH$_4$ starting from NaH–MgB$_2$ reactive hydride composite system, **International Journal of Hydrogen Energy**, 38, **2363-2369.**

Garroni, S., Pistidda, C., Brunelli, M., Vaughan, G. B. M., Suriñach, S. & Baró, M. D. (2009) Hydrogen desorption mechanism of 2NaBH$_4$+MgH$_2$ composite prepared by high-energy ball milling, **Scripta Materialia**, 60, **1129-1132.**

George, L., Drozd, V., Saxena, S. K., Bardaji, E. G. & Fichtner, M. (2009) Structural Phase Transitions of Mg(BH$_4$)$_2$ under Pressure, **Journal of Physical Chemistry C**, 113, **486-492.**

Giannasi, A., Colognesi, D., Ulivi, L., Zoppi, M., Ramirez-Cuesta, A. J., Bardaji, E. G., Roehm, E. & Fichtner, M. (2010) High Resolution Raman and Neutron Investigation of Mg(BH$_4$)$_2$ in an Extensive Temperature Range, **Journal of Physical Chemistry A**, 114, **2788-2793.**

Gingl, F., Bonhomme, F., Yvon, K. & Fischer, P. (1992) Tetracalcium trimagnesium tetradecahydride, Ca$_4$Mg$_3$H$_{14}$ - the 1st ternary alkaline-earth hydride, **Journal of Alloys and Compounds**, 185, **273-278.**

Gomes, S., Hagemann, H. & Yvon, K. (2002) Lithium boro-hydride LiBH$_4$ II. Raman spectroscopy, **Journal of Alloys and Compounds**, 346, **206-210.**

Greenwood, N. N. & Earnshaw, A. (1997) **Chemistry of the elements**, Oxford, UK, Butterworth-Heinemann Ltd.

Greenwood, N. N. & Greatrex, R. (1987) Kinetics and mechanism of the thermolysis and photolysis of binary boranes, **Pure and Applied Chemistry**, 59, **857-868.**

Gremaud, R., Borgschulte, A., Friedrichs, O. & Züttel, A. (2011) Synthesis mechanism of alkali borohydrides by heterolytic diborane splitting, **Journal of Physical Chemistry C**, 115, **2489-2496.**

Gremaud, R., Łodziana, Z., Hug, P., Willenberg, B., Racu, A. M., Schoenes, J., Ramirez-Cuesta, A. J., Clark, S. J., Refson, K., Züttel, A. & Borgschulte, A. (2009) Evidence for hydrogen transport in deuterated LiBH$_4$ from low-temperature Raman-scattering measurements and first-principles calculations, **Physical Review B**, 80, **100301.**

Grochala, W. & Edwards, P. P. (2004) Thermal decomposition of the non-interstitial hydrides for the storage and production of hydrogen, **Chemical Reviews**, 104, **1283-1315.**

Gross, A. F., Vajo, J. J., Van Atta, S. L. & Olson, G. L. (2008) Enhanced hydrogen storage kinetics of LiBH$_4$ in nanoporous carbon scaffolds, **Journal of Physical Chemistry C**, 112, **5651-5657.**

Guo, S., Chan, H. Y. L., Reed, D. & Book, D. (2013) Investigation of dehydrogenation processes in disordered γ-Mg(BH$_4$)$_2$, **Journal of Alloys and Compounds**, 580, Supplement 1, **S296-S300.**

Gupta, S., Hlova, I. Z., Kobayashi, T., Denys, R. V., Chen, F., Zavaliy, I. Y., Pruski, M. & Pecharsky, V. K. (2013) Facile synthesis and regeneration of Mg(BH$_4$)$_2$ by high energy reactive ball milling of MgB$_2$, **Chemical Communications**, 49, **828-830.**

REFERENCES

Hagemann, H., Filinchuk, Y., Chernyshov, D. & van Beek, W. (2009) Lattice anharmonicity and structural evolution of $LiBH_4$: an insight from Raman and X-ray diffraction experiments, **Phase Transitions**, 82, 344-355.

Hagemann, H., Gomes, S., Renaudin, G. & Yvon, K. (2004) Raman studies of reorientation motions of $[BH_4]^-$ anionsin alkali borohydrides, **Journal of Alloys and Compounds**, 363, 129-132.

Hanada, N., Chopek, K., Frommen, C., Lohstroh, W. & Fichtner, M. (2008) Thermal decomposition of $Mg(BH_4)_2$ under He flow and H_2 pressure, **Journal of Materials Chemistry**, 18, 2611-2614.

Hanada, N., Ichikawa, T., Hino, S. & Fujii, H. (2006) Remarkable improvement of hydrogen sorption kinetics in magnesium catalyzed with Nb_2O_5, **Journal of Alloys and Compounds**, 420, 46-49.

Hao, S. Q. & Sholl, D. S. (2012) Effect of TiH_2-induced strain on thermodynamics of hydrogen release from MgH_2, **Journal of Physical Chemistry C**, 116, 2045-2050.

Harbach, F. & Fischer, F. (1975) Raman spectra of lithium hydroxide single crystals, **Journal of Physics and Chemistry of Solids**, 36, 601-603.

Harris, P. M. & Meibohm, E. P. (1947) the crystal structure of lithium borohydride $LiBH_4$, **Journal of the American Chemical Society**, 69, 1231-1232.

Hartman, M. R., Rush, J. J., Udovic, T. J., Bowman, R. C. & Hwang, S. J. (2007) Structure and vibrational dynamics of isotopically labeled lithium borohydride using neutron diffraction and spectroscopy, **Journal of Solid State Chemistry**, 180, 1298-1305.

Harvey, K. B. & McQuaker, N. R. (1971a) Infrared and raman spectra of potassium and sodium borohydride, **Canadian Journal of Chemistry**, 49, 3272-3281.

Harvey, K. B. & McQuaker, N. R. (1971b) Low temperature infrared and Raman spectra of lithium borohydride, **Canadian Journal of Chemistry**, 49, 3282-3286.

Hemminger, W. & Sarge, S. M. (1998) Chapter 1 Definitions, Nomenclature, Terms and Literature. *In:* Michael, E. B. (ed.) **Handbook of Thermal Analysis and Calorimetry**. Elsevier Science B.V.

Her, J.-H., Zhou, W., Stavila, V., Brown, C. M. & Udovic, T. J. (2009) Role of cation size on the structural behavior of the alkali-metal dodecahydro-closo-dodecaborates, **The Journal of Physical Chemistry C**, 113, 11187-11189.

Her, J. H., Stephens, P. W., Gao, Y., Soloveichik, G. L., Rijssenbeek, J., Andrus, M. & Zhao, J. C. (2007) Structure of unsolvated magnesium borohydride $Mg(BH_4)_2$, **Acta Crystallographica Section B-Structural Science**, 63, 561-568.

Her, J. H., Yousufuddin, M., Zhou, W., Jalisatgi, S. S., Kulleck, J. G., Zan, J. A., Hwang, S. J., Bowman, R. C. & Udovic, T. J. (2008) Crystal Structure of $Li_2B_{12}H_{12}$: a Possible Intermediate Species in the Decomposition of $LiBH_4$, **Inorganic Chemistry**, 47, 9757-9759.

Herbstein, F. H. & Averbach, B. L. (1956) The structure of lithium-magnesium solid solutions .1. measurements on the bragg reflections, **Acta Metallurgica**, 4, 407-413.

Hisatomi, T., Kubota, J. & Domen, K. (2014) Recent advances in semiconductors for photocatalytic and photoelectrochemical water splitting, **Chemical Society Reviews**, 43, 7520-7535.

Hoang, K. & Van de Walle, C. G. (2012) Mechanism for the decomposition of lithium borohydride, **International Journal of Hydrogen Energy**, 37, 5825-5832.

Hofmann, K. & Albert, B. (2005) Crystal structures of $M_2B_{10}H_{10}$ (M = Na, K, Rb) via real-space simulated annealing powder techniques, **Zeitschrift Fur Kristallographie**, 220, 142-146.

Housecroft, C. E. (1994) **Boranes and metallaboranes: structure, bonding and reactivity**, Great Britain, Ellis Horwood Limited, p136.

Housecroft, C. E. & Sharpe, A. G. (2012) **Inorganic chemistry**, Harlow, Harlow : Prentice Hall.

REFERENCES

Hua, T. Q., Ahluwalia, R. K., Peng, J. K., Kromer, M., Lasher, S., McKenney, K., Law, K. & Sinha, J. (2011) Technical assessment of compressed hydrogen storage tank systems for automotive applications, **International Journal of Hydrogen Energy**, 36, 3037-3049.

Huot, J., Boily, S., Akiba, E. & Schulz, R. (1998) Direct synthesis of Mg_2FeH_6 by mechanical alloying, **Journal of Alloys and Compounds**, 280, 306-309.

Huot, J., Liang, G., Boily, S., Van Neste, A. & Schulz, R. (1999) Structural study and hydrogen sorption kinetics of ball-milled magnesium hydride, **Journal of Alloys and Compounds**, 293, 495-500.

Hwang, S. J., Bowman, R. C., Reiter, J. W., Rijssenbeek, J., Soloveichik, G. L., Zhao, J. C., Kabbour, H. & Ahn, C. C. (2008) NMR confirmation for formation of $B_{12}H_{12}^{2-}$ complexes during hydrogen desorption from metal borohydrides, **Journal of Physical Chemistry C**, 112, 3164-3169.

Hyundai. (2013) *Hyundai ix35 Hydrogen Fuel Cell Vehicle* [Online]. Available: http://www.hyundai.co.uk/about-us/environment/hydrogen-fuel-cell [Accessed 29th May, 2014].

ICSD Web. (2013) *Inorganic Crystal Structure Database* [Online]. Available: http://icsd.cds.rsc.org/ [Accessed 14 October, 2013].

Ikeda, K., Kogure, Y., Nakamori, Y. & Orimo, S. (2005a) Reversible hydriding and dehydriding reactions of perovskite-type hydride $NaMgH_3$, **Scripta Materialia**, 53, 319-322.

Ikeda, K., Nakamori, Y. & Orimo, S. (2005b) Formation ability of the perovskite-type structure in $Li_xNa_{1-x}MgH_3$ (x=0, 0.5 and 1.0), **Acta Materialia**, 53, 3453-3457.

International Energy Agency. (2013) *World Energy Outlook 2013* [Online]. London: International Energy Agency,. Available: http://www.worldenergyoutlook.org/publications/weo-2013/ [Accessed 14 May, 2014].

Jaffe, L. D. (1956) Metallographic identification and crystal symmetry of titanium hydride, **Transactions of the American Institute of Mining and Metallurgical Engineers**, 206, 861-861.

Jain, I. P., Jain, P. & Jain, A. (2010a) Novel hydrogen storage materials: A review of lightweight complex hydrides, **Journal of Alloys and Compounds**, 503, 303-339.

Jain, I. P., Lal, C. & Jain, A. (2010b) Hydrogen storage in Mg: A most promising material, **International Journal of Hydrogen Energy**, 35, 5133-5144.

James, B. D. & Wallbridge, M. G. H. (1970) Metal tetrahydroborates, **Progress in Inorganic Chemistry** 11, 99-231.

Jiang, J., Senkowicz, B. J., Larbalestier, D. C. & Hellstrom, E. E. (2006) Influence of boron powder purification on the connectivity of bulk MgB_2, **Superconductor Science & Technology**, 19, L33-L36.

Johnson, J. W. & Brody, J. F. (1982) Lithium closoborane electrolytes 3. preparation and characterization, **Journal of the Electrochemical Society**, 129, 2213-2219.

Kato, S., Bielmann, M., Borgschulte, A., Zakaznova-Herzog, V., Remhof, A., Orimo, S. & Züttel, A. (2010) Effect of the surface oxidation of $LiBH_4$ on the hydrogen desorption mechanism, **Physical Chemistry Chemical Physics**, 12, 10950-10955.

Kennedy, A. R. & Lopez, V. H. (2003) The decomposition behavior of as-received and oxidized TiH_2 foaming-agent powder, **Materials Science and Engineering a-Structural Materials Properties Microstructure and Processing**, 357, 258-263.

Ketelaar, J. A. A. & Schutte, C. J. H. (1961) The borohydride ion (BH_4^-) in a face-centred cubic alkali-halide lattice, **Spectrochimica Acta**, 17, 1240-1243.

Kim, J. H., Jin, S. A., Shim, J. H. & Cho, Y. W. (2008) Thermal decomposition behavior of calcium borohydride $Ca(BH_4)_2$, **Journal of Alloys and Compounds**, 461, L20-L22.

REFERENCES

Kim, Y., Hwang, S. J., Lee, Y. S., Suh, J. Y., Han, H. N. & Cho, Y. W. (2012a) Hydrogen back-pressure effects on the dehydrogenation reactions of $Ca(BH_4)_2$, **Journal of Physical Chemistry C**, 116, 25715-25720.

Kim, Y., Hwang, S. J., Shim, J. H., Lee, Y. S., Han, H. N. & Cho, Y. W. (2012b) Investigation of the dehydrogenation reaction pathway of $Ca(BH_4)_2$ and reversibility of intermediate phases, **Journal of Physical Chemistry C**, 116, 4330-4334.

Kim, Y., Reed, D., Lee, Y. S., Lee, J. Y., Shim, J. H., Book, D. & Cho, Y. W. (2009) Identification of the Dehydrogenated Product of $Ca(BH_4)_2$, **Journal of Physical Chemistry C**, 113, 5865-5871.

Kim, Y., Reed, D., Lee, Y. S., Shim, J. H., Han, H. N., Book, D. & Cho, Y. W. (2010) Hydrogenation reaction of CaH_2-CaB_6-Mg mixture, **Journal of Alloys and Compounds**, 492, 597-600.

Klebanoff, L. (2012) **Hydrogen storage technology: materials and applications**, Taylor & Francis, p156.

Klebanoff, L. E. & Keller, J. O. (2013) 5 Years of hydrogen storage research in the US DOE Metal Hydride Center of Excellence (MHCoE), **International Journal of Hydrogen Energy**, 38, 4533-4576.

Kojima, Y. & Haga, T. (2003) Recycling process of sodium metaborate to sodium borohydride, **International Journal of Hydrogen Energy**, 28, 989-993.

Kollonitsch, J., Fuchs, O. & Gábor, V. (1955) New and known complex borohydrides and some of their applications in organic syntheses, **Nature** 173, 125-126.

Konoplev, V. N. & Bakulina, V. M. (1971) Some properties of magnesium hydridoborate, **Izvestiya Akademii Nauk Sssr-Seriya Khimicheskaya,** 159-162.

Kuhlmann, U., Werheit, H., Lundström, T. & Robers, W. (1994) Optical properties of amorphous boron, **Journal of Physics and Chemistry of Solids**, 55, 579-587.

Kulkarni, A. D., Wang, L. L., Johnson, D. D., Sholl, D. S. & Johnson, J. K. (2010) First-principles characterization of amorphous phases of $MB_{12}H_{12}$, M = Mg, Ca, **Journal of Physical Chemistry C**, 114, 14601-14605.

Kyoi, D., Sato, T., Ronnebro, E., Kitamura, N., Ueda, A., Ito, M., Katsuyama, S., Hara, S., Noreus, D. & Sakai, T. (2004) A new ternary magnesium-titanium hydride Mg_7TiH_x with hydrogen desorption properties better than both binary magnesium and titanium hydrides, **Journal of Alloys and Compounds**, 372, 213-217.

Lee, H. S., Hwang, S. J., Kim, H. K., Lee, Y. S., Park, J., Yu, J. S. & Cho, Y. W. (2012) In situ NMR study on the interaction between $LiBH_4$-$Ca(BH_4)_2$ and mesoporous Scaffolds, **Journal of Physical Chemistry Letters**, 3, 2922-2927.

Lee, H. S., Lee, Y. S., Suh, J. Y., Kim, M., Yu, J. S. & Cho, Y. W. (2011) Enhanced Desorption and Absorption Properties of Eutectic $LiBH_4$-$Ca(BH_4)_2$ Infiltrated into Mesoporous Carbon, **Journal of Physical Chemistry C**, 115, 20027-20035.

Lee, J. Y., Ravnsbaek, D., Lee, Y. S., Kim, Y., Cerenius, Y., Shim, J. H., Jensen, T. R., Hur, N. H. & Cho, Y. W. (2009a) Decomposition Reactions and Reversibility of the $LiBH_4$-$Ca(BH_4)_2$ Composite, **Journal of Physical Chemistry C**, 113, 15080-15086.

Lee, Y. S., Kim, Y., Cho, Y. W., Shapiro, D., Wolverton, C. & Ozolins, V. (2009b) Crystal structure and phonon instability of high-temperature beta-$Ca(BH_4)_2$, **Physical Review B**, 79, 104107.

Leites, L. A. (1992) Vibrational spectroscopy of carboranes and parent boranes and its capabilities in carborane chemistry, **Chemical Reviews**, 92, 279-323.

Leites, L. A., Bukalov, S. S., Kurbakova, A. P., Kaganski, M. M., Gaft, Y. L., Kuznetsov, N. T. & Zakharova, I. A. (1982) Vibraional spectra of icosahedral closoborate anions $B_{12}X_{12}^{2-}$ (X = H, D, Cl, Br, I), **Spectrochimica Acta Part a-Molecular and Biomolecular Spectroscopy**, 38, 1047-1056.

Leites, L. A., Kurbakova, A. P., Kaganskii, M. M., Gaft, Y. L., Zakharova, I. A. & Kuznetsov, N. T. (1983) Vibrational spectra of polyhedral closo-decarborate $B_{10}X_{10}^{2-}$ anions (X = H, D, Cl, Br,

REFERENCES

 l), **Bulletin of the Academy of Sciences of the Ussr Division of Chemical Science**, 32, 2062-2069.

Lewkowicz, I. (1996) Hydrogen metal systems i: titanium-hydrogen, **Solid State Phenomena**, 49-50, 239-280.

Li, D. X., Zhang, T. R., Yang, S. Q., Tao, Z. L. & Chen, J. (2011a) Ab initio investigation of structures, electronic and thermodynamic properties for Li-Mg-H ternary system, **Journal of Alloys and Compounds**, 509, 8228-8234.

Li, H. W., Kikuchi, K., Nakamori, Y., Miwa, K., Towata, S. & Orimo, S. (2007a) Effects of ball milling and additives on dehydriding behaviors of well-crystallized $Mg(BH_4)_2$, **Scripta Materialia**, 57, 679-682.

Li, H. W., Kikuchi, K., Nakamori, Y., Ohba, N., Miwa, K., Towata, S. & Orimo, S. (2008) Dehydriding and rehydriding processes of well-crystallized $Mg(BH_4)_2$ accompanying with formation of intermediate compounds, **Acta Materialia**, 56, 1342-1347.

Li, H. W., Matsunaga, T., Yan, Y. G., Maekawa, H., Ishikiriyama, M. & Orimo, S. (2010a) Nanostructure-induced hydrogenation of layered compound MgB_2, **Journal of Alloys and Compounds**, 505, 654-656.

Li, H. W., Miwa, K., Ohba, N., Fujita, T., Sato, T., Yan, Y., Towata, S., Chen, M. W. & Orimo, S. (2009) Formation of an intermediate compound with a $B_{12}H_{12}$ cluster: experimental and theoretical studies on magnesium borohydride $Mg(BH_4)_2$, **Nanotechnology**, 20, 204013.

Li, H. W., Orimo, S., Nakamori, Y., Miwa, K., Ohba, N., Towata, S. & Zuttel, A. (2007b) Materials designing of metal borohydrides: viewpoints from thermodynamical stabilities, **Journal of Alloys and Compounds**, 446, 315-318.

Li, H. W., Yan, Y. G., Orimo, S., Züttel, A. & Jensen, C. M. (2011b) Recent progress in metal borohydrides for hydrogen storage, **Energies**, 4, 185-214.

Li, J., Xia, S. P. & Gao, S. Y. (1995) FT-IR and Raman-spectroscopic study of hydrated borates, **Spectrochimica Acta Part a-Molecular and Biomolecular Spectroscopy**, 51, 519-532.

Li, S., Willis, M. & Jena, P. (2010b) Reaction intermediates during the dehydrogenation of metal borohydrides: a cluster perspective, **Journal of Physical Chemistry C**, 114, 16849-16854.

Li, Z. P., Liu, B. H., Morigasaki, N. & Suda, S. (2003) Preparation of potassium borohydride by a mechano-chemical reaction of saline hydrides with dehydrated borate through ball milling, **Journal of Alloys and Compounds**, 354, 243-247.

Liang, G., Huot, J., Boily, S., Van Neste, A. & Schulz, R. (1999) Catalytic effect of transition metals on hydrogen sorption in nanocrystalline ball milled MgH_2-T_m (T_m = Ti, V, Mn, Fe and Ni) systems, **Journal of Alloys and Compounds**, 292, 247-252.

Liang, G. & Schulz, R. (2003) Synthesis of Mg-Ti alloy by mechanical alloying, **Journal of Materials Science**, 38, 1179-1184.

Liu, R. X., Reed, D. & Book, D. (2012) Decomposition behaviour of $Mn(BH_4)_2$ formed by ball-milling $LiBH_4$ and $MnCl_2$, **Journal of Alloys and Compounds**, 515, 32-38.

Liu, X., Peaslee, D., Jost, C. Z., Baumann, T. F. & Majzoub, E. H. (2011) Systematic pore-size effects of nanoconfinement of $LiBH_4$: elimination of diborane release and tunable behavior for hydrogen storage applications, **Chemistry of Materials**, 23, 1331-1336.

Llamas-Jansa, I., Friedrichs, O., Fichtner, M., Bardaji, E. G., Zuttel, A. & Hauback, B. C. (2012) The role of $Ca(BH_4)_2$ polymorphs, **Journal of Physical Chemistry C**, 116, 13472-13479.

Lu, J., Choi, Y. J., Fang, Z. Z., Sohn, H. Y. & Ronnebro, E. (2009) hydrogen storage properties of nanosized MgH_2-$0.1TiH_2$ prepared by ultrahigh-energy-high-pressure milling, **Journal of the American Chemical Society**, 131, 15843-15852.

Luck, R. L. & Schelter, E. J. (1999) Potassium borohydride, **Acta Crystallographica Section C**, 55.

Ma, L. P., Wang, P. & Cheng, H. M. (2010) Hydrogen sorption kinetics of MgH_2 catalyzed with titanium compounds, **International Journal of Hydrogen Energy**, 35, 3046-3050.

REFERENCES

Ma, L. P., Wang, P., Kang, X. D. & Cheng, H. M. (2007) Preliminary investigation on the catalytic mechanism of TiF_3 additive in MgH_2-TiF_3 H-storage system, **Journal of Materials Research**, 22**,** 1779-1786.

Majzoub, E. H. & Ronnebro, E. (2009) Crystal structures of calcium borohydride: theory and experiment, **Journal of Physical Chemistry C**, 113**,** 3352-3358.

Mao, J. F., Guo, Z. P., Yu, X. B. & Liu, H. K. (2011) Improved hydrogen storage properties of $NaBH_4$ destabilized by CaH_2 and $Ca(BH_4)_2$, **Journal of Physical Chemistry C**, 115**,** 9283-9290.

Mao, J. F., Yu, X. B., Guo, Z. P., Liu, H. K., Wu, Z. & Ni, J. (2009) Enhanced hydrogen storage performances of $NaBH_4$–MgH_2 system, **Journal of Alloys and Compounds**, 479**,** 619-623.

Marks, T. J. & Kolb, J. R. (1977) Covalent transition-metal, lanthanide, and actinide tetrahydroborate complexes, **Chemical Reviews**, 77**,** 263-293.

Martelli, P., Caputo, R., Remhof, A., Mauron, P., Borgschulte, A. & Züttel, A. (2010a) Stability and decomposition of $NaBH_4$, **Journal of Physical Chemistry C**, 114**,** 7173-7177.

Martelli, P., Remhof, A., Borgschulte, A., Mauron, P., Wallacher, D., Kemner, E., Russina, M., Pendolino, F. & Zuttel, A. (2010b) BH_4- self-diffusion in liquid $LiBH_4$, **Journal of Physical Chemistry A**, 114**,** 10117-10121.

Martinez-Coronado, R., Sanchez-Benitez, J., Retuerto, M., Fernandez-Diaz, M. T. & Alonso, J. A. (2012) High-pressure synthesis of $Na_{1-x}Li_xMgH_3$ perovskite hydrides, **Journal of Alloys and Compounds**, 522**,** 101-105.

Matsunaga, T., Buchter, F., Mauron, P., Bielman, A., Nakamori, Y., Orimo, S., Ohba, N., Miwa, K. & Züttel, A. (2008) Hydrogen storage properties of $Mg(BH_4)_2$, **Journal of Alloys and Compounds**, 459**,** 583-588.

Matsuo, M., Nakamori, Y., Orimo, S., Maekawa, H. & Takamura, H. (2007) Lithium superionic conduction in lithium borohydride accompanied by structural transition, **Applied Physics Letters**, 91**,** 224103.

Matsuo, M. & Orimo, S. (2011) Lithium fast-ionic conduction in complex hydrides: review and prospects, **Advanced Energy Materials**, 1**,** 161-172.

Mauron, P., Buchter, F., Friedrichs, O., Remhof, A., Bielmann, M., Zwicky, C. N. & Zuttel, A. (2008) Stability and reversibility of $LiBH_4$, **Journal of Physical Chemistry B**, 112**,** 906-910.

Mikheeva, V. & Titov, L. (1964) O borogidride kaltsiya, **Zhurnal Neorganicheskoi Khimii**, 9**,** 789-793.

Mills, B. (2008) *Ball-and-stick model of the diborane molecule, B_2H_6* [Online]. Available: http://en.wikipedia.org/wiki/File:Diborane-3D-balls-A.png [Accessed 24th May 2014].

Minella, C. B., Garroni, S., Olid, D., Teixidor, F., Pistidda, C., Lindemann, I., Gutfleisch, O., Baro, M. D., Bormann, R., Klassen, T. & Dornheim, M. (2011) Experimental evidence of $CaB_{12}H_{12}$ formation during decomposition of a $Ca(BH_4)_2$+MgH_2 based reactive hydride composite, **Journal of Physical Chemistry C**, 115**,** 18010-18014.

Miwa, K., Aoki, M., Noritake, T., Ohba, N., Nakamori, Y., Towata, S., Züttel, A. & Orimo, S. (2006) Thermodynamical stability of calcium borohydride $Ca(BH_4)_2$, **Physical Review B**, 74**,** 155122.

Miwa, K., Ohba, N., Towata, S., Nakamori, Y. & Orimo, S. (2004) First-principles study on lithium borohydride $LiBH_4$, **Physical Review B**, 69**,** 245120.

Miyaoka, H., Kuze, T., Sano, H., Mori, H., Mizutani, G., Ushioda, S., Otsuka, N. & Terano, M. (2000) Raman spectrum of ball-milled α-$TiCl_3$, **Journal of Luminescence**, 87–89**,** 709-711.

Mohtadi, R., Matsui, M., Arthur, T. S. & Hwang, S. J. (2012) Magnesium borohydride: from hydrogen storage to magnesium battery, **Angewandte Chemie-International Edition**, 51**,** 9780-9783.

Muetterties, E. L., Balthis, J. H., Miller, H. C., Chia, Y. T. & Knoth, W. H. (1964) Chemistry of boranes 8. salts + acids of $B_{10}H_{10}^{2-}$ + $B_{12}H_{12}^{2-}$, **Inorganic Chemistry**, 3**,** 444-451.

REFERENCES

Muetterties, E. L., Merrifield, R. E., Knoth, W. H., Downing, J. R. & Miller, H. C. (1962) Chemistry of boranes .3. infrared and raman spectra of $B_{12}H_{12}^{2-}$ and related anions, **Journal of the American Chemical Society***,* 84**,** 2506-2508.

Mulder, F. M., Singh, S., Bolhuis, S. & Eijt, S. W. H. (2012) Extended solubility limits and nanograin refinement in Ti/Zr fluoride-catalyzed MgH_2, **Journal of Physical Chemistry C***,* 116**,** 2001-2012.

Nakamori, Y., Li, H. W., Kikuchi, K., Aoki, M., Miwa, K., Towata, S. & Orimo, S. (2007) Thermodynamical stabilities of metal-borohydrides, **Journal of Alloys and Compounds***,* 446**,** 296-300.

Nakamori, Y., Li, H. W., Matsuo, M., Miwa, K., Towata, S. & Orimo, S. (2008) Development of metal borohydrides for hydrogen storage, **Journal of Physics and Chemistry of Solids***,* 69**,** 2292-2296.

Nakamori, Y., Li, H. W., Miwa, K., Towata, S. & Orimo, S. (2006a) Syntheses and hydrogen Desorption properties of metal-borohydrides $M(BH_4)_n$ (M = Mg, Sc, Zr, Ti, and Zn; n=2-4) as advanced hydrogen storage materials, **Materials Transactions***,* 47**,** 1898-1901.

Nakamori, Y., Miwa, K., Ninomiya, A., Li, H. W., Ohba, N., Towata, S. I., Zuttel, A. & Orimo, S. I. (2006b) Correlation between thermodynamical stabilities of metal borohydrides and cation electronegativites: First-principles calculations and experiments, **Physical Review B***,* 74**,** 045126.

Nale, A., Catti, M., Bardaji, E. G. & Fichtner, M. (2011) On the decomposition of the $0.6LiBH_4$-$0.4Mg(BH_4)_2$ eutectic mixture for hydrogen storage, **International Journal of Hydrogen Energy***,* 36**,** 13676-13682.

National Renewable Energy Laboratory. (2000) **Proceedings of the 2000 U.S. DOE Hydrogen Program Review** [Online], NREL/CP-570-28990, California, U.S. Available: http://www.nrel.gov/docs/fy01osti/28890.pdf [Accessed 21st May, 2014].

Nayeb-Hashemi, A. A., Clark, J. B. & Pelton, A. D. (1984) The Li-Mg (Lithium-Magnesium) system, **Bulletin of Alloy Phase Diagrams***,* 5**,** 365-374.

Nelson, G. (2013) *Hyundai, Mercedes, Nissan, Toyota join DOE in fuel cells push* [Online]. Automotive News. Available: http://www.autonews.com/apps/pbcs.dll/article?AID=/20130513/OEM05/130519963#axzz2V AcsyqKI [Accessed 21st May, 2013].

Newhouse, R. J., Stavila, V., Hwang, S. J., Klebanoff, L. E. & Zhang, J. Z. (2010) Reversibility and improved hydrogen release of magnesium borohydride, **Journal of Physical Chemistry C***,* 114**,** 5224-5232.

Ngene, P., van den Berg, R., Verkuijlen, M. H. W., de Jong, K. P. & de Jongh, P. E. (2011) Reversibility of the hydrogen desorption from $NaBH_4$ by confinement in nanoporous carbon, **Energy & Environmental Science***,* 4**,** 4108-4115.

Nickels, E. A. (2010) Structural and thermogravimetric studies of group I and II borohydrides*.* **DPhil thesis**, University of Oxford.

Nickels, E. A., Jones, M. O., David, W. I. F., Johnson, S. R., Lowton, R. L., Sommariva, M. & Edwards, P. P. (2008) Tuning the decomposition temperature in complex hydrides: Synthesis of a mixed alkali metal borohydride, **Angewandte Chemie-International Edition***,* 47**,** 2817-2819.

Noritake, T., Aoki, M., Matsumoto, M., Miwa, K., Towata, S., Li, H. W. & Orimo, S. (2010) Crystal structure and charge density analysis of $Ca(BH_4)_2$, **Journal of Alloys and Compounds***,* 491**,** 57-62.

Noritake, T., Aoki, M., Towata, S., Seno, Y., Hirose, Y., Nishibori, E., Takata, M. & Sakata, M. (2002) Chemical bonding of hydrogen in MgH_2, **Applied Physics Letters***,* 81**,** 2008-2010.

Ohba, N., Miwa, K., Aoki, M., Noritake, T., Towata, S., Nakamori, Y., Orimo, S. & Züttel, A. (2006) First-principles study on the stability of intermediate compounds of $LiBH_4$, **Physical Review B***,* 74**,** 0751101.

REFERENCES

Orimo, S., Nakamori, Y., Kitahara, G., Miwa, K., Ohba, N., Towata, S. & Züttel, A. (2005) Dehydriding and rehydriding reactions of LiBH$_4$, **Journal of Alloys and Compounds**, 404, 427-430.

Orimo, S., Nakamori, Y. & Züttel, A. (2004) Material properties of MBH$_4$ (M = Li, Na and K), **Materials Science and Engineering: B**, 108, 51-53.

Orimo, S. I., Nakamori, Y., Eliseo, J. R., Züttel, A. & Jensen, C. M. (2007) Complex hydrides for hydrogen storage, **Chemical Reviews**, 107, 4111-4132.

Orimo, S. I., Nakamori, Y., Ohba, N., Miwa, K., Aoki, M., Towata, S. & Züttel, A. (2006) Experimental studies on intermediate compound of LiBH$_4$, **Applied Physics Letters**, 89, 021920.

Ozolins, V., Majzoub, E. H. & Wolverton, C. (2009) First-principles prediction of thermodynamically reversible hydrogen storage reactions in the Li-Mg-Ca-B-H System, **Journal of the American Chemical Society**, 131, 230-237.

Park, K., Lee, H. S., Remhof, A., Lee, Y. S., Yan, Y. G., Kim, M. Y., Kim, S. J., Züttel, A. & Cho, Y. W. (2013) Thermal properties of Y(BH$_4$)$_3$ synthesized via two different methods, **International Journal of Hydrogen Energy**, 38, 9263-9270.

Parker, S. F. (2010) Spectroscopy and bonding in ternary metal hydride complexes-potential hydrogen storage media, **Coordination Chemistry Reviews**, 254, 215-234.

Parrott, V. (2013) *Mazda's hydrogen future: Hydrogen rotary engine here by 2013* [Online]. Available: http://www.autocar.co.uk/car-news/industry/mazda%E2%80%99s-hydrogen-future [Accessed 21st May, 2013].

Paskevicius, M., Pitt, M. P., Webb, C. J., Sheppard, D. A., Filso, U., Gray, E. M. & Buckley, C. E. (2012) In-Situ X-ray diffraction study of gamma-Mg(BH$_4$)$_2$ decomposition, **Journal of Physical Chemistry C**, 116, 15231-15240.

Pendolino, F., Mauron, P., Borgschulte, A. & Züttel, A. (2009) Effect of Boron on the Activation Energy of the Decomposition of LiBH$_4$, **The Journal of Physical Chemistry C**, 113, 17231-17234.

Pistidda, C., Garroni, S., Dolci, F., Bardaji, E. G., Khandelwal, A., Nolis, P., Dornheim, M., Gosalawit, R., Jensen, T., Cerenius, Y., Surinach, S., Baro, M. D., Lohstroh, W. & Fichtner, M. (2010) Synthesis of amorphous Mg(BH$_4$)$_2$ from MgB$_2$ and H$_2$ at room temperature, **Journal of Alloys and Compounds**, 508, 212-215.

Pitt, M. P., Paskevicius, M., Brown, D. H., Sheppard, D. A. & Buckley, C. E. (2013) Thermal stability of Li$_2$B$_{12}$H$_{12}$ and its role in the decomposition of LiBH$_4$, **Journal of the American Chemical Society**, 135, 6930-6941.

Pitt, M. P., Webb, C. J., Paskevicius, M., Sheptyakov, D., Buckley, C. E. & Gray, E. M. (2011) In situ neutron diffraction study of the deuteration of isotopic Mg^{11}B$_2$, **Journal of Physical Chemistry C**, 115, 22669-22679.

Plešek, J. & Heřmánek, S. (1966) Chemistry of boranes IV. on preparation properties and behavior towards lewis bases of magnesium borohydride, **Collection Of Czechoslovak Chemical Communications**, 31, 3854-3858.

Polak, R. J. & Obenland, C. (1964) Pyrolysis of diborane - formation of decaborane in continuous flow reactor, **Industrial & Engineering Chemistry Product Research and Development**, 3, 234-238.

Polanski, M., Nielsen, T. K., Cerenius, Y., Bystrzycki, J. & Jensen, T. R. (2010) Synthesis and decomposition mechanisms of Mg$_2$FeH$_6$ studied by in-situ synchrotron X-ray diffraction and high-pressure DSC, **International Journal of Hydrogen Energy**, 35, 3578-3582.

Ponthieu, M., Cuevas, F., Fernandez, J. F., Laversenne, L., Porcher, F. & Latroche, M. (2013) Structural properties and reversible deuterium loading of MgD$_2$-TiD$_2$ nanocomposites, **Journal of Physical Chemistry C**, 117, 18851-18862.

Pottmaier, D., Pinatel, E. R., Vitillo, J. G., Garroni, S., Orlova, M., Baro, M. D., Vaughan, G. B. M., Fichtner, M., Lohstroh, W. & Baricco, M. (2011) Structure and thermodynamic properties of the NaMgH$_3$ perovskite: a comprehensive study, **Chemistry of Materials**, 23, 2317-2326.

REFERENCES

Predel, B. (1996) H-Ti (Hydrogen-Titanium). *In:* Madelung, O. (ed.) **Ga-Gd – Hf-Zr**. Springer Berlin Heidelberg.

Racu, A. M., Schoenes, J., Lodziana, Z., Borgschulte, A. & Züttel, A. (2008) High-resolution Raman spectroscopy study of phonon modes in $LiBH_4$ and $LiBD_4$, **Journal of Physical Chemistry A**, 112**,** 9716-9722.

Ravnsbæk, D. B., Filinchuk, Y., Cerenius, Y., Jakobsen, H. J., Besenbacher, F., Skibsted, J. & Jensen, T. R. (2009) A series of mixed-metal borohydrides, **Angewandte Chemie-International Edition**, 48**,** 6659-6663.

Ravnsbæk, D. B., Filinchuk, Y., Černý, R. & Jensen, T. R. (2010a) Powder diffraction methods for studies of borohydride-based energy storage materials, **Zeitschrift Fur Kristallographie**, 225**,** 557-569.

Ravnsbæk, D. B., Filinchuk, Y., Černý, R., Ley, M. B., Haase, D., Jakobsen, H. J., Skibsted, J. & Jensen, T. R. (2010b) Thermal polymorphism and decomposition of $Y(BH_4)_3$, **Inorganic Chemistry**, 49**,** 3801-3809.

Reed, D. (2010) An investigation into the synthesis and characterisation of metal borohydrides for hydrogen storage*. **PhD thesis**, University of Birmingham.

Reed, D. (2011)*: Calculated Raman vibrations of $CaB_{12}H_{12}$.* Personal Communication.

Reed, D. & Book, D. (2009) In-situ Raman study of the thermal decomposition of $LiBH_4$, **Materials Research Society Proceedings**, 1216**,** W06-05.

Reed, D. & Book, D. (2011) Recent applications of Raman spectroscopy to the study of complex hydrides for hydrogen storage, **Current Opinion in Solid State & Materials Science**, 15**,** 62-72.

Remhof, A., Borgschulte, A., Friedrichs, O., Mauron, P., Yan, Y. & Zuttel, A. (2012a) Solvent-free synthesis and decomposition of $Y(BH_4)_3$, **Scripta Materialia**, 66**,** 280-283.

Remhof, A., Friedrichs, O., Buchter, F., Mauron, P., Zuttel, A. & Wallacher, D. (2008) Solid-state synthesis of $LiBD_4$ observed by in situ neutron diffraction, **Physical Chemistry Chemical Physics**, 10**,** 5859-5862.

Remhof, A., Yan, Y., Friedrichs, O., Kim, J. W., Mauron, P., Borgschulte, A., Wallacher, D., Buchsteiner, A., Hoser, A., Oh, K. H., Cho, Y. W. & Züttel, A. (2012b) Towards room temperature, direct, solvent free synthesis of tetraborohydrides. **5th European Conference on Neutron Scattering**. Bristol: Iop Publishing Ltd.

Remhof, A., Yan, Y., Rentsch, D., Borgschulte, A., Jensen, C. M. & Zuttel, A. (2014) Solvent-free synthesis and stability of $MgB_{12}H_{12}$, **Journal of Materials Chemistry A**, 2**,** 7244-7249.

Renaudin, G., Gomes, S., Hagemann, H., Keller, L. & Yvon, K. (2004) Structural and spectroscopic studies on the alkali borohydrides MBH_4 (M = Na, K, Rb, Cs), **Journal of Alloys and Compounds**, 375**,** 98-106.

Renishaw plc. (2008). Renishaw WiRE Version 3.2, Program, Gloucestershire: Renishaw plc,.

Retsch GmbH. (2014) **Materials and Material Analyses** [Online], Haan, Germany Available: http://www.retsch.com/dltmp/www/53e4b558-acc0-4661-9d7f-636500000000-b6c762a3fae3/material_analyses_of_grinding_tools_en_de.pdf [Accessed 5 January, 2015].

Riktor, M. D., Filinchuk, Y., Vajeeston, P., Bardaji, E. G., Fichtner, M., Fjellvag, H., Sorby, M. H. & Hauback, B. C. (2011) The crystal structure of the first borohydride borate, $Ca_3(BD_4)_3(BO_3)$, **Journal of Materials Chemistry**, 21**,** 7188-7193.

Riktor, M. D., Sorby, M. H., Chlopek, K., Fichtner, M., Buchter, F., Zuettel, A. & Hauback, B. C. (2007) In situ synchrotron diffraction studies of phase transitions and thermal decomposition of $Mg(BH_4)_2$ and $Ca(BH_4)_2$, **Journal of Materials Chemistry**, 17**,** 4939-4942.

Riktor, M. D., Sorby, M. H., Chlopek, K., Fichtner, M. & Hauback, B. C. (2009) The identification of a hitherto unknown intermediate phase CaB_2H_x from decomposition of $Ca(BH_4)_2$, **Journal of Materials Chemistry**, 19**,** 2754-2759.

REFERENCES

Rongeat, C., D'Anna, V., Hagemann, H., Borgschulte, A., Zuttel, A., Schultz, L. & Gutfleisch, O. (2010) Effect of additives on the synthesis and reversibility of $Ca(BH_4)_2$, **Journal of Alloys and Compounds**, 493, 281-287.

Rönnebro, E. (2011) Development of group II borohydrides as hydrogen storage materials, **Current Opinion in Solid State & Materials Science**, 15, 44-51.

Rönnebro, E., Kyoi, D., Kitano, A., Kitano, Y. & Sakai, T. (2005) Hydrogen sites analysed by X-ray synchrotron diffraction in Mg_7TiH_{13-16} made at gigapascal high-pressures, **Journal of Alloys and Compounds**, 404, 68-72.

Rönnebro, E. & Majzoub, E. (Year) Discovery and development of metal hydrides for reversible on-board storage. **DOE hydrogen program and annual peer review meeting proceedings**.

Rönnebro, E. & Majzoub, E. H. (2007) Calcium borohydride for hydrogen storage: Catalysis and reversibility, **Journal of Physical Chemistry B**, 111, 12045-12047.

Rönnebro, E., Noreus, D., Kadir, K., Reiser, A. & Bogdanovic, B. (2000) Investigation of the perovskite related structures of $NaMgH_3$, $NaMgF$, and Na_3AlH_6, **Journal of Alloys and Compounds**, 299, 101-106.

Rude, L. H., Nielsen, T. K., Ravnsbaek, D. B., Bosenberg, U., Ley, M. B., Richter, B., Arnbjerg, L. M., Dornheim, M., Filinchuk, Y., Besenbacher, F. & Jensen, T. R. (2011) Tailoring properties of borohydrides for hydrogen storage: A review, **Physica Status Solidi a-Applications and Materials Science**, 208, 1754-1773.

Sabitu, S. T., Gallo, G. & Goudy, A. J. (2010) Effect of TiH_2 and Mg_2Ni additives on the hydrogen storage properties of magnesium hydride, **Journal of Alloys and Compounds**, 499, 35-38.

San-Martin, A. & Manchester, F. D. (1987) The H−Mg (Hydrogen-Magnesium) system, **Journal of Phase Equilibria**, 8, 431-437.

Sartori, S., Knudsen, K. D., Hage, F. S., Heyn, R. H., Bardaji, E. G., Zhao-Karger, Z., Fichtner, M. & Hauback, B. C. (2012) Influence of nanoconfinement on morphology and dehydrogenation of the $Li^{11}BD_4$-$Mg(^{11}BD_4)_2$ system, **Nanotechnology**, 23, 255704.

Sato, T., Miwa, K., Nakamori, Y., Ohoyama, K., Li, H. W., Noritake, T., Aoki, M., Towata, S. I. & Orimo, S. I. (2008) Experimental and computational studies on solvent-free rare-earth metal borohydrides $R(BH_4)_3$ (R = Y, Dy, and Gd), **Physical Review B**, 77.

Satyapal, S., Petrovic, J., Read, C., Thomas, G. & Ordaz, G. (2007) The US Department of Energy's national hydrogen storage project: progress towards meeting hydrogen-powered vehicle requirements, **Catalysis Today**, 120, 246-256.

Schlapbach, L. & Züttel, A. (2001) Hydrogen-storage materials for mobile applications, **Nature**, 414, 353-358.

Schlesinger, H. I. & Brown, H. C. (1940) Metallo borohydrides. III. Lithium borohydride, **Journal of the American Chemical Society**, 62, 3429-3435.

Schlesinger, H. I., Brown, H. C., Abraham, B., Bond, A. C., Davidson, N., Finholt, A. E., Gilbreath, J. R., Hoekstra, H., Horvitz, L., Hyde, E. K., Katz, J. J., Knight, J., Lad, R. A., Mayfield, D. L., Rapp, L., Ritter, D. M., Schwartz, A. M., Sheft, I., Tuck, L. D. & Walker, A. O. (1953a) New developments in the chemistry of diborane and the borohydrides .1. general summary, **Journal of the American Chemical Society**, 75, 186-190.

Schlesinger, H. I., Brown, H. C. & Finholt, A. E. (1953b) New developments in the chemistry of diborane and of the borohydrides .6. the preparation of sodium borohydride by the high temperature reaction of sodium hydride with borate esters, **Journal of the American Chemical Society**, 75, 205-209.

Schlesinger, H. I., Brown, H. C., Hoekstra, H. R. & Rapp, L. R. (1953c) New developments in the chemistry of diborane and the borohybrides .5. reactions of diborane with alkali metal hydrides and their addition compounds - new syntheses of borohydrides - sodium and potassium borohydrides, **Journal of the American Chemical Society**, 75, 199-204.

REFERENCES

Schrader, B. (1995) **Infrared and Raman Spectroscopy**, Weinheini, Germany; New York, USA, Wiley-VCH Verlag GmbH.

Severa, G., Hagemann, H., Longhini, M., Kaminski, J. W., Wesolowski, T. A. & Jensen, C. M. (2010a) Thermal Desorption, Vibrational Spectroscopic, and DFT Computational Studies of the Complex Manganese Borohydrides $Mn(BH_4)_2$ and $[Mn(BH_4)_4]^{2-}$, **Journal of Physical Chemistry C**, 114, 15516-15521.

Severa, G., Ronnebro, E. & Jensen, C. M. (2010b) Direct hydrogenation of magnesium boride to magnesium borohydride: demonstration of > 11 weight percent reversible hydrogen storage, **Chemical Communications**, 46, 421-423.

Shannon, R. D. (1976) Revised effective ionic-radii and systematic studies of interatomic distances in halides and chalcogenides, **Acta Crystallographica Section A**, 32, 751-767.

Shao, H., Felderhoff, M. & Schuth, F. (2011) Hydrogen storage properties of nanostructured MgH_2/TiH_2 composite prepared by ball milling under high hydrogen pressure, **International Journal of Hydrogen Energy**, 36, 10828-10833.

Sheppard, D. A., Paskevicius, M. & Buckley, C. E. (2011) Thermodynamics of Hydrogen Desorption from $NaMgH_3$ and Its Application As a Solar Heat Storage Medium, **Chemistry of Materials**, 23, 4298-4300.

Shi, Z., Liu, M., Naik, D. & Gole, J. L. (2001) Electrochemical properties of Li–Mg alloy electrodes for lithium batteries, **Journal of Power Sources**, 92, 70-80.

Smith, E. & Dent, G. (2005) Introduction, basic theory and principles. **Modern Raman Spectroscopy – A Practical Approach**. John Wiley & Sons, Ltd.

Soderlund, M., Maki-Arvela, P., Eranen, K., Salmi, T., Rahkola, R. & Murzin, D. Y. (2005) Catalyst deactivation in diborane decomposition, **Catalysis Letters**, 105, 191-202.

Soloveichik, G. L. (2007) Metal borohydrides as hydrogen storage materials, **Material Matters**, 2, 11.

Soloveichik, G. L., Andrus, M., Gao, Y., Zhao, J. C. & Kniajanski, S. (2009) Magnesium borohydride as a hydrogen storage material: Synthesis of unsolvated $Mg(BH_4)_2$, **International Journal of Hydrogen Energy**, 34, 2144-2152.

Song, Y., Guo, Z. X. & Yang, R. (2004) Influence of titanium on the hydrogen storage characteristics of magnesium hydride: a first principles investigation, **Materials Science and Engineering a-Structural Materials Properties Microstructure and Processing**, 365, 73-79.

Soulié, J. P., Renaudin, G., Černý, R. & Yvon, K. (2002) Lithium borohydride $LiBH_4$, **Journal of Alloys and Compounds**, 346, 200-205.

Srinivasan, S., Escobar, D., Jurczyk, M., Goswami, Y. & Stefanakos, E. (2008) Nanocatalyst doping of $Zn(BH_4)_2$ for on-board hydrogen storage, **Journal of Alloys and Compounds**, 462, 294-302.

Stampfer, J. F., Holley, C. E. & Suttle, J. F. (1960) The magnesium hydrogen system, **Journal of the American Chemical Society**, 82, 3504-3508.

Stavila, V., Her, J. H., Zhou, W., Hwang, S. J., Kim, C., Ottley, L. A. M. & Udovic, T. J. (2010) Probing the structure, stability and hydrogen storage properties of calcium dodecahydro-closo-dodecaborate, **Journal of Solid State Chemistry**, 183, 1133-1140.

Stockmayer, W. H. & Stephenson, C. C. (1953) The nature of the gradual transition in sodium borohydride, **The Journal of Chemical Physics**, 21, 1311-1312.

Stowe, A. C. & Smyrl, N. (2012) Raman spectroscopy of lithium hydride corrosion: Selection of appropriate excitation wavelength to minimize fluorescence, **Vibrational Spectroscopy**, 60, 133-136.

Studer, S., Stucki, S. & Speight, J. D. (2008) Hydrogen as a fuel. **Hydrogen as a Future Energy Carrier**. Wiley-VCH Verlag GmbH & Co. KGaA.

REFERENCES

Suda, S., Sun, Y. M., Liu, B. H., Zhou, Y., Morimitsu, S., Arai, K., Tsukamoto, N., Uchida, M., Candra, Y. & Li, Z. P. (2001) Catalytic generation of hydrogen by applying fluorinated-metal hydrides as catalysts, **Applied Physics A***, 72**, 209-212.

Suryanarayana, C. (2001) Mechanical alloying and milling, **Progress in Materials Science***, 46**, 1-184.

Swanson, H. E. & Tatge, E. (1953) **Standard X-ray diffraction powder patterns. Vol. I***, Washington, D.C., National Bureau of Standards circular, p10.

Tao, S., Notten, P. H. L., van Santen, R. A. & Jansen, A. P. J. (2011) Dehydrogenation properties of epitaxial MgH_2/TiH_2 multilayers – A DFT study, **Computational Materials Science***, 50**, 2960-2966.

Taylor, R. H., Curtarolo, S. & Hart, G. L. W. (2010) Ordered magnesium-lithium alloys: First-principles predictions, **Physical Review B***, 81**, 024112.

Tedds, S., Walton, A., Broom, D. P. & Book, D. (2011) Characterisation of porous hydrogen storage materials: carbons, zeolites, MOFs and PIMs, **Faraday Discussions***, 151**, 75-94.

Tomkinson, J., Ludman, C. J. & Waddington, T. C. (1979) IR Raman and inelastic neutron-scattering spectra of cesium octahydridotriborate, CsB_3H_8, **Spectrochimica Acta Part A-Molecular and Biomolecular Spectroscopy***, 35**, 117-122.

Udovic, T. J., Matsuo, M., Unemoto, A., Verdal, N., Stavila, V., Skripov, A. V., Rush, J. J., Takamura, H. & Orimo, S.-i. (2014) Sodium superionic conduction in $Na_2B_{12}H_{12}$, **Chemical Communications***, 50**, 3750-3752.

Umegaki, T., Yan, J.-M., Zhang, X.-B., Shioyama, H., Kuriyama, N. & Xu, Q. (2009) Boron- and nitrogen-based chemical hydrogen storage materials, **International Journal of Hydrogen Energy***, 34**, 2303-2311.

Urgnani, J., Torres, F. J., Palumbo, M. & Baricco, M. (2008) Hydrogen release from solid state $NaBH_4$, **International Journal of Hydrogen Energy***, 33**, 3111-3115.

US Department of Energy. (2007) *Status of hydrogen storage technologies* [Online]. U.S. Department of Energy. Available: http://energy.gov/eere/fuelcells/status-hydrogen-storage-technologies [Accessed 1st June, 2014].

US Department of Energy. (2012) *Types of fuel cells* [Online]. Available: http://energy.gov/eere/fuelcells/types-fuel-cells#pem [Accessed 10th May, 2012].

US Department of Energy. (2014a) *Chemical hydrogen storage* [Online]. U.S. Department of Energy. Available: http://energy.gov/eere/fuelcells/chemical-hydrogen-storage [Accessed 1st June, 2014].

US Department of Energy. (2014b) *Hydrogen Production - Basics* [Online]. The U.S. Department of Energy,. Available: http://energy.gov/eere/fuelcells/hydrogen-production-basics-0 [Accessed 27th May, 2014].

Vajeeston, P., Ravindran, P. & Fjellvag, H. (2007) A new series of high hydrogen content hydrogen-storage materials - A theoretical prediction, **Journal of Alloys and Compounds***, 446**, 44-47.

Vajeeston, P., Ravindran, P., Hauback, B. C. & Fjellvag, H. (2011) Prediction of crystal structure, lattice dynamical, and mechanical properties of CaB_2H_2, **International Journal of Hydrogen Energy***, 36**, 10149-10158.

Vajeeston, P., Ravindran, P., Kjekshus, A. & Fjellvag, H. (2006) High hydrogen content complex hydrides: A density-functional study, **Applied Physics Letters***, 89**, 071906.

Vajeeston, P., Ravindran, P., Kjekshus, A. & Fjellvag, H. (2008) First-principles investigations of the $MMgH_3$ (M = Li, Na, K, Rb, Cs) series, **Journal of Alloys and Compounds***, 450**, 327-337.

Vajo, J. J., Skeith, S. L. & Mertens, F. (2005) Reversible storage of hydrogen in destabilized $LiBH_4$, **Journal of Physical Chemistry B***, 109**, 3719-3722.

van Setten, M. J., Lohstroh, W. & Fichtner, M. (2009) A new phase in the decomposition of Mg(BH$_4$)$_2$: first-principles simulated annealing, **Journal of Materials Chemistry**, 19**,** 7081-7087.

Varin, R. A., Czujko, T. & Wronski, Z. (2006) Particle size, grain size and gamma-MgH$_2$ effects on the desorption properties of nanocrystalline commercial magnesium hydride processed by controlled mechanical milling, **Nanotechnology**, 17**,** 3856-3865.

Varin, R. A., Czujko, T. & Wronski, Z. (2009) **Nanomaterials for solid state hydrogen storage**, New York, USA, Springer Science+Business Media. LLC, 102-174.

Varin, R. A., Zbroniec, L., Polanski, M. & Bystrzycki, J. (2011) A review of recent advances on the effects of microstructural refinement and nano-catalytic additives on the hydrogen storage properties of metal and complex hydrides, **Energies**, 4**,** 1-25.

Vigeholm, B., Kjøller, J., Larsen, B., Vigeholm, B., Kjøller, J. & Larsen, B. (Year) Magnesium for hydrogen storage. *In:* Libowitz, G. G. & Sandrock, G. D., eds. **Metal Hydrides 1980: Proceedings of the International Symposium on the Properties and Applications of Metal Hydrides,** Colorado, US. Elsevier Science.

von Helmolt, R. & Eberle, U. (2007) Fuel cell vehicles: Status 2007, **Journal of Power Sources**, 165**,** 833-843.

Wahab, M. A., Jia, Y., Yang, D. J., Zhao, H. J. & Yao, X. D. (2013) Enhanced hydrogen desorption from Mg(BH$_4$)$_2$ by combining nanoconfinement and a Ni catalyst, **Journal of Materials Chemistry A**, 1**,** 3471-3478.

Walker, G., Institute of Materials, M. & Mining (2008) **Solid-state hydrogen storage: materials and chemistry**, Woodhead Publishing.

Wang, H., Wu, W., Lu, T., Wang, X., Ge, F., Cao, L., Bai, L. & Dai, Y. (2010) The synthesis of LiBH$_4$ films under low hydrogen pressure at ambient temperature, **Materials Letters**, 64**,** 320-322.

Wang, L. & Yang, R. T. (2008) New sorbents for hydrogen storage by hydrogen spillover - a review, **Energy & Environmental Science**, 1**,** 268-279.

Wang, L. L., Graham, D. D., Robertson, I. M. & Johnson, D. D. (2009) On the reversibility of hydrogen-storage reactions in Ca(BH$_4$)$_2$: characterization via experiment and theory, **Journal of Physical Chemistry C**, 113, 20088-20096.

Westerwaal, R. J. & Haije, W. G. (2008) **Evaluation solid-state hydrogen storage systems: current status**, ECN.

White, C. M., Steeper, R. R. & Lutz, A. E. (2006) The hydrogen-fueled internal combustion engine: a technical review, **International Journal of Hydrogen Energy**, 31**,** 1292-1305.

Wiberg, E. & Bauer, R. (1950) Zur kenntnis eins magnesium-aluminium-wasserstoffs Mg(AlH$_4$)$_2$, **Zeitschrift für Naturforschung Section B-a Journal of Chemical Sciences**, 5**,** 397-398.

Wiberg, E. & Hartwimmer, R. (1955) zur kenntnis von erdalkaliboranaten Me[BH$_4$]$_2$ .3. synthese aus erdalkalihydriden und diboran, **Zeitschrift für naturforschung part B-chemie biochemie biophysik biologie und verwandten gebiete**, 10**,** 295-296.

Wiberg, E., Noth, H. & Hartwimmer, R. (1955) Zur kenntnis von erdalkaliboranaten Me[BH$_4$]$_2$ .1. darstellung aus erdalkali-tetramethoxoboraten und diboran, **Zeitschrift für naturforschung part B-chemie biochemie biophysik biologie und verwandten gebiete**, 10**,** 292-294.

Winter, C. J. (2004) The hydrogen energy economy: an address to the World Economic Forum 2004, **International Journal of Hydrogen Energy**, 29**,** 1095-1097.

Wunderlich, J. A. & Lipscomb, W. N. (1960) Structure of B$_{12}$H$_{12}{}^{2-}$ ion, **Journal of the American Chemical Society**, 82**,** 4427-4428.

Yan, Y., Remhof, A., Hwang, S.-J., Li, H.-W., Mauron, P., Orimo, S.-i. & Zuttel, A. (2012) Pressure and temperature dependence of the decomposition pathway of LiBH$_4$, **Physical Chemistry Chemical Physics**, 14**,** 6514-6519.

REFERENCES

Yan, Y., Remhof, A., Mauron, P., Rentsch, D., Łodziana, Z., Lee, Y.-S., Lee, H.-S., Cho, Y. W. & Züttel, A. (2013a) Controlling the Dehydrogenation Reaction toward Reversibility of the LiBH$_4$–Ca(BH$_4$)$_2$ Eutectic System, **The Journal of Physical Chemistry C**, 117, 8878-8886.

Yan, Y. G., Li, H. W., Maekawa, H., Aoki, M., Noritake, T., Matsumoto, M., Miwa, K., Towata, S. & Orimo, S. (2011) Formation Process of B$_{12}$H$_{12}{}^{2-}$ from BH$_4{}^-$ during the Dehydrogenation Reaction of Mg(BH$_4$)$_2$, **Materials Transactions**, 52, 1443-1446.

Yan, Y. G., Li, H. W., Sato, T., Umeda, N., Miwa, K., Towata, S. & Orimo, S. (2009) Dehydriding and rehydriding properties of yttrium borohydride Y(BH$_4$)$_3$ prepared by liquid-phase synthesis, **International Journal of Hydrogen Energy**, 34, 5732-5736.

Yan, Y. G., Remhof, A., Rentsch, D., Lee, Y. S., Cho, Y. W. & Zuttel, A. (2013b) Is Y$_2$(B$_{12}$H$_{12}$)$_3$ the main intermediate in the decomposition process of Y(BH$_4$)$_3$?, **Chemical Communications**, 49, 5234-5236.

Yang, J. Z., Zhang, X. Z., Zheng, J., Song, P. & Li, X. G. (2011) Decomposition pathway of Mg(BH$_4$)$_2$ under pressure: Metastable phases and thermodynamic parameters, **Scripta Materialia**, 64, 225-228.

Yu, X. B., Grant, D. M. & Walker, G. S. (2006) A new dehydrogenation mechanism for reversible multicomponent borohydride systems-The role of Li-Mg alloys, **Chemical Communications,** 3906-3908.

Yvon, K. & Bertheville, B. (2006) Magnesium based ternary metal hydrides containing alkali and alkaline-earth elements, **Journal of Alloys and Compounds**, 425, 101-108.

Zachariasen, W. H., Stamper, J. F. & Holley, C. E. (1963) Neutron diffraction study of magnesium deuteride, **Acta Crystallographica**, 16, 352-&.

Zaluska, A., Zaluski, L. & Strom-Olsen, J. O. (1999) Nanocrystalline magnesium for hydrogen storage, **Journal of Alloys and Compounds**, 288, 217-225.

Zavorotynska, O., Corno, M., Damin, A., Spoto, G., Ugliengo, P. & Baricco, M. (2011) Vibrational properties of MBH$_4$ and MBF$_4$ crystals (M = Li, Na, K): A combined DFT, Infrared, and Raman Study, **Journal of Physical Chemistry C**, 115, 18890-18900.

Zhang, H. & Kisi, E. (1997) Formation of titanium hydride at room temperature by ball milling, **Journal of Physics: Condensed Matter**, 9, L185–L190.

Zhang, Y., Majzoub, E., Ozoliņš, V. & Wolverton, C. (2012a) Theoretical Prediction of Metastable Intermediates in the Decomposition of Mg(BH$_4$)$_2$, **The Journal of Physical Chemistry C**, 116, 10522-10528.

Zhang, Y. S., Majzoub, E., Ozolins, V. & Wolverton, C. (2010) Theoretical prediction of different decomposition paths for Ca(BH$_4$)$_2$ and Mg(BH$_4$)$_2$, **Physical Review B**, 82, 174107.

Zhang, Z. G., Luo, F. P., Wang, H., Liu, J. W. & Zhu, M. (2012b) Direct synthesis and hydrogen storage characteristics of Mg-B-H compounds, **International Journal of Hydrogen Energy**, 37, 926-931.

Zhang, Z. G., Wang, H., Liu, J. W. & Zhu, M. (2013) Synthesis and hydrogen storage characteristics of Mg-B-H compounds by a gas-solid reaction, **International Journal of Hydrogen Energy**, 38, 5309-5315.

Züttel, A. (2003) Materials for hydrogen storage, **Materials Today**, 6, 24-33.

Züttel, A., Borgschulte, A. & Orimo, S. I. (2007) Tetrahydroborates as new hydrogen storage materials, **Scripta Materialia**, 56, 823-828.

Züttel, A., Rentsch, S., Fischer, P., Wenger, P., Sudan, P., Mauron, P. & Emmenegger, C. (2003a) Hydrogen storage properties of LiBH$_4$, **Journal of Alloys and Compounds**, 356, 515-520.

Züttel, A., Wenger, P., Rentsch, S., Sudan, P., Mauron, P. & Emmenegger, C. (2003b) LiBH$_4$ a new hydrogen storage material, **Journal of Power Sources**, 118, 1-7.

Publications

Publications

- **Sheng Guo**, Hoi Yan Lydia Chan, Daniel Reed, David Book (2013) Investigation of dehydrogenation processes in disordered γ-Mg(BH$_4$)$_2$, *Journal of Alloys and Compounds*, 580, Supplement 1, S296-S300.

- **Sheng Guo**, Jean-Philippe Soulié, Brian Elliot Hayden, Daniel Reed, David Book (2015) Direct Hydrogenation of Li-Mg Alloy by High-energy Reactive Milling, *Journal of Physical Chemistry C*, to be submitted.

Oral Presentations

- **Sheng Guo**, Daniel Reed, David Book (2011) Borohydride-Based Compounds for Use as Hydrogen Storage Media, *UK Sustainable Hydrogen Energy Consortium 3rd Researchers Workshop*, Bath, UK

- **Sheng Guo**, Daniel Reed, David Book (2012) Investigation of Dehydrogenation Processes in γ-Mg(BH$_4$)$_2$, *International Symposium on Metal-Hydrogen Systems (MH2012)*, Kyoto, Japan

- **Sheng Guo**, Daniel Reed, David Book (2014) Alkali and Alkaline-earth Borohydrides for Hydrogen Storage, *8th International Symposium Hydrogen & Energy*, Zhaoqing, China

- Jean-Philippe Soulié, **Sheng Guo**, Daniel Reed, David Book, Brian Elliot Hayden (2014) Optimized Complex Hydride Powder From High-Throughput Screening, *International Symposium on Metal-Hydrogen Systems (MH2014)*, Manchester, UK

Poster Presentations (selected)

- **Sheng Guo**, Daniel Reed, David Book (2011) Higher Boranes in the Decomposition and Formation of LiBH$_4$, *Faraday Discussion 151: Hydrogen Storage Materials*, Didcot, UK

- **Sheng Guo**, Daniel Reed, David Book (2013) The Phase Transformation and Decomposition of Eutectic Mixture 0.68LiBH$_4$+0.32Ca(BH$_4$)$_2$, *Gordon Research Conference & Seminar (GRC & GRS): Hydrogen – Metal Hydride Systems*, Lucca, Italy

- **Sheng Guo** (2013) Hydrogen: A Clean Energy Carrier for Future Energy Needs?, *Universitas 21 Energy Conference*, Dublin, Ireland

- **Sheng Guo**, Jean-Philippe Soulié, Brian Elliot Hayden, Daniel Reed, David Book (2014) Direct Hydrogenation of Li-Mg Alloy by High-energy Reactive Milling, *International Symposium on Metal-Hydrogen Systems (MH2014)*, Manchester, UK (Highly Commended Poster Prize)

List of Figures

LIST OF FIGURES

List of Tables